

A Framework for Enhancing the Accuracy  
of Ultra Precision Machining

A FRAMEWORK FOR ENHANCING THE ACCURACY  
OF ULTRA PRECISION MACHINING

By

PAULA ALEXANDRA MEYER, B.Eng.Soc. (Mechanical Engineering)  
M.Eng.(Mechanical Engineering)  
McMaster University  
Hamilton, Ontario, Canada

A Thesis

Submitted to the School of Graduate Studies  
in Partial Fulfilment of the Requirements  
for the Degree  
Doctor of Philosophy

McMaster University

© Copyright by Paula Alexandra Meyer, July 2009

DOCTOR OF PHILOSOPHY (2009)  
(Mechanical Engineering)

McMaster University  
Hamilton, Ontario

TITLE: A Framework for Enhancing the Accuracy  
of Ultra Precision Machining

AUTHOR: Paula Alexandra Meyer  
B.Eng.Soc. (Mechanical Engineering)  
M.Eng.(Mechanical Engineering)  
McMaster University  
Hamilton, Ontario, Canada

SUPERVISORS: Dr. M.A. Elbestawi  
Dr. S.C. Veldhuis  
Department of Mechanical Engineering  
McMaster University

NUMBER OF PAGES: xxxi, 220

© Copyright 2009

by

Paula Alexandra Meyer

# Abstract

This thesis is titled “A Framework for Enhancing the Accuracy of Ultra Precision Machining.” In this thesis unwanted relative tool / workpiece vibration is identified as a major contributor to workpiece inaccuracy. The phenomenon is studied via *in situ* vibrational measurements during cutting and also by the analysis of the workpiece surface metrology of ultra precision diamond face turned aluminum 6061-T6.

The manifestation of vibrations in the feed and in-feed directions of the workpiece was studied over a broadband of disturbance frequencies. It is found that the waviness error measured on the cut workpiece surface was significantly larger than that caused by the feed marks during cutting. Thus it was established that unwanted relative tool / workpiece vibrations are the dominant source of surface finish error in ultra precision machining.

By deriving representative equations in the polar coordinate system, it was found that the vibrational pattern repeats itself, leading to what are referred to in this thesis as surface finish lobes. The surface finish lobes describe the waviness or form error associated with a particular frequency of unwanted relative tool / workpiece vibration, given a particular feed rate and spindle speed. With the surface finish lobes, the study of vibrations is both simplified and made more systematic. Knowing *a priori* the wavelength range caused by relative tool / workpiece vibration also allows one to

extract considerable vibration content information from a small white light interferometry field of view. It was demonstrated analytically that the error caused by relative tool / workpiece vibration is always distinct from the surface roughness caused by the feed rate. It was also shown that the relative tool / workpiece vibration-induced wavelength in the feed direction has a limited and repeating range. Additionally, multiple disturbance frequencies can produce the same error wavelength on the workpiece surface. Since the meaningful error wavelength range is finite given the size of the part and repeating, study then focussed on this small and manageable range of wavelengths. This range of wavelengths in turn encompasses a broadband range of possible disturbance frequencies, due to the repetition described by the surface finish lobes.

Over this finite range of wavelengths, for different machining conditions, the magnitude of the waviness error resulting on the cut workpiece surface was compared with the actual relative tool / workpiece vibrational magnitude itself. It was found that several opportunities occur in ultra precision machining to mitigate the vibrational effect on the workpiece surface. The first opportunity depends only on the feed rate and spindle speed. Essentially, it is possible to force the wavelength resulting from an unwanted relative tool / workpiece vibration to a near infinite length, thus eliminating its effect in the workpiece feed direction. Further, for a given disturbance frequency, various speed and feed rate combinations are capable of producing this effect. However, this possibility exists only when a single, dominant and fixed disturbance frequency is present in the process.

By considering the tool nose geometry, depth of cut, and vibrational amplitude over the surface finish lobe finite range, it was found that the cutting parameters

exhibit an attenuating or filtering effect on vibrations. Thus, cutting parameters serve to mitigate the vibrational effect on the finished workpiece over certain wavelengths. The filter curves associated with various feed rates were compared. These filter curves describe the magnitude of error on the ultra precision face turned workpiece surface compared with the original unwanted tool / workpiece vibrational magnitude. It was demonstrated with experimental data that these filter curves are physically evident on the ultra precision diamond face turned workpiece surface. It was further shown that the surface roughness on the workpiece surface caused by the feed rate was reduced with relative tool / workpiece vibrations, and in some cases the feed mark wavelength was changed altogether.

Mean arithmetic surface roughness curves were also constructed, and the filtering phenomenon was demonstrated over a broadband of disturbance frequencies. It is well established that a decrease in the feed rate reduces the surface roughness in machining. However, it was demonstrated that the improved surface finish observed with a slower feed rate in ultra precision diamond face turning was actually because it more effectively mitigated the vibrational effect on the workpiece surface over a broadband of disturbance frequencies. Experimental findings validated this observation. By only considering the effect of vibrations on the surface finish waviness error, it was shown that the workpiece diamond face turned with a feed rate of  $2 \mu\text{m} / \text{rev}$  has a mean arithmetic surface roughness,  $R_a$ , that was 43 per cent smaller than when a feed rate of  $10 \mu\text{m} / \text{rev}$  was used.

# Acknowledgements

The author would first like to thank her supervisors, Dr. M. A. Elbestawi and Dr. S. C. Veldhuis, for their support and guidance throughout the course of this work.

The author would also like to express sincere thanks for the McMaster Manufacturing Research Institute (M.M.R.I.) Scholarship of Distinction and Merit, the McMaster University General Motors Ontario Graduate Scholarship in Science and Technology (O.G.S.S.T.), the Ontario Centres of Excellence (O.C.E.) Talent Program Professional Outreach Award - Conference and Tradeshow Travel Award, and the McMaster University Scholarship. Also, thank you to the National Science and Engineering Research Council of Canada (N.S.E.R.C.), the Ontario Centres of Excellence (O.C.E.) and B-Con Engineering Limited for their project funding.

The author would like to thank members of the McMaster University Department of Mechanical Engineering for their friendship and encouragement throughout this degree.

Last but not least, the author wishes to thank her family and friends for their support and encouragement. The author says thank you to her parents for their constant support, encouragement and faith in her. Also, special thanks to Ella, Charlotte, and Busser. Most especially, the author says thank you to Peter for his understanding, incredible support and love.

To my parents

# Contents

<b>Abstract</b>	<b>iv</b>
<b>Acknowledgements</b>	<b>vii</b>
<b>1 Introduction</b>	<b>1</b>
1.1 Scope of Thesis . . . . .	1
1.2 Introductory Concepts . . . . .	2
1.2.1 Accuracy and Vibration . . . . .	2
1.2.2 Face Turning . . . . .	3
1.2.3 Ultra Precision Machining . . . . .	4
1.3 Organization of the Thesis . . . . .	6
<b>2 Literature Review</b>	<b>7</b>
2.1 Introduction . . . . .	7
2.2 Ultra Precision Machining . . . . .	8
2.2.1 Single Crystal Diamond Tooling in Ultra Precision Machining	8
2.2.2 Applications of Ultra Precision Machining . . . . .	8
2.2.3 Workpiece Materials in Ultra Precision Machining . . . . .	9
2.3 Sources of Ultra Precision Machining Vibrations . . . . .	10

2.3.1	Structural Dynamics . . . . .	10
2.3.2	Sources of Environmental Disturbance . . . . .	11
2.3.3	Grain Orientation . . . . .	12
2.3.4	Other Sources of Vibration . . . . .	12
2.4	Active Vibration Isolation and Control . . . . .	13
2.5	Studies of Vibrations Affecting the Workpiece Surface Finish in Ultra Precision Machining . . . . .	15
2.6	Chapter Summary . . . . .	19
<b>3</b>	<b>Vibrations in Ultra Precision Machining</b>	<b>20</b>
3.1	Introduction . . . . .	20
3.2	Significant Vibrations Apparent on the Surface of the Ultra Precision Face Turned Workpiece . . . . .	21
3.2.1	Predicted Geometric Surface Roughness and Vibration in Tra- ditional Machining <i>versus</i> Ultra Precision Machining . . . . .	25
3.2.2	Benefits and Limitations of White Light Interferometry . . . . .	28
3.3	Ultra Precision Machine Tool Structural Vibrations . . . . .	32
3.3.1	Structural Modal Analysis . . . . .	33
3.4	Measurement of <i>In Situ</i> Vibrations During Ultra Precision Machining	38
3.4.1	Sensor Placement and Data Acquisition . . . . .	38
3.5	Chapter Summary . . . . .	45
<b>4</b>	<b>Vibrational Equations and Applications</b>	<b>46</b>
4.1	Introduction . . . . .	46
4.2	Cutting Direction Relative Tool / Workpiece Vibrations . . . . .	47

4.2.1	Factors Limiting the Ability to Discern Vibrations from Surface Metrology in the Cutting Direction . . . . .	49
4.3	Feed Direction Relative Tool / Workpiece Vibrations . . . . .	51
4.3.1	Derivation of Polar Coordinate System Equations . . . . .	52
4.4	Finding the Disturbance Frequency in the White Light Interferometry Image . . . . .	54
4.4.1	Simulation Results . . . . .	56
4.5	The Repeating Nature of Vibrational Manifestation in the Feed Direction	59
4.5.1	Introduction to the Concept of Surface Finish Lobes . . . . .	62
4.6	The Surface Finish Lobes in Ultra Precision Machining . . . . .	65
4.6.1	Effect of Changing the Feed Rate on the Surface Finish Lobes	68
4.6.2	Generating the Surface Finish Lobes Analytically . . . . .	70
4.6.3	Effect of Changing the Spindle Speed on the Surface Finish Lobes	73
4.6.4	Experimental Validation of the Surface Finish Lobes . . . . .	74
4.7	Implications and Potential Applications of the Surface Finish Lobes .	84
4.7.1	Surface Finish Error Characterization with the Surface Finish Lobes . . . . .	84
4.7.2	Surface Finish Error Correction with the Surface Finish Lobes	87
4.7.3	Identifying Ultra Precision Machine Tool Inaccuracies with the Surface Finish Lobes . . . . .	88
4.7.4	Surface Finish Lobes <i>versus</i> Stability Lobes . . . . .	88
4.8	Chapter Summary . . . . .	91
<b>5</b>	<b>The Filtering Effect and Error Mitigation</b>	<b>92</b>
5.1	Introduction . . . . .	92

5.2	Simulating and Assessing Ultra Precision Face Turned Surface Finish in the Presence of Relative / Tool Workpiece Movement . . . . .	93
5.2.1	Surface Finish Errors: Roughness, Waviness and Form . . . . .	94
5.2.2	Tool Orbit . . . . .	96
5.2.3	The Cut Workpiece Surface . . . . .	101
5.2.4	Spatial Frequency Analysis of Relative Tool / Workpiece Move- ment and of the Cut Workpiece Surface . . . . .	102
5.2.5	Surface Roughness in the Presence of Machining Vibrations . . . . .	103
5.2.6	The Bounds of Vibrational Spatial Frequency - Surface Finish Lobes . . . . .	105
5.3	Assembling the Filters - Big Picture Behavior . . . . .	107
5.3.1	Filter Curves for a Feed Rate of $4 \mu\text{m} / \text{rev}$ . . . . .	108
5.3.2	Filter Curves for a Feed Rate of $2 \mu\text{m} / \text{rev}$ . . . . .	118
5.3.3	Cutting Parameter Filtering and the Surface Finish Lobes over a Broadband of Disturbance Frequencies . . . . .	126
5.4	Experimental Validation and Discussion of the Filtering Effect . . . . .	130
5.5	Mitigating the Effects of Vibration in Ultra Precision Machining . . . . .	140
5.5.1	Option 1 for Vibrational Mitigation on the Surface Finish Lobe . . . . .	140
5.5.2	Option 2 for Vibrational Mitigation on the Surface Finish Lobe . . . . .	142
5.5.3	Mean Arithmetic Roughness, $R_a$ . . . . .	144
5.5.4	Cutting Conditions Used to Illustrate the Mitigation of Vibra- tions on the Workpiece Surface . . . . .	145
5.5.5	Filter Curves for a Feed Rate of $10 \mu\text{m} / \text{rev}$ and for a Feed Rate of $2 \mu\text{m} / \text{rev}$ . . . . .	147

5.5.6	Maximum Vibrational Amplitude Discussion With Respect to the Surface Finish Lobes . . . . .	151
5.6	The Filtering and Frequency Shifting Effect of Cutting Parameters on Surface Roughness Error in the Presence of Relative Tool / Workpiece Vibration . . . . .	157
5.6.1	The Vibrational Effect on Feed Lines for a Feed Rate of 10 $\mu\text{m}$ / rev . . . . .	158
5.6.2	The Vibrational Effect on Feed Lines for a Feed Rate of 2 $\mu\text{m}$ / rev . . . . .	159
5.7	The Filtering Effect of Cutting Parameters on Vibration According to Mean Arithmetic Roughness, $R_a$ . . . . .	160
5.7.1	Filtering the Cut Workpiece Surface to Properly Attribute the Error Source . . . . .	160
5.7.2	Comparing Low Pass Filtered Mean Arithmetic Roughness Curves	167
5.8	Experimental Validation of Vibrational Mitigation and Discussion . .	171
5.9	Chapter Summary . . . . .	186
<b>6</b>	<b>Contributions and Conclusions</b>	<b>187</b>
6.1	Contributions . . . . .	187
6.1.1	Publications . . . . .	188
6.2	Conclusions . . . . .	190
<b>A</b>	<b>Additional Experimental Information</b>	<b>191</b>
A.1	Sensor Details . . . . .	191
A.2	<i>In Situ</i> Cutting Accelerometer Data . . . . .	192

A.2.1	Spindle Speed of 1000 RPM and Feed Rate of 2 micrometres per revolution, Radius 1 . . . . .	192
A.2.2	Spindle Speed of 1000 RPM and Feed Rate of 2 micrometres per revolution, Radius 2 . . . . .	195
A.2.3	Spindle Speed of 1201.3 RPM and Feed Rate of 4 micrometres per revolution . . . . .	198
A.2.4	Spindle Speed of 1196.3 RPM and Feed Rate of 10 micrometres per revolution . . . . .	201
<b>B</b>	<b>Mean Arithmetic Roughness, <math>R_a</math>, Curves</b>	<b>204</b>
B.1	Predicted Mean Arithmetic Roughness Curves for a Feed Rate of 10 $\mu\text{m} / \text{rev}$ . . . . .	204
B.2	Predicted Mean Arithmetic Roughness Curves for a Feed Rate of 2 $\mu\text{m}$ / rev . . . . .	210
	<b>Bibliography</b>	<b>215</b>

# List of Figures

1.1	Accuracy, surface roughness, surface texture and related concepts defined	3
1.2	Face turning on the ASG 2500 . . . . .	4
1.3	Face turning and surface finish parameters . . . . .	5
1.4	Relative tool / workpiece movement . . . . .	5
3.1	Illustration of face turned workpiece and white light interferometry location . . . . .	22
3.2	An ultra precision diamond face turned workpiece and white light interferometry image of the workpiece surface . . . . .	22
3.3	Workpiece surface metrology showing cutting, feed and in-feed direction	23
3.4	White light interferometry measurement of face turned surface showing dominant waviness pattern, $N = 1196.3$ RPM, $f = 10 \mu\text{m} / \text{rev}$ , zoom 200x . . . . .	25
3.5	Feed direction segment of white light interferometry showing significant waviness pattern, $\lambda_{\text{dominant}}$ , $N = 1196.3$ RPM, $f = 10 \mu\text{m} / \text{rev}$ . . . .	26
3.6	Zoomed view of the feed direction segment showing significant waviness pattern, $\lambda_{\text{dominant}}$ , $N = 1196.3$ RPM, $f = 10 \mu\text{m} / \text{rev}$ . . . . .	27
3.7	FFT in the feed direction segment showing significant waviness pattern compared with the feed, $N = 1196.3$ RPM, $f = 10 \mu\text{m} / \text{rev}$ . . . . .	28

3.8	Feed rate normalized horizontal axis FFT in the feed direction segment showing significant waviness pattern compared with the feed, $N = 1196.3$ RPM, $f = 10 \mu\text{m} / \text{rev}$ . . . . .	29
3.9	ASG ultra precision machine tool . . . . .	34
3.10	Kulite sensor on ASG 2500 for modal testing . . . . .	35
3.11	Spindle impact locations ASG 2500 for modal testing . . . . .	35
3.12	Tool and spindle impact locations ASG 2500 for modal testing . . . . .	36
3.13	Kulite accelerometer to Kistler force sensor cross spectrum and coherence for horizontal base hit . . . . .	37
3.14	Kulite accelerometer to Kistler force sensor cross spectrum and coherence for horizontal spindle housing hit . . . . .	37
3.15	Face turning experimental set-up on ASG 2500 showing accelerometer placement . . . . .	39
3.16	Data acquisition for in-feed vibration measurement on the ASG 2500 . . . . .	39
3.17	Aluminum workpiece ultra precision face turned with diamond, $N = 1200$ RPM, $f = 10 \mu\text{m} / \text{rev}$ . . . . .	40
3.18	Measured relative tool / spindle acceleration, $N = 1200$ RPM, $f = 10 \mu\text{m} / \text{rev}$ . . . . .	41
3.19	Spindle acceleration FFT, $N = 1200$ RPM, $f = 10 \mu\text{m} / \text{rev}$ , number of averages = 103, $\Delta f = 0.8548$ Hz . . . . .	42
3.20	Tool acceleration FFT, $N = 1200$ RPM, $f = 10 \mu\text{m} / \text{rev}$ , number of averages = 103, $\Delta f = 0.8548$ Hz . . . . .	42
3.21	Relative tool / workpiece acceleration FFT, $N = 1200$ RPM, $f = 10 \mu\text{m} / \text{rev}$ , number of averages = 103, $\Delta f = 0.8548$ Hz . . . . .	43

3.22	Relative tool / workpiece vibrations observed during cutting and on workpiece surface . . . . .	44
4.1	Spiral on the workpiece surface and viewing the time series . . . . .	48
4.2	Workpiece on spindle, tool, feed direction and in-feed relative tool / workpiece motion . . . . .	48
4.3	Sparsely sampled time series geometry from white light interferometry	51
4.4	Radial segmentation of workpiece . . . . .	52
4.5	Simulated Zygo surface, $f_d = 4976$ Hz, $N = 1200$ RPM, $f = 10 \mu\text{m} / \text{rev}$	57
4.6	Simulated first and last radial lines, $f_d = 4976$ Hz, $N = 1200$ RPM, $f = 10 \mu\text{m} / \text{rev}$ . . . . .	57
4.7	Magnitude and phase of first 20 simulated radial lines . . . . .	58
4.8	Radial in-feed vibration for different disturbance frequencies resulting in identical feed direction wavelength . . . . .	61
4.9	Radial in-feed vibration for different disturbance frequencies resulting in identical feed direction wavelength . . . . .	62
4.10	Radial lines (spokes) showing repeating vibrational pattern for a range of disturbance frequencies, $N = 1200$ RPM, $f = 10 \mu\text{m} / \text{rev}$ , with arrows drawn at the 19 Hz, 29 Hz and 37 Hz radial lines . . . . .	63
4.11	Radial in-feed vibration lines for disturbance frequencies of 19 Hz, 29 Hz and 37 Hz . . . . .	64
4.12	Surface finish lobes from FFT Method for $N = 1200$ RPM and $f = 10 \mu\text{m} / \text{rev}$ . . . . .	66
4.13	Inverse surface finish lobes from the FFT method for $N = 1200$ RPM and $f = 10 \mu\text{m} / \text{rev}$ . . . . .	69

4.14	Surface finish lobes the from FFT method for $N = 1200$ RPM, and $f = 4 \mu\text{m} / \text{rev}$ compared with $N = 1200$ RPM, and $f = 10 \mu\text{m} / \text{rev}$ .	70
4.15	Surface finish lobes from the analytical method for $f = 10 \mu\text{m} / \text{rev}$ , and $N = 600$ RPM and $N = 1200$ RPM . . . . .	74
4.16	Ultra precision face turned workpiece surface measured via white light interferometry at 10 mm from the outer radius showing dominant waviness patterns, zoom 260x . . . . .	76
4.17	White light interferometry measured workpiece section in the feed direction compared with simulated feed lines . . . . .	77
4.18	Feed direction spatial frequency results of workpiece surface measured via white light interferometry at 10 mm from the outer radius . . . . .	78
4.19	Relative tool / workpiece displacement FFT and corresponding surface finish lobes for the frequency range of 320 to 440 Hz . . . . .	81
4.20	Relative tool / workpiece displacement FFT and corresponding surface finish lobes for the frequency range of 700 to 860 Hz . . . . .	83
4.21	Relative tool / workpiece displacement FFT and corresponding surface finish lobes for the frequency range of 4940 to 5010 Hz . . . . .	85
4.22	Feed direction surface finish error type caused by relative tool / workpiece vibration for $N = 1200$ RPM, and $f = 10 \mu\text{m} / \text{rev}$ , and workpiece radius of 50 mm . . . . .	86
4.23	Resulting spatial frequency for various spindle speed and feed rate combinations with constant disturbance frequency, $f_d = 37$ Hz . . . . .	89
4.24	Spatial frequency approaching zero for various spindle speed and feed rate combinations with constant disturbance frequency, $f_d = 37$ Hz .	90

5.1	In-feed relative tool / workpiece motion, feed direction, tool, and workpiece on spindle . . . . .	93
5.2	Relative tool / workpiece harmonic motion and tool incremented by the feed rate . . . . .	94
5.3	Simulation of relative tool workpiece movement, cut workpiece surface and FFT results $f = 4 \mu\text{m} / \text{rev}$ , $d = 5 \mu\text{m}$ , $R_n = 0.630 \text{ mm}$ , $z_{amp} = 5 \text{ nm}$ , and $\nu = 8 \text{ 1/mm}$ . . . . .	95
5.4	Tool orbit definitions . . . . .	97
5.5	The tool orbit showing the discretization of the tool surface, for $f = 4 \mu\text{m} / \text{rev}$ , $d = 5 \mu\text{m}$ , $R_n = 0.630 \text{ mm}$ , $z_{amp} = 15 \text{ nm}$ , and $\nu = 70 \text{ 1/mm}$ . . . . .	99
5.6	Finding tool nose coordinates for each pass . . . . .	100
5.7	The tool orbit and the relative tool / workpiece movement, 10 passes, for $f = 4 \mu\text{m} / \text{rev}$ , $d = 5 \mu\text{m}$ , $R_n = 0.630 \text{ mm}$ , $z_{amp} = 15 \text{ nm}$ , and $\nu = 70 \text{ 1/mm}$ . . . . .	101
5.8	The relative tool / workpiece movement and the cut workpiece surface for $f = 4 \mu\text{m} / \text{rev}$ , $d = 5 \mu\text{m}$ , $R_n = 0.630 \text{ mm}$ , $z_{amp} = 15 \text{ nm}$ , and $\nu = 70 \text{ 1/mm}$ . . . . .	102
5.9	The FFT magnitude of relative tool / workpiece movement and of the cut workpiece surface for $f = 4 \mu\text{m} / \text{rev}$ , $d = 5 \mu\text{m}$ , $R_n = 0.630 \text{ mm}$ , $z_{amp} = 15 \text{ nm}$ , and $\nu = 70 \text{ 1/mm}$ . . . . .	103
5.10	Surface finish lobes for $N = 1201.3 \text{ RPM}$ and $f = 4 \mu\text{m} / \text{rev}$ . . . . .	106
5.11	Surface finish lobes for $N = 1000 \text{ RPM}$ and $f = 2 \mu\text{m} / \text{rev}$ . . . . .	106
5.12	Filtering effect based on FFT results for $d = 5 \mu\text{m}$ , $R_n = 0.630 \text{ mm}$ , $f = 4 \mu\text{m} / \text{rev}$ , and $z_{amp} = 5 \text{ nm}$ . . . . .	109

5.13	Simulation of relative tool workpiece movement, cut workpiece surface and FFT results $f = 4 \mu\text{m} / \text{rev}$ , $d = 5 \mu\text{m}$ , $R_n = 0.630 \text{ mm}$ , $z_{amp} = 5 \text{ nm}$ , and $\nu = 70 \text{ 1/mm}$ . . . . .	110
5.14	Filtering effect based on FFT results for $d = 5 \mu\text{m}$ , $R_n = 0.630 \text{ mm}$ , $f = 4 \mu\text{m} / \text{rev}$ , and $z_{amp} = 10 \text{ nm}$ . . . . .	112
5.15	Filtering effect based on FFT results for $d = 5 \mu\text{m}$ , $R_n = 0.630 \text{ mm}$ , $f = 4 \mu\text{m} / \text{rev}$ , and $z_{amp} = 15 \text{ nm}$ . . . . .	114
5.16	Simulation of relative tool workpiece movement, cut workpiece surface and FFT results $f = 4 \mu\text{m} / \text{rev}$ , $d = 5 \mu\text{m}$ , $R_n = 0.630 \text{ mm}$ , $z_{amp} = 15 \text{ nm}$ , and $\nu = 116 \text{ 1/mm}$ . . . . .	115
5.17	Simulation of relative tool workpiece movement, cut workpiece surface and FFT results $f = 4 \mu\text{m} / \text{rev}$ , $d = 5 \mu\text{m}$ , $R_n = 0.630 \text{ mm}$ , $z_{amp} = 15 \text{ nm}$ , and $\nu = 100 \text{ 1/mm}$ . . . . .	116
5.18	The shifting of the dominant spatial frequency caused by the tool interference . . . . .	117
5.19	Filtering effect based on FFT results for $d = 5 \mu\text{m}$ , $R_n = 0.630 \text{ mm}$ , $f = 2 \mu\text{m} / \text{rev}$ , and $z_{amp} = 5 \text{ nm}$ . . . . .	119
5.20	Filtering effect based on FFT results for $d = 5 \mu\text{m}$ , $R_n = 0.630 \text{ mm}$ , $f = 2 \mu\text{m} / \text{rev}$ , and $z_{amp} = 10 \text{ nm}$ . . . . .	120
5.21	Filtering effect based on FFT results for $d = 5 \mu\text{m}$ , $R_n = 0.630 \text{ mm}$ , $f = 2 \mu\text{m} / \text{rev}$ , and $z_{amp} = 15 \text{ nm}$ . . . . .	122
5.22	Simulation of relative tool workpiece movement, cut workpiece surface and FFT results $f = 2 \mu\text{m} / \text{rev}$ , $d = 5 \mu\text{m}$ , $R_n = 0.630 \text{ mm}$ , $z_{amp} = 15 \text{ nm}$ , and $\nu = 165 \text{ 1/mm}$ . . . . .	123

5.23	Regions 1 through 4 showing the shifting of the dominant spatial frequency caused by the tool interference . . . . .	124
5.24	Three dimensional representation of regions 1 through 4 showing the shifting of the dominant spatial frequency caused by the tool interference	125
5.25	Surface finish lobes and maximum vibrational amplitude, $N = 1000$ RPM and $f = 2 \mu\text{m} / \text{rev}$ , $d = 5 \mu\text{m}$ , $R_n = 0.630 \text{ mm}$ , $z_{amp} = 15 \text{ nm}$	127
5.26	Simulated surfaces illustrating workpiece waviness, $N = 1000$ RPM and $f = 2 \mu\text{m} / \text{rev}$ , $d = 5 \mu\text{m}$ , $R_n = 0.630 \text{ mm}$ , $z_{amp} = 15 \text{ nm}$ . . . .	128
5.27	The surface finish lobe where the spatial frequency is zero, $f = 2 \mu\text{m} / \text{rev}$ . . . . .	129
5.28	Relative tool / workpiece acceleration FFT of $f = 4 \mu\text{m} / \text{rev}$ and $N = 1201.3$ RPM measured during ultra precision face turning on the ASG 2500, number of averages = 103, $\Delta f = 0.8548 \text{ Hz}$ . . . . .	131
5.29	Relative tool / workpiece acceleration FFT of $f = 2 \mu\text{m} / \text{rev}$ and $N = 1000$ RPM measured during ultra precision face turning on the ASG 2500, number of averages = 103, $\Delta f = 0.8548 \text{ Hz}$ . . . . .	132
5.30	Workpiece white light interferometry measured surface, $f = 4 \mu\text{m} / \text{rev}$ , $N = 1201.3$ RPM, $d = 5 \mu\text{m}$ , $R_n = 0.630 \text{ mm}$ . . . . .	134
5.31	Workpiece white light interferometry measured surface, $f = 2 \mu\text{m} / \text{rev}$ , $N = 1000$ RPM, $d = 5 \mu\text{m}$ , $R_n = 0.630 \text{ mm}$ . . . . .	135
5.32	White light interferometry measured cut workpiece surface for $f = 4 \mu\text{m} / \text{rev}$ , $N = 1201.3$ RPM, $d = 5 \mu\text{m}$ , $R_n = 0.630 \text{ mm}$ . . . . .	136

5.33	White light interferometry measured cut workpiece surface and simulated filter lines for $f = 4 \mu\text{m} / \text{rev}$ , $N = 1201.3 \text{ RPM}$ , $d = 5 \mu\text{m}$ , $R_n = 0.630 \text{ mm}$ . . . . .	137
5.34	White light interferometry measured cut workpiece surface for $f = 2 \mu\text{m} / \text{rev}$ , $N = 1000 \text{ RPM}$ , $d = 5 \mu\text{m}$ , $R_n = 0.630 \text{ mm}$ . . . . .	138
5.35	White light interferometry measured cut workpiece surface and simulated filter lines for $f = 2 \mu\text{m} / \text{rev}$ , $N = 1000 \text{ RPM}$ , $d = 5 \mu\text{m}$ , $R_n = 0.630 \text{ mm}$ . . . . .	139
5.36	Regions of opportunity to mitigate the vibrational effect on the cut workpiece surface, $N = 1000 \text{ RPM}$ and $f = 2 \mu\text{m} / \text{rev}$ , $d = 5 \mu\text{m}$ , $R_n = 0.630 \text{ mm}$ , $z_{amp} = 15 \text{ nm}$ . . . . .	141
5.37	Effect of deviation of spindle speed from nominal on the resulting surface finish lobe . . . . .	143
5.38	Filtering effect based on FFT results for $d = 5 \mu\text{m}$ , $R_n = 0.630 \text{ mm}$ , $f = 10 \mu\text{m} / \text{rev}$ , and $z_{amp} = 5 \text{ nm}$ . . . . .	148
5.39	Filtering effect based on FFT results for $d = 5 \mu\text{m}$ , $R_n = 0.630 \text{ mm}$ , $f = 10 \mu\text{m} / \text{rev}$ , and $z_{amp} = 10 \text{ nm}$ . . . . .	148
5.40	Filtering effect based on FFT results for $d = 5 \mu\text{m}$ , $R_n = 0.630 \text{ mm}$ , $f = 10 \mu\text{m} / \text{rev}$ , and $z_{amp} = 15 \text{ nm}$ . . . . .	149
5.41	Filtering effect based on FFT results for $d = 5 \mu\text{m}$ , $R_n = 0.630 \text{ mm}$ , $f = 10 \mu\text{m} / \text{rev}$ , and $z_{amp} = 20 \text{ nm}$ . . . . .	149
5.42	Filtering effect based on FFT results for $d = 5 \mu\text{m}$ , $R_n = 0.630 \text{ mm}$ , $f = 2 \mu\text{m} / \text{rev}$ , and $z_{amp} = 20 \text{ nm}$ . . . . .	150

5.43	Surface finish lobes and maximum vibrational amplitude, $N = 1000$ RPM and $f = 10 \mu\text{m} / \text{rev}$ , $d = 5 \mu\text{m}$ , $R_n = 0.630 \text{ mm}$ , $z_{amp} = 15 \text{ nm}$	151
5.44	Surface finish lobes and regions of best vibrational attenuation for $f = 10 \mu\text{m} / \text{rev}$ , $N = 1196.3 \text{ RPM}$ , $d = 5 \mu\text{m}$ , $R_n = 0.630 \text{ mm}$ , $z_{amp} = 15 \text{ nm}$	153
5.45	Surface finish lobes and regions of best vibrational attenuation for $f = 2 \mu\text{m} / \text{rev}$ , $N = 1196.3 \text{ RPM}$ , $d = 5 \mu\text{m}$ , $R_n = 0.630 \text{ mm}$ , $z_{amp} = 15 \text{ nm}$	154
5.46	Summary of vibrational attenuation results for $f = 10 \mu\text{m} / \text{rev}$ and $f = 2 \mu\text{m} / \text{rev}$ , $d = 5 \mu\text{m}$ , $R_n = 0.630 \text{ mm}$ , $z_{amp} = 15 \text{ nm}$	155
5.47	Maximum vibrational amplitude for $f = 2 \mu\text{m} / \text{rev}$ and $N = 1000 \text{ RPM}$ , and $f = 10 \mu\text{m} / \text{rev}$ and $N = 1196.3 \text{ RPM}$ , $d = 5 \mu\text{m}$ , $R_n = 0.630 \text{ mm}$ , $z_{amp} = 15 \text{ nm}$	156
5.48	Magnitude of surface roughness (caused by feed), based on FFT results, for $d = 5 \mu\text{m}$ , $R_n = 0.630 \text{ mm}$ , $f = 10 \mu\text{m} / \text{rev}$ , and $z_{amp} = 5 \text{ nm}$ , $10 \text{ nm}$ , $15 \text{ nm}$ and $20 \text{ nm}$	159
5.49	Filtering effect on the surface roughness, based on FFT results, for $d = 5 \mu\text{m}$ , $R_n = 0.630 \text{ mm}$ , $f = 2 \mu\text{m} / \text{rev}$ , and $z_{amp} = 5 \text{ nm}$	161
5.50	Filtering effect on the surface roughness, based on FFT results, for $d = 5 \mu\text{m}$ , $R_n = 0.630 \text{ mm}$ , $f = 2 \mu\text{m} / \text{rev}$ , and $z_{amp} = 15 \text{ nm}$	162
5.51	Ninth order low pass Butterworth filter for cut surface simulation data, $f = 10 \mu\text{m} / \text{rev}$ , cut-off $\nu = 70 \text{ 1/mm}$	164
5.52	Ninth order high pass Butterworth filter for cut surface simulation data, $f = 10 \mu\text{m} / \text{rev}$ , cut-off $\nu = 70 \text{ 1/mm}$	165

5.53	Ninth order low pass Butterworth filter for cut surface simulation data, f = 2 $\mu\text{m}$ / rev, cut-off $\nu = 260$ 1/mm . . . . .	166
5.54	Ninth order high pass Butterworth filter for cut surface simulation data, f = 2 $\mu\text{m}$ / rev, cut-off $\nu = 260$ 1/mm . . . . .	166
5.55	Comparing low pass filtered data $R_a$ curves for different machining conditions, d = 5 $\mu\text{m}$ , $R_n = 0.630$ mm, , and $z_{amp} = 5$ nm . . . . .	168
5.56	Comparing low pass filtered data $R_a$ curves for different machining conditions, d = 5 $\mu\text{m}$ , $R_n = 0.630$ mm, , and $z_{amp} = 10$ nm . . . . .	168
5.57	Comparing low pass filtered data $R_a$ curves for different machining conditions, d = 5 $\mu\text{m}$ , $R_n = 0.630$ mm, , and $z_{amp} = 15$ nm . . . . .	169
5.58	Comparing low pass filtered data $R_a$ curves for different machining conditions, d = 5 $\mu\text{m}$ , $R_n = 0.630$ mm, , and $z_{amp} = 20$ nm . . . . .	169
5.59	Average $R_a$ values for each machining condition for all vibration am- plitudes, d = 5 $\mu\text{m}$ , $R_n = 0.630$ mm . . . . .	170
5.60	Comparing low pass filtered data $R_a$ curves with different spindle speeds, d = 5 $\mu\text{m}$ , $R_n = 0.630$ mm, f = 2 $\mu\text{m}$ / rev, and $z_{amp} =$ 20 nm . . . . .	171
5.61	Workpiece 1 white light interferometry measured surface, f = 10 $\mu\text{m}$ / rev, $N_{nominal} = 1196.3$ RPM, d = 5 $\mu\text{m}$ , $R_n = 0.630$ mm . . . . .	173
5.62	FFT of the white light interferometry measured cut workpiece 1 surface for f = 10 $\mu\text{m}$ / rev, N = 1196.3 RPM, d = 5 $\mu\text{m}$ , $R_n = 0.630$ mm .	174
5.63	The resulting cut workpiece surface error amplitude (filtering effect) based on FFT results for f = 10 $\mu\text{m}$ / rev, N = 1196.3 RPM, d = 5 $\mu\text{m}$ , $R_n = 0.630$ mm . . . . .	174

5.64	Workpiece 2 white light interferometry measured surface, $f = 2 \mu\text{m} / \text{rev}$ , $N_{\text{nominal}} = 1000 \text{ RPM}$ , $d = 5 \mu\text{m}$ , $R_n = 0.630 \text{ mm}$ . . . . .	176
5.65	FFT of the white light interferometry measured cut workpiece 2 surface for $f = 2 \mu\text{m} / \text{rev}$ , $N = 1196.3 \text{ RPM}$ , $d = 5 \mu\text{m}$ , $R_n = 0.630 \text{ mm}$ . .	177
5.66	Relative tool / workpiece acceleration FFT for workpiece 1, $N = 1196.3 \text{ RPM}$ , $f = 10 \mu\text{m} / \text{rev}$ , number of averages = 103, $\Delta f = 0.8548 \text{ Hz}$ .	178
5.67	Relative tool / workpiece acceleration FFT for workpiece 2, $N = 1000 \text{ RPM}$ , $f = 2 \mu\text{m} / \text{rev}$ , number of averages = 103, $\Delta f = 0.8548 \text{ Hz}$ . .	179
5.68	Low pass filtered white light interferometry measured workpiece 1 segment $f = 10 \mu\text{m} / \text{rev}$ , $N = 1196.3 \text{ RPM}$ , $d = 5 \mu\text{m}$ , $R_n = 0.630 \text{ mm}$ . . . . .	180
5.69	$R_a$ for each feed direction segment of the white light interferometry workpiece 1 image, $f = 10 \mu\text{m} / \text{rev}$ , $N = 1196.3 \text{ RPM}$ , $d = 5 \mu\text{m}$ , $R_n = 0.630 \text{ mm}$ . . . . .	181
5.70	Simulated workpiece 1 cut surface based on the top two peaks of figure 5.62 and the filter curves of figures 5.41 and 5.40, $f = 10 \mu\text{m} / \text{rev}$ .	183
5.71	Simulated workpiece 1 cut surface based on the top two peaks of figure 5.62 and the filter curves of figures 5.41 and 5.40, with low pass filtering, $f = 10 \mu\text{m} / \text{rev}$ . . . . .	184
5.72	$R_a$ for each feed direction segment of the white light interferometry workpiece 2 image, $f = 2 \mu\text{m} / \text{rev}$ , $N = 1196.3 \text{ RPM}$ , $d = 5 \mu\text{m}$ , $R_n = 0.630 \text{ mm}$ . . . . .	185
A.1	Measured relative tool / spindle acceleration, $N = 1000 \text{ RPM}$ , $f = 2 \mu\text{m} / \text{rev}$ . . . . .	192

A.2	Spindle acceleration FFT, $N = 1000$ RPM, $f = 2 \mu\text{m} / \text{rev}$ , number of averages = 103, $\Delta f = 0.8548$ Hz . . . . .	193
A.3	Tool acceleration FFT, $N = 1000$ RPM, $f = 2 \mu\text{m} / \text{rev}$ , number of averages = 103, $\Delta f = 0.8548$ Hz . . . . .	194
A.4	Measured relative tool / spindle acceleration, $N = 1000$ RPM, $f = 2 \mu\text{m} / \text{rev}$ . . . . .	195
A.5	Spindle acceleration FFT, $N = 1000$ RPM, $f = 2 \mu\text{m} / \text{rev}$ , number of averages = 103, $\Delta f = 0.8548$ Hz . . . . .	196
A.6	Tool acceleration FFT, $N = 1000$ RPM, $f = 2 \mu\text{m} / \text{rev}$ , number of averages = 103, $\Delta f = 0.8548$ Hz . . . . .	197
A.7	Measured relative tool / spindle acceleration, $N = 1201.3$ RPM, $f = 4 \mu\text{m} / \text{rev}$ . . . . .	198
A.8	Spindle acceleration FFT, $N = 1201.3$ RPM, $f = 4 \mu\text{m} / \text{rev}$ , number of averages = 103, $\Delta f = 0.8548$ Hz . . . . .	199
A.9	Tool acceleration FFT, $N = 1201.3$ RPM, $f = 4 \mu\text{m} / \text{rev}$ , number of averages = 103, $\Delta f = 0.8548$ Hz . . . . .	200
A.10	Measured relative tool / spindle acceleration, $N = 1196.3$ RPM, $f = 10 \mu\text{m} / \text{rev}$ . . . . .	201
A.11	Spindle acceleration FFT, $N = 1196.3$ RPM, $f = 10 \mu\text{m} / \text{rev}$ , number of averages = 103, $\Delta f = 0.8548$ Hz . . . . .	202
A.12	Tool acceleration FFT, $N = 1196.3$ RPM, $f = 10 \mu\text{m} / \text{rev}$ , number of averages = 103, $\Delta f = 0.8548$ Hz . . . . .	203
B.1	$R_a$ from simulated cut surface, $d = 5 \mu\text{m}$ , $R_n = 0.630$ mm, $f = 10 \mu\text{m} / \text{rev}$ , and $z_{amp} = 5$ nm . . . . .	205

B.2	$R_a$ from simulated cut surface, $d = 5 \mu\text{m}$ , $R_n = 0.630 \text{ mm}$ , $f = 10 \mu\text{m}$ / rev, and $z_{amp} = 10 \text{ nm}$ . . . . .	207
B.3	$R_a$ from simulated cut surface, $d = 5 \mu\text{m}$ , $R_n = 0.630 \text{ mm}$ , $f = 10 \mu\text{m}$ / rev, and $z_{amp} = 15 \text{ nm}$ . . . . .	208
B.4	$R_a$ from simulated cut surface, $d = 5 \mu\text{m}$ , $R_n = 0.630 \text{ mm}$ , $f = 10 \mu\text{m}$ / rev, and $z_{amp} = 20 \text{ nm}$ . . . . .	209
B.5	$R_a$ from simulated cut surface, $d = 5 \mu\text{m}$ , $R_n = 0.630 \text{ mm}$ , $f = 2 \mu\text{m}$ / rev, and $z_{amp} = 5 \text{ nm}$ . . . . .	211
B.6	$R_a$ from simulated cut surface, $d = 5 \mu\text{m}$ , $R_n = 0.630 \text{ mm}$ , $f = 2 \mu\text{m}$ / rev, and $z_{amp} = 10 \text{ nm}$ . . . . .	212
B.7	$R_a$ from simulated cut surface, $d = 5 \mu\text{m}$ , $R_n = 0.630 \text{ mm}$ , $f = 2 \mu\text{m}$ / rev, and $z_{amp} = 15 \text{ nm}$ . . . . .	213
B.8	$R_a$ from simulated cut surface, $d = 5 \mu\text{m}$ , $R_n = 0.630 \text{ mm}$ , $f = 2 \mu\text{m}$ / rev, and $z_{amp} = 20 \text{ nm}$ . . . . .	214

# List of Tables

3.1	Zygo zoom, field of view and resolution [62] . . . . .	30
3.2	Measurement and filtering parameters of white light interferometry example, $N = 1200$ RPM, $f = 10 \mu\text{m} / \text{rev}$ . . . . .	31
3.3	Cutting conditions for ultra precision face turning of a 100 mm diam- eter aluminum 6061-T6 workpiece on the ASG 2500, $N = 1200$ RPM, $f = 10 \mu\text{m} / \text{rev}$ . . . . .	40
4.1	Disturbance frequency, wavelength and spatial frequency as depicted for specific disturbance frequencies in surface finish lobes for $N = 1200$ RPM and $f = 10 \mu\text{m} / \text{rev}$ . . . . .	67
4.2	Summary of workpiece peak spatial frequencies found in figure 4.18 .	78
4.3	Summary of disturbance frequency peak displacements and correspond- ing spatial frequencies found in figure 4.18 . . . . .	84
4.4	Definitions of surface finish defects . . . . .	86
5.1	Cutting conditions for finish turning of 100 mm diameter aluminum 6061-T6 workpiece . . . . .	104
5.2	Predicted surface roughness $R_t$ for $f = 4 \mu\text{m} / \text{rev}$ and for $f = 2 \mu\text{m}$ $/ \text{rev}$ , both with $R_n = 0.630$ mm . . . . .	104

5.3	Summary of surface finish lobes for $f = 4 \mu\text{m} / \text{rev}$ and $N = 1201.3$ RPM and for $f = 2 \mu\text{m} / \text{rev}$ and $N = 1000$ RPM . . . . .	105
5.4	Summary of cutting patterns in the feed direction given vibrational amplitude for $f = 4 \mu\text{m} / \text{rev}$ . . . . .	113
5.5	Summary of cutting patterns in the feed direction given vibrational amplitude for $f = 2 \mu\text{m} / \text{rev}$ . . . . .	126
5.6	Rapid change in wavelength near where the surface finish lobe approaches zero ( $\nu, 1/\text{mm}$ ) . . . . .	129
5.7	Measurement and filtering parameters of white light interferometry .	133
5.8	Cutting conditions for finish turning of 100 mm diameter aluminum 6061-T6 workpiece . . . . .	146
5.9	Summary of surface finish lobes for $f = 10 \mu\text{m} / \text{rev}$ and $f = 2 \mu\text{m} / \text{rev}$	146
5.10	Predicted surface roughness $R_t$ for $f = 10 \mu\text{m} / \text{rev}$ and for $f = 2 \mu\text{m} / \text{rev}$ , both with $R_n = 0.630$ mm . . . . .	158
5.11	Measurement and filtering parameters of white light interferometry .	172
5.12	$R_a$ summary for the imported and low pass filtered white light interferometry data of figure 5.61(a) for workpiece 1 . . . . .	181
5.13	$R_a$ summary for the imported and low pass filtered white light interferometry data of figure 5.64(a) for workpiece 2 . . . . .	186
A.1	In-situ vibration measurement accelerometer, selected specifications [23]	191

# Nomenclature

- $\lambda$  Wavelength ( $\mu\text{m}$ )
- $\lambda_f$  Form error wavelength ( $\mu\text{m}$ )
- $\lambda_r$  Surface roughness error wavelength ( $\mu\text{m}$ )
- $\lambda_w$  Waviness error wavelength ( $\mu\text{m}$ )
- $\lambda_{\text{dominant}}$  Dominant wavelength found on the workpiece surface in the feed direction ( $\mu\text{m}$ )
- $\nu$  Spatial frequency (1/mm)
- $\Omega$  Angular velocity (rad / rev)
- $\omega_d$  Disturbance frequency (rad/s)
- $\phi$  Phase angle (rad)
- $\theta$  The angle from the point of tool entry about the center of the workpiece (rad)
- $\vec{x}_{\text{cut}}$  Cut workpiece surface in the feed direction (nm)
- $\vec{z}_{\text{cut}}$  Cut workpiece surface in the in-feed direction (nm)

$d$	Depth of cut ( $\mu\text{m}$ )
$f$	Feed rate ( $\mu\text{m} / \text{rev}$ )
$f_d$	Disturbance frequency (Hz)
$m$	Workpiece revolutions
$N$	Spindle speed (RPM)
$R_n$	Tool nose radius (mm)
$R_t$	Ideal geometric surface roughness (peak-to-valley height) (nm)
$R_t$	Mean arithmetic roughness (nm)
$t$	Time (s)
$x_{inc}$	Feed direction increment describing the tool surface (nm)
$x_{tc}$	Tool center in the feed direction (nm)
$x_{tp}$	Tool surface in the feed direction (nm)
$z$	In-feed direction error (nm)
$z_{amp}$	Amplitude of relative tool / workpiece vibration (nm)
$z_{tc}$	Tool center in the in-feed direction (nm)
$z_{tp}$	Tool surface in the in-feed direction (nm)

# Chapter 1

## Introduction

The title of this thesis is “A Framework for Enhancing the Accuracy of Ultra Precision Machining.” This thesis explores the effect of asynchronous relative tool / workpiece vibrations on surface finish in ultra precision diamond face turning of aluminum. It was found that vibrations are a dominant source of surface finish error in ultra precision machining. In this thesis the manifestation of vibrations on the workpiece surface were studied and analyzed, and a systematic framework was developed to describe and also facilitate mitigation of the vibrational effect on the workpiece surface.

### 1.1 Scope of Thesis

The ultimate objective of this thesis was to improve the accuracy of ultra precision machining. The approach of this work was to make engineering efforts most meaningful and directed. To this end, it was not only considered important to simply control vibrations, but to understand how vibrations impact the finished workpiece.

The thesis focuses on harmonic asynchronous relative tool / workpiece vibration during ultra precision face turning in the workpiece feed and in-feed directions. Analysis shows how the vibration actually affected workpiece accuracy. Also, opportunities for mitigation of vibration based on cutting parameters are described.

## 1.2    Introductory Concepts

### 1.2.1    Accuracy and Vibration

**Accuracy** Listed in order of decreasing wavelength, accuracy can entail geometric feature, form, waviness and surface roughness. This work entails mainly waviness error, and also form and surface roughness. Justification for this scope occurs later with development of workpiece spatial frequency theory. Form, waviness and roughness are all part of the surface finish. Form may also be referred to as shape, or for a nominally flat surface the slope or lay [48]. The surface roughness may be considered to have a wavelength equivalent to the feed. According to [4], the grouping of roughness and waviness are considered the surface texture. These terms and concepts are summarized in figure 1.1. In face turning, the wavelengths associated with form, waviness and surface roughness errors depend on the feed rate and the workpiece size used. Considering measurements in the feed direction, the form error has a wavelength greater than the workpiece radius. The surface roughness error has a wavelength equivalent to the feed rate. Lastly, the waviness error wavelength can be larger than the surface roughness error wavelength, but smaller than the form error wavelength.

**Vibration** Vibration of interest is that between the workpiece and the cutting tool. If relative motion between the tool and workpiece (relative tool / workpiece movement) does not occur, then workpiece accuracy is considered unaffected by vibration.

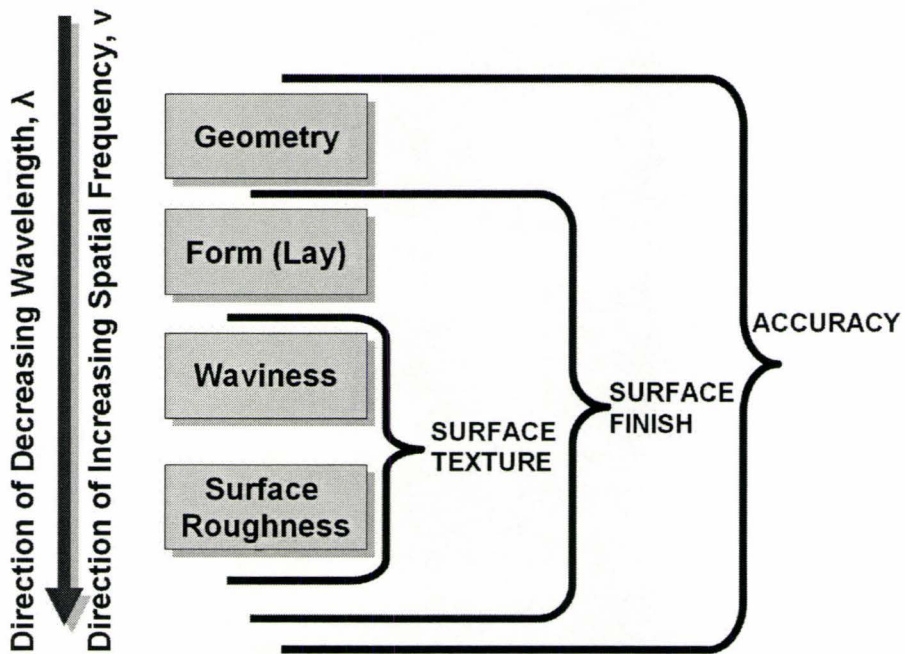


Figure 1.1: Accuracy, surface roughness, surface texture and related concepts defined

### 1.2.2 Face Turning

Face turning of aluminum on a Rank Pneumo ASG 2500 is depicted in figure 1.2. The workpiece is held on the spindle which rotates according to spindle speed,  $N$ , in revolutions per minute (RPM). The cutting tool is on the feed drive which moves across the workpiece face according to the feed rate,  $f$ , in micrometres per revolution ( $\mu\text{m} / \text{rev}$ ). In figure 1.3, the spindle movement of the workpiece, the feed movement

of the tool and the surface finish direction are defined for face turning. The surface finish direction is also called the in-feed direction. The depth of cut,  $d$ , also occurs in the in-feed direction. Accuracy of the surface finish in the in-feed direction is the focus of this thesis. In figure 1.4, the relative tool / workpiece movement in the in-feed direction is defined. The resulting time series is called  $z(t)$ .

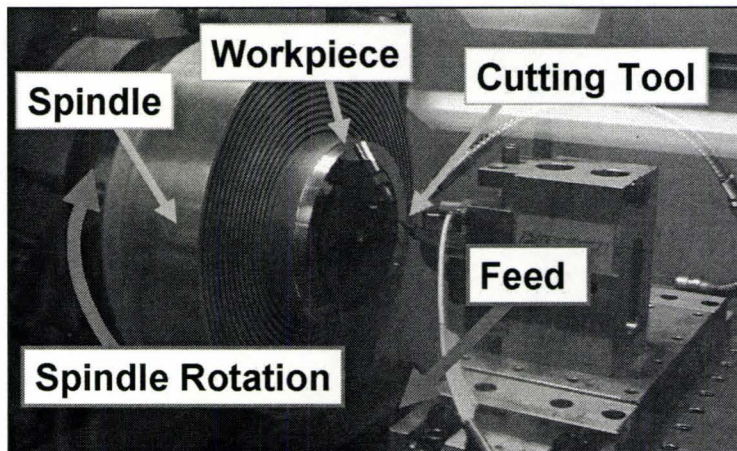


Figure 1.2: Face turning on the ASG 2500

### 1.2.3 Ultra Precision Machining

Ultra precision machining is a special branch of machining which produces parts with micrometric geometries and surface finish on the order of nanometres [20]. According to [5] in [16], the accuracy of ultra precision machining is an order of magnitude greater than that for precision (conventional) machining.

In ultra precision machining, single point diamond cutting tools are often employed to machine brittle non-ferrous materials, such as ceramic and glass. Ductile non-ferrous metals are also diamond turned, such as copper and aluminum. Single point diamond turning is another often encountered description of ultra precision turning

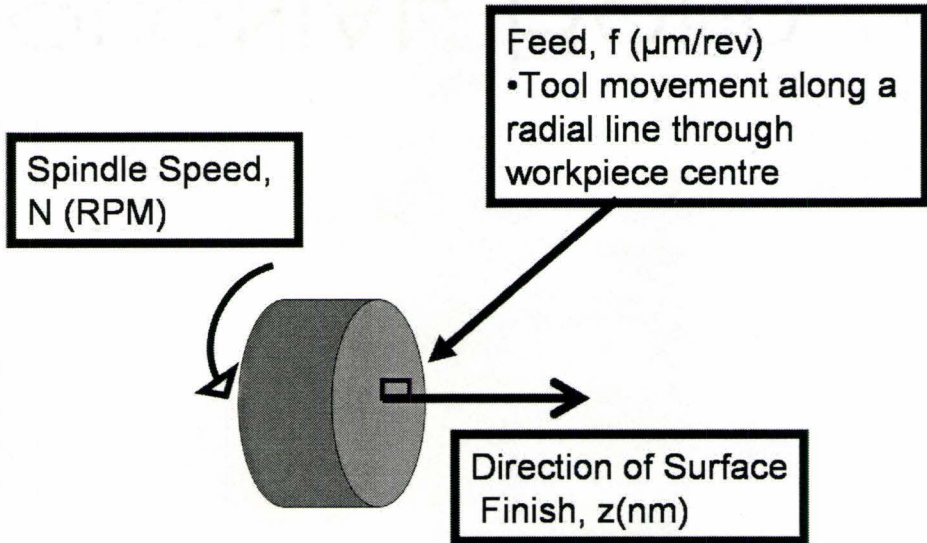


Figure 1.3: Face turning and surface finish parameters

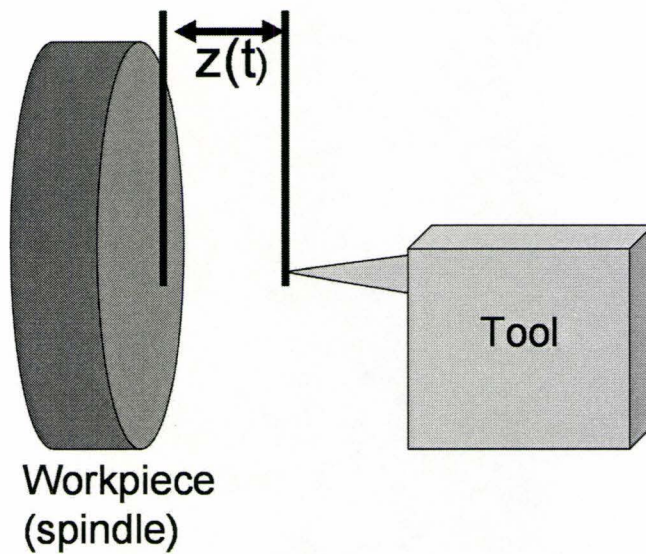


Figure 1.4: Relative tool / workpiece movement

with this particular cutting tool. In this thesis 6061-T6 aluminum was ultra precision face turned with single point diamond on an ASG 2500.

### **1.3 Organization of the Thesis**

This thesis is organized as follows. First is a critical literature survey in chapter 2. Then in chapter 3 vibrations in ultra precision machining are explored. In chapter 4 equations describing relative tool / workpiece vibration are developed in the feed direction of the workpiece, and the surface finish lobes are introduced and described. In chapter 5 the filtering effect of cutting parameters is identified and opportunities for the mitigation of vibrations on the workpiece surface are described in detail. The thesis ends with contributions and conclusions in chapter 6.

## Chapter 2

# Literature Review

### 2.1 Introduction

The literature review begins with a further introduction to ultra precision machining including tooling, applications and workpiece materials. Then some sources of vibrations in ultra precision machine tools found in the literature are discussed. Then active isolation and control of vibrations in ultra precision machining are reviewed. Finally, studies pertaining to the effect of vibrations on the ultra precision machined workpiece are described in detail.

## **2.2    Ultra Precision Machining**

### **2.2.1    Single Crystal Diamond Tooling in Ultra Precision Machining**

The specific type of cutting tool used in this research was a single crystal diamond. Single crystal diamond tools are made from large natural or synthetic diamonds [58]. In [57] it is recommended to use a single crystal diamond tool when a sharp edge is required, for example to create a precise finish or geometry. As a process, single point diamond turning with single crystal diamond tools includes such benefits as form reproducibility, nanometric edge sharpness and wear resistance [20] cited in [10]. As recommended in [31], hard tool material should be employed in ultra precision cutting.

### **2.2.2    Applications of Ultra Precision Machining**

A typical application for single crystal diamond turning is optics. Traditionally optics were produced with techniques such as polishing and lapping. Research in diamond machining presents an alternative form of manufacture for these components [20] cited in [21]. Another industry to benefit from diamond micro machining is the electronics industry [33]. Overall, ultra precision machining has the capacity to create a near mirror surface finish, high-profile accuracy and also low level of subsurface damage [33]. This thesis focuses on surface finish issues in single crystal diamond face turning (ultra precision machining). Ultra precision machined aluminum is found in various applications including disc drives, rotating mirrors and mirrors in lasers [26]. Another application is in the machining of custom photo-copier drums [24]. It is common knowledge in the domain of ultra precision machining that the surface finish

of an ultra precision machined part is such that oxygen cannot attack and oxidize the surface layer. However, if the surface is damaged then oxidation has an initiation site and the surface finish degrades rapidly.

### **2.2.3 Workpiece Materials in Ultra Precision Machining**

In ultra precision machining, typical workpieces include brittle materials such as silicon and glass, and ductile non-ferrous metals like copper and aluminum. Ferrous workpieces, however, are not typically diamond turned, despite the sharp edge offered by a single crystal diamond. This is because the high temperatures incurred during cutting cause a diffusion of the carbon from the diamond into the iron, leading to rapid tool wear [26].

Ultra precision diamond turning of aluminum and copper for mirror-like finish is preferable to other techniques such as grinding, polishing or lapping [33]. This is because other machining methods may scratch the finished surface due to the softness of these metals, and are not able to achieve the flatness requirements at the workpiece edge [33] who cites [52]. Machining metals with optical surface quality is also discussed in [14] where it was observed that an economic benefit is expected since lapping and polishing processes, which are slower processes and often involve manual effort, may be eliminated.

## 2.3 Sources of Ultra Precision Machining Vibrations

### 2.3.1 Structural Dynamics

Referring to machining in general, dynamic forces are described by Slocum [46] as causing the machine to vibrate such that the workpiece surface finish is adversely affected, or the machine is prevented from servoing to the desired position. The causes of these effects are most often structural vibrations and friction [46]. According to Slocum “Precision assembly machines, electron microscopes, diamond-turning machines, and wafer steppers are all examples of machines whose performance relies on isolation from the environment” ([46], p. 105). Diamond turning machines are ultra precision machine tools. Included in the list of potential vibration sources possibly contributing to degradation of machine performance is transmission of vibration through the floor [46]. Similarly, DeBra [15] writes that for a machine tool, the relative tool to workpiece position can be changed due to acceleration induced machine strains from such inputs as ground vibrations.

### Traditional versus Ultra Precision Machine Tool Dynamics

Byrne *et al.* [5] write that process stability is most important for surface quality and accuracy, and “the structural dynamic stiffness of the machine tool mainly influences the machining results” ([5], p. 496). Here, the reference is specifically to high speed machine movements exciting the machine structure. If the use of ultra precision machine tools is to include productive machining of more complex free-form

geometries with a very fine surface finish, then it is expected that ultra precision machine tool stiffness requirements would increase, thus posing a challenge for isolation from environmental disturbance [42].

Also mentioned in [5] is chatter. A general search of books and articles available on machine tool dynamics also brings forth the subject of chatter [53], [2], [54], [49], [25], [3] and [56]. However, chatter is not a prevalent issue in ultra precision machining. According to Marsh *et al.* in [30], chatter is less of a concern in ultra precision machining due to the small depth of cut. The intent of the research presented in [30] is to understand chatter for small cutting depths. In [30], for a diamond turning operation, the normally stiff tool holder is replaced with a more compliant one. The depth of cut employed is large by ultra precision standards at 130 microns. In [9] self-excited chatter, and also tool wear, are explicitly ignored by Cheung and Lee due to the large depth of cut in comparison to the sharpness of the tool used.

### **2.3.2 Sources of Environmental Disturbance**

According to Rivin various sources of vibration exist in the machine tool environment including other machine tools, presses, internal-combustion engines, cranes, compressors, rail and road vehicles and carts, all of which may create vibration transmitted to other machines through the foundation, setting these machines into forced vibration [19]. Further, shop floor vibration contains a frequency spectrum that is wide [19] and might not all be isolated from the machine through its isolation support system. Rivin writes that it is very likely that for a particular machine tool, one of these environmental vibrations should occur near one of that machine tool's natural frequencies [19]. While the vibration amplitude is often small, precision machine tools

and also measuring equipment can be adversely affected [19].

### 2.3.3 Grain Orientation

According to [33], vibrations can also result from workpiece impurities and inhomogeneities as well as polycrystalline workpiece grain boundaries. In turn, these vibrations deteriorate the finished surface [33]. In [27] the material-induced vibration caused by inconsistent workpiece crystal orientation was studied in ultra precision machining. Choi *et al.* write that if there is any randomness in the workpiece profile, it is often a result of tool vibration caused by the grain orientation [12].

In this thesis, asynchronous harmonic relative tool / workpiece vibration was considered and, thus, the effects of grain orientation were not included in the study. Further, the harmonic waviness error on the workpiece surface dominated the observed surface finish error. Also, the source of vibration considered was not limited to structural vibrations excited by environmental disturbances.

### 2.3.4 Other Sources of Vibration

Other vibrational sources also occur in ultra precision machining. In [13] a spindle imbalance is of concern for a diamond turning machine. In Cheung *et al.* [11] axial run-out error of the air bearing spindle is discussed as a vibration source. In [11], this is the largest magnitude error found compared with error due to base excitation. Ikawa *et al.* [20] mention vibrations induced by acoustic noise, and also by imperfect coupling of machine components including spindles, spindle drive motors, errors in the manufacturing of machine components, and eccentricity.

## 2.4 Active Vibration Isolation and Control

In [60] by Yuxian *et al.*, an ultra precision turning machine tool was isolated from floor vibrations with a combination of air springs and electro-magnetic actuators, the latter controlled by fuzzy-neural networks. The air springs were for support and isolation of high-frequency vibrations, while the electro-magnetic actuators were to isolate the machine tool from low-frequency vibration. The authors claim to experimentally show that for all frequency ranges, the base vibration was effectively isolated by the active vibration isolation system. Overall, there was an improvement of workpiece surface roughness. According to Yuxian *et al.*, in each direction the main frequency of vibration was controlled from 1.25 Hz to 12.5 Hz. Surface roughness of a machined Si-workpiece was inspected to show improvements with control. The paper concludes by noting that flat transmissibility characteristics are obtained when suitable feedback gain terms are selected. Overall improvement in the amplitude of vibration from  $10^{-4}$  g to  $10^{-6}$  g was measured. Not discussed in [60] is the relationship between base movement and relative movement between tool and workpiece. It is only asynchronous motion between the cutting tool and the workpiece that leads to surface finish errors. Also, the actual manifestation of relative tool / workpiece motion on the cut workpiece surface is not presented in this work.

In [61], a six-degree of freedom vibration isolation system for an ultra precision grinding machine is presented, providing isolation from ground vibrations. In the system, air springs are passive vibration isolation elements and giant magnetostrictive actuators are active vibration isolation elements. All work presented in [61] is simulation based, and no experimental work is discussed. The authors in [61] mention that because such soft springs are required in passive vibration isolation of environmental

disturbance, positioning accuracy of the system is compromised and, hence, found to not be satisfactory for this application. The active vibration isolation scheme was designed to remedy this issue. In [61], controller feedback is from the position and velocity of the machine's centre of gravity. Simulation work was done for the dynamic model with linear control and with the proposed control scheme, and the results compared. Isolation of ground disturbance at the machine's centre of gravity in x, y and z were examined with noted improvement using the proposed scheme. Again, in [61], the actual relative tool / workpiece movement was not discussed.

In Wang *et al.* [59], active vibration isolation was applied to an ultra precision lathe. This research differed from that presented in [60] and [61] in that isolation occurred on the drive at the tool location. A slide in [59] has an active air bearing, which also provided passive support. A piezo-electric actuator (PZT) changed the air film thickness and PID control was employed [59]. Surface roughness was improved from  $0.02 \mu\text{m}$  to  $0.01 \mu\text{m}$  [59].

On a diamond turning machine Crudele *et al.* in [13] integrated a fast tool servo system with piezoelectric actuation. The intention was to monitor and improve surface roughness and waviness errors when face turning aluminum. In [13], actuation occurred in the in-feed direction, i.e. perpendicular to the workpiece surface. In [13], a spindle imbalance was causing the waviness error, and the uncorrected error magnitude was large by ultra precision machining standards at over  $8 \mu\text{m}$ . The corrected magnitude was less than  $6 \mu\text{m}$ , which is still a very large number for ultra precision machining. The system was found to be useful for low frequency events of less than 100 Hz due to the use of an eddy current probe for sensing. Position feedback occurs on the spindle face and on the tool.

In Sze-Wei *et al.* [50], a fine tool servo system was used to compensate for position errors on a miniature ultra precision lathe. Straightness errors of the translational slide were measured and compensated. In this example, the waviness error considered was caused not by relative tool / workpiece vibration, but by the x-translational slide.

Overall, in [60], [61], [59] and [13] the intention was to minimize the vibrational error on the workpiece surface. In [60] and [61], the active control scheme does not include an analysis of base movement as it pertains to the relative tool / workpiece vibration. Also, other sources of vibration are not addressed. Further, in [60], [61] and [59] no mention was made of how vibrations actually impact the workpiece surface.

## **2.5 Studies of Vibrations Affecting the Workpiece Surface Finish in Ultra Precision Machining**

In the literature, there are also various studies that consider in more detail how vibrations in ultra precision machining affect the workpiece surface finish. These fundamental studies are an important precursor to active compensation schemes since they can be used to guide control efforts and make compensation more directed and meaningful.

In Takasu *et al.* [51], relative vibration induced waviness and phase angle in the feed direction for low frequency vibration was discussed. Equations were developed in [51] describing relative tool / workpiece vibrations in the feed direction. In [51] the effect of round and straight nose tools on surface roughness are compared in the feed and in-feed directions.

In [51] machine vibration measurements were made but not during actual cutting.

Instead, low frequency vibrations of less than 10 Hz were measured with a capacitance gauge during air cutting. Frequencies considered in [51] were 2.2 Hz (similar to the vertical mode of the machine) and 5.8 Hz, the vibration coming from the floor. The cut surface was measured with a Talystep contact surface profiler. While the equations developed by Takasu *et al.* described vibration and, hence, waviness, the focus of this study was strictly on surface roughness. This meant that the analysis was restricted to the feed marks of the tool. Meanwhile, the relative tool / workpiece vibration considered in [51] had a peak-to-valley amplitude of 30 nm, and the largest round nose tool feed mark peak-to-valley amplitude,  $R_t$ , would have been just 60 per cent of this value at 18 nm<sup>1</sup>. Therefore, the greatest surface finish error was not pursued in [51]. The authors did find that the straight nose tools provided better surface roughness values in machining.

In 2000 and 2001, Cheung and Lee published several articles ([9] [11] [7] [8] and [10]) applying the equations, measurement method and theory developed by Takasu *et al.* [51]. In all instances, the vibration considered was in the in-feed direction. Like the work of Takasu *et al.*, only the effect low frequencies were studied, and relative tool / workpiece vibrations were not measured during actual cutting. Instead a displacement sensor was used during air cutting. With the exception of [9], the workpiece surface finish was measured post-machining with a Form Talysurf contact surface profiler. In [7] an optical interferometer was used instead. While the effect of various cutting parameters are considered by Cheung and Lee in their publications, an overall framework is not presented. The individual articles are outlined below.

In [9] the formation of workpiece surface roughness in ultra precision diamond

---

<sup>1</sup> $R_t$  is also called the ideal geometric surface roughness. The calculation of  $R_t$  is described in chapter 3 of this thesis, and is presented in equation 3.1.

turning was considered. The ideal geometric surface roughness,  $R_t$ , results from the tool nose radius,  $R_n$  and the feed rate  $f$ . This is summed with relative tool / workpiece vibration to produce the total surface roughness. Again, it should be noted that 'surface roughness' describes the tool feed marks, and not a waviness pattern. In [9], Cheung and Lee also explored vibrational wavelengths beyond the feed lines, performing spectral analysis in the feed direction. In [9], the effect of various cutting parameters on the mean arithmetic roughness,  $R_a$ , while machining with relative tool workpiece vibrations were considered. Parameters included the feed rate, the tool nose geometry, the spindle speed, the depth of cut, and the frequency and amplitude of relative tool / workpiece vibration.

Spectral analysis in the feed direction of a workpiece was also outlined in the 1985 CIRP publication by Sata *et al.* [43]. This work was referred to by Cheung *et al.* [9]. In [43], Sata *et al.* considered a turned surface, but not an ultra precision turned surface.

In [11], vibrations during ultra precision diamond turning were again considered, but this time material properties were also included. Again spectral analysis was employed. In [11], variation between analytical and experimental results were attributed to workpiece material property variation and to material induced vibration.

Cheung and Lee in [7] presented a model of surface topography using the cutting parameters of feed, spindle speed, tool nose geometry, and relative tool / workpiece vibration. The  $R_t$  and  $R_a$  descriptors of surface roughness were analyzed analytically and experimentally. The expected  $R_a$  for relative tool / workpiece vibrations of various frequencies and amplitudes was depicted in [7]. Additionally, for a particular vibration frequency and amplitude, the change in  $R_a$  with different spindle speed and

feed rate combinations was shown in [7].

In [8], Cheung and Lee studied process and material factors in ultra precision diamond turning. The process factors were the same ones used in [7] and material factors pertained to the workpiece and included anisotropy, swelling and crystal orientation. Vibrational frequencies and amplitudes were not quantified.

In [10], Cheung and Lee discussed the effect of different process parameters on surface finish. Material swelling was considered. Tool interference was also described. Tool interference was also discussed by Takasu *et al.* in [51].

In Cheung *et al.* [6], surface quality was studied with the use of a fast tool servo. A fast tool servo has been used in ultra precision machining to create optical microstructures, like for example a pyramid or groove, during turning [6].

Finally, in Sohn *et al.* [47], a model was built to simulate the effect of vibrations on the surface finish in diamond turning. Experimental equipment used included an ASG 2500 diamond turning machine and a Zygo NewView 5000 white light interferometer for surface metrology. The workpiece material was plated copper. In [47], only the amplitude of the feed lines was considered, as opposed to the overall waviness pattern, which resulted from vibration. An observation was made in [47] that finer feed rates minimized the impact of vibration on the surface finish. However, only the surface roughness caused by the tool feed marks was considered, as opposed to the overall waviness pattern. However, the peak-to-valley vibrational amplitude considered in [47] was 60 nm, and the predicted peak-to-valley geometric roughness of the feed lines was less than 19 nm for 6 of 7 test cases. Thus, the greatest source of surface finish error, the surface waviness error, was not addressed in [47].

In this section, literature describing relative tool / workpiece vibrations as they

pertain to ultra precision machining have been reviewed. Various aspects have been considered including surface roughness, surface waviness, the effect of material properties, and the effect of cutting parameters. However, several issues have not been addressed in the prior research. For example, the vibrations studied were not measured during cutting, but off-line. Also, the bandwidth of vibrations was limited to low frequencies. Further, while there are studies indicating how certain cutting parameters might improve surface finish in ultra precision machining where vibrations are present, an overall framework encapsulating the physical behavior does not exist. Lastly, the existing literature neglected to note the significance of the relative tool / workpiece vibrational amplitude compared to the geometric surface roughness under study.

## **2.6 Chapter Summary**

In this chapter, literature pertaining to ultra precision machining and vibrations has been reviewed. Also, some deficiencies in the current literature have been identified. This thesis aims in part to fill existing gaps in knowledge related to the role vibration plays in determining surface finish, and also to continue the work already performed in this field.

## Chapter 3

# Vibrations in Ultra Precision Machining

### 3.1 Introduction

As previously stated, the surface finish sought in ultra precision machining is on the order of nanometers. Any unwanted relative tool / workpiece motion during cutting contributes to inaccuracy of the workpiece. In this chapter, vibrations are identified as a significant source of workpiece error. First, vibrational patterns are identified from the surface metrology of the ultra precision face turned surface. Then the ultra precision machine tool structural dynamics are considered. Finally *in situ* measurement of relative tool / workpiece acceleration is described.

## 3.2 Significant Vibrations Apparent on the Surface of the Ultra Precision Face Turned Workpiece

From workpiece surface topography measurements taken with a Zygo New View 5000 white light interferometry system, it is apparent that significant waviness error patterns appear on the workpiece surface. Figure 3.1 describes how a white light interferometry image is taken relative to the workpiece. The surface is cut from the outer radius in toward the centre. The gray spiral represents a face turned workpiece surface. The spiral line spacing in the radial direction is the feed,  $f$ . The feed direction is the radial direction from the outside in, like spokes on a wheel. The cutting direction is along the spiral. A white light interferometry image field of view represents a small area of the surface. The Zygo field of view size is presented in table 3.1 for various magnifications. In this thesis, Zygo images were always taken with the orientation described in figure 3.1. Because the Zygo field of view is so small, the image curvature is typically negligible, and linear feed and cutting directions were assumed. However, unlike the illustration of figure 3.1, multiple spiral lines are viewable in a Zygo field of view, despite the small size.

In figure 3.2, an actual diamond face turned workpiece is shown, along with a corresponding white light interferometry measured segment of the workpiece surface. The dominant pattern in the measured surface was caused by relative tool / workpiece vibration during cutting.

In figure 3.3, the same workpiece surface metrology image is shown. At the top of figure 3.3, the three dimensional image showing the feed, cutting and in-feed directions

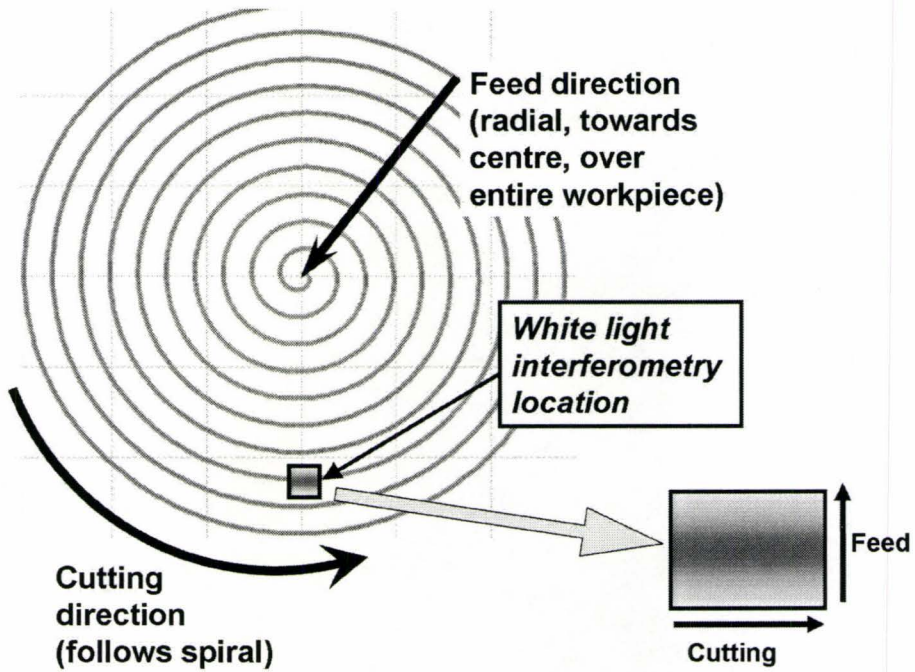


Figure 3.1: Illustration of face turned workpiece and white light interferometry location

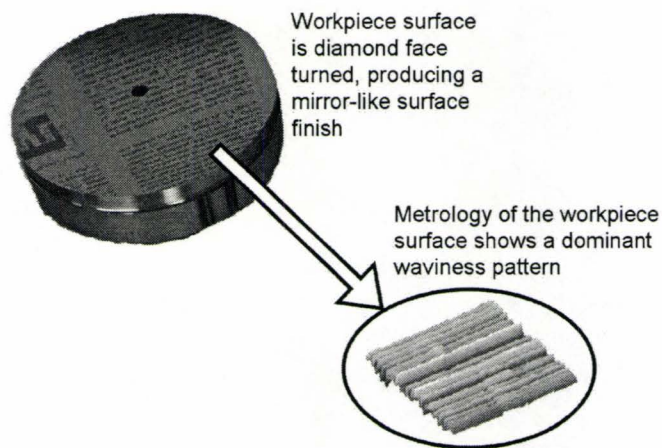


Figure 3.2: An ultra precision diamond face turned workpiece and white light interferometry image of the workpiece surface

are given. As previously noted, the feed direction is along a radial spoke of the workpiece, and the in-feed direction is perpendicular to the workpiece surface. On the bottom left of figure 3.3, the surface is shown with the in-feed direction coming out of the page. This is the same orientation as the illustration in figure 3.1. On the bottom right of figure 3.3, the in-feed height is given on the vertical axis, and the feed is along the horizontal axis, and one measured radial section is shown.

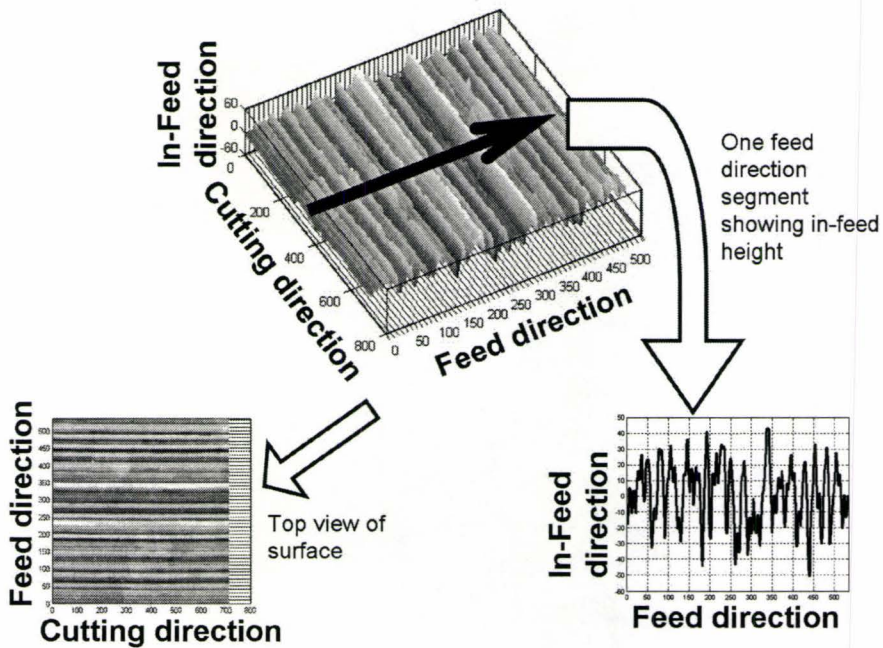


Figure 3.3: Workpiece surface metrology showing cutting, feed and in-feed direction

In figure 3.4, the topographical image of an ultra precision face turned aluminum 6061-T6 surface is shown. The cutting conditions include a spindle speed of 1196.3 RPM, and a feed rate of  $10 \mu\text{m} / \text{rev}$ . The horizontal axis is the cutting direction and the vertical axis is the feed direction. The horizontal grid is in increments of feed, i.e. of  $10 \mu\text{m}$ . The graybar represents height in the in-feed direction. Horizontal lines

are apparent on the measured surface of figure 3.4. However, the dominant lines are not feed lines and instead represent waviness. This is known because of the spacing of the dominant periodic pattern.

In figure 3.5, a feed direction segment of the measured workpiece is shown with the feed direction on the horizontal axis, and the in-feed direction on the vertical axis. The waviness pattern is more pronounced than that of surface roughness, which has wavelength equivalent to the feed. To further illustrate the point, a simulated feed line is included in figure 3.5. The formation of the simulated feed line is discussed in detail in chapter 5. The dominant wavelength in the feed direction is noted as  $\lambda_{dominant}$  in figure 3.6, which is a magnified segment of figure 3.5. In figure 3.6, the tool marks on the cut surface are visible, but clearly eclipsed by the waviness pattern.

In figure 3.7, the Fast Fourier Transform (FFT) in the feed direction of the surface in figure 3.4 is provided. The largest spike represents a wavelength,  $\lambda_{dominant}$ , of approximately  $29 \mu\text{m}$ . (Note that wavelength,  $\lambda$ , is the inverse of the spatial frequency,  $\nu$ , expressed in  $1/\text{mm}$ .) The feed lines are also apparent in figure 3.7 in the spike labeled  $\nu_{feed}$ , but the amplitude is clearly less at  $7.3 \text{ nm}$  versus the amplitude of  $17.1 \text{ nm}$  for the waviness error. As discussed in section 1.2, the error with wavelength of feed,  $f$ , is called the surface roughness. If the surface roughness was the dominant source of inaccuracy, its magnitude would be greater than waviness in figure 3.7, and it would also dominate the waviness patterns in figure 3.5.

In figure 3.7, other waviness errors are also evident, including those at the spatial frequencies of  $7.6 \text{ 1/mm}$ ,  $16.8 \text{ 1/mm}$ ,  $21.0 \text{ 1/mm}$  and  $45.9 \text{ 1/mm}$ . In all instances, the spatial frequency is smaller than the surface roughness, while the amplitude is larger. Overall, the large magnitudes of these periodic errors indicate that the waviness error

is a more significant contributor to the surface finish error than the surface roughness caused by the feed. In figure 3.8, the same plot is shown again, but the horizontal axis has been normalized according to the feed wavelength,  $\nu_{feed}$ , in order to emphasize the proportionately larger wavelength of the waviness patterns.

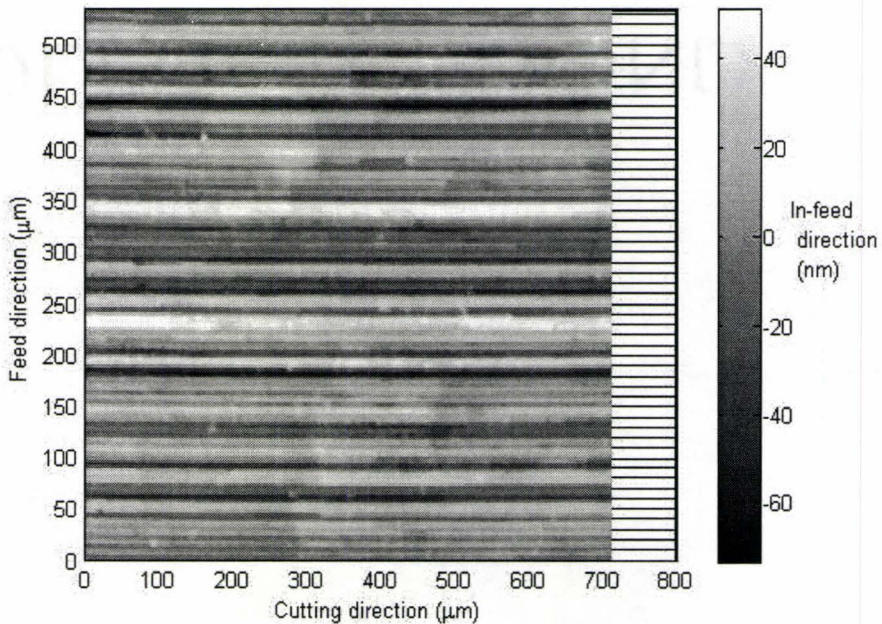


Figure 3.4: White light interferometry measurement of face turned surface showing dominant waviness pattern,  $N = 1196.3$  RPM,  $f = 10 \mu\text{m} / \text{rev}$ , zoom 200x

### 3.2.1 Predicted Geometric Surface Roughness and Vibration in Traditional Machining *versus* Ultra Precision Machining

The ideal geometric surface roughness is predicted by the following equation [7]

$$R_t = \frac{f^2}{8R_n} \tag{3.1}$$

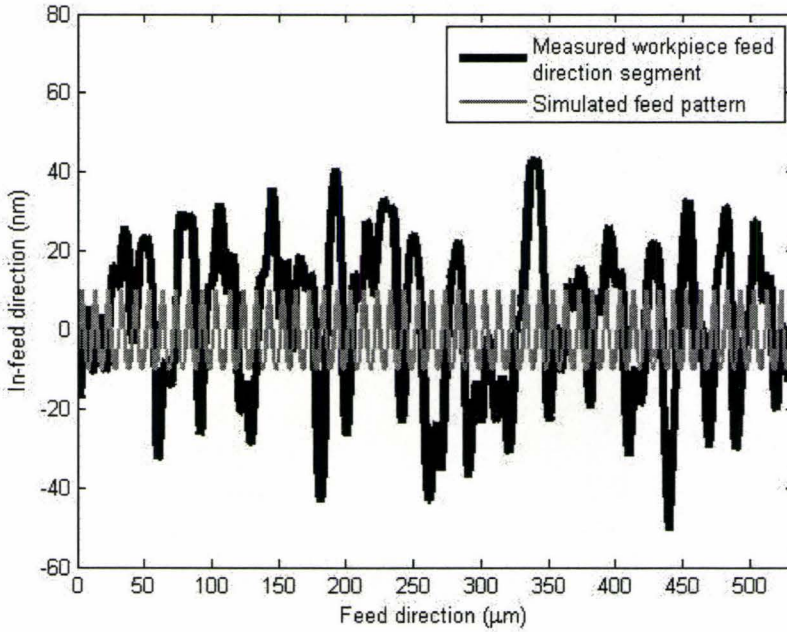


Figure 3.5: Feed direction segment of white light interferometry showing significant waviness pattern,  $\lambda_{dominant}$ ,  $N = 1196.3$  RPM,  $f = 10 \mu\text{m} / \text{rev}$

The surface roughness in equation 3.1 describes the peak-to-valley height of the tool marks in the feed direction. Thus, the spacing, or wavelength, is equivalent to the feed,  $f$ . The FFT magnitude in the feed direction is approximately one half of the peak-to-valley roughness, or  $R_t/2$ . It is demonstrated in chapter 5 how the feed component of surface finish is affected by vibrations.

For a feed rate of  $10 \mu\text{m} / \text{rev}$ , and a tool nose radius,  $R_n$  of  $0.630$  mm, the anticipated roughness  $R_t$  is approximately  $19.8$  nm, and one half of this is  $9.9$  nm. As a basis of comparison, consider a typical feed rate for traditional machining of  $250 \mu\text{m} / \text{rev}$ . The anticipated roughness in this case is  $12400$  nm, and one half of this value is  $6200$  nm. This roughness pattern is very large in comparison, with an

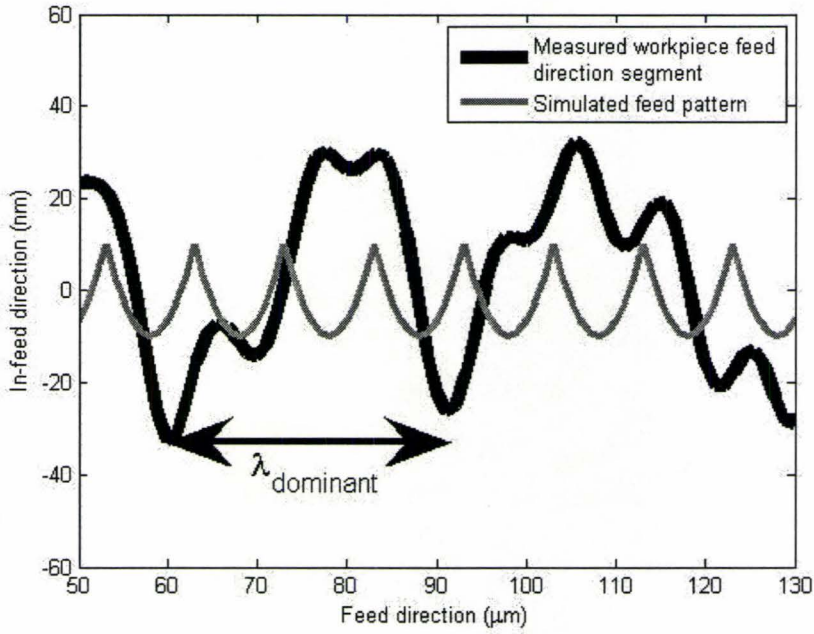


Figure 3.6: Zoomed view of the feed direction segment showing significant waviness pattern,  $\lambda_{dominant}$ ,  $N = 1196.3$  RPM,  $f = 10 \mu\text{m} / \text{rev}$

amplitude of  $6.2 \mu\text{m}$ , compared with  $0.0099 \mu\text{m}$  for ultra precision machining.

Further, this means that in traditional machining, a relative tool / workpiece vibration of amplitude 20 nm seems inconsequential, since it would be only 0.3 per cent of the roughness amplitude measure. Meanwhile, in this example of ultra precision machining, the same vibrational amplitude would be 202 per cent of the roughness amplitude. Thus, it poses a very significant source of error, and one greater than the tool nose marks.

This discussion also describes why it is important to study the wavelength or spatial frequency of a periodic surface finish error. If one were accustomed to traditional machining, it would be conceivable to mistake the dominant waviness patterns caused

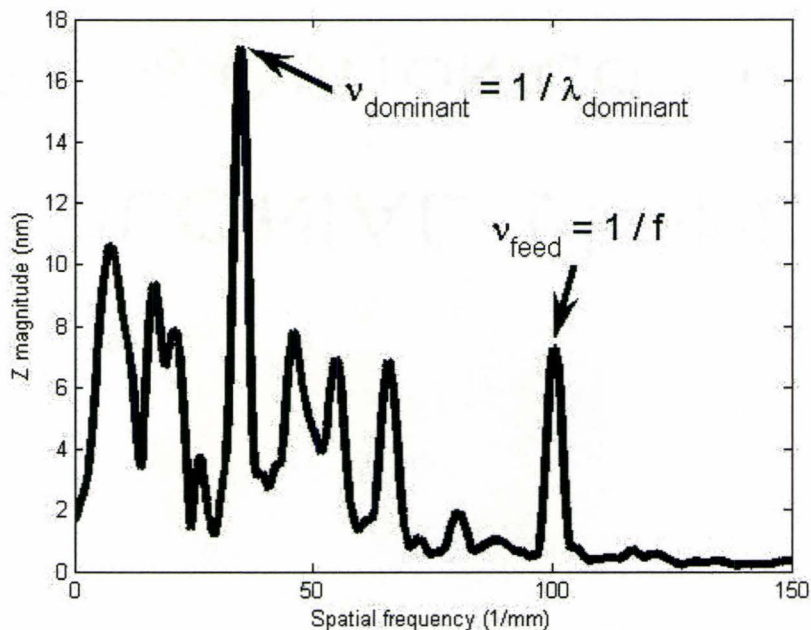


Figure 3.7: FFT in the feed direction segment showing significant waviness pattern compared with the feed,  $N = 1196.3$  RPM,  $f = 10 \mu\text{m} / \text{rev}$

by relative tool / workpiece vibration for a surface roughness pattern. For ultra precision machining, the analysis performed in this section indicates that the dominant surface finish error is waviness and not surface roughness.

### 3.2.2 Benefits and Limitations of White Light Interferometry

The ultra precision machined surface presented in figure 3.4 is measured via a Zygo Newview 5000, white light interferometer. This device acquires a three dimensional image of the workpiece surface. The advantage of the Zygo image is the in-feed topographical accuracy of 0.5 nanometres. However, the observed field view is quite small, with a fixed number of pixels of 640 by 480. This imposes restrictions on measurement capabilities, namely imaged area and resolution. Available zoom,

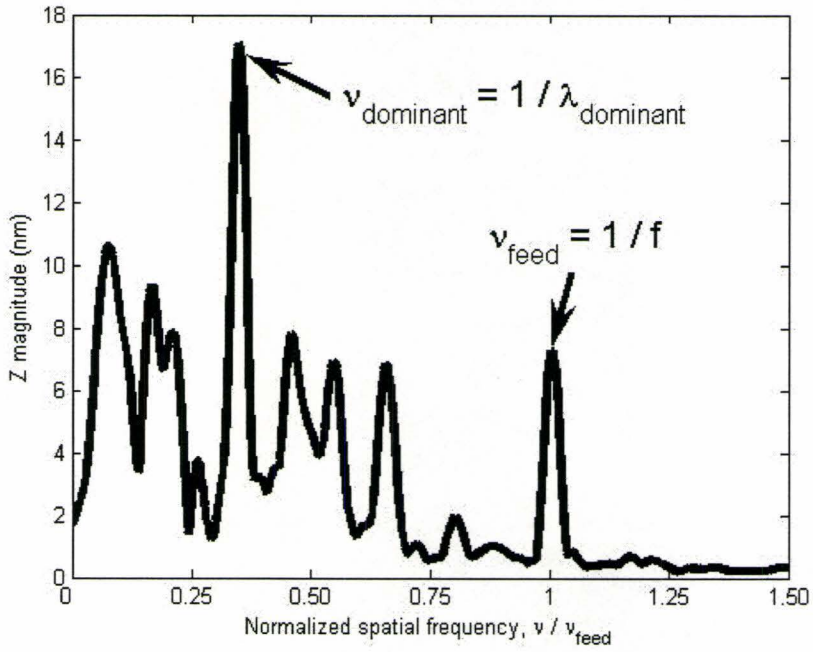


Figure 3.8: Feed rate normalized horizontal axis FFT in the feed direction segment showing significant waviness pattern compared with the feed,  $N = 1196.3$  RPM,  $f = 10 \mu\text{m} / \text{rev}$

Zoom	x (mm)	y (mm)	Resolution ( $\mu\text{m}$ )
1 x 0.4	18.2	13.6	28.42
1 x 0.5	14.5	10.9	22.65
1 x 0.8	9.08	6.81	14.18
1 x 1.0	7.16	5.37	11.19
1 x 1.3	5.509	4.132	8.608
1 x 2.0	3.58	2.685	5.595
10 x 0.4	1.81	1.35	2.82
10 x 0.5	1.44	1.08	2.25
10 x 0.8	0.9	0.68	1.41
10 x 1.0	0.71	0.53	1.11
10 x 1.3	0.53	0.4	0.83
10 x 2.0	0.35	0.27	0.55
50 x 0.4	0.36	0.27	0.57
50 x 0.5	0.29	0.22	0.45
50 x 0.8	0.18	0.14	0.28
50 x 1.0	0.14	0.11	0.22
50 x 1.3	0.11	0.08	0.17
50 x 2.0	0.07	0.05	0.11

Table 3.1: Zygo zoom, field of view and resolution [62]

field of view, and resolution are outlined in table 3.1. Note that all zoom values are first multiplied by 20, which is the Zygo's internal zoom factor.

The importance of the number and resolution of pixels size is described in [4]. In [4] the maximum measurable wavelength is described, as well as the smallest wavelength using 5 pixels.

In figure 3.4, a zoom of 10x1.0(x20) is used. The resolution from table 3.1 is thus 1.11  $\mu\text{m}$  in both the feed and cutting directions. Also in figure 3.4, 640 feed line segments comprise the surface. The FFT results of figure 3.7 represent the average results for all 640 image feed lines. Specifically, a Root Mean Square (RMS) average is taken, i.e. the vector norm over the square root of the mean [44]. Each feed line is also Hanning windowed. The Hanning window addresses the issue of spectral leakage,

while also allowing observation of signal components [29].

The image in figure 3.4 has also been bandpass filtered using the Zygo software. Data is then exported to Matlab where the analysis is performed. For figure 3.4, bandpass information is given in table 3.2. The maximum filter wavelength is about 72 per cent of the total feed direction length. Meanwhile the minimum filter length means the shortest wavelength is represented by 6 pixels.

Parameter	Units	Value
Maximum filter spatial frequency	1/mm	151.5
Minimum filter spatial frequency	1/mm	2.6
Minimum filter wavelength	$\mu\text{m}$	6.6
Maximum filter wavelength	$\mu\text{m}$	383.4
Measurement resolution (feed and cutting directions)	$\mu\text{m}$	1.11
Feed direction measured length	$\mu\text{m}$	530
Number of feed direction lines	-	640

Table 3.2: Measurement and filtering parameters of white light interferometry example,  $N = 1200$  RPM,  $f = 10 \mu\text{m} / \text{rev}$

For a 100 mm radius workpiece, the face turned surface area is approximately  $31416 \text{ mm}^2$ . The measured Zygo field of view of 0.71 mm by 0.53 mm has an area of  $0.38 \text{ mm}^2$ , or 0.0012 per cent of the total machined surface. It will be shown in chapter 4, and also in chapter 5, that most vibration-induced surface finish waviness errors are in fact discernible from a surface metrology field of view of this size.

### 3.3 Ultra Precision Machine Tool Structural Vibrations

Initially, waviness patterns observed on the machined surfaces were thought to be caused by very low frequency vibrations. This phenomenon is described in equation 3.2.

$$frequency_{estimated} = \frac{fN}{60\lambda_{dominant}} \quad (3.2)$$

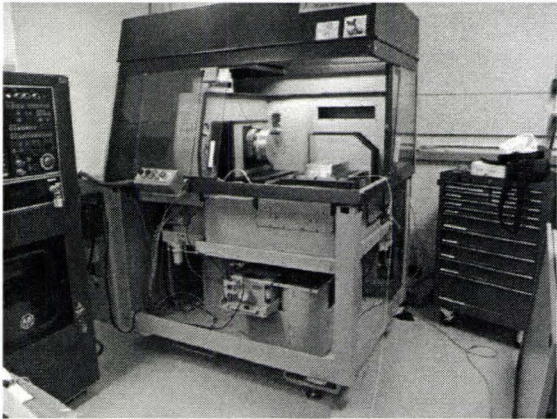
From equation 3.2, a wavelength equivalent to the feed gives a frequency equivalent to the spindle speed,  $N$ . In the example of section 3.2, a spindle speed of 1196.3 RPM is equivalent to 20 Hz. Thus, it was initially assumed that a feed direction wavelength greater than the feed rate corresponded to a lower frequency. For the case of a dominant wavelength of 29  $\mu\text{m}$ , the corresponding estimated frequency is 6.9 Hz. Meanwhile, the next largest peak has a wavelength of 130  $\mu\text{m}$ , giving an estimated frequency of 1.5 Hz. Similarly, other low frequency values were estimated from other workpiece surface metrology results. For example, in figure 5.65 of chapter 5, the peak measured wavelength is approximately 75  $\mu\text{m}$ , despite a feed rate of 2  $\mu\text{m} / \text{rev}$ . The spindle speed in this case was 1000 RPM. From equation 3.2, the estimated disturbance frequency is 0.4 Hz. Observations such as these from surface metrology prompted a structural analysis of the ultra precision machine tool that included the observation of very low frequency vibrations.

### 3.3.1 Structural Modal Analysis

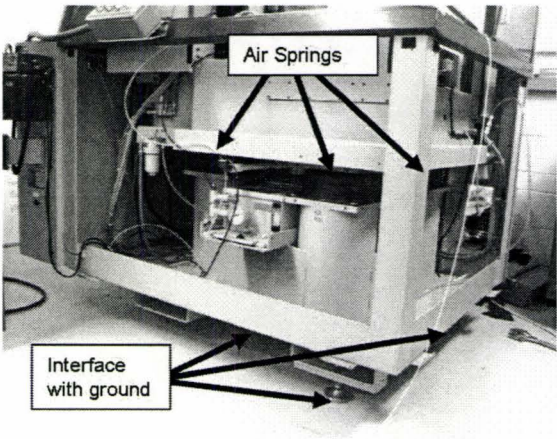
The objective of performing the modal analysis was to discern if a very low structural mode existed for the ASG ultra precision machine tool. The ASG ultra precision machine tool structure is depicted in figure 3.9. The ultra precision machine tool base rests on three air springs. These air springs provide passive vibration isolation. The suspension system is labeled in figure 3.9(b). Also, a survey performed by Rivin [41] was found describing typical industrial floor vibrations. In [41] the horizontal direction represents the in-feed direction,  $z$ , on the ASG 2500. Thus, it was desirable to study the ultra precision machine tool's structural vibrations between approximately 0 and 50 Hz. To this end, a Kulite strain-gauge based sensor was used at the tool location. The lowest range of the Kulite sensor approaches 0 Hz.

The Kulite sensor has a natural resonant frequency of 450 Hz. It was connected to a full bridge amplifier, and the signal was passed through an analogue low-pass filter at 45 Hz, i.e. one tenth the sensor natural resonant frequency. The Kulite sensor placement during modal testing is shown in figure 3.10. The structural vibrations have been measured on the ASG 2500 with a roving hammer test. Excitation of the structure occurred via an instrumented Kistler 9725A force hammer with green hard rubber tip 9908. The dynamic response of the hammer with this tip is provided in Appendix A [22]. The signals were acquired and processed by an Agilent Dynamic Signal Analyzer, and 10 tests were averaged. The spindle impact location is noted in figure 3.11, and the base hit location is noted in figure 3.12. All hammer hits occurred in the horizontal in-feed direction.

Results are provided in figures 3.13 and 3.14. Figure 3.13 is the cross spectrum and coherence of the Kulite accelerometer to Kistler force sensor, resulting from a base hit.



(a) ASG ultra precision machine tool without side panels



(b) ASG ultra precision machine tool suspension

Figure 3.9: ASG ultra precision machine tool

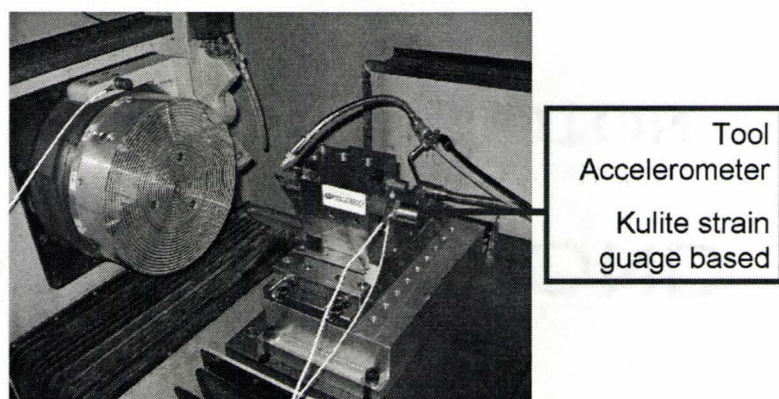


Figure 3.10: Kulite sensor on ASG 2500 for modal testing

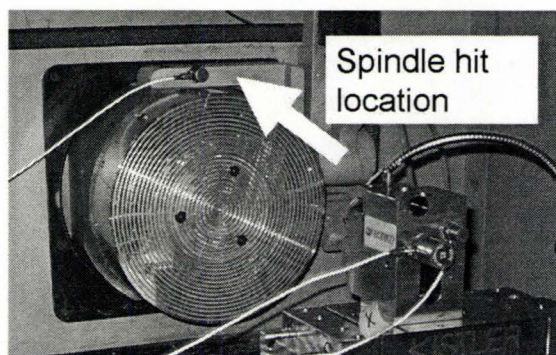


Figure 3.11: Spindle impact locations ASG 2500 for modal testing

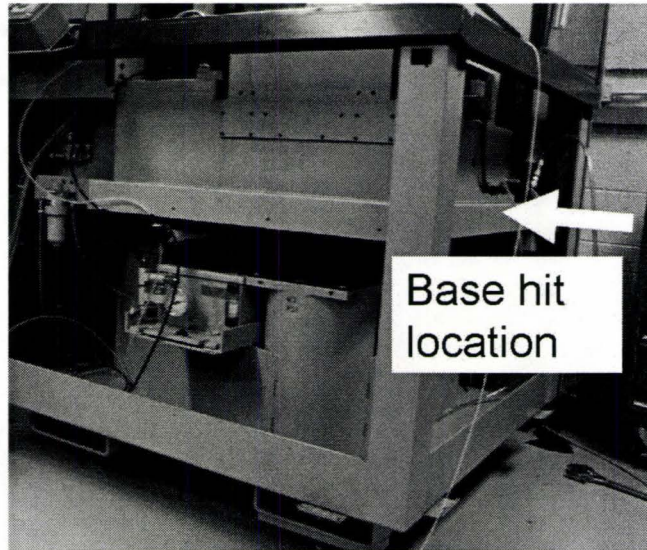


Figure 3.12: Tool and spindle impact locations ASG 2500 for modal testing

Meanwhile, figure 3.14 shows the same cross spectrum and coherence resulting from a spindle housing strike. Figures 3.13 and 3.14 indicate that the lowest structural mode of the ASG 2500 is around 5 Hz. Figure 3.13 also shows a mode around 10 Hz. Based on magnitude, it appears that the 5 Hz and 10 Hz modes are associated with the machine's base. Meanwhile, the spike at 42 Hz is of greater magnitude with a spindle hit, and is thus most likely associated with the spindle housing structure. In [35], the effect of structural vibrations on ultra precision relative tool / workpiece movement is discussed. The coherence in figures 3.13 and 3.14 approaches 1, indicating good signal to noise ratio for measured structural modes [19].

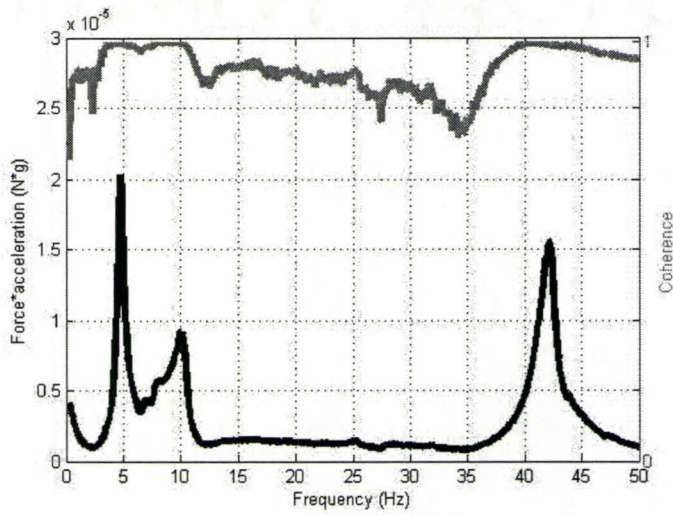


Figure 3.13: Kulite accelerometer to Kistler force sensor cross spectrum and coherence for horizontal base hit

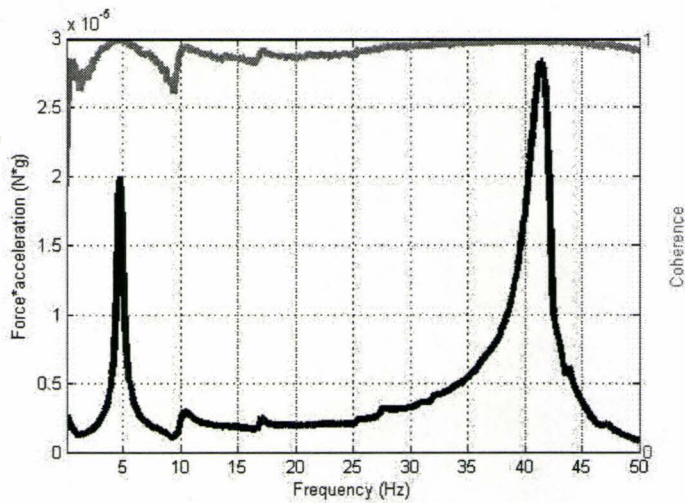


Figure 3.14: Kulite accelerometer to Kistler force sensor cross spectrum and coherence for horizontal spindle housing hit

## 3.4 Measurement of *In Situ* Vibrations During Ultra Precision Machining

### 3.4.1 Sensor Placement and Data Acquisition

For face turning of aluminum on the ASG 2500 ultra precision machine tool, the accelerometer set-up is depicted in figure 3.15. The spindle accelerometer measures acceleration on the spindle housing (workpiece location) and the tool accelerometer measures acceleration on the tool. The difference between these two signals is the relative tool / workpiece acceleration. The data acquisition procedure used is described in figure 3.16. Originally, broadband examination of ultra precision machine tool dynamic behavior was examined with the Agilent Dynamic Signal Analyzer equipped with anti-aliasing filtering, in order to determine the best sampling and filtering procedure to use for the time series data collection in the future. Following this, data were acquired synchronously with a NI-DAQ A/D card using Labview after first passing the signal through an analogue low-pass filter to prevent aliasing. Post-processing of data was then performed in Matlab. Sensor specifications are included in Appendix A, table A.1.

Table 3.3 lists the cutting parameters used to generate the surface whose *in situ* vibrations are presented in this section. The aluminum 6061-T6 workpiece face turned with the parameters of table 3.3 is depicted in figure 3.17. In figure 3.17, the mirror-like surface finish achieved with ultra precision diamond face turning is apparent.

In figure 3.18, the difference between the measured tool acceleration and the measured spindle acceleration during the cutting of the workpiece is shown. Figure 3.18 shows a 0.05 second segment, representing a minimum frequency of 20 Hz. Overall,

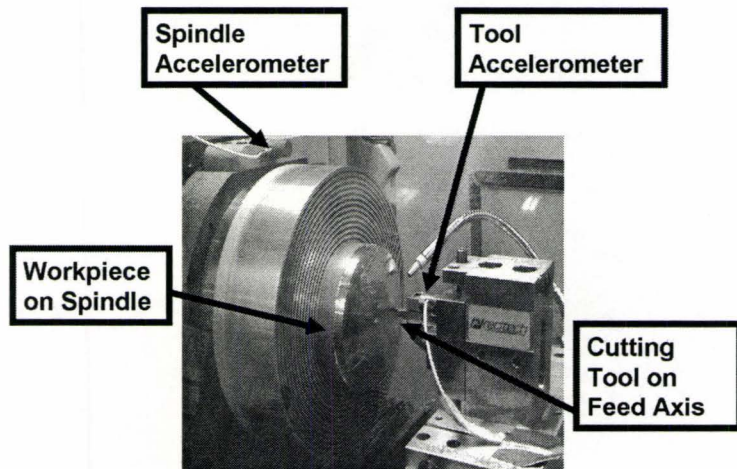


Figure 3.15: Face turning experimental set-up on ASG 2500 showing accelerometer placement

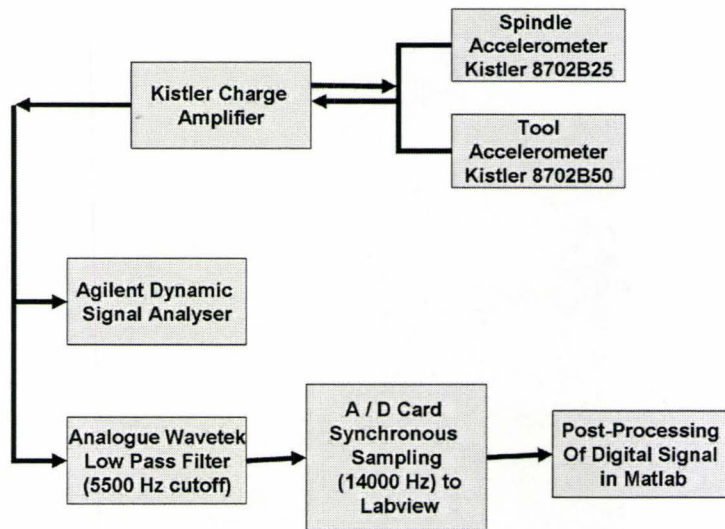


Figure 3.16: Data acquisition for in-feed vibration measurement on the ASG 2500

Cutting parameter	Symbol	Value
Spindle speed	$N$	1200 RPM
Feed rate	$f$	$10 \mu\text{m} / \text{rev}$
Depth of cut	$d$	$5 \mu\text{m}$
Tool nose radius	$R_n$	0.630 mm

Table 3.3: Cutting conditions for ultra precision face turning of a 100 mm diameter aluminum 6061-T6 workpiece on the ASG 2500,  $N = 1200 \text{ RPM}$ ,  $f = 10 \mu\text{m} / \text{rev}$

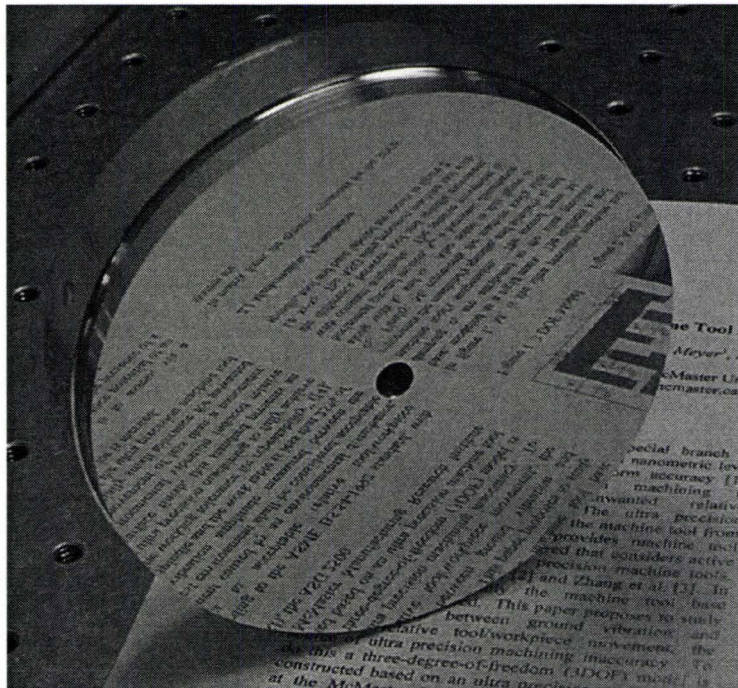


Figure 3.17: Aluminum workpiece ultra precision face turned with diamond,  $N = 1200 \text{ RPM}$ ,  $f = 10 \mu\text{m} / \text{rev}$

121 seconds of data are measured synchronously from both sensors and used in FFT analysis.

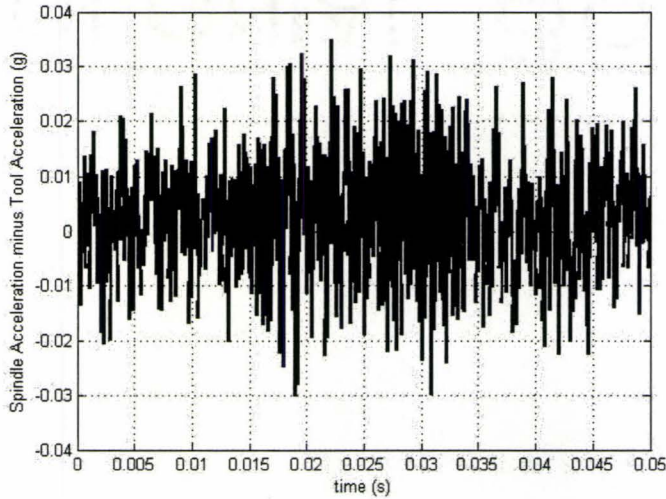


Figure 3.18: Measured relative tool / spindle acceleration,  $N = 1200$  RPM,  $f = 10 \mu\text{m} / \text{rev}$

In figure 3.20, the FFT of the tool acceleration is shown, and in figure 3.19 the FFT of the spindle acceleration is shown. Finally, in figure 3.21 the FFT of the relative tool / workpiece acceleration in the in-feed direction is depicted. The Matlab data was Hanning windowed, and the RMS average of the magnitude was taken. The FFT algorithm used in Matlab with Labview acquired data has been validated against the Agilent Dynamic Signal Analyzer for frequency content.

The maximum disturbance frequency occurs at 4976 Hz in figure 3.21, and was observed primarily by the spindle accelerometer. This vibration exists on the machine tool during air and workpiece cutting, and also when the machine is idling. The vibration disappears when the emergency stop is engaged. The second largest vibration of 812.9 Hz is observed by the tool sensor. This frequency exists very weakly with the emergency stop engaged, somewhat more strongly in idling, considerably more

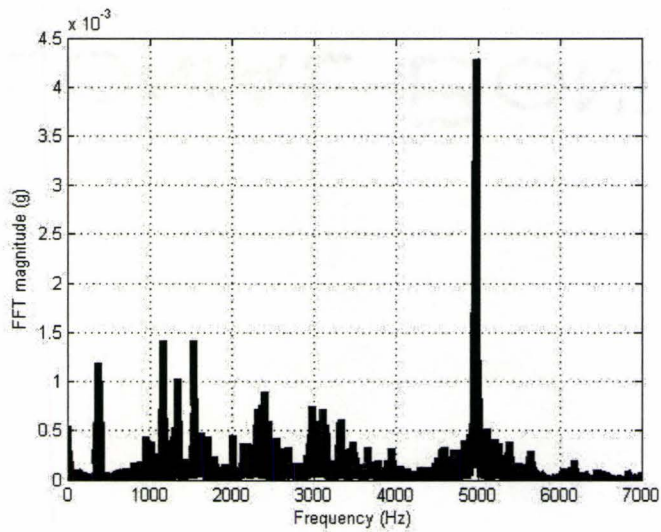


Figure 3.19: Spindle acceleration FFT,  $N = 1200$  RPM,  $f = 10 \mu\text{m} / \text{rev}$ , number of averages = 103,  $\Delta f = 0.8548$  Hz

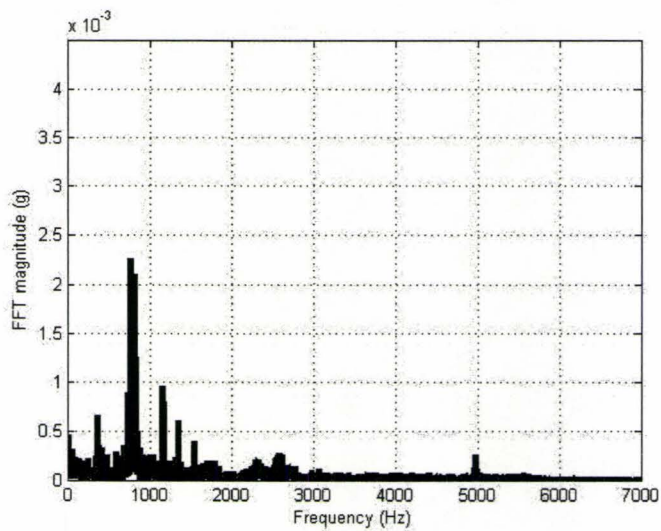


Figure 3.20: Tool acceleration FFT,  $N = 1200$  RPM,  $f = 10 \mu\text{m} / \text{rev}$ , number of averages = 103,  $\Delta f = 0.8548$  Hz

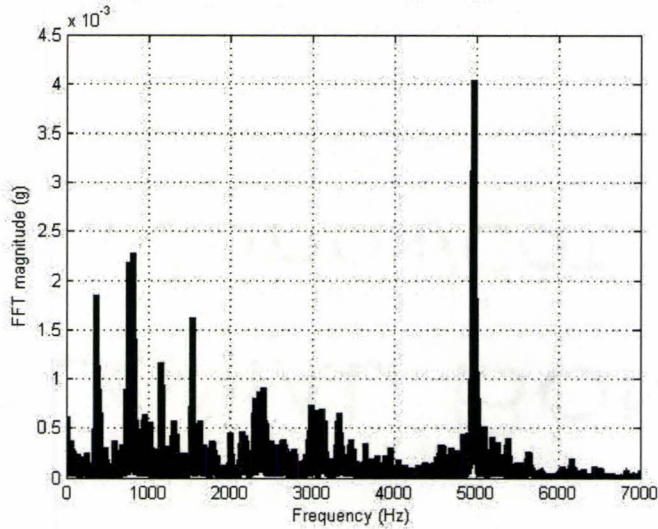


Figure 3.21: Relative tool / workpiece acceleration FFT,  $N = 1200$  RPM,  $f = 10 \mu\text{m}$  / rev, number of averages = 103,  $\Delta f = 0.8548$  Hz

strongly with air cutting, and strongest with actual cutting. From the *in situ* vibrational measurements, it was apparent that the significant vibrational frequencies were not the structural vibrations identified in the modal analysis. This means that environmental disturbances in the vicinity of the ultra precision machine tool, as discussed in chapter 2, are small compared with other vibrational sources that exist on the machine itself.

In figure 3.22 <sup>1</sup>, the process of measuring vibrations during cutting and also on the workpiece surface after cutting via white light interferometry is summarized.

---

<sup>1</sup>Zygo Newview 5000 image from [1]

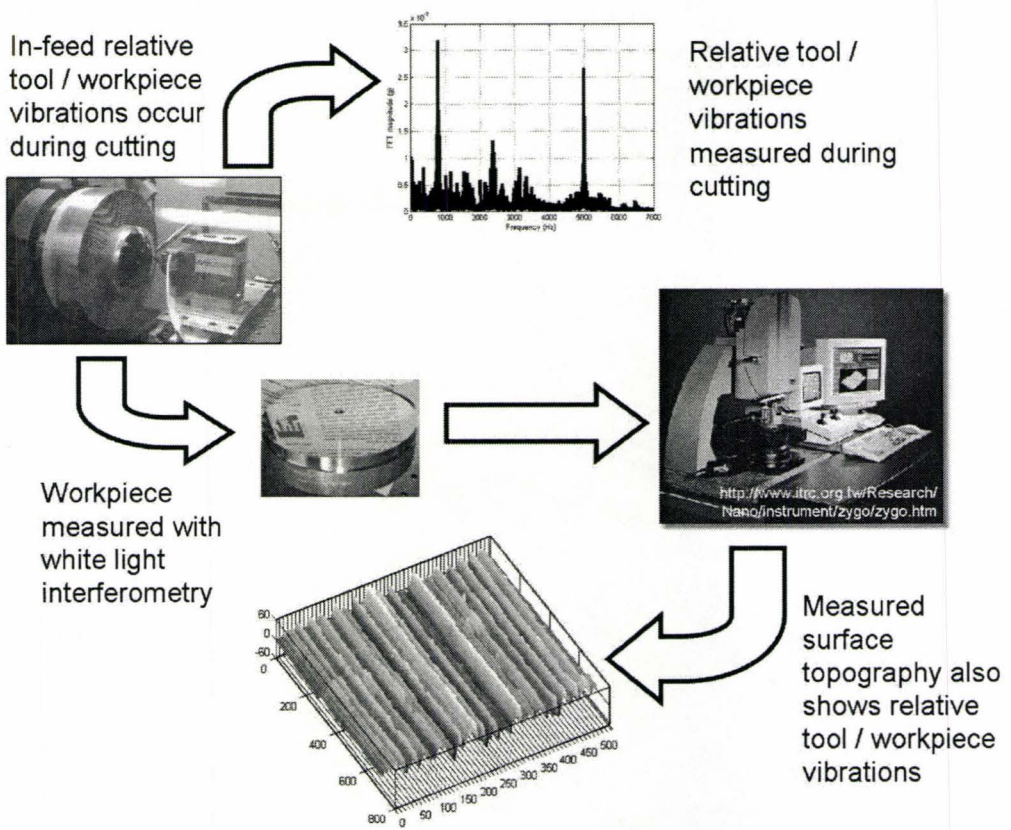


Figure 3.22: Relative tool / workpiece vibrations observed during cutting and on workpiece surface

### 3.5 Chapter Summary

In this chapter the study of vibrations has been described in ultra precision machining. First, from white light interferometry, dominant waviness patterns are observed on the ultra precision diamond face turned surface. Then, preliminary calculations to estimate the frequency causing the waviness pattern are presented. Following this structural modal analysis of the ultra precision machine tool is presented. Finally, *in situ* vibrational measurements during cutting are shown and related to the modal analysis data. It is clear from this analysis that unwanted relative tool / workpiece vibrations are occurring during cutting. In the following chapters, the relationship between the unwanted relative tool / workpiece vibrations and the significant periodic waviness errors is described.

## Chapter 4

# Vibrational Equations and Applications

### 4.1 Introduction

In chapter 3, vibrations in ultra precision machining are discussed. It is noted from workpiece surface metrology that the dominant error on the workpiece surface consists of periodic waviness patterns, and not feed marks. The initial hypothesis was that the waviness lines were caused by a very low frequency vibration. However, modal testing and *in situ* cutting measurements confirmed that this was not the case. In this chapter, the harmonic relative tool / workpiece motion in the cutting and feed directions is derived. Also, the bounds of relative tool / workpiece motion, which are named in this thesis the surface finish lobes, are presented.

## 4.2 Cutting Direction Relative Tool / Workpiece Vibrations

Turning is a continuous cutting process. In face turning, a spiral is formed on the machined surface. If measured in the in-feed direction, this spiral is essentially a time series of any unwanted relative tool / workpiece movement during cutting. The spiral resulting from face turning is illustrated in figure 4.1(a). The spacing between grooves is equivalent to the feed rate,  $f$ . Movement along the spiral is called the cutting direction.

In figure 4.1(b), the effect of in-feed vibration is included in the illustration. In figure 4.1(b), the information on the cut surface is being unwound or stretched out. If this can be done then a time history of all relative tool / workpiece movement causing surface errors could be discerned. Further, if this time series could be acquired, then frequency analysis could be performed to determine frequencies causing unwanted waviness errors on the workpiece surface.

In-feed direction harmonic relative tool / workpiece movement is expressed in equation 4.3. Constant amplitude,  $z_{amp}$ , harmonic motion is assumed, with frequency  $\omega_d$  in rad/s. The frequency  $\omega_d$  is referred to as the ‘disturbance frequency.’ With equation 4.3, other constant amplitude vibrations can also be included via superposition. In-feed motion  $z(t)$  is also described in figure 4.2.

$$z(t) = z_{amp} \sin(\omega_d t) \quad (4.3)$$

With fixed feed rate and spindle speed in face turning, the cutting speed  $v_c(t)$  changes with time. The radius of tool contact changes with time  $t$  in seconds according

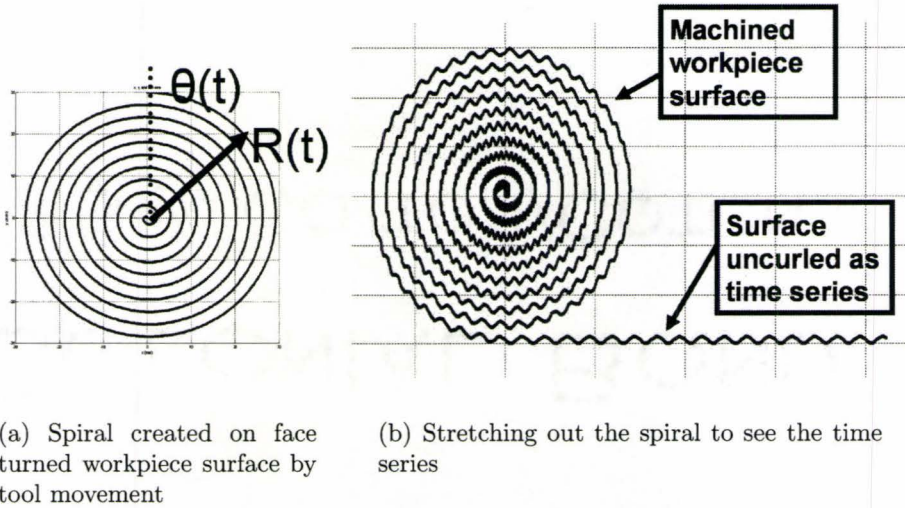


Figure 4.1: Spiral on the workpiece surface and viewing the time series

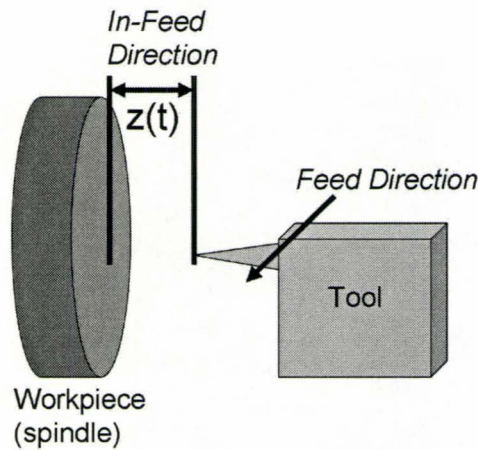


Figure 4.2: Workpiece on spindle, tool, feed direction and in-feed relative tool / workpiece motion

to

$$R(t) = R_{start} - \frac{fN}{60}t \quad (4.4)$$

The cutting speed  $v_c$  expressed in  $mm/min$  (based on [48]) is

$$v_c(t) = N2\pi R(t) \quad (4.5)$$

Finally, substituting equation 4.4 into equation 4.5 gives

$$v_c(t) = N2\pi \left[ R_{start} - \frac{fN}{60}t \right] \quad (4.6)$$

## 4.2.1 Factors Limiting the Ability to Discern Vibrations from Surface Metrology in the Cutting Direction

### Finding the Feed Lines

The cutting tool parameters and also the surface metrology equipment make unwinding the surface in the cutting direction very difficult. As will be shown later in chapter 5, there is considerable tool overlap during ultra precision machining. In the examples described in this thesis, the feed rate was between  $2 \mu m / rev$  and  $10 \mu m / rev$ , while the tool nose radius was  $630 \mu m$ . With slower feed rates, identifying feed lines becomes problematic. Also, as shown later in chapter 5, feed lines become obscured by vibrations, especially at slower feed rates because of the tool geometry.

### Changing Time Interval

Further, as noted in equation 4.6, the cutting direction cutting speed changes during face turning. In the Zygo image the spatial spacing is constant and, thus, represents a changing time increment. Specifically, for a constantly sized spatial increment  $\Delta inc$ , the time interval changes according to  $\Delta t = v_c(t)/\Delta inc$ . This makes frequency assessment of cutting conditions challenging.

### Sparsely Sampled Time Series

Finally, the white light surface metrology equipment that provides high in-feed direction resolution only presents a very limited field of view, as outlined in table 3.1. This means that an observable time series is very sparsely sampled. As described in chapter 3, the white light interferometry measures a very small square of the workpiece, providing a very sparsely sampled time series in the cutting direction.

As an example, consider the workpiece where the feed,  $f$ , is  $10 \mu\text{m} / \text{rev}$  and spindle speed,  $N$ , is 1200 RPM. The white light interferometry image shown in figure 3.4 was measured at an approximate workpiece radius of 56 mm. The cutting direction length of the image is 0.71 mm. In figure 3.4, the feed direction is horizontal. Figure 4.3 describes the measurement length compared with the workpiece radius. In figure 4.3, distance  $x$  is half of the measured cutting direction length, i.e.  $x = 0.355 \text{ mm}$ , and  $R = 66 \text{ mm}$ . In figure 4.3, angle  $\alpha$  is calculated to be 0.308 degrees, or 0.0054 rad.

The workpiece perimeter at the point of measurement is approximately 352 mm, compared with the measured length of 0.71 mm, and one workpiece rotation comprises 0.05 seconds. From equation 4.5, the cutting speed,  $v_c$ , at the start of measurement

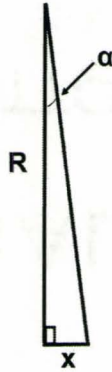


Figure 4.3: Sparsely sampled time series geometry from white light interferometry is 497 628 mm / min, or equivalently 8294 mm / s. This means that 0.71 mm of measurement represents  $8.56 \times 10^{-5}$  seconds. Thus, only approximately 0.17 per cent of the time series has been captured in the cutting direction for one workpiece revolution. If only one cutting direction segment of  $8.56 \times 10^{-5}$  seconds is considered, employing Shannon's Law, then the smallest observable disturbance frequency is greater than 23 365 Hz.

### 4.3 Feed Direction Relative Tool / Workpiece Vibrations

In section 4.2, challenges to assessing relative tool / workpiece movement in the cutting direction were identified. Due to these difficulties, instead of 'stretching out' the time series to accommodate traditional FFT analysis, the equations of study are instead adapted to the radial (feed) representation and spatial FFT performed. This accommodates the white light interferometry image.

### 4.3.1 Derivation of Polar Coordinate System Equations

The adaptation to feed representation occurs by re-expressing equation 4.3 in the polar coordinate system. The workpiece is discretized into radial segments as illustrated in figure 4.4, and the conversion between time,  $t$ , in seconds, and the angle of rotation,  $\theta$ , is

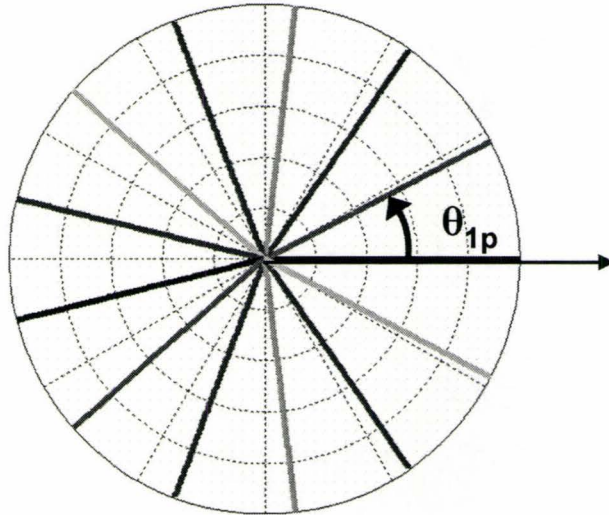


Figure 4.4: Radial segmentation of workpiece

$$t = \frac{60\theta}{2\pi N} \quad (4.7)$$

Substituting equation 4.7 into equation 4.3 gives

$$z(\theta) = z_{amp} \sin\left(\frac{60\omega_d\theta}{2\pi N}\right) \quad (4.8)$$

In figure 4.4, each radial spoke is defined by its angle from 0 degrees as  $\theta_{1p}$ , where  $p$  is the spoke number. These spokes are also all in the feed direction.

During cutting, the workpiece is rotated by the spindle. For  $m$  workpiece revolutions, the angle at each radii is increased by  $2\pi m$ . Angle  $\theta$  is required in further detail. Thus,

$$\theta(m, p) = 2\pi m + \theta_{1p} \quad (4.9)$$

Substituting equation 4.9 into equation 4.8 gives

$$z(m) = z_{amp} \sin \left( \frac{60\omega_d}{N} m + \frac{60\omega_d\theta_{1p}}{2\pi N} \right) \quad (4.10)$$

The disturbance frequency  $\omega_d$  discussed is in units radians per second. The equivalent disturbance frequency  $f_d$  in Hz is found as follows:

$$f_d = \frac{\omega_d}{2\pi} \quad (4.11)$$

Finally, making the substitution in equation 4.10 of  $\omega_d$  for  $f_d$  gives

$$z(m) = z_{amp} \sin \left( \frac{2\pi 60 f_d}{N} m + \frac{60 f_d \theta_{1p}}{N} \right) \quad (4.12)$$

Equation 4.12 explains how a harmonic constant amplitude vibration during ultra precision machining manifests itself radially (feed direction) on a workpiece. Note that in equation 4.12 dependence on time has been eliminated. In [51], [9], [11], [7], [8] and [10] expressions for the relative tool / workpiece movement in the feed direction are also given. However, their development of equations is not to accommodate white light interferometry equipment. Also, their presentation of equations is not in the classical configuration of frequency and phase angle. Meanwhile, in equation 4.12

this configuration does occur. Consider equation 4.12 with the following notations

$$z(m) = z_{amp} \sin \left( \underbrace{\left[ \frac{2\pi 60 f_d}{N} \right]}_{\text{spatial frequency (rad/rev)}} m + \underbrace{\left[ \frac{60 f_d \theta_{1p}}{N} \right]}_{\text{spatial phase angle (rad)}} \right) \quad (4.13)$$

This configuration provides opportunities to further understand how vibrations manifest on an ultra precision face turned workpiece. From equation 4.13, the angular velocity  $\Omega$  in radians / revolution is given in equation 4.14 and the phase angle  $\phi(p)$  in radians is given in equation 4.15.

$$\Omega = \frac{2\pi 60 f_d}{N} \quad (4.14)$$

$$\phi(p) = \frac{60 f_d \theta_{1p}}{N} \quad (4.15)$$

## 4.4 Finding the Disturbance Frequency in the White Light Interferometry Image

In equation 4.14, only the disturbance frequency and the spindle speed are present. The radial line under examination does not factor in to the expression for  $\Omega$ . This means that for all workpiece radial lines, the spatial frequency is always the same over the entire workpiece.

Meanwhile, equation 4.15 for phase angle  $\phi(p)$  also contains information regarding the radial line being examined. Thus, while the spatial frequency of each radial line is the same, the phase angle varies according to equation 4.15.

Later in this chapter, in section 4.6, what are named in this thesis the surface finish lobes will be described. It will be shown that the same feed direction spatial frequencies can occur on a workpiece for a very wide range of disturbance frequencies. This means that identifying a specific disturbance frequency from the feed direction spatial frequency alone is not possible. However, the phase angle of equation 4.15 is unique.

One can, in fact, identify a specific disturbance frequency  $f_d$  from a white light interferometry image by discerning the difference in phase angle for two closely spaced radial lines. In simulation, the error of this method is less than 1 per cent.

From a Zygo sample, it would be an onerous task to know the absolute value of  $\theta_{1p}$ . However, one can easily discern the distance between two radial lines, and thus a  $\Delta\theta_1$ .

Consider two arbitrary radii represented by  $\theta_{1a}$  and  $\theta_{1b}$ . If both have been analyzed by FFT and the magnitude plot shows a common waviness pattern  $\lambda$ , two phase angles,  $\phi_a$  and  $\phi_b$ , for this spatial frequency can be found from the phase plot. From equation 4.15, for two closely spaced radii,  $a$  and  $b$  with surface error wavelength  $\lambda$  caused by the same disturbance frequency  $f_d$

$$\begin{aligned}\phi_b - \phi_a &= \frac{60f_d\theta_{1b}}{N} - \frac{60f_d\theta_{1a}}{N} \\ \phi_b - \phi_a &= \frac{60f_d}{N} [\theta_{1b} - \theta_{1a}]\end{aligned}\tag{4.16}$$

Isolating the disturbance frequency,  $f_d$  on the left hand side gives

$$f_d = \frac{60 [\theta_{1b} - \theta_{1a}]}{N [\phi_b - \phi_a]} \quad (4.17)$$

Equation 4.17 shows that the disturbance frequency  $f_d$  can be discerned from the measured workpiece surface.

#### 4.4.1 Simulation Results

A simulated Zygo surface is shown in figure 4.5. The peak frequency of 4976 Hz from figure 3.21 is used to create this image. Note that no tool geometry information is included in the simulation. The simulated surface is generated from equation 4.12 and depicted in figure 4.5. In figure 4.5, 100 radial lines are depicted representing a “pie slice” workpiece view of approximately  $7.42 \times 10^{-2}$  degrees. Thus, each radial line has a spacing of approximately  $7.42 \times 10^{-4}$  degrees. This radial spacing represents  $\theta_{1b} - \theta_{1a}$  in equation 4.17. In figure 4.6 a portion of the first and last radial line are shown together.

An FFT was performed on each radial line comprising the surface of figure 4.5. From each FFT a peak spatial frequency (and thus wavelength) was found, and a corresponding phase angle. Figure 4.7 shows the peak spatial magnitude and wrapped phase angle for the first 20 radial lines. The peak spatial magnitude,  $\nu$ , in figure 4.7 is 20 1/mm, with an equivalent wavelength,  $\lambda$ , of 50  $\mu\text{m}$ . The spacing between phase angles at the peak spatial frequency is identical.

Equation 4.17 was employed over the surface to determine whether the input disturbance frequency of 4976 Hz could be found. The phase angles in radians were employed. The success of this method was greater than 99 per cent; for the 100

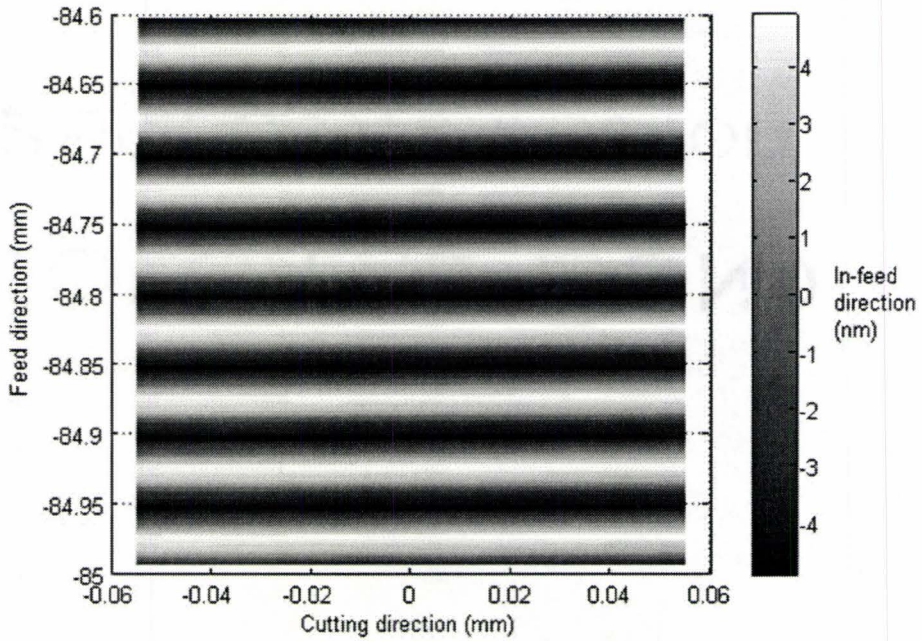


Figure 4.5: Simulated Zygo surface,  $f_d = 4976$  Hz,  $N = 1200$  RPM,  $f = 10 \mu\text{m} / \text{rev}$

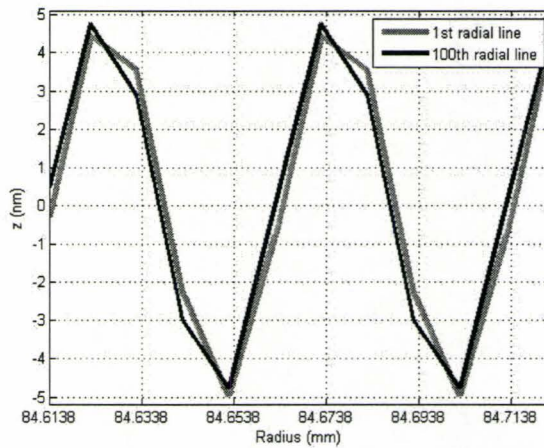


Figure 4.6: Simulated first and last radial lines,  $f_d = 4976$  Hz,  $N = 1200$  RPM,  $f = 10 \mu\text{m} / \text{rev}$

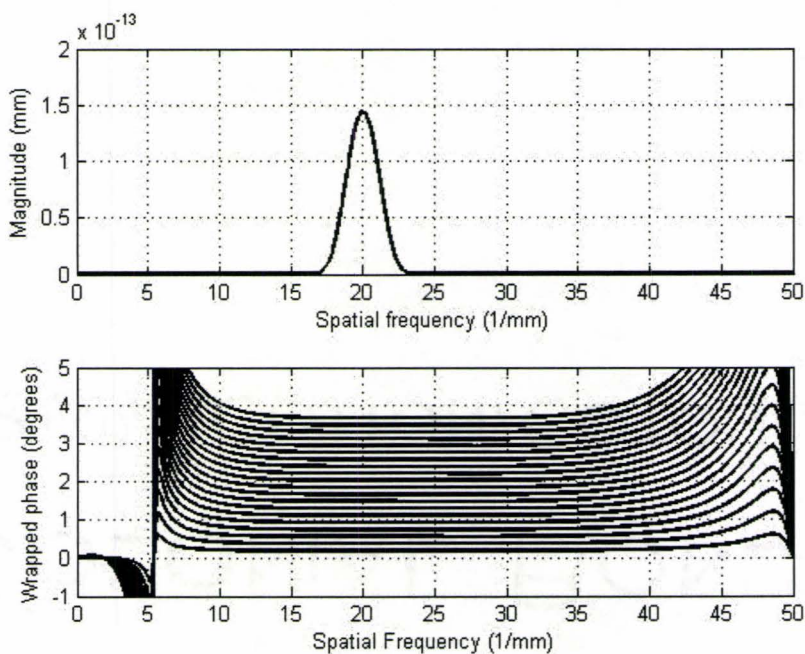


Figure 4.7: Magnitude and phase of first 20 simulated radial lines

calculations performed the largest error between the actual and estimated disturbance frequency was  $1.14 \times 10^{-4}$  per cent, and the smallest error was  $6.97 \times 10^{-5}$  per cent. This result was achieved with a simulated Zygo sized field of view, consisting of 0.53 mm in the feed direction. Thus, with the feed direction representation of the vibrational equations, a small white light interferometry field of view provided a substantial amount of information. This observation is further described in section 4.6, and also in chapter 5.

## 4.5 The Repeating Nature of Vibrational Manifestation in the Feed Direction

In this section the repeating manifestation of relative tool / workpiece vibration in the feed direction is discussed. Further, the behavior of equation 4.12 as it pertains to the generation of the surface finish lobes is illustrated in this section with an example. Consider equation 4.12 with a spindle speed of 1200 RPM, and the first workpiece spoke where  $\theta_{1p}$  is simply equal to zero. Further, let the vibrational amplitude be 10 nm. Equation 4.12 with substitutions becomes

$$z(m) = 10 \sin((0.314f_d)m) \quad (4.18)$$

where  $0.314f_d$  in equation 4.18 is in units of radians / revolution as described in equation 4.14 for  $\Omega$ . As already noted, workpiece rotations represent the sampling rate in the feed direction.

Intuitively, as described in chapter 3, one may expect that very low frequency vibrations manifest themselves as waviness lines on the workpiece surface. For example, consider a 1 Hz disturbance frequency. Making the substitution into equation 4.18 gives

$$z(m) = 10 \sin(0.314m) \quad (4.19)$$

For a complete wave to manifest itself on the workpiece surface in the radial direction,  $\frac{2\pi}{0.314}$  or 20 workpiece revolutions must occur. The frequency  $\Omega_1$  in radians / revolution for a 1 Hz vibration is thus 0.314.

Larger disturbance frequencies can also create the same pattern in the feed direction as the 1 Hz vibration. For a particular radial line in the feed direction, sampling occurs every  $2\pi$  radians per revolution of the workpiece. This is called the sampling rate along a workpiece radial line,  $\Omega_{s,radial}$ , specifically

$$\Omega_{s,radial} = 2\pi \frac{\text{radians}}{\text{revolution}} \quad (4.20)$$

Now, consider a disturbance frequency vibration of 19 Hz for these cutting conditions. Equation 4.18 now gives

$$z(m) = 10 \sin(5.97m) \quad (4.21)$$

The frequency described in equation 4.21 is 5.97 radians / revolution. This new disturbance frequency of 19 Hz will look like the 1 Hz disturbance frequency in the feed direction. Using the derivation found in Franklin *et al.* ([18], p. 162), the resulting signal with sampling of equation 4.20 is found as follows:

$$\Omega_{workpiece} = \Omega_{19} - \Omega_{s,radial}$$

$$\Omega_{workpiece} = 5.97 - 2\pi$$

$$\Omega_{workpiece} = -0.31$$

$$\Omega_{workpiece} = -\Omega_1$$

This means that a 19 Hz disturbance frequency looks identical in the feed direction to a 1 Hz disturbance frequency, but of opposite sign. The phenomenon is illustrated

in figure 4.8. The short wavelength sine wave represents the relative tool / workpiece vibration in the cutting direction with a frequency of 19 Hz. Meanwhile the dotted line represents the sine wave that appears in the feed direction of the workpiece.

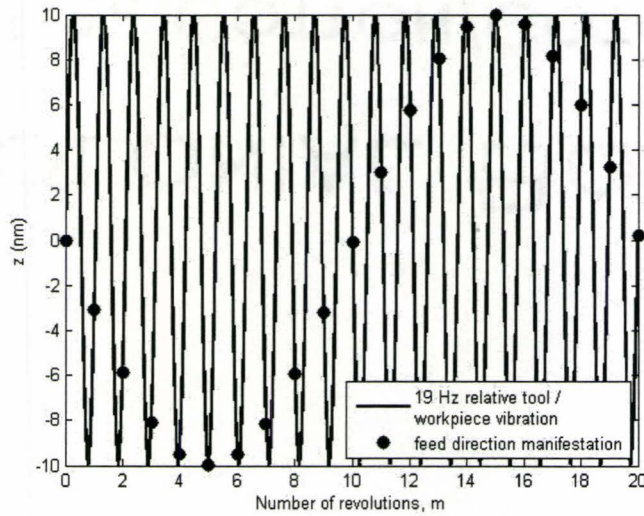


Figure 4.8: Radial in-feed vibration for different disturbance frequencies resulting in identical feed direction wavelength

The same phenomenon also occurs with much larger disturbance frequencies. Consider this time a disturbance frequency of 541 Hz, which has  $\Omega_{541}$  of 169.96 radians / revolution. Using a definition from Franklin *et al.* ([18], p. 162), this frequency will also give the same result as the 1 Hz disturbance frequency. This can be demonstrated as follows, where  $a$  is an integer value from 0 to infinity.

$$\begin{aligned} \Omega_{541} &= \Omega_1 + 2\pi a \\ 169.96 &= 0.31 + 2\pi a \\ a &= 27 \end{aligned}$$

The feed direction patterns for the 1 Hz, 19 Hz and 541 Hz signals using equation 4.12 are shown in figure 4.9. Here, disturbance frequencies of 1 Hz and of 541 Hz are the same phase, while the 19 Hz signal shows an opposite phase.

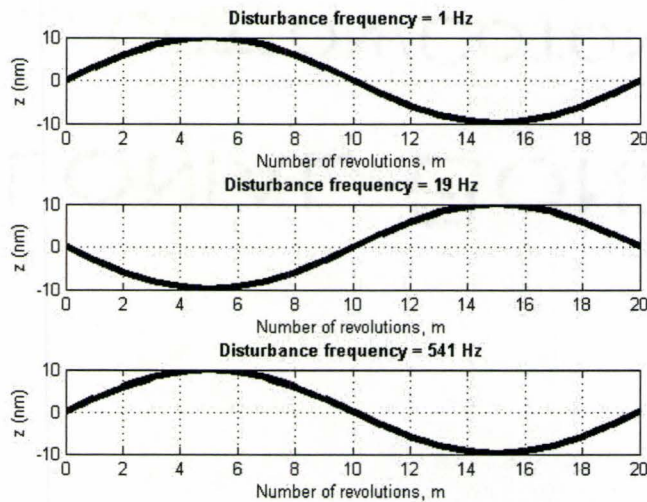


Figure 4.9: Radial in-feed vibration for different disturbance frequencies resulting in identical feed direction wavelength

#### 4.5.1 Introduction to the Concept of Surface Finish Lobes

Multiple feed direction lines are plotted together for a range of disturbance frequencies,  $f_d$ , from 0 to 47 Hz and an amplitude  $z_{amp}$  of 10 nm for 20 spindle rotations at 1200 RPM, generating the surface in figure 4.10. The gray scale represents the in-feed direction height in nm, i.e. parameter  $z$  defined in equation 4.12. An actual feed rate is not included at this point and, instead, the number of workpiece revolutions is considered. The repeatability of spatial frequency in the feed-direction is observable in figure 4.10. Extending the disturbance frequency range in figure 4.10 simply extends the same repeating pattern. Because the x-axis is in rotations instead of in

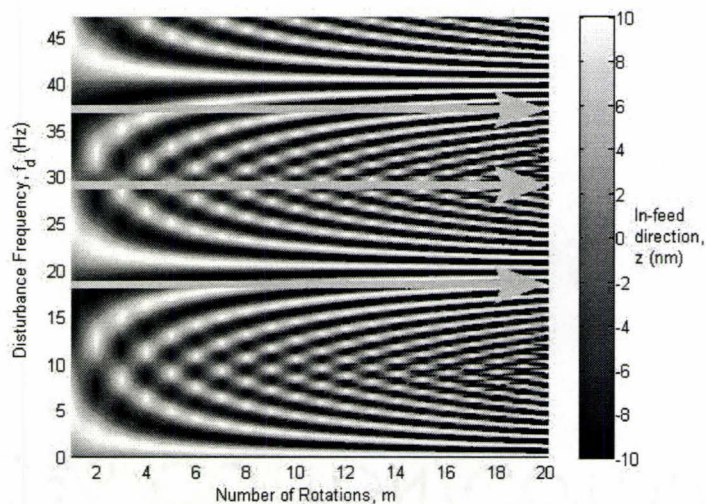


Figure 4.10: Radial lines (spokes) showing repeating vibrational pattern for a range of disturbance frequencies,  $N = 1200$  RPM,  $f = 10 \mu\text{m} / \text{rev}$ , with arrows drawn at the 19 Hz, 29 Hz and 37 Hz radial lines

$\mu\text{m}$ , this surface can be applied to any feed rate for this spindle speed. (Similarly, the surface could also be created for other spindle speeds.)

In figure 4.10, three particular feed direction segments are noted, specifically those for 19 Hz, 29 Hz and 37 Hz. These are reproduced individually in figure 4.11. For a disturbance frequency of 19 Hz, a very long wavelength pattern is produced on the workpiece surface in the feed direction. Meanwhile, at 29 Hz a short wavelength pattern is observed. At 37 Hz, a mid-wavelength pattern is produced. From this example, one can see how a relative tool / workpiece vibration can manifest itself as either a waviness or form error on a workpiece surface. The repetition and quantification of form and waviness surface finish errors over a broadband of unwanted relative tool / workpiece vibration frequencies is fundamental to the surface finish lobes.

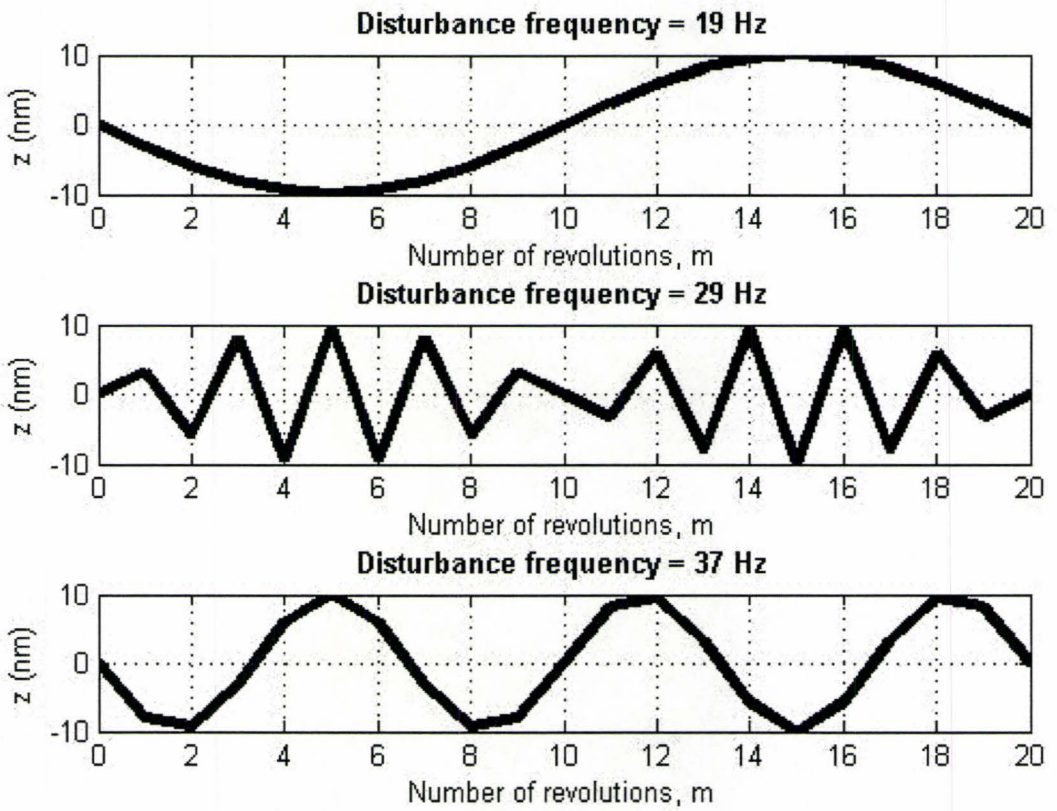


Figure 4.11: Radial in-feed vibration lines for disturbance frequencies of 19 Hz, 29 Hz and 37 Hz

## 4.6 The Surface Finish Lobes in Ultra Precision Machining

With the surface finish lobes, the waviness and form errors caused by relative tool / workpiece error are considered over a large range of disturbance frequencies. Unlike the work of [51], [9], [11], [7], [8] and [10], a broad range of in-feed disturbance frequencies are considered. Also, instead of considering  $R_t$  and  $R_a$ <sup>1</sup> magnitudes, the overall frequency relationship between relative tool / workpiece motion and surface finish errors is studied. A systematic framework, described using the concept of surface finish lobes, is presented that identifies expected waviness and form patterns that will occur on a surface for particular cutting conditions and disturbance frequencies. The surface finish lobes also describe the maximum and minimum vibration-induced wavelengths possible in the feed direction. The methodology as outlined is then validated with experimental findings.

The surface finish lobe diagrams plot the disturbance frequency  $f_d$  in Hz *versus* the feed direction spatial frequency  $\nu$  in 1/mm. The figure informs the user of the feed direction spatial frequency that will occur on a face turned surface when machined in the presence of a particular disturbance frequency. In figure 4.12 frequencies from 0 to 100 Hz are considered in 0.1 Hz increments. The spindle speed used is still 1200 RPM, but the feed of 10  $\mu\text{m}$  is also included in order to provide spatial information. The feed rate is considered as the sampling rate in the radial (feed) direction. A spatial FFT is performed on each radial line (spoke) after being first Hanning windowed. Then, the maximum resulting frequency from each FFT is stored and plotted against

---

<sup>1</sup> $R_a$  is the mean arithmetic roughness, and this measure of surface finish is discussed in chapter 5.

the disturbance frequency. The phase angle is either 0 like the 1 Hz and 541 Hz examples of figure 4.11, or  $\pi$  radians, like the 19 Hz example of figure 4.11.

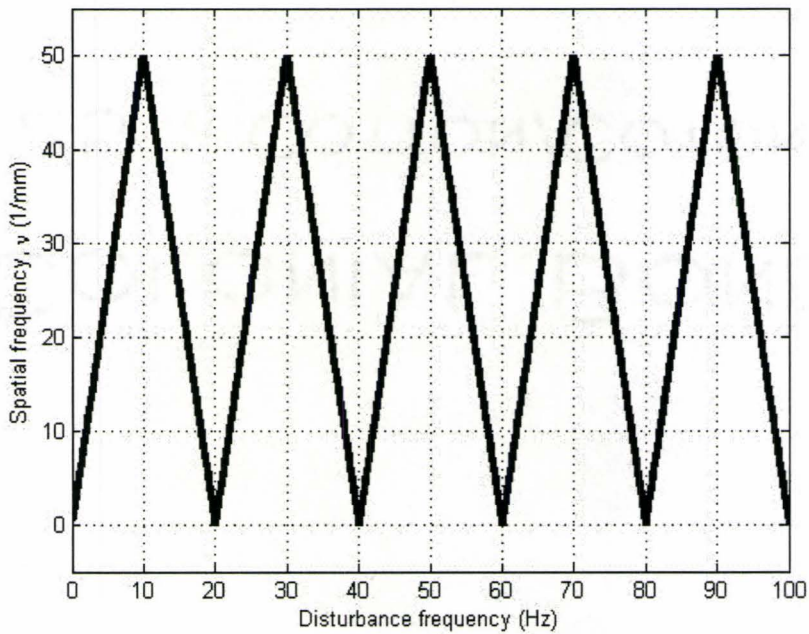


Figure 4.12: Surface finish lobes from FFT Method for  $N = 1200$  RPM and  $f = 10 \mu\text{m} / \text{rev}$

In this work it is assumed that the phase angles of disturbance frequencies are equivalent to a simulated worst case. Otherwise, for the case of ‘harmonics’ like the 1 Hz and 19 Hz disturbance frequencies, the overall amplitude on the cut workpiece surface would be affected.

As an example, take the 37 Hz feed direction line of figure 4.11. With a feed rate of  $10 \mu\text{m} / \text{rev}$ , the associated wavelength of this line is  $66.7 \mu\text{m}$ . The spatial frequency of this line is the inverse of wavelength which gives  $15000 \text{ } 1/\mu\text{m}$  or  $15 \text{ } 1/\text{mm}$ . Similarly, the other 2 feed direction lines of figure 4.11 can be analyzed. The

Disturbance frequency (Hz)	Feed direction wavelength ( $\mu\text{m}$ )	Feed direction spatial frequency (1/mm)
19	200	5
29	22	45
37	67	15

Table 4.1: Disturbance frequency, wavelength and spatial frequency as depicted for specific disturbance frequencies in surface finish lobes for  $N = 1200$  RPM and  $f = 10 \mu\text{m} / \text{rev}$

results are summarized in table 4.1. The disturbance frequency and corresponding feed direction spatial frequency can be equivalently found on the surface finish lobe of figure 4.12.

Figure 4.12, like figure 4.10, shows that the spatial frequency pattern repeats itself over various disturbance frequencies. However, it also indicates the maximum and minimum values of spatial frequency in the feed direction of an ultra precision face turned workpiece. Under these cutting conditions, the spatial frequency  $\nu$  varies between 0 and 50 1/mm, and minimum to maximum  $\nu$  occurs approximately every 10 Hz. Now, consider the plot of the inverse of spatial frequency *versus* disturbance frequency. This inverse spatial frequency is simply the wavelength, i.e.

$$\lambda = \frac{1}{\nu} \quad (4.22)$$

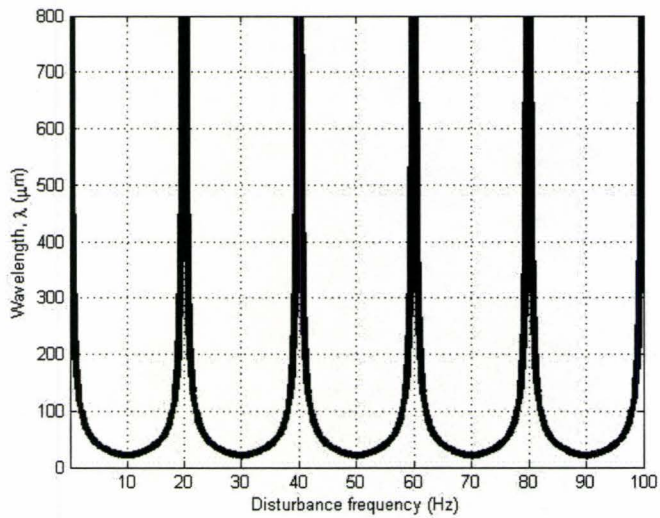
The corresponding wavelengths for spatial frequencies in figure 4.12 are depicted in figure 4.13(a). The wavelength values in table 4.1 can be found with corresponding disturbance frequency values in figure 4.13(a). The peaks in the figure 4.13(a) can theoretically go to infinity if a spatial frequency of 0 1/mm is considered. In figure 4.13(b), the valley portion for the first inverse surface finish lobe in figure 4.13(a) is

shown. The smallest wavelength caused by vibration of  $20\ \mu\text{m}$  is clearly larger than the wavelength of  $10\ \mu\text{m}$  that would be caused by the feed (in the form of feed lines).

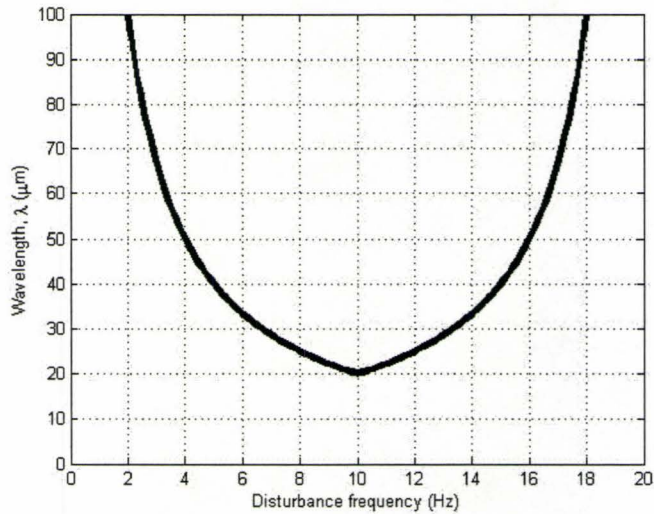
#### **4.6.1 Effect of Changing the Feed Rate on the Surface Finish Lobes**

The feed rate used in generating figures 4.12, 4.13(a) and 4.13(b) is  $10\ \mu\text{m} / \text{rev}$ . As a spatial frequency this is equivalent to  $100\ 1/\text{mm}$ . In figure 4.12, the maximum spatial frequency obtained is  $50\ 1/\text{mm}$ . The spatial frequency of  $100\ 1/\text{mm}$  represents the 'feed lines' and, hence, surface roughness. Thus, the waviness and form error patterns caused by the relative tool / workpiece vibration are very distinct from surface roughness, as their wavelength and hence spatial frequency in the feed direction are bound by very different values. Further, the surface finish lobes can be used to describe the type of surface finish defect caused by vibration. For comparison, a surface finish lobe plot is created in figure 4.14 for a feed rate of  $4\ \mu\text{m} / \text{rev}$  along with those already discussed at  $10\ \mu\text{m} / \text{rev}$ . The equivalent feed rate spatial frequency is  $250\ 1/\text{mm}$  for a feed rate of  $4\ \mu\text{m} / \text{rev}$ , and the range of spatial frequencies caused by relative tool / workpiece vibration is between 0 and  $125\ 1/\text{mm}$ .

Similarly, this analysis can be made in terms of wavelength. For a feed rate of  $10\ \mu\text{m} / \text{rev}$ , the smallest feed direction wavelength caused by vibration is  $20\ \mu\text{m}$ , compared with feed lines of spacing  $10\ \mu\text{m}$ . Meanwhile, for a feed rate of  $4\ \mu\text{m} / \text{rev}$ , the smallest feed direction wavelength caused by vibration is  $8\ \mu\text{m}$ . In both instances, the longest wavelength caused by vibration approaches infinity as the spatial frequency approaches zero.



(a) Inverse surface finish lobes



(b) Inverse surface finish lobes showing smallest vibration induced wavelength is greater than feed

Figure 4.13: Inverse surface finish lobes from the FFT method for  $N = 1200$  RPM and  $f = 10 \mu\text{m} / \text{rev}$

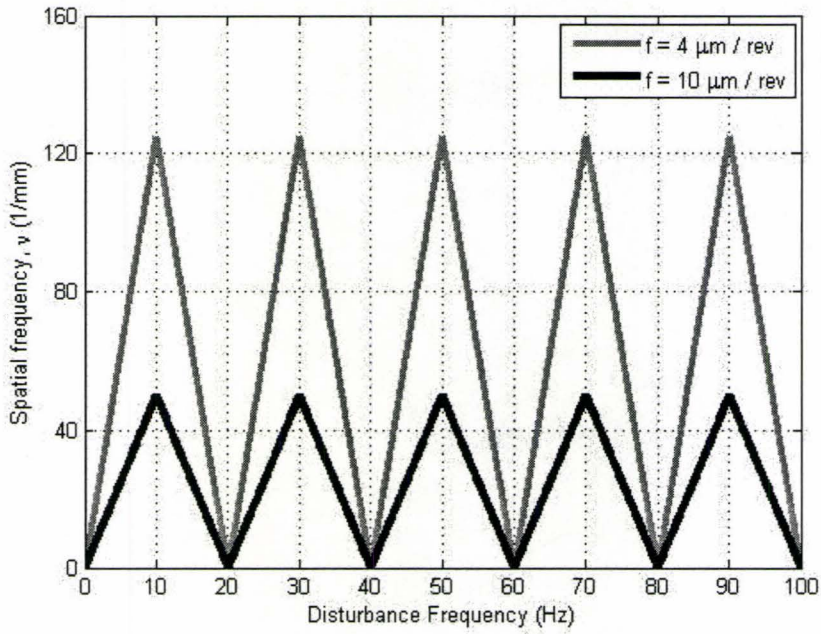


Figure 4.14: Surface finish lobes the from FFT method for  $N = 1200$  RPM, and  $f = 4 \mu\text{m} / \text{rev}$  compared with  $N = 1200$  RPM, and  $f = 10 \mu\text{m} / \text{rev}$

### 4.6.2 Generating the Surface Finish Lobes Analytically

The surface finish lobes generated from the FFT analysis can also be generated analytically. To do this the following equations are employed. First,  $\Omega$ , as described in equation 4.14, is considered for one rotation  $m$ , i.e.  $m = 1$ . This produces a value  $\Theta$  in radians, and the quadrant in which  $\Theta$  exists and the number of  $2\pi$  radian cycles,  $C$ , that it represents can thus be determined. Then, based on quadrant and number of rotations, an alternate frequency,  $\Omega_{reduced}$ , also in radians per rotation, is produced via the following process.

If the quadrant count is either 1 or 2 then

$$\Omega_{reduced} = \Omega - 2\pi C \tag{4.23}$$

If the quadrant count is either 3 or 4 then

$$\Omega_{reduced} = 2\pi - (\Omega - 2\pi C) \quad (4.24)$$

From  $\Omega_{reduced}$ , the number of spindle rotations  $M$  for a complete cycle of  $2\pi$  radians in the feed direction is found as follows

$$M = \frac{2\pi}{\Omega_{reduced}} \quad (4.25)$$

Now the spatial frequency  $\nu$  in 1/mm can be determined using  $M$  and the feed rate  $f$  as follows, where the feed is in  $\mu\text{m} / \text{rev}$

$$\nu = \frac{1}{1000fM} \quad (4.26)$$

Similarly, the wavelength  $\lambda$  in  $\mu\text{m}$  can also be found.

$$\lambda = fM \quad (4.27)$$

### Finding the Surface Finish Lobe Bounds

Quadrant 2 ends at  $\pi$  radians, and quadrant 4 ends at  $2\pi$  radians. This information combined with equation 4.14 define what are called in this thesis the surface finish lobe cornering disturbance frequencies. The surface finish lobes start where  $f_d = 0$  Hz. The next cornering disturbance frequency is found from equation 4.14 where  $\Omega = \pi$ , giving the second cornering disturbance frequency in Hz of

$$f_{d \text{ corner}2} = \frac{N}{(2)(60)} \quad (4.28)$$

The third cornering frequency occurs where  $\Omega = 2\pi$  giving the third cornering disturbance frequency in Hz of

$$f_{d \text{ corner}3} = \frac{N}{(60)} \quad (4.29)$$

This pattern then repeats itself indefinitely over a broadband of disturbance frequencies. Equations 4.28 and 4.29 indicate that the cornering frequencies are a function of the spindle speed only. This means that various feed rates will all have the same cornering disturbance frequencies if the spindle speed does not change, as illustrated in figure 4.14.

The maximum spatial frequency,  $\nu_{max}$  from the surface finish lobe diagram can also be determined analytically. At the second cornering disturbance frequency,  $\Omega_{reduced} = \pi$  radians, and thus  $M = 2$ . Substituting this into equation 4.26 gives

$$\nu_{max} = \frac{1}{1000(2)f} \quad (4.30)$$

Equivalently, the smallest feed direction wavelength  $\lambda_{min}$  can be deduced. This is

$$\lambda_{min} = 2f \quad (4.31)$$

Equation 4.31 makes it clear that the smallest feed direction relative tool / work-piece motion is always two times greater, and, thus, distinct from the feed rate,  $f$ .

From equation 4.12, a singularity point exists at the second cornering frequency,  $f_{d \text{ corner}2}$ . For the example under consideration, when the disturbance frequency is equal to 10 Hz, the spindle speed is equal to 1200 RPM, and  $\theta_{1p}$  is equal to zero,

equation 4.12 becomes

$$z(m) = z_{amp} \sin(\pi m) \quad (4.32)$$

Equation 4.32 indicates that an infinitely long wavelength is produced in the midst of the shortest possible wavelengths at the peak of the surface finish lobe due to a 180 degree phase shift. However, in practice, it would be unlikely to achieve this scenario due to the difficulty of controlling cutting parameters this tightly.

### 4.6.3 Effect of Changing the Spindle Speed on the Surface Finish Lobes

In figure 4.15, the surface finish lobes for a reduced spindle speed of 600 RPM and a feed rate of  $10 \mu\text{m} / \text{rev}$  are depicted using the analytical method. In figure 4.15, the surface finish lobes for 1200 RPM and  $10 \mu\text{m} / \text{rev}$  are included for comparison. Note that with spindle speed reduced by a factor of 2, the frequency of the surface finish lobes increases linearly also by a factor of 2. Meanwhile, spatial frequency values still range between 0 and 50 1/mm, as with the spindle speed of 1200 RPM.

Equations 4.30 and 4.31 indicate that the maximum spatial frequency,  $\nu_{max}$ , and, hence, the smallest wavelength,  $\lambda_{min}$ , are a function of the feed rate only. This means that various spindle speeds will all have the same  $\nu_{max}$  and, hence,  $\lambda_{min}$  if feed rates are equivalent.

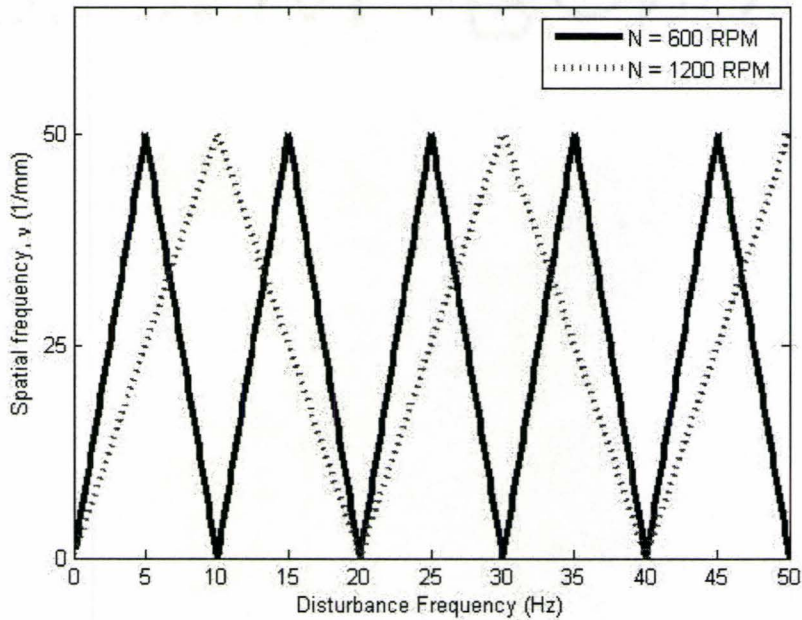


Figure 4.15: Surface finish lobes from the analytical method for  $f = 10 \mu\text{m} / \text{rev}$ , and  $N = 600 \text{ RPM}$  and  $N = 1200 \text{ RPM}$

#### 4.6.4 Experimental Validation of the Surface Finish Lobes

Experimental validation of the surface finish lobes was accomplished by ultra precision face turning a 100 mm diameter aluminum 6061-T6 workpiece on an ASG 2500 with machining conditions described in table 3.3.

Vibrations that occur during cutting in the in-feed direction were measured via accelerometers as described in section 3.4. Then, the workpiece surface was measured in the in-feed direction via white light interferometry to observe the resulting waviness patterns in the in-feed direction. Finally, given measured peak disturbance frequencies, the predicted waviness patterns were found via the surface finish lobes. Predicted and experimental values were found to be in agreement, and are discussed in detail in this section. The workpiece surface displacement in the in-feed direction

is analyzed in the frequency domain by double integrating the acceleration data [17] shown in figure 3.21.

### **Ultra Precision Face Turned Surface Assessment via White Light Interferometry and Spatial Frequency Analysis**

Following machining, the workpiece was measured via white light interferometry. The image was taken 10 mm from the workpiece outside diameter, a position that corresponds with that of the accelerometer measurement during machining. The image was taken with a median  $\theta_{1p}$  of approximately 270 degrees, with reference to figure 4.4. The data was bandpass filtered with the Zygo software and then exported for analysis in Matlab.

In figure 4.16, the measured surface is displayed. Note from the axes of figure 4.16 that information is garnered from a measured rectangle of 520  $\mu\text{m}$  by 400  $\mu\text{m}$  in the cutting and feed directions, respectively. This data has been bandpass filtered by wavelengths of 286.86  $\mu\text{m}$  and 8.36  $\mu\text{m}$ , or equivalently by spatial frequencies of 3.49 1/mm and 119.62 1/mm. The resolution in the cutting and feed directions is 0.84  $\mu\text{m}$ .

Since the bandpass filter used is 3.49 1/mm to 119.62 1/mm, almost all possible spatial frequencies caused by relative tool / workpiece rotation, as identified by the surface finish lobes of figure 4.12 (0 to 50 1/mm), are observable in the white light interferometry image, with the exception of very low spatial frequency patterns. Overall, the spatial frequency range defined by the surface finish lobes is beneficial in surface metrology. Knowing *a priori* the range of spatial frequencies means that the appropriate field of view, resolution and filtering are employed in order to observe the

vibrational pattern on the workpiece surface. The upper bound of the filter used in this case also allowed measurement of the feed lines subject to Shannon's Law, given the image resolution.

In figure 4.16, dominant waviness patterns are seen. The feed line spacing has been included vertically on the right hand side of the plot to make it clear that the dominant observable pattern in figure 4.16 is not feed lines.

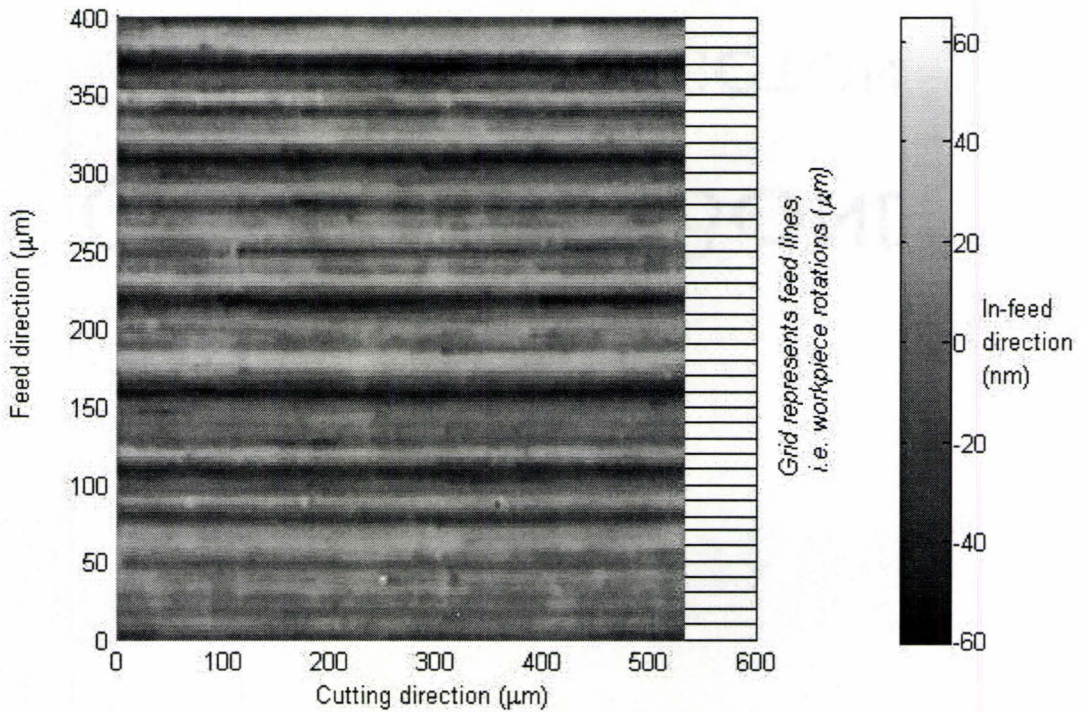


Figure 4.16: Ultra precision face turned workpiece surface measured via white light interferometry at 10 mm from the outer radius showing dominant waviness patterns, zoom 260x

In figure 4.17, one radial line in the feed direction of figure 4.16 is plotted. Also included is a simulated feed pattern showing the ideal geometric roughness,  $R_t$ , caused by the tool nose and feed, as expressed in equation 3.1. The formation of the simulated line is described later in chapter 5. It is included here to contrast magnitude and

spatial frequency.

From figure 4.16, it is again clear that the spatial frequency of the dominant pattern observed on the workpiece is significantly greater than that of the feed lines, and, therefore, represents waviness and not surface roughness.

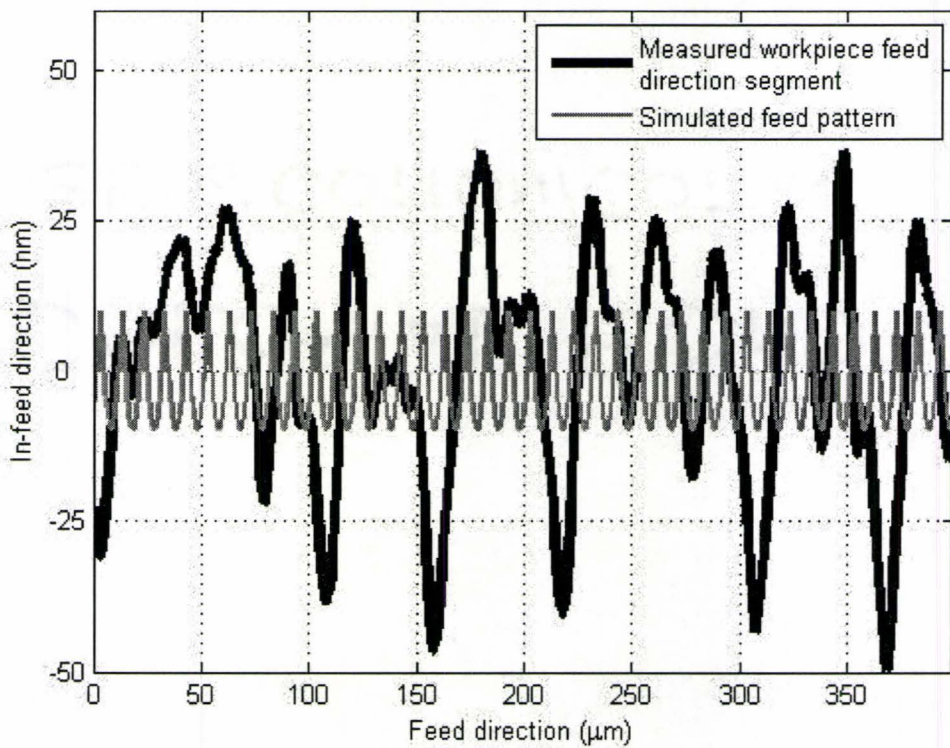


Figure 4.17: White light interferometry measured workpiece section in the feed direction compared with simulated feed lines

For each of the radial segments an FFT was performed. A Hanning window was employed on each feed line and the individual FFT results were also normalized and magnitude corrected for the windowing function. Lastly, all the FFT magnitude results were root mean square averaged. In figure 4.18, the resulting spatial frequency assessment of the measured surface in the feed direction is presented. In table 4.3 the results are summarized.

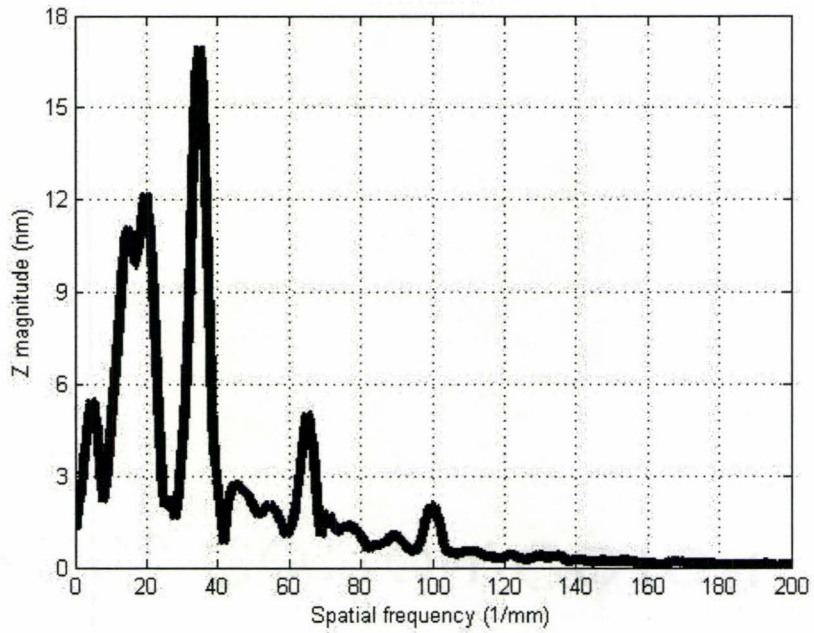


Figure 4.18: Feed direction spatial frequency results of workpiece surface measured via white light interferometry at 10 mm from the outer radius

Peak Spatial frequency (1/mm)	Magnitude (nm)
34.7	17.0
19.7	12.2
14.9	11.1
4.4	5.4

Table 4.2: Summary of workpiece peak spatial frequencies found in figure 4.18

Observing figure 4.18, the significant spatial frequencies are less than 50 1/mm, as predicted by the surface finish lobes of figure 4.12. A small bump of unknown origin exists at 65 1/mm<sup>2</sup>. Finally, a small peak is also observable at 100 1/mm. This peak represents the feed lines at a rate of 10  $\mu\text{m}$  / rev. From figure 4.18, it is clear that the waviness error caused by the relative tool / workpiece movement is significantly greater than the surface roughness error caused by the feed lines. The surface roughness error of 2.02 nm is, in fact, only 12 per cent of the peak waviness error of 17.0 nm.

### **Comparing In-Situ Machining Vibration with the Resulting Workpiece Surface via the Surface Finish Lobes**

*In situ* accelerometers and correlation of peak frequencies to surface finish lobes were used to predict surface finish defects in ultra precision machining. This is demonstrated by looking at displacement values calculated from the FFT of relative tool / workpiece acceleration depicted in figure 3.21. The measured surface indicates that the feed rate was steady at about 10  $\mu\text{m}$  / rev. The measured surface also indicates that the spindle speed was consistent. However, it was determined that the spindle spun slightly faster than nominal at 1200.7 RPM. This was determined by creating surface finish lobes with different spindle speeds and comparing surface FFT results. Figures showing correlation between this spindle speed and measured results are provided in this section. It should be noted that peak measured displacement values presented in figures 4.19(a), 4.20(a) and 4.21(a) are less than the measured error magnitude on the workpiece surface. This is most likely due to measurement noise

---

<sup>2</sup>It is later discerned that this is a result of the tool nose geometry with vibration.

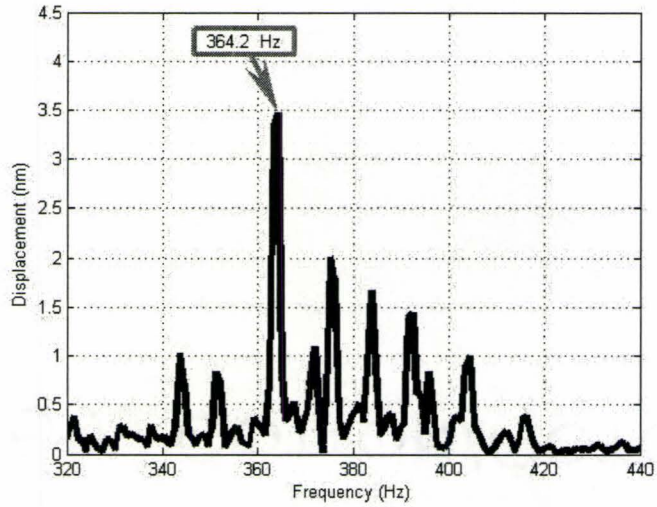
during cutting. The issue of inaccurate displacement magnitudes acquired from the double integration of accelerometer data for use in frequency analysis is also noted in Liu and Cheng [28]. To address the issue in this thesis, the peak frequencies of accelerometer-measured displacements, and not the exact displacement magnitudes, are considered. Thus, only the overall shape indicating the significant disturbance frequencies is considered important in this analysis. The frequencies of significant peak magnitudes found in the displacement data match those found in the original *in situ* relative tool / workpiece acceleration data.

The spatial frequency of 19.7 1/mm (or equivalently a wavelength of 50.8  $\mu\text{m}$ ) in figure 4.18 can be explained by the peak displacement of 364.2 Hz provided in figure 4.19(a). Looking up the spatial frequency of 364.2 Hz on the surface finish lobes of figure 4.19(b) gives a spatial frequency value of 19.9 1/mm.

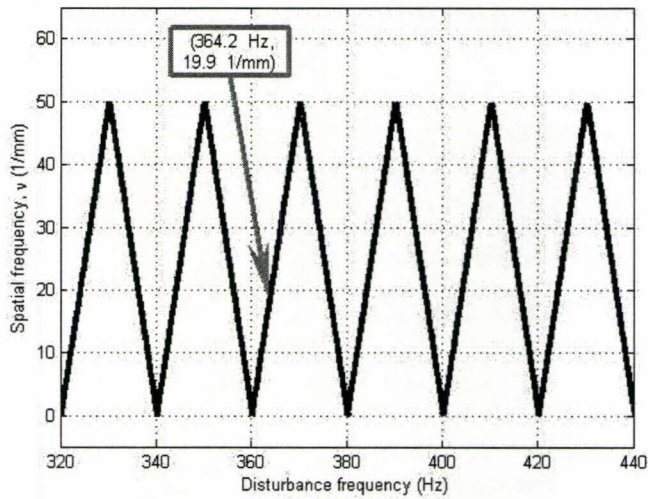
Note from figure 4.19(a) that the frequency interval is 0.8548 Hz. Meanwhile the slope of the surface finish lobe is approximately  $\pm 5$  1/mm/Hz. If the tolerance of a frequency measurement is approximately  $\pm 0.43$  Hz, then the corresponding tolerance on the surface finish lobe is  $\pm 2.13$  1/mm.

The next most significant range of displacement values measured during cutting is presented in figure 4.20(a) for the frequency range of 700 to 860 Hz. In figure 4.20(a), four displacement FFT peaks were noted, and their corresponding predicted spatial frequencies are provided in figure 4.20(b). First, the peak at 763.4 Hz has a corresponding spatial frequency of 14.8 1/mm. This is practically identical to the peak of 14.9 1/mm found in figure 4.18.

Next considered are the two peaks of 781.3 Hz and 783.0 Hz in figure 4.20(a). The 783.0 Hz disturbance has a corresponding spatial frequency of 12.7 1/mm, which is



(a) Relative tool / workpiece displacement FFT measured during ultra precision face turning for the frequency range of 320 to 440 Hz, number of averages = 103,  $\Delta f = 0.8548$  Hz



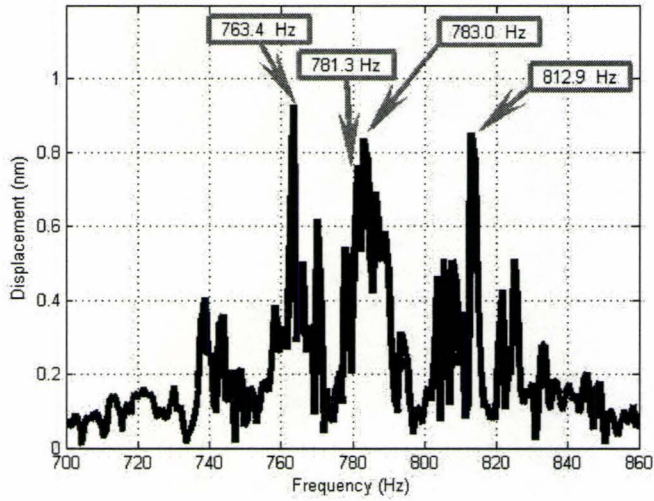
(b) Surface finish lobes for the disturbance frequency range of 320 to 440 Hz,  $N = 1200.7$  RPM,  $f = 10 \mu\text{m} / \text{rev}$

Figure 4.19: Relative tool / workpiece displacement FFT and corresponding surface finish lobes for the frequency range of 320 to 440 Hz

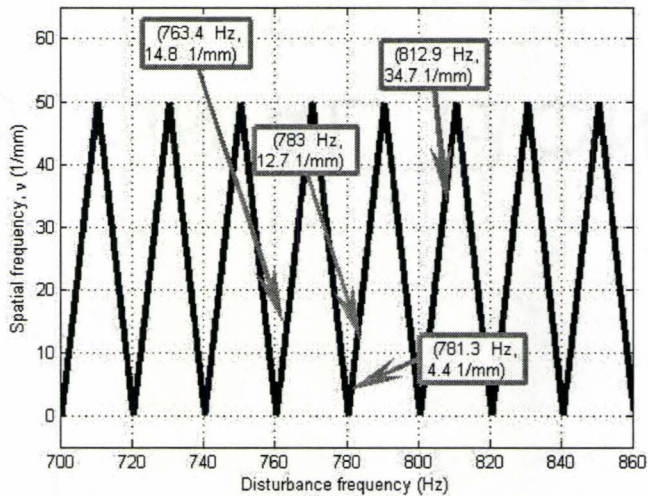
very similar to the 14.9 1/mm peak in figure 4.18 already discussed. Because of the repeating nature of the surface finish lobes, the individual contribution of the 763.4 Hz disturbance and of the 783.0 Hz disturbance are practically indistinguishable given the measurement resolution, and also the resolution of the white light interferometer. The peak at 781.3 Hz has a corresponding spatial frequency of 4.2 1/mm from figure 4.20(b). This value is very similar to the 4.4 1/mm peak found in figure 4.18.

Finally, the peak of 812.9 Hz observed in figure 4.20(a) has a corresponding spatial frequency of 37.9 1/mm from figure 4.20(b). This spatial frequency is close to the observed peak of 34.7 Hz, the largest peak of figure 4.18. The spatial frequency of 37.9 1/mm is actually accounted for by spatial frequency results of the 4976.0 Hz frequency, presented in figure 4.21(a).

In figure 3.21, a large peak occurs at 4976.0 Hz. The corresponding displacement curve for the region of 4940 to 5010 Hz is provided in figure 4.21(a). The actual peak displacement value is considered much larger than that of figure 4.21(a). Note the accelerometer placement on the ASG 2500 in figure 3.15 for *in situ* vibration measurement. The 4976.0 Hz is primarily captured by the spindle accelerometer which is on the spindle housing and not on the actual spindle or workpiece itself. The spindle rests on an air bearing. This means that the accelerometer captures movement of the spindle housing, but only remotely detects movement of the spindle and workpiece itself. The air bearing thus attenuates the spindle movement observed by the spindle housing accelerometer. As an example, the air bearing's isolation is such that the spindle speed of 1200.7 RPM, or equivalently of 20 Hz, is not observed by the accelerometer. However, despite accelerometer observability of the workpiece movement, the workpiece indicates a large peak at a spatial frequency of 34.7 1/mm



(a) Relative tool / workpiece displacement FFT measured during ultra precision face turning for the frequency range of 700 to 860 Hz, number of averages = 103,  $\Delta f = 0.8548$  Hz



(b) Surface finish lobes for the disturbance frequency range of 700 to 860 Hz,  $N = 1200.7$  RPM,  $f = 10 \mu\text{m} / \text{rev}$

Figure 4.20: Relative tool / workpiece displacement FFT and corresponding surface finish lobes for the frequency range of 700 to 860 Hz

Peak disturbance frequency (Hz)	Corresponding spatial frequency from surface finish lobes (1/mm)	Corresponding spatial frequency from measured workpiece (1/mm)
364.2	19.9	19.7
763.4	14.8	14.9
781.3	4.2	4.4
783.0	12.7	14.9
812.9	37.9	34.7
4976.0	34.5	34.7

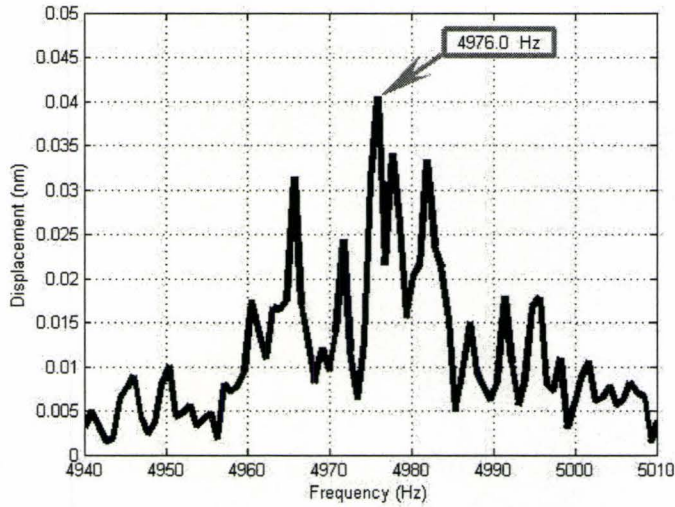
Table 4.3: Summary of disturbance frequency peak displacements and corresponding spatial frequencies found in figure 4.18

(equivalently a wavelength of  $28.8 \mu\text{m}$ ). From figure 4.21(b) a 4976.0 Hz disturbance frequency corresponds to a spatial frequency of 34.5 1/mm.

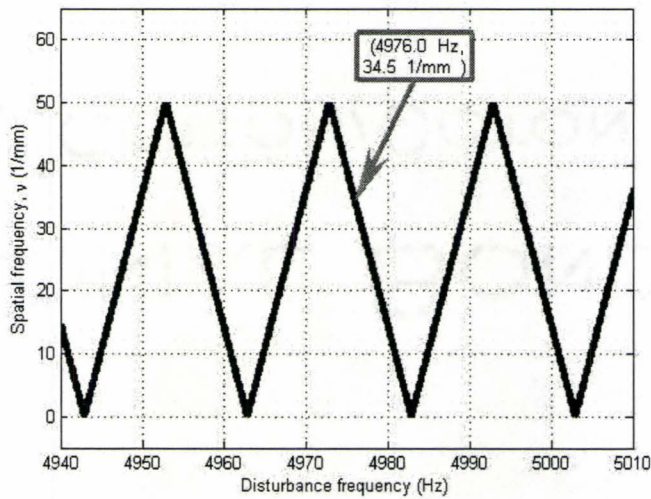
## 4.7 Implications and Potential Applications of the Surface Finish Lobes

### 4.7.1 Surface Finish Error Characterization with the Surface Finish Lobes

The type of defect caused by vibration on a face turned surface can also be characterized via the surface finish lobes. Take the following definition, based roughly on [48], of three wavelength categories for the surface finish errors of surface roughness, waviness and form. The workpiece radius  $r$  is used in the definition. The surface roughness wavelength is considered to be the ideal geometric surface roughness, and equal to the feed rate. The form error wavelength is considered to be greater than or equal to the workpiece radius. Meanwhile the waviness error wavelength is considered



(a) Relative tool / workpiece displacement FFT measured during ultra precision face turning for the frequency range of 4940 to 5010 Hz, number of averages = 103,  $\Delta f = 0.8548$  Hz



(b) Surface finish lobes for the disturbance frequency range of 4940 to 5010 Hz,  $N = 1200.7$  RPM,  $f = 10 \mu\text{m} / \text{rev}$

Figure 4.21: Relative tool / workpiece displacement FFT and corresponding surface finish lobes for the frequency range of 4940 to 5010 Hz

Defect type	Symbol	Quantification
Surface roughness	$\lambda_r$	$\lambda_r = \text{Feed}$
Waviness	$\lambda_w$	$\lambda_r < \lambda_w < \lambda_f$
Form	$\lambda_f$	$\lambda_f \geq r$

Table 4.4: Definitions of surface finish defects

to be greater than the surface roughness error wavelength and less than the form error wavelength. The workpiece surface finish errors are summarized in the feed direction in table 4.4. In figure 4.22 the type of error associated with each disturbance frequency for the finishing conditions of spindle speed equal to 1000 RPM and feed rate of  $10 \mu\text{m} / \text{rev}$  and workpiece radius of 50 mm is depicted. Note that vibration only causes errors of type waviness and form, and not surface roughness, as has already been noted.

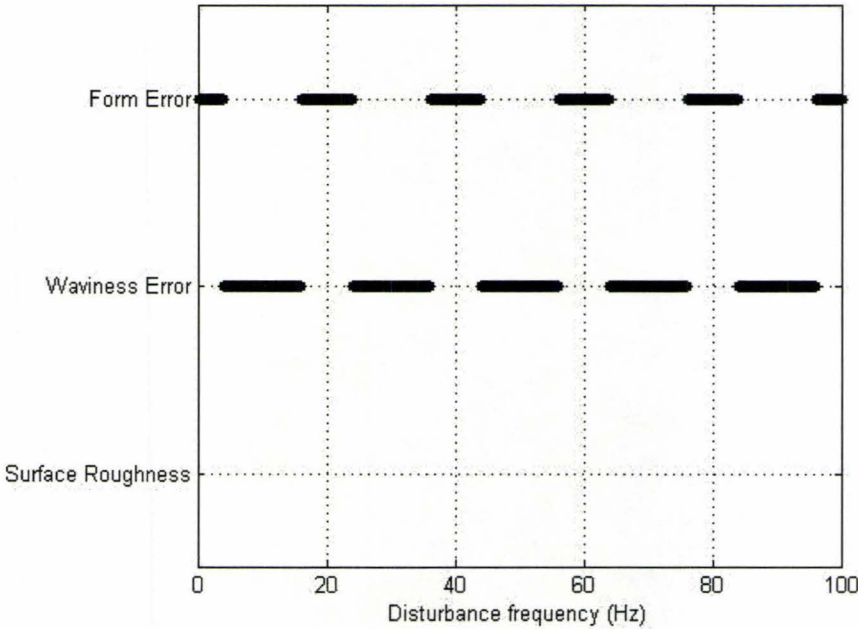


Figure 4.22: Feed direction surface finish error type caused by relative tool / workpiece vibration for  $N = 1200 \text{ RPM}$ , and  $f = 10 \mu\text{m} / \text{rev}$ , and workpiece radius of 50 mm

## 4.7.2 Surface Finish Error Correction with the Surface Finish Lobes

In ultra precision machining, it may not always be possible to eliminate all disturbance frequencies. Further, *in situ* frequency monitoring may not be possible as described in section 4.6.4 of this thesis. Despite this, tight tolerances are still required. Certain waviness patterns, even of low amplitude, may still interfere with end product function and, thus, necessitate expensive post-processing.

Consider now the example of a 50 mm radius workpiece with the disturbance frequency used earlier in this chapter of 37 Hz. This disturbance frequency will create an undesirable wavelength pattern of 67  $\mu\text{m}$ , or 15 1/mm, with a spindle speed of 1200 RPM and a feed rate of 10  $\mu\text{m}$  / rev. If the same disturbance frequency could instead be forced to a value producing a very large wavelength of, for example, 1000 mm, or 0.001 1/mm, then the disturbance's effect on the ultra precision workpiece in this application may be negligible. With reference to figure 4.12, this could involve a shift of disturbance frequency from, for example, 37 Hz to either 20 Hz or 40 Hz, while retaining the same machining parameters. If shifting the disturbance frequency is not feasible, then a change in machining parameter could be used. In this case, changing the spindle speed from 1200 to 1110 RPM would push the spatial frequency to close to zero. The same analysis is also valid for smaller feed rates and spindle speeds. Being leveraged is the fact that as the feed direction spatial frequency approaches zero, the wavelength approaches infinity, i.e. as  $\nu \rightarrow 0, \lambda \rightarrow \infty$ . Further, a sufficiently large form error may not prove problematic in the ultra precision face turned workpiece. This analysis assumes that tight control is possible with the ultra precision machine tool's cutting parameters, and also that other significant disturbance frequencies do

not also exist during ultra precision machining. Cheung *et al.* [9] also observed the possibility of forcing a vibrational wavelength to zero by changing the spindle speed based on their relative tool / workpiece vibration equations, specifically considering disturbance frequencies that are multiples of spindle speed. A spindle speed of 2200 RPM is equivalent to 37 Hz. Meanwhile, the surface finish lobes indicate more machining parameter possibilities.

#### **4.7.3 Identifying Ultra Precision Machine Tool Inaccuracies with the Surface Finish Lobes**

In section 4.6.4, the surface finish lobes, in conjunction with the FFT of the measured workpiece surface in the feed direction, and knowledge of the disturbance frequencies during cutting, were used to determine how close the ASG 2500 ultra precision machine tool's machining parameters were to nominal. It has been determined that while the actual feed rate was very close to the nominal feed rate of  $10 \mu\text{m} / \text{rev}$ , the spindle speed was slightly faster than nominal at 1200.7 RPM instead of the nominal 1200 RPM.

#### **4.7.4 Surface Finish Lobes *versus* Stability Lobes**

Surface finish lobes do not denote regions of machining stability and instability as with the stability lobes, for example, as presented in Tlustý *et al.* [55]. Surface finish lobe diagrams also are not intended to maximize the metal removal rate (MRR). However, they can be used to improve the surface finish in ultra precision machining, for example, by shifting relative tool / workpiece motion from short wavelengths which result in feed direction waviness errors to long wavelengths where their impact

on quality is less. If a surface free of undesired waviness patterns is generated in ultra precision machining, then post processing may be reduced or even avoided.

In figure 4.23, the spatial frequencies are depicted for various spindle speed and feed rate combinations for a constant disturbance frequency,  $f_d$ , of 37 Hz. Finally, in figure 4.24, spatial frequencies approaching zero are shown for various spindle speed and feed rate combinations, with a constant disturbance frequency,  $f_d$ , of 37 Hz.

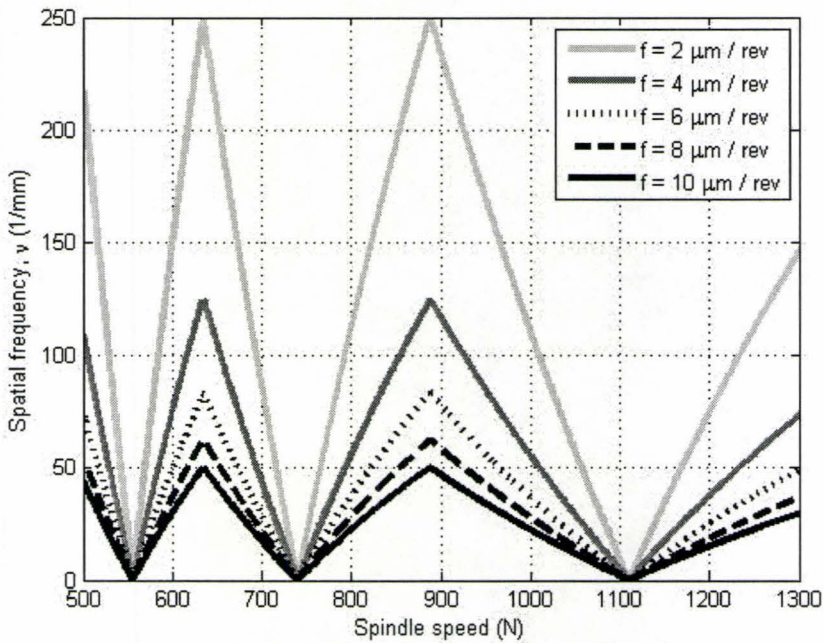


Figure 4.23: Resulting spatial frequency for various spindle speed and feed rate combinations with constant disturbance frequency,  $f_d = 37$  Hz

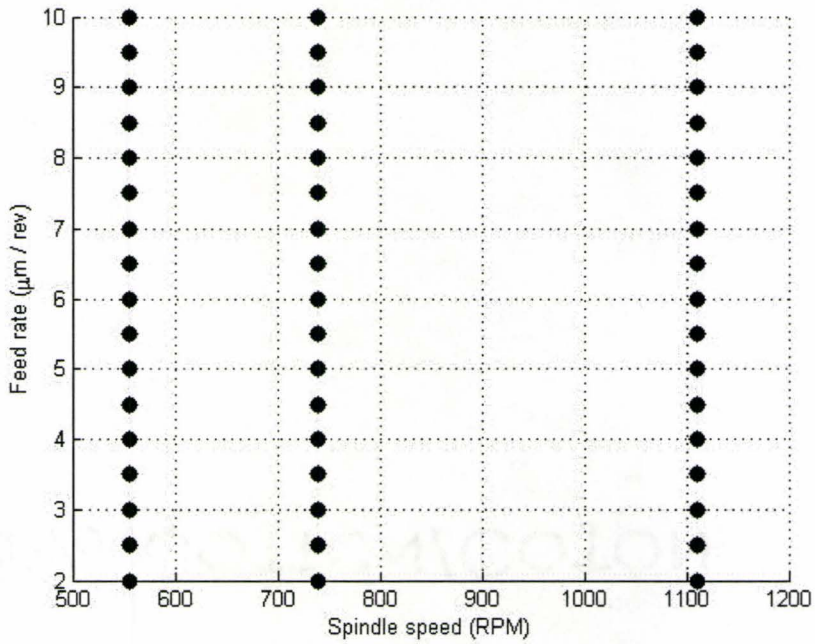


Figure 4.24: Spatial frequency approaching zero for various spindle speed and feed rate combinations with constant disturbance frequency,  $f_d = 37$  Hz

## 4.8 Chapter Summary

In this chapter, the vibrational equations in ultra precision face turning are described in both the cutting and feed directions. Justification for and derivation of vibrational equations in the feed direction are given. The usefulness of this derivation is further described by finding the disturbance frequency from a simulated white light interferometry image, and also from the surface finish lobes. It has been shown that waviness errors caused by relative tool / workpiece vibration are a significant source of inaccuracy in ultra precision machining. The surface finish lobes clearly demonstrate that waviness patterns are distinct from feed patterns and also they provide geometric guidelines for surface metrology.

Section 4.4, finding the disturbance frequency,  $f_d$ , from a simulated image is the subject of publication [36]. Meanwhile, sections 4.5 and 4.6 concerning surface finish lobes are the subject of publication [39].

## **Chapter 5**

# **The Filtering Effect and Error Mitigation**

### **5.1 Introduction**

In this chapter, the filtering effect of cutting parameters on vibration in ultra precision machining is studied. The surface finish lobes of chapter 4 are used as a starting point, and cutting tool geometry, depth of cut, and vibrational amplitude are included in the analysis. It is shown how the surface finish error in ultra precision machining, in the presence of vibration, can be mitigated by employing the developed theory.

## 5.2 Simulating and Assessing Ultra Precision Face Turned Surface Finish in the Presence of Relative / Tool Workpiece Movement

This chapter focusses on an ultra precision diamond face turned surface cut in the presence of unwanted relative tool / workpiece movement. The relative tool / workpiece movement considered is harmonic, constant amplitude and in the in-feed direction. In figure 5.1, the in-feed relative tool / workpiece movement,  $z(m)$ , is defined, where  $m$  is the number of rotations. The feed direction,  $x$ , is a spoke or radial line of the workpiece.

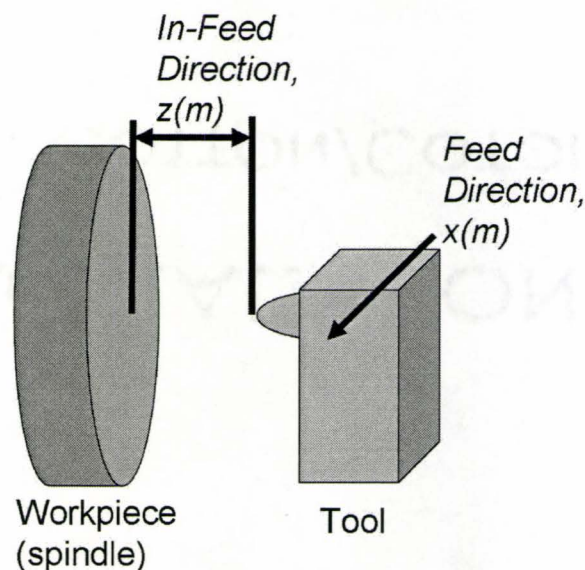


Figure 5.1: In-feed relative tool / workpiece motion, feed direction, tool, and workpiece on spindle

Figure 5.2 illustrates the concept of harmonic relative tool / workpiece movement in the in-feed direction,  $z$ . Each tool profile in figure 5.2 is incremented by the feed rate,  $f$ . Note the overlap of each tool pass. In [51], and later in [9], [8], and [10], this is described as tool interference.

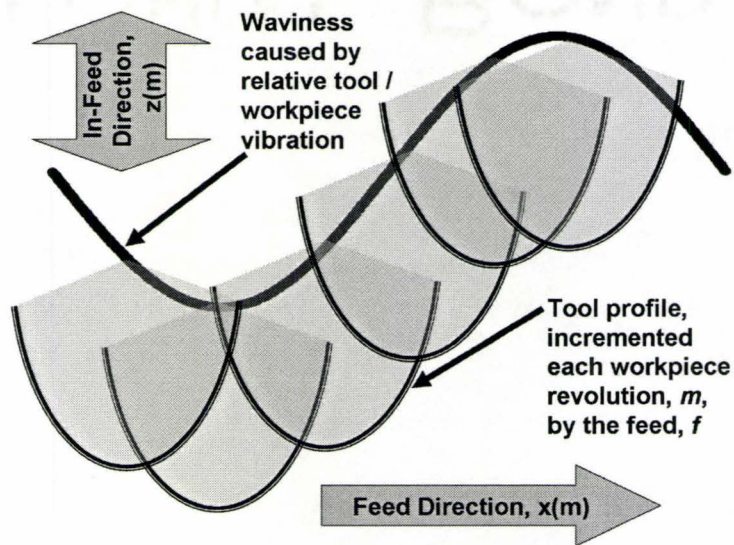
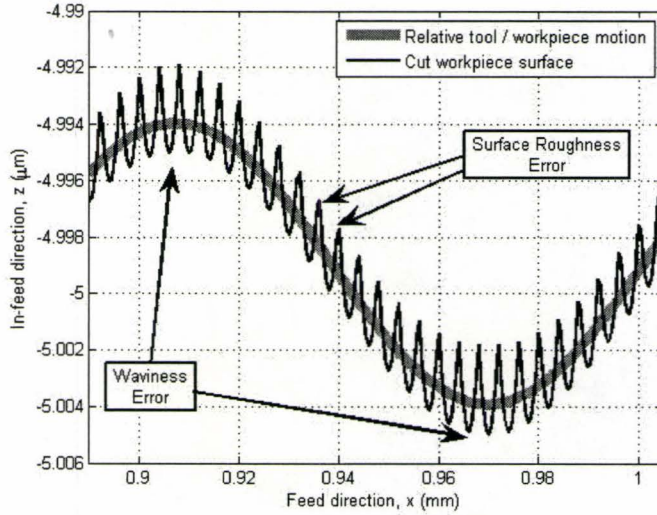


Figure 5.2: Relative tool / workpiece harmonic motion and tool incremented by the feed rate

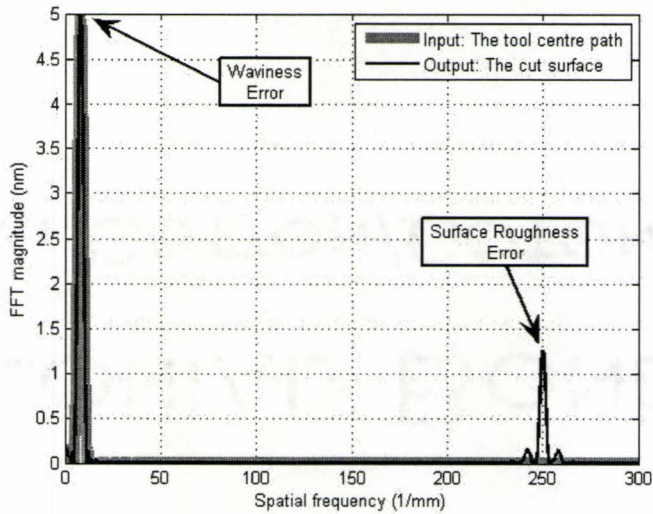
### 5.2.1 Surface Finish Errors: Roughness, Waviness and Form

An example of waviness error compared with surface roughness error on one surface in the feed direction is provided in figures 5.3(a) and 5.3(b).

In figure 5.3(a), the horizontal axis is the feed direction,  $x$ , and the vertical axis is the in-feed direction,  $z$ . The long wavelength represents waviness, while the short wavelength is the surface roughness. Cutting parameters used in this simulation include a depth of cut,  $d$ , of  $5 \mu\text{m}$  and a tool nose radius,  $R_n$ , of  $0.630 \text{ mm}$ . In



(a) The relative tool / workpiece movement and the cut workpiece surface



(b) The FFT magnitude of relative tool / workpiece movement and of the cut workpiece surface

Figure 5.3: Simulation of relative tool workpiece movement, cut workpiece surface and FFT results  $f = 4 \mu\text{m} / \text{rev}$ ,  $d = 5 \mu\text{m}$ ,  $R_n = 0.630 \text{ mm}$ ,  $z_{amp} = 5 \text{ nm}$ , and  $\nu = 8 \text{ 1/mm}$

figure 5.3(a) the light gray line represents the relative tool / workpiece movement. Meanwhile, the cut workpiece surface is represented by the black line.

In figure 5.3(a), the feed rate is  $4 \mu\text{m} / \text{rev}$ , and hence the surface roughness wavelength is also  $4 \mu\text{m}$ . As already noted, the inverse of wavelength is the spatial frequency in the feed direction,  $\nu$ . The feed rate spatial frequency is thus  $250 \text{ 1/mm}$ .

The long wavelength in figure 5.3(a) is  $125 \mu\text{m}$  in length, and has amplitude  $z_{amp}$  of  $5 \text{ nm}$ . Equivalently, the long wavelength spatial frequency,  $\nu$ , is  $8 \text{ 1/mm}$ . This is an example of waviness error. In chapter 4, it was shown that wavelengths caused by relative tool / workpiece harmonic motion are distinct and always larger than those caused by the feed.

In figure 5.3(b), the FFT magnitude results of figure 5.3(a) are shown for the relative tool / workpiece motion and for the cut workpiece surface. The large spike at the beginning of the plot is for the waviness pattern of  $8 \text{ 1/mm}$  and  $5 \text{ nm}$  magnitude. Meanwhile, the small spike represents the feed spatial frequency of  $250 \text{ 1/mm}$ . Note that the cut workpiece surface shows the tool feed and the relative tool workpiece vibration. The tool feed marks are, of course, not visible in the relative tool / workpiece movement alone.

## 5.2.2 Tool Orbit

To make the simulated cut workpiece surface, first the tool orbit is generated. The concept of tool orbit is shown in figure 5.2. The tool orbit exhibits the change in relative tool / workpiece movement with harmonic motion in the in-feed direction. For simplicity, all movement is assumed to occur at the tool center as illustrated in figure 5.4. The tool center moves to the right in figure 5.4 with every pass,  $m$ , by an

amount equivalent to the feed,  $f$ . The feed can be considered the sampling of tool center in the feed direction per pass. The center of the tool is assumed to oscillate harmonically in the in-feed direction,  $z$ . The effective depth of cut is the addition of the desired depth of cut,  $d$ , and the relative / tool workpiece displacement caused by harmonic motion in the in-feed direction. As already noted, the relative tool / workpiece movement considered is harmonic, of constant amplitude and in the in-feed direction as described in figure 5.1. Equation 4.12 is again used, but for simplicity  $\theta_{1p}$  is assumed to be equal to zero, giving

$$z(m) = z_{amp} \sin\left(\frac{2\pi 60 f_d}{N} m\right) \quad (5.33)$$

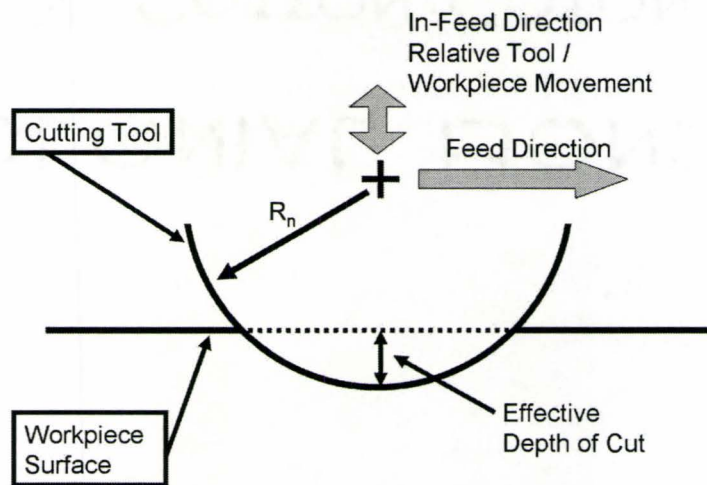


Figure 5.4: Tool orbit definitions

The tool center changes with each pass,  $m$ , in the feed direction,  $x$ , as follows

$$x_{tc}(m) = R_n + f(m - 1) \quad (5.34)$$

The tool center height is affected by the depth of cut,  $d$ , and also varies harmonically per pass. In equation 5.35, the disturbance frequency,  $f_d$ , is converted to spatial frequency,  $\nu$ . The  $2\pi$  term in equation 5.35 converts revolution  $m$  to radians.

$$z_{tc}(m) = R_n - d + z_{amp}\sin(2\pi\nu fm) \quad (5.35)$$

The conversion from disturbance frequency,  $f_d$ , to spatial frequency,  $\nu$ , occurs via the surface finish lobes as described in chapter 4.

To create the tool orbit, the tool surface is discretized according to  $x_{inc}$  which is a fraction of the feed. Specifically,

$$x_{inc} = \frac{f}{10} \quad (5.36)$$

In equation 5.36, the feed direction discretization is one tenth of the feed rate. In the feed direction during cutting, the sampling, or spacing per pass, is the feed. Making  $x_{inc}$  one tenth of the feed rate means that the tool orbit sampling is ten times the highest spatial frequency event. Also, the tool geometry considered is based solely on the tool nose radius and, thus, one tenth of the feed provides sufficient description of this geometry. An example of the discretization is depicted in figure 5.5. In Sohn *et al.* [47], tool orbit discretization is also depicted. While the discretization used by Sohn *et al.* is not stated explicitly in [47], it is visually very similar to that portrayed in figure 5.5 and dictated by equation 5.36.

The uncut workpiece surface is assumed to occur at  $z = 0$ . The in-workpiece tool orbit is created by recording the tool nose values below the surface, i.e. where  $z < 0$ . The  $z$  coordinates for the tool nose at each pass is based on the Pythagorean

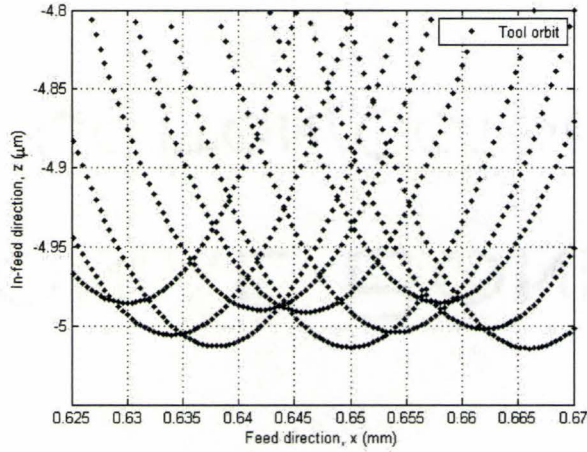


Figure 5.5: The tool orbit showing the discretization of the tool surface, for  $f = 4 \mu\text{m} / \text{rev}$ ,  $d = 5 \mu\text{m}$ ,  $R_n = 0.630 \text{ mm}$ ,  $z_{amp} = 15 \text{ nm}$ , and  $\nu = 70 \text{ 1/mm}$

Theorem. The geometry is illustrated in figure 5.6. The co-ordinate  $x_{tp}$  is calculated as follows:

$$x_{tp} = (a - 1)x_{inc} + f(m - 1) \quad (5.37)$$

In equation 5.37,  $a$  is the increment number. Length  $l_x$  depicted in figure 5.6 is  $|x_{tc} - x_{tp}|$ . Length  $l_z$  is calculated as

$$l_z = \sqrt{R_n^2 - l_x^2} \quad (5.38)$$

Coordinate  $z_{tp}$  is found from

$$z_{tp} = z_{tc} - l_z \quad (5.39)$$

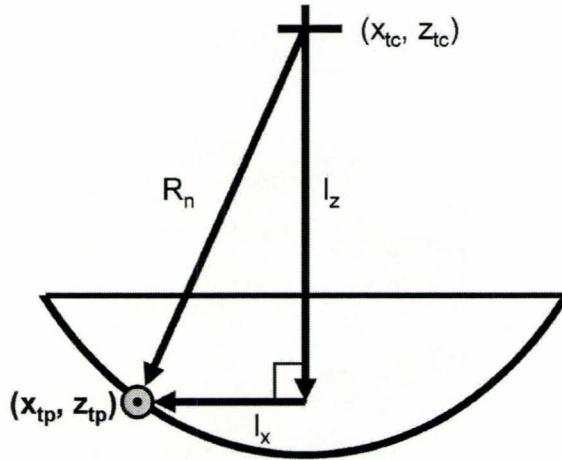


Figure 5.6: Finding tool nose coordinates for each pass

Then equation 5.39 is substituted in equation 5.40 to give

$$z_{tp} = z_{tc} - \sqrt{R_n^2 - (x_{tc} - x_{tp})^2} \quad (5.40)$$

In figure 5.7, the tool orbit is depicted for 10 passes with a spatial frequency of 70 1/mm and a relative tool / workpiece amplitude of 15 nm. In figure 5.7, the black sine wave represents the movement of the tool center. Meanwhile, the large gray tool shapes show the resulting tool movement per pass. Studying the tool center path shows that each  $2\pi$  revolutions of the tool center occurs over  $14.3 \mu\text{m}$ , or with a frequency of 70 1/mm. Also, each tool center point occurs at an interval of  $4 \mu\text{m}$ , which is equivalent to feed,  $f$ . In [9], [10], and [47], tool orbit curves are also presented.

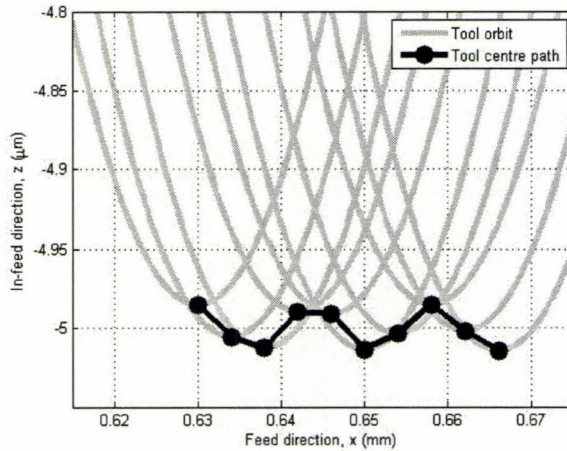


Figure 5.7: The tool orbit and the relative tool / workpiece movement, 10 passes, for  $f = 4 \mu\text{m} / \text{rev}$ ,  $d = 5 \mu\text{m}$ ,  $R_n = 0.630 \text{ mm}$ ,  $z_{amp} = 15 \text{ nm}$ , and  $\nu = 70 \text{ 1/mm}$

### 5.2.3 The Cut Workpiece Surface

The cut surface is generated from the tool orbit. Considering figure 5.7, and the observation that tool paths overlap, the cut surface is the smallest  $z$  value for each value of  $x$ . Numerically, the cut surface is found from  $x_{tp}$  and  $z_{tp}$  with a search algorithm that records the smallest  $z_{tp}$  for each  $x_{tp}$ . The vectors of cut surface are called  $x_{cut}$  and  $z_{cut}$  and are shorter in length than the tool path vectors.

In figure 5.8, the cut surface and tool orbit movement are depicted together for the same machining conditions as figure 5.7. However, in figure 5.8, the result of 35 tool passes is visible. The gray line is the relative tool / workpiece movement and the black line is the resulting cut surface. The dominant spatial frequency of both lines is equivalent, as is the phase. Meanwhile, the resulting amplitude of vibration on the cut surface is considerably less than that of relative tool workpiece movement. Also, in the cut workpiece surface feed marks are visible only sporadically, and are reduced in amplitude when compared with those labeled “surface roughness” in figure 5.3(a).

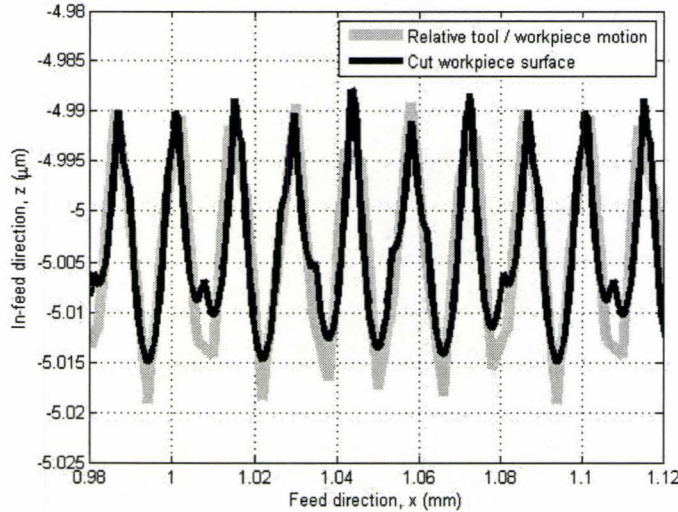


Figure 5.8: The relative tool / workpiece movement and the cut workpiece surface for  $f = 4 \mu\text{m} / \text{rev}$ ,  $d = 5 \mu\text{m}$ ,  $R_n = 0.630 \text{ mm}$ ,  $z_{amp} = 15 \text{ nm}$ , and  $\nu = 70 \text{ 1/mm}$

### 5.2.4 Spatial Frequency Analysis of Relative Tool / Workpiece Movement and of the Cut Workpiece Surface

Once the relative tool / workpiece movement and the cut workpiece surfaces are generated, a spatial FFT is performed. For the surface in figure 5.8, this is done for 178 workpiece rotations. Data is Hanning windowed and the FFT results are scaled appropriately. Results are provided in figure 5.9.

From figure 5.9, both the relative tool / workpiece movement and the cut workpiece surface have the same dominant spatial frequency of  $70 \text{ 1/mm}$ , the original input spatial frequency. However, both amplitudes are smaller than the input  $z_{amp}$  of  $15 \text{ nm}$ . The relative tool / workpiece movement maximum magnitude is approximately  $11.5 \text{ nm}$ , while that of the cut workpiece surface is approximately  $9.6 \text{ nm}$ . Also, unlike figure 5.3(a), the feed rate is no longer observable at  $250 \text{ 1/mm}$ . In [10], Cheung *et*

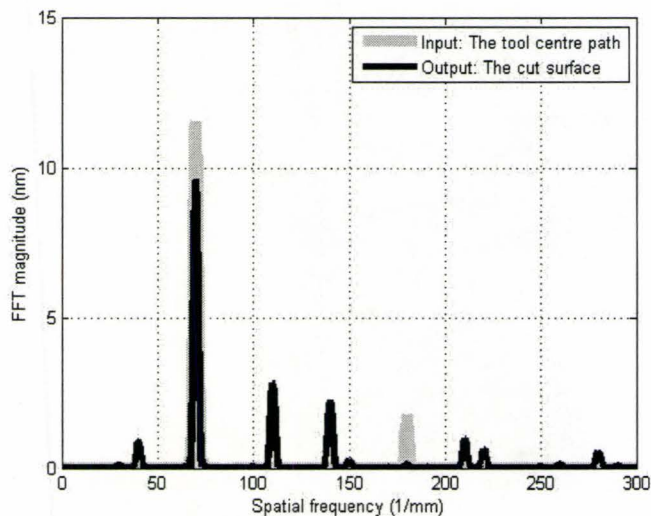


Figure 5.9: The FFT magnitude of relative tool / workpiece movement and of the cut workpiece surface for  $f = 4 \mu\text{m} / \text{rev}$ ,  $d = 5 \mu\text{m}$ ,  $R_n = 0.630 \text{ mm}$ ,  $z_{amp} = 15 \text{ nm}$ , and  $\nu = 70 \text{ 1/mm}$

*al.* mentioned that tool interference shifts this roughness to a lower spatial frequency. From figures 5.8 and 5.9, this observation is not conclusive. What is evident, however, is that the magnitude of feed lines is reduced with relative tool / workpiece vibration.

### 5.2.5 Surface Roughness in the Presence of Machining Vibrations

From the FFT of the simulated cut workpiece surface it is shown that the magnitude of the feed marks is often reduced by relative tool / workpiece vibrations. In some cases, the expected feed mark frequency changes altogether. This phenomenon is discussed in detail in section 5.6. For now, the concept is simply introduced.

Consider two sets of cutting conditions for a 100 mm diameter aluminum 6061-T6 workpiece described in table 5.1.

Cutting Parameter	Symbol	Units	Workpiece	Workpiece
Feed rate	f	$\mu\text{m} / \text{rev}$	4	2
Spindle speed	N	RPM	1201.3	1000
Depth of cut	d	$\mu\text{m}$	5	5
Tool nose radius	$R_n$	mm	0.630	0.630

Table 5.1: Cutting conditions for finish turning of 100 mm diameter aluminum 6061-T6 workpiece

The surface roughness peak-to-valley,  $R_t$ , can be predicted for each workpiece via equation 3.1. In table 5.2, the predicted roughness for each workpiece is given. Simulation and experimental work indicates that the predicted surface roughness value,  $R_t$ , is not valid in the presence of relative tool / workpiece motion. As already mentioned, this observation is discussed further in section 5.6. The value  $R_t/2$  is provided in table 5.2 as this is similar to the amplitude value that would be produced by the FFT of the cut workpiece surface machined without vibrations.

Roughness Value	Units	Workpiece $f = 4 \mu\text{m} / \text{rev}$	Workpiece $f = 2 \mu\text{m} / \text{rev}$
$R_t$	nm	3.18	0.80
$R_t/2$	nm	1.59	0.40

Table 5.2: Predicted surface roughness  $R_t$  for  $f = 4 \mu\text{m} / \text{rev}$  and for  $f = 2 \mu\text{m} / \text{rev}$ , both with  $R_n = 0.630 \text{ mm}$

## 5.2.6 The Bounds of Vibrational Spatial Frequency - Surface Finish Lobes

The resulting waviness or form error pattern of relative tool / workpiece movement caused by a disturbance frequency,  $f_d$ , is expressed by equation 5.33. In figures 5.10 and 5.11, the surface finish lobes for the two machining conditions considered are presented over a disturbance frequency range of 0 to 100 Hz. The same finite pattern presented in each figure repeats itself indefinitely for a broadband of disturbance frequencies. In figure 5.10 for a feed,  $f$ , of  $4 \mu\text{m} / \text{rev}$ , the spatial frequencies range from 0 to 125 1/mm. Meanwhile, in figure 5.11 for a feed,  $f$ , of  $2 \mu\text{m} / \text{rev}$ , the spatial frequencies range from 0 to 250 1/mm. The maximum and minimum spatial frequencies and associated wavelengths are summarized in table 5.3. For a spindle speed,  $N$ , of 1201.3 RPM the surface finish lobe pattern repeats itself approximately every 20 Hz. Meanwhile for a spindle speed,  $N$ , of 1000 RPM the surface finish lobe pattern repeats itself approximately every 16.7 Hz.

Parameter	units	Workpiece $f = 4 \mu\text{m} / \text{rev}$ and $N = 1201.3 \text{ RPM}$	Workpiece $f = 2 \mu\text{m} / \text{rev}$ and $N = 1000 \text{ RPM}$
Maximum nominal spatial frequency	1/mm	125	250
Minimum nominal spatial frequency	1/mm	0	0
Minimum nominal wavelength	$\mu\text{m}$	8	4
Maximum nominal wavelength	$\mu\text{m}$	$\rightarrow \infty$	$\rightarrow \infty$

Table 5.3: Summary of surface finish lobes for  $f = 4 \mu\text{m} / \text{rev}$  and  $N = 1201.3 \text{ RPM}$  and for  $f = 2 \mu\text{m} / \text{rev}$  and  $N = 1000 \text{ RPM}$

Indicated in table 5.3 is the smallest possible wavelength caused by relative tool

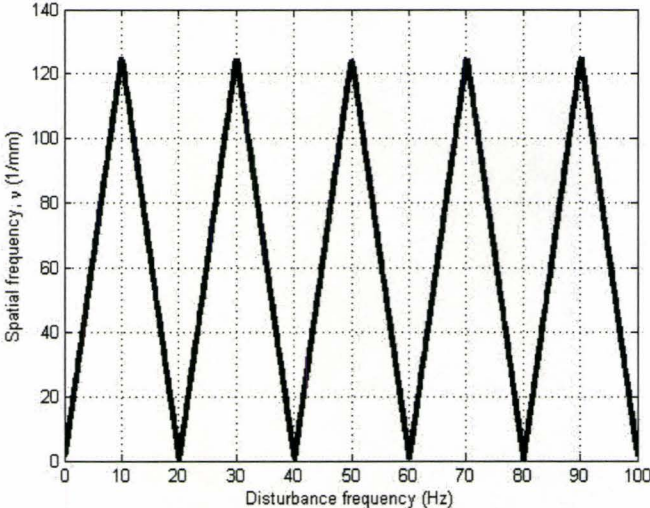


Figure 5.10: Surface finish lobes for  $N = 1201.3$  RPM and  $f = 4 \mu\text{m} / \text{rev}$

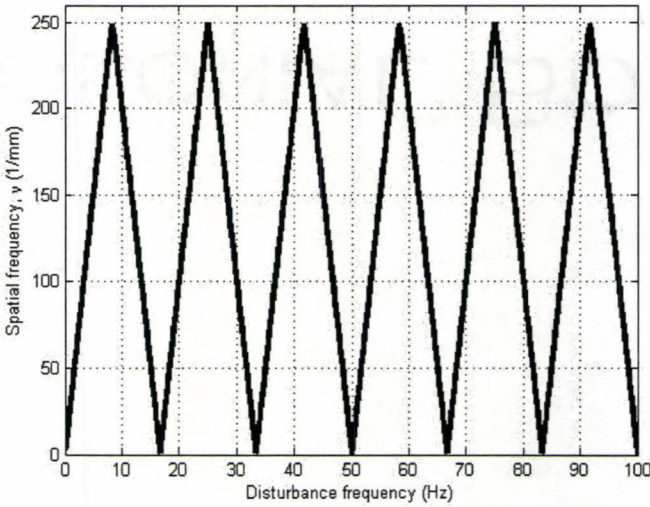


Figure 5.11: Surface finish lobes for  $N = 1000$  RPM and  $f = 2 \mu\text{m} / \text{rev}$

/ workpiece vibrations for each workpiece. In each case, the smallest possible wavelength is two times greater than the feed rate. This means that the waviness pattern caused by relative tool / workpiece motion is distinct from the surface roughness caused by the feed on the workpiece. This observation has already been discussed in chapter 4. In the case of the workpiece presented in section 4.6 for a feed rate,  $f$ , of  $10 \mu\text{m} / \text{rev}$ , the spatial frequency patterns described by the surface finish lobes are equivalent to those on the cut workpiece surface. However, for slower feed rates, as will be shown, the same dominant spatial frequency does not always manifest itself on the cut workpiece in the feed direction. Instead, a smaller spatial frequency appears. This phenomenon is described in detail in section 5.3.

### 5.3 Assembling the Filters - Big Picture Behavior

From the surface finish lobes, the bounds of relative tool / workpiece spatial frequency in the feed direction are known for a given spindle speed and feed rate combination. Then, given the amplitude of vibration,  $z_{amp}$ , the depth of cut,  $d$ , and the tool nose radius,  $R_n$ , the actual cut surface profile can be determined.

In this section, the information is assembled together in order to understand overall how various amplitudes of disturbance frequency manifest themselves on the cut workpiece surface. It is shown that a filtering effect occurs for larger spatial frequencies. The filtering curves are assembled for the cutting conditions described in table 5.1. Vibrational amplitudes,  $z_{amp}$ , considered are 5 nm, 10 nm and 15 nm.

### 5.3.1 Filter Curves for a Feed Rate of $4 \mu\text{m} / \text{rev}$

The first set of curves presented are in figures 5.12(a) and 5.12(b). Over a range of 125 1/mm spatial frequencies, relative tool / workpiece motion and cut surface profiles are generated, like those presented in figure 5.3(a), and FFTs are performed on each curve like the results in figure 5.3(b). Then the maximum spatial frequency and magnitude for the relative tool workpiece motion and cut workpiece surface finish are saved. Over the range of spatial frequencies, these results are shown in figures 5.12(a) and 5.12(b) for an amplitude of vibration,  $z_{amp}$ , of 5 nm and a feed rate of  $4 \mu\text{m} / \text{rev}$ .

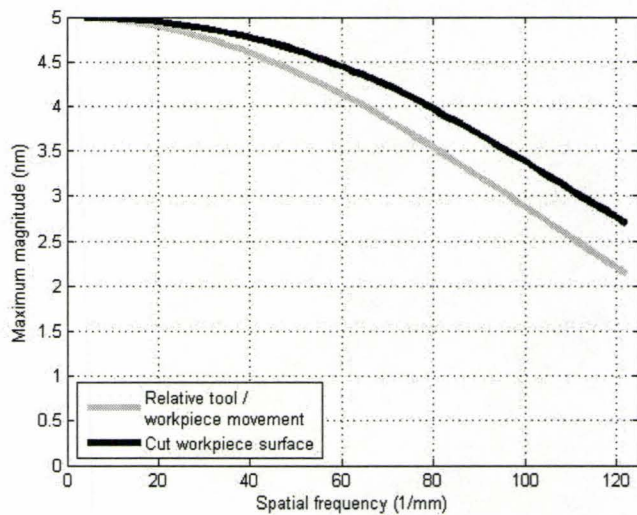
Figure 5.12(a) indicates that the input spatial frequency of relative tool / workpiece movement translates itself exactly on the cut surface. For example, if the input spatial frequency of relative tool / workpiece movement is 100 1/mm, then the same dominant spatial frequency will be present on the cut workpiece surface.

Figure 5.12(b) shows the maximum magnitude for the dominant spatial frequencies on the cut workpiece surface. Despite the fact that the amplitude of vibration,  $z_{amp}$ , remains constant, the resulting relative tool / workpiece movement and pattern on the cut surface decreases with increasing spatial frequency. This is a significant observation, indicating that for a particular range of spatial frequencies, the impact of vibrational amplitude on the cut workpiece surface is less at larger spatial frequencies.

An example is provided in figures 5.13(a) and 5.13(b) for a spatial frequency,  $\nu$ , of 70 1/mm with an amplitude of vibration,  $z_{amp}$ , of 5 nm. The simulation of the relative tool / workpiece motion is shown in gray and the cut surface is shown in black in figure 5.13(a). The FFT of both lines is given in figure 5.13(b). As noted in figure 5.12(b), both lines have a peak amplitude less than the input  $z_{amp}$  of 5 nm.

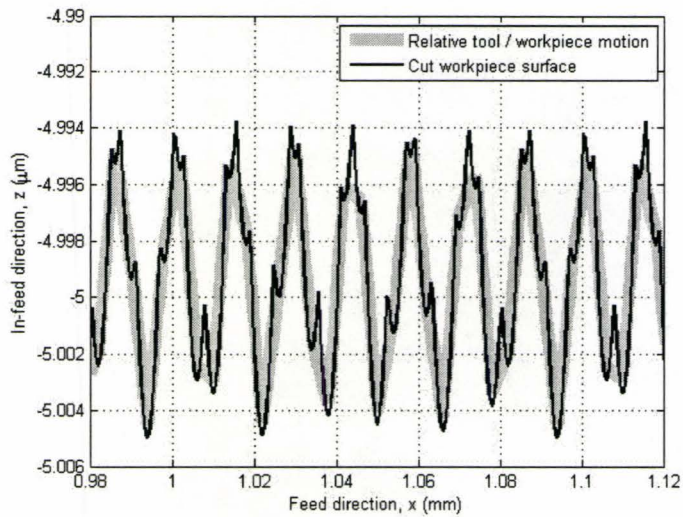


(a) Relative tool / workpiece spatial frequency and resulting spatial frequency on the cut workpiece surface, based on maximum FFT magnitude

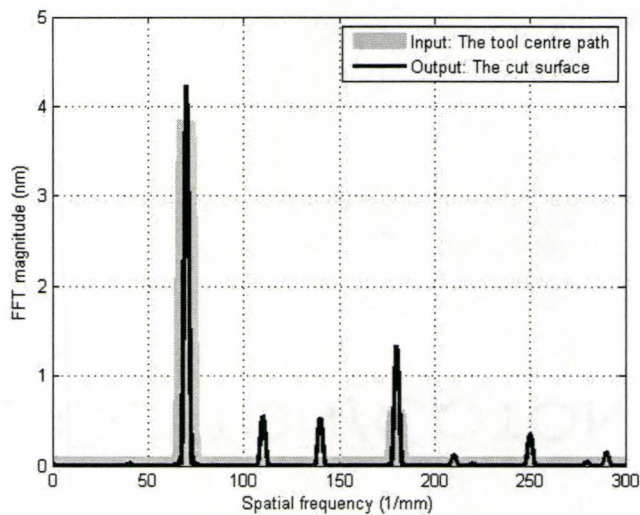


(b) Maximum spatial FFT magnitude and frequency for relative tool / workpiece motion and cut workpiece surface

Figure 5.12: Filtering effect based on FFT results for  $d = 5 \mu\text{m}$ ,  $R_n = 0.630 \text{ mm}$ ,  $f = 4 \mu\text{m / rev}$ , and  $z_{amp} = 5 \text{ nm}$



(a) The relative tool / workpiece movement and the cut workpiece surface



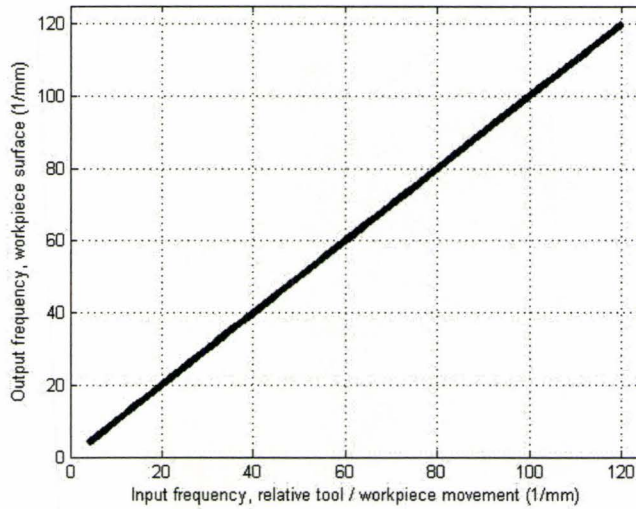
(b) The FFT magnitude of relative tool / workpiece movement and of the cut workpiece surface

Figure 5.13: Simulation of relative tool workpiece movement, cut workpiece surface and FFT results  $f = 4 \mu\text{m} / \text{rev}$ ,  $d = 5 \mu\text{m}$ ,  $R_n = 0.630 \text{ mm}$ ,  $z_{amp} = 5 \text{ nm}$ , and  $\nu = 70 \text{ 1/mm}$

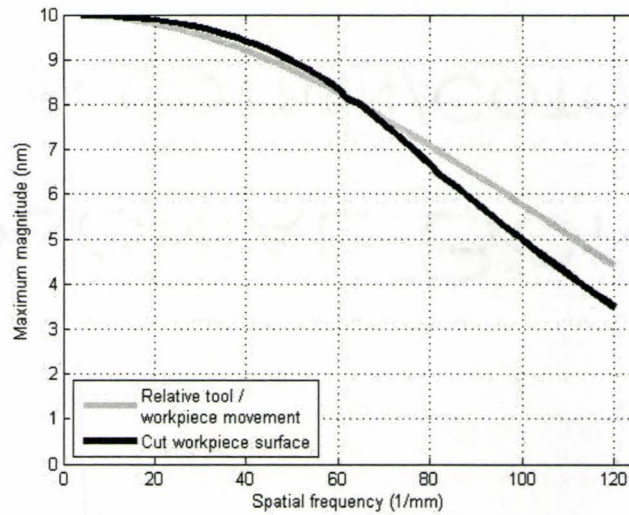
In figures 5.14(a) and 5.14(b), curves are provided for an amplitude of vibration,  $z_{amp}$ , of 10 nm. These curves exhibit behavior very similar to those in figures 5.12(a) and 5.12(b). Again, the dominant spatial frequencies of relative tool / workpiece motion and of the cut workpiece surface are equivalent. Meanwhile, the slope showing magnitude attenuation of the cut workpiece surface is greater in figure 5.14(b) than it is in figure 5.12(b).

The filter curves for an amplitude of vibration,  $z_{amp}$ , of 15 nm are provided in figures 5.15(a) and 5.15(b). The behavior of the filter curve is different for this larger amplitude of vibration. In figure 5.15(a) the dominant spatial frequency of the cut workpiece surface does not match that of the input relative tool / workpiece movement for spatial frequencies greater than 104 1/mm. The filter curve of figure 5.15(b) is not a continuous line as it was in figures 5.12(b) and 5.14(b). The attenuation for relative tool / workpiece spatial frequencies larger than 104 1/mm is much greater than for lower spatial frequencies. This increased attenuation is evidenced in the bottom curve of figure 5.15(b) of approximately 6 nm, compared with the input amplitude,  $z_{amp}$ , of 15 nm.

An example from this lower region is provided in figures 5.16(a) and 5.16(b) for a spatial frequency,  $\nu$ , of 116 1/mm. While the spatial frequency of 116 1/mm is still evident on the cut workpiece surface, the dominant spatial frequency is less at 18 1/mm. The cut workpiece surface magnitude at 18 1/mm is 5.7 nm, or 38 per cent of the input magnitude,  $z_{amp}$ , of 15 nm. For comparison, the same plots are provided for an input spatial frequency of,  $\nu$ , of 100 1/mm in figures 5.17(a) and 5.17(b). This time the dominant spatial frequency on the cut workpiece surface matches that of the input frequency. However, a lower spatial frequency of around 50 1/mm is



(a) Relative tool / workpiece spatial frequency and resulting spatial frequency on the cut workpiece surface, based on maximum FFT magnitude



(b) Maximum spatial FFT magnitude and frequency for relative tool / workpiece motion and cut workpiece surface

Figure 5.14: Filtering effect based on FFT results for  $d = 5 \mu\text{m}$ ,  $R_n = 0.630 \text{ mm}$ ,  $f = 4 \mu\text{m} / \text{rev}$ , and  $z_{amp} = 10 \text{ nm}$

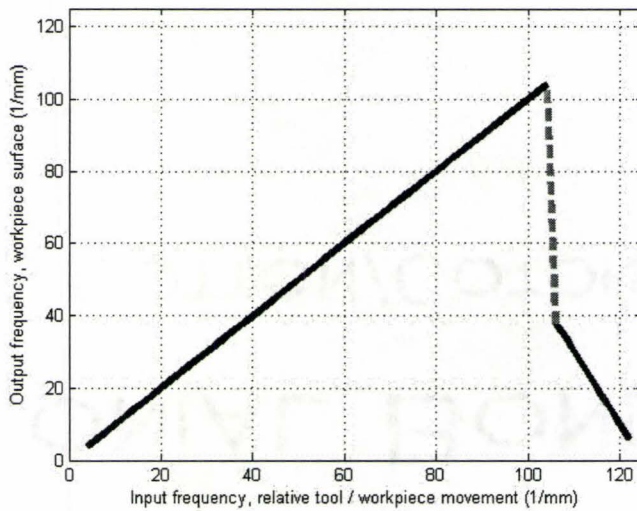
also evident. The reason for the appearance of this lower spatial frequency is tool interference.

In figures 5.18(a) and 5.18(c) the tool orbits corresponding to the input spatial frequencies of 116 1/mm and 100 1/mm are shown. In both instances, the resulting cut workpiece surface is the pattern traced out by the bottom of the tool orbit. In figure 5.18(c) for the input spatial frequency of 100 1/mm, all of the tool passes are still evident on the cut workpiece surface. However, in figure 5.18(c) for the input spatial frequency of 116 1/mm, some tool passes are obscured by proceeding tool passes. The result is that a lower dominant spatial frequency manifests itself on the cut workpiece surface. In figures 5.18(b) and 5.18(d), the resulting cut workpiece surfaces are illustrated in three dimensions to facilitate visualization. As predicted from figure 5.15(b), the attenuation for both input spatial frequencies is similar. Also, as expected from the FFT results of figure 5.16(b), the input spatial frequency is apparent in the surface of figure 5.18(b); however, the dominant spatial frequency is lower.

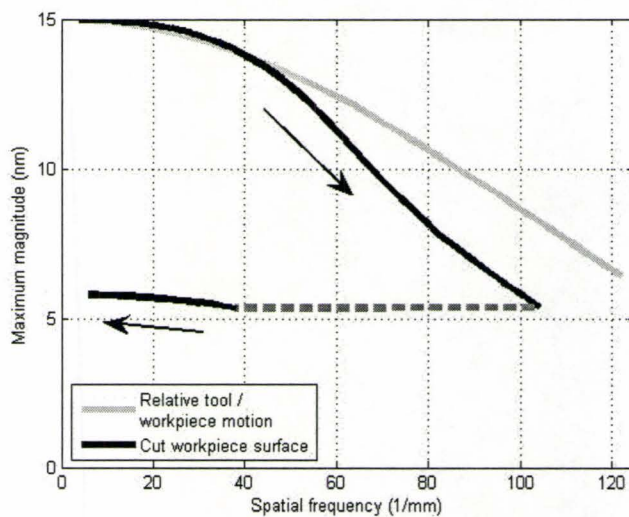
In table 5.4, the dominant spatial frequency and corresponding wavelength expected on the cut workpiece surface for different input vibrational amplitudes,  $z_{amp}$ , are summarized for  $f = 4 \mu\text{m} / \text{rev}$ .

Parameter	units	$z_{amp}$	$z_{amp}$	$z_{amp}$
		= 5 nm	= 10 nm	= 15 nm
Maximum dominant spatial frequency	1/mm	125	125	104
Minimum dominant wavelength	$\mu\text{m}$	8	8	9.6

Table 5.4: Summary of cutting patterns in the feed direction given vibrational amplitude for  $f = 4 \mu\text{m} / \text{rev}$

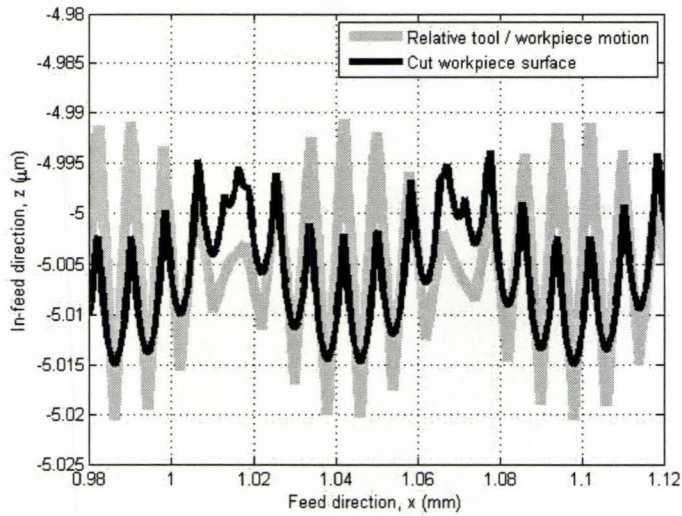


(a) Relative tool / workpiece spatial frequency and resulting spatial frequency on the cut workpiece surface, based on maximum FFT magnitude

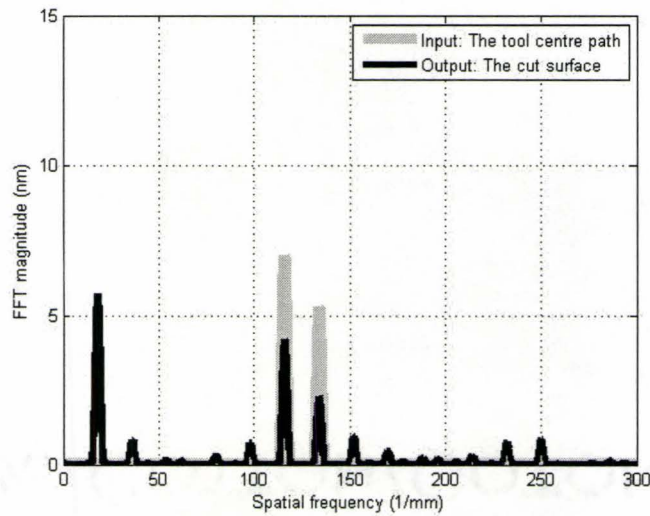


(b) Maximum spatial FFT magnitude and frequency for relative tool / workpiece motion and cut workpiece surface

Figure 5.15: Filtering effect based on FFT results for  $d = 5 \mu\text{m}$ ,  $R_n = 0.630 \text{ mm}$ ,  $f = 4 \mu\text{m / rev}$ , and  $z_{amp} = 15 \text{ nm}$

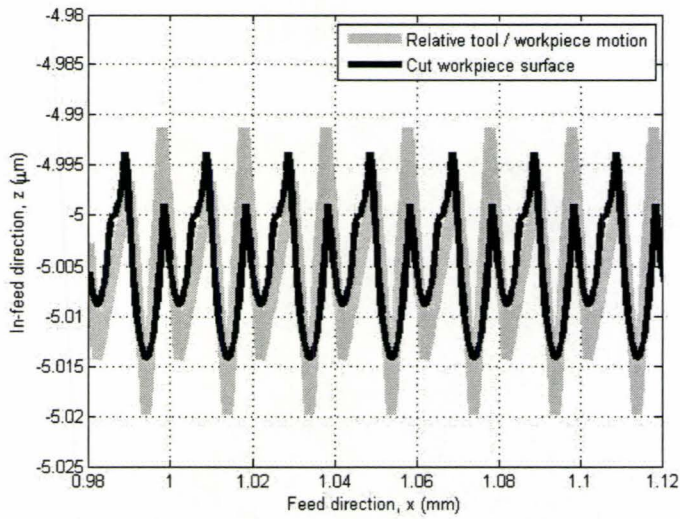


(a) The relative tool / workpiece movement and the cut workpiece surface

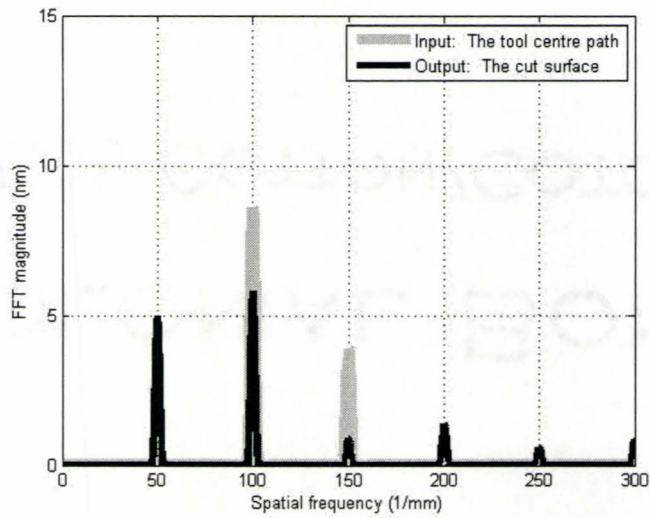


(b) The FFT magnitude of relative tool / workpiece movement and of the cut workpiece surface

Figure 5.16: Simulation of relative tool workpiece movement, cut workpiece surface and FFT results  $f = 4 \mu\text{m} / \text{rev}$ ,  $d = 5 \mu\text{m}$ ,  $R_n = 0.630 \text{ mm}$ ,  $z_{amp} = 15 \text{ nm}$ , and  $\nu = 116 \text{ 1/mm}$

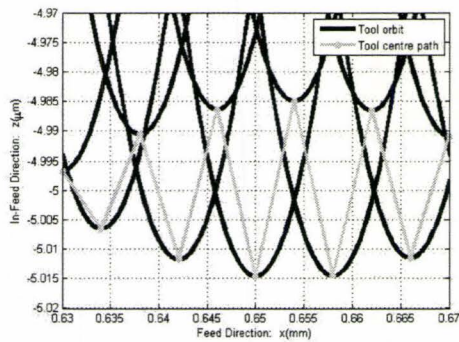


(a) The relative tool / workpiece movement and the cut workpiece surface

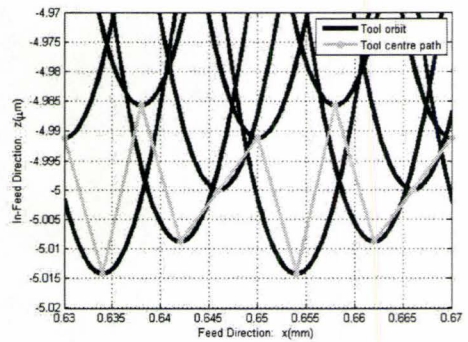


(b) The FFT magnitude of relative tool / workpiece movement and of the cut workpiece surface

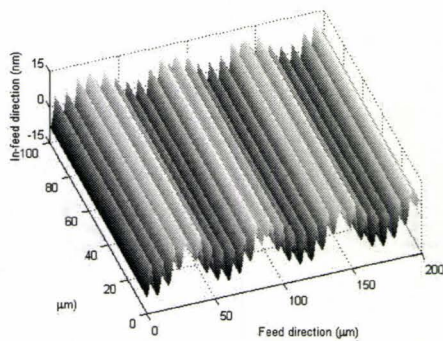
Figure 5.17: Simulation of relative tool workpiece movement, cut workpiece surface and FFT results  $f = 4 \mu\text{m} / \text{rev}$ ,  $d = 5 \mu\text{m}$ ,  $R_n = 0.630 \text{ mm}$ ,  $z_{amp} = 15 \text{ nm}$ , and  $\nu = 100 \text{ 1/mm}$



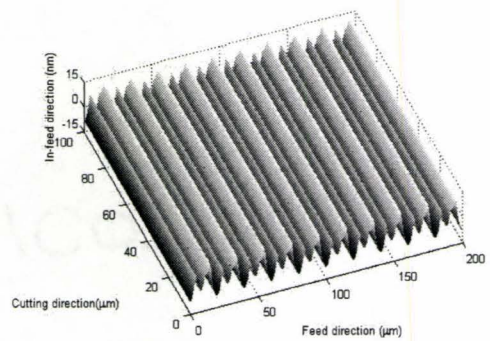
(a) Tool interference for  $f = 4 \mu\text{m} / \text{rev}$ ,  $d = 5 \mu\text{m}$ ,  $R_n = 0.630 \text{ mm}$ ,  $z_{amp} = 15 \text{ nm}$ , and  $\nu = 116 \text{ 1/mm}$



(c) Tool interference for  $f = 4 \mu\text{m} / \text{rev}$ ,  $d = 5 \mu\text{m}$ ,  $R_n = 0.630 \text{ mm}$ ,  $z_{amp} = 15 \text{ nm}$ , and  $\nu = 100 \text{ 1/mm}$



(b) Simulated three dimensional cut workpiece surface for  $f = 4 \mu\text{m} / \text{rev}$ ,  $d = 5 \mu\text{m}$ ,  $R_n = 0.630 \text{ mm}$ ,  $z_{amp} = 15 \text{ nm}$ , and  $\nu = 116 \text{ 1/mm}$



(d) Simulated three dimensional cut workpiece surface for  $f = 4 \mu\text{m} / \text{rev}$ ,  $d = 5 \mu\text{m}$ ,  $R_n = 0.630 \text{ mm}$ ,  $z_{amp} = 15 \text{ nm}$ , and  $\nu = 100 \text{ 1/mm}$

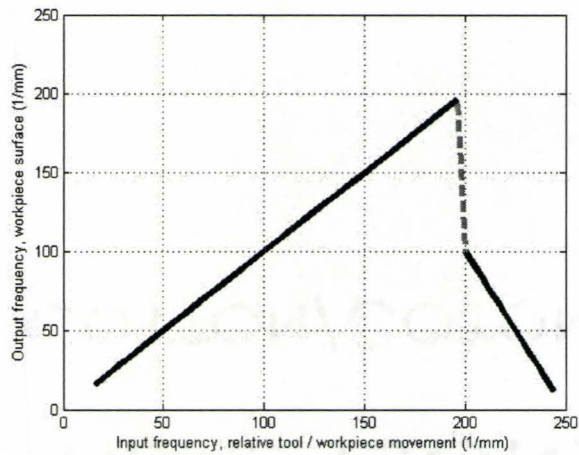
Figure 5.18: The shifting of the dominant spatial frequency caused by the tool interference

### 5.3.2 Filter Curves for a Feed Rate of $2 \mu\text{m} / \text{rev}$

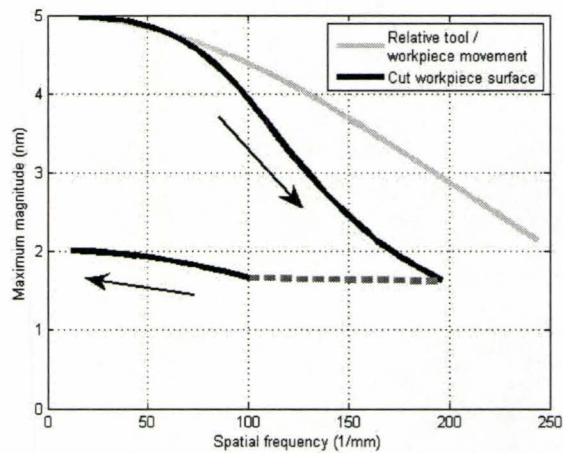
The same series of curves are produced for a feed rate of  $2 \mu\text{m} / \text{rev}$ . The first of these are presented in figures 5.19(a) and 5.19(b). Like the filters of figures 5.15(a) and 5.15(b), the dominant spatial frequency pattern on the cut surface is smaller than that of the relative tool / workpiece movement after a certain point, this time  $196 \text{ 1/mm}$ , compared with the possible range of  $250 \text{ 1/mm}$ . Also, the attenuation in this region is very good in figure 5.19(b), ranging between about  $1.7 \text{ nm}$  and  $2 \text{ nm}$ , or equivalently between  $34$  and  $40$  per cent of the actual vibrational amplitude.

Next, in figures 5.20(a) and 5.20(b), the curves for a vibrational amplitude of  $10 \text{ nm}$  are shown. This time the maximum dominant spatial frequency produced is  $180 \text{ 1/mm}$ . With input spatial frequencies greater than  $180 \text{ 1/mm}$ , the attenuation of the waviness pattern on the cut surface is between  $58$  and  $80$  per cent.

In figures 5.21(a) and 5.21(b), the curves for a vibrational amplitude of  $15 \text{ nm}$  are shown. This time dominant spatial frequencies on the cut surface do not exceed  $154 \text{ 1/mm}$ , despite the possible range of  $250 \text{ 1/mm}$ . In figure 5.21(b), the filter curve is more complicated than those previously observed. The best attenuation exists within the input spatial frequency range of  $156 \text{ 1/mm}$  to  $186 \text{ 1/mm}$ . These are regions noted 2 and 3 in figures 5.21(a) and 5.21(b). The maximum magnitude on the cut surface in regions 2 and 3 are between  $2.6$  and  $2.9 \text{ nm}$ , despite a relative tool / workpiece vibrational amplitude of  $15 \text{ nm}$ . This region provides an attenuation of between  $81$  to  $83$  per cent. An example of the relative tool / workpiece movement and the resulting cut workpiece surface from region 2 is provided in figure 5.22(a), with the corresponding FFT analysis shown in figure 5.22(b). While the input spatial frequency of  $165 \text{ 1/mm}$  is still visible on the cut workpiece surface, its magnitude is

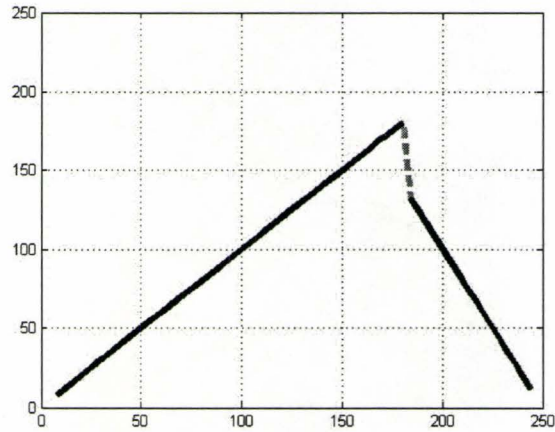


(a) Relative tool / workpiece spatial frequency and resulting spatial frequency on the cut workpiece surface, based on maximum FFT magnitude

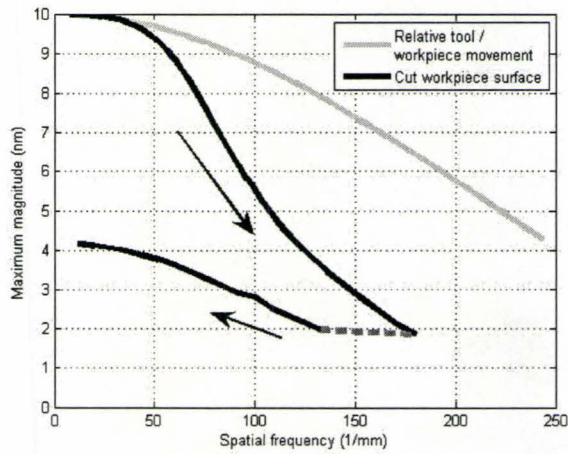


(b) Maximum spatial FFT magnitude and frequency for relative tool / workpiece motion and cut workpiece surface

Figure 5.19: Filtering effect based on FFT results for  $d = 5 \mu\text{m}$ ,  $R_n = 0.630 \text{ mm}$ ,  $f = 2 \mu\text{m} / \text{rev}$ , and  $z_{amp} = 5 \text{ nm}$



(a) Relative tool / workpiece spatial frequency and resulting spatial frequency on the cut workpiece surface, based on maximum FFT magnitude



(b) Maximum spatial FFT magnitude and frequency for relative tool / workpiece motion and cut workpiece surface

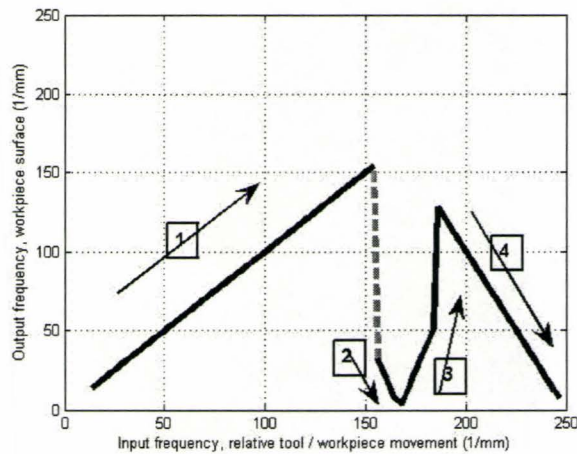
Figure 5.20: Filtering effect based on FFT results for  $d = 5 \mu\text{m}$ ,  $R_n = 0.630 \text{ mm}$ ,  $f = 2 \mu\text{m} / \text{rev}$ , and  $z_{amp} = 10 \text{ nm}$

smaller than that of the lower dominant spatial frequency of 5 1/mm. Notice the absence of feed lines at 500 1/mm in figure 5.22(b).

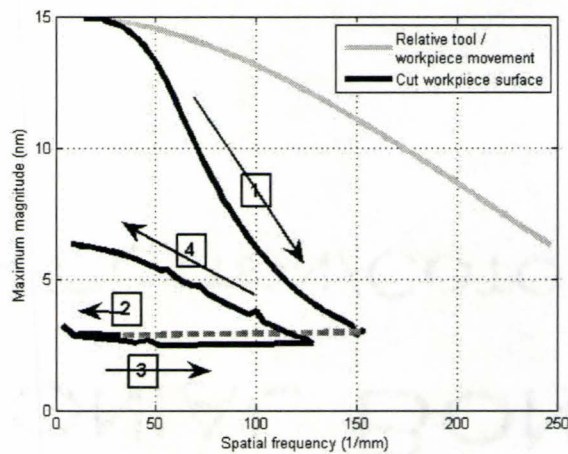
The tool interference for regions 1 through 4 are shown in figures 5.23(a), 5.23(b), 5.23(c) and 5.23(d) for the input spatial frequencies of 50 1/mm, 165 1/mm, 180 1/mm and 240 1/mm respectively. In figures 5.24(a), 5.24(b), 5.24(c) and 5.24(d), the simulated three dimensional cut workpiece surface for each case is provided in order to facilitate visualization.

Figure 5.23(a) represents region 1, and therefore the dominant output spatial frequency matches the input spatial frequency, and each tool pass is present in the waviness pattern. In figure 5.23(b) region 2 is represented. The very long wavelength waviness pattern caused by the tool interference is evident in the outline created at the very bottom of figure 5.23(b), representing the cut workpiece surface. In figure 5.23(c) for region 3, the tool interference is greater still, but despite this a higher spatial frequency component is now evident. Finally, in figure 5.23(d) for region 4, the even larger tool interference actually contributes to poorer attenuation than in regions 2 and 3. Meanwhile, even though the input spatial frequency is considerably larger, the dominant spatial frequency in figure 5.24(d) for region 4 is noticeably smaller than it is in figure 5.24(a) for region 1.

In table 5.5, the maximum dominant spatial frequencies are summarized for  $f = 2 \mu\text{m} / \text{rev}$ , when face turning with vibrations of noted amplitudes.

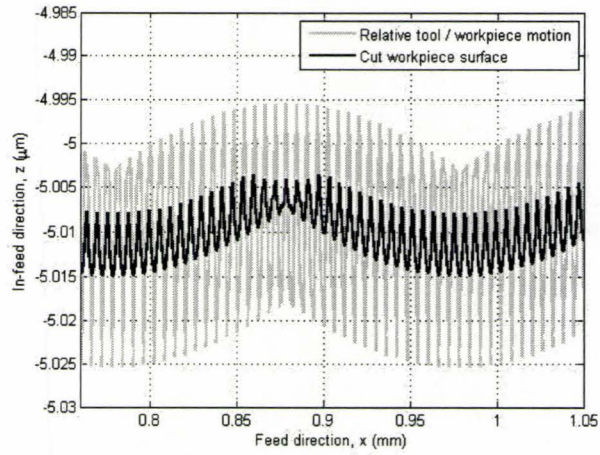


(a) Relative tool / workpiece spatial frequency and resulting spatial frequency on the cut workpiece surface, based on maximum FFT magnitude

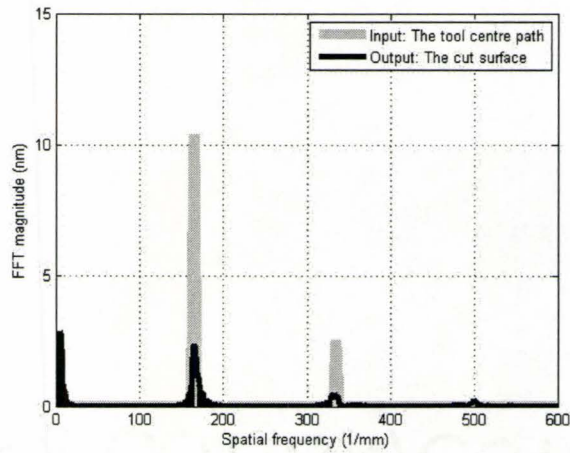


(b) Maximum spatial FFT magnitude and frequency for relative tool / workpiece motion and cut workpiece surface

Figure 5.21: Filtering effect based on FFT results for  $d = 5 \mu\text{m}$ ,  $R_n = 0.630 \text{ mm}$ ,  $f = 2 \mu\text{m / rev}$ , and  $z_{amp} = 15 \text{ nm}$

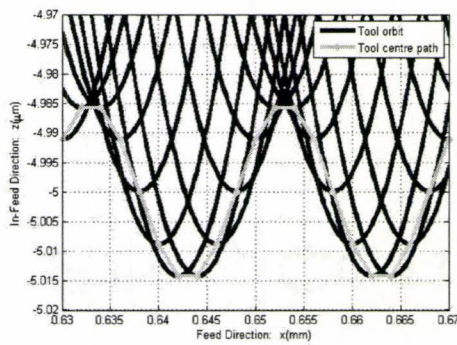


(a) The relative tool / workpiece movement and the cut workpiece surface

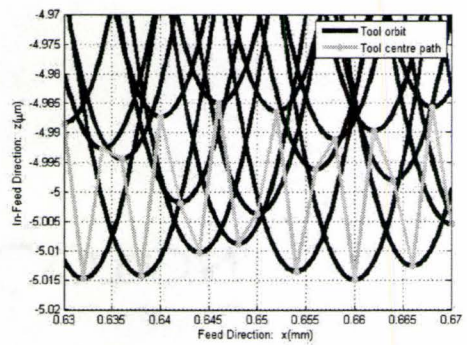


(b) The FFT magnitude of relative tool / workpiece movement and of the cut workpiece surface

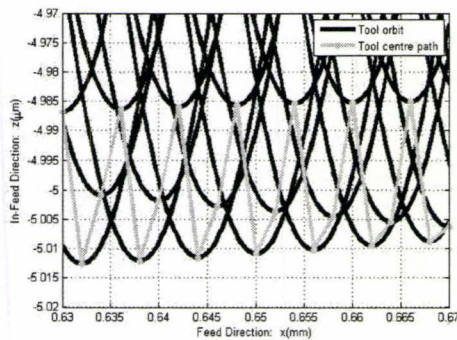
Figure 5.22: Simulation of relative tool workpiece movement, cut workpiece surface and FFT results  $f = 2 \mu\text{m} / \text{rev}$ ,  $d = 5 \mu\text{m}$ ,  $R_n = 0.630 \text{ mm}$ ,  $z_{amp} = 15 \text{ nm}$ , and  $\nu = 165 \text{ 1/mm}$



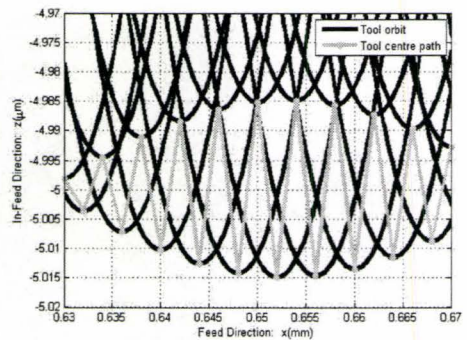
(a) Region 1 tool interference for  $f = 2 \mu\text{m} / \text{rev}$ ,  $d = 5 \mu\text{m}$ ,  $R_n = 0.630 \text{ mm}$ ,  $z_{amp} = 15 \text{ nm}$ , and  $\nu = 50 \text{ 1/mm}$



(c) Region 3 tool interference for  $f = 2 \mu\text{m} / \text{rev}$ ,  $d = 5 \mu\text{m}$ ,  $R_n = 0.630 \text{ mm}$ ,  $z_{amp} = 15 \text{ nm}$ , and  $\nu = 180 \text{ 1/mm}$

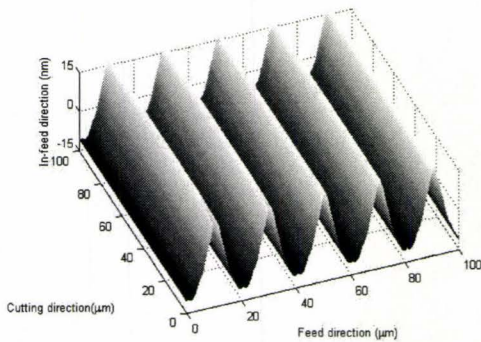


(b) Region 2 tool interference for  $f = 2 \mu\text{m} / \text{rev}$ ,  $d = 5 \mu\text{m}$ ,  $R_n = 0.630 \text{ mm}$ ,  $z_{amp} = 15 \text{ nm}$ , and  $\nu = 165 \text{ 1/mm}$

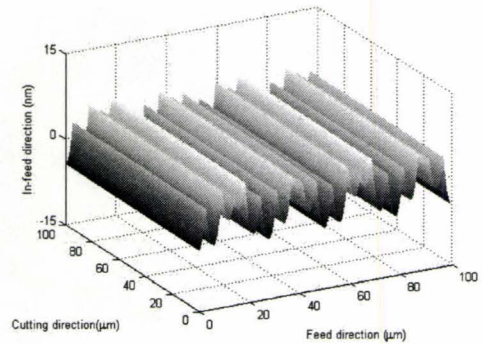


(d) Region 4 tool interference for  $f = 2 \mu\text{m} / \text{rev}$ ,  $d = 5 \mu\text{m}$ ,  $R_n = 0.630 \text{ mm}$ ,  $z_{amp} = 15 \text{ nm}$ , and  $\nu = 240 \text{ 1/mm}$

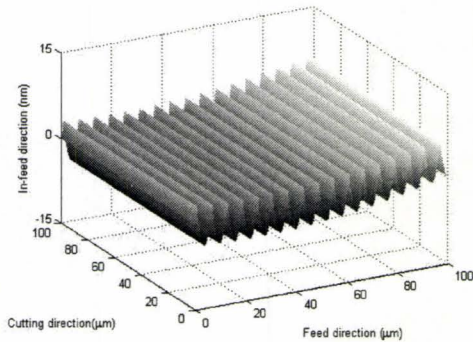
Figure 5.23: Regions 1 through 4 showing the shifting of the dominant spatial frequency caused by the tool interference



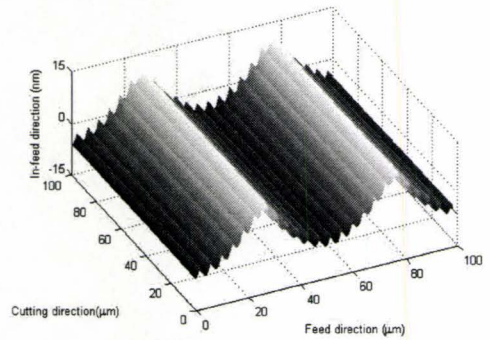
(a) Region 1 simulated three dimensional cut workpiece surface for  $f = 2 \mu\text{m} / \text{rev}$ ,  $d = 5 \mu\text{m}$ ,  $R_n = 0.630 \text{ mm}$ ,  $z_{amp} = 15 \text{ nm}$ , and  $\nu = 50 \text{ 1/mm}$



(c) Region 3 simulated three dimensional cut workpiece surface for  $f = 2 \mu\text{m} / \text{rev}$ ,  $d = 5 \mu\text{m}$ ,  $R_n = 0.630 \text{ mm}$ ,  $z_{amp} = 15 \text{ nm}$ , and  $\nu = 180 \text{ 1/mm}$



(b) Region 2 simulated three dimensional cut workpiece surface for  $f = 2 \mu\text{m} / \text{rev}$ ,  $d = 5 \mu\text{m}$ ,  $R_n = 0.630 \text{ mm}$ ,  $z_{amp} = 15 \text{ nm}$ , and  $\nu = 165 \text{ 1/mm}$



(d) Region 4 simulated three dimensional cut workpiece surface for  $f = 2 \mu\text{m} / \text{rev}$ ,  $d = 5 \mu\text{m}$ ,  $R_n = 0.630 \text{ mm}$ ,  $z_{amp} = 15 \text{ nm}$ , and  $\nu = 240 \text{ 1/mm}$

Figure 5.24: Three dimensional representation of regions 1 through 4 showing the shifting of the dominant spatial frequency caused by the tool interference

Parameter	units	$z_{amp}$ = 5 nm	$z_{amp}$ = 10 nm	$z_{amp}$ = 15 nm
Maximum dominant spatial frequency	1/mm	196	180	154
Minimum dominant wavelength	$\mu\text{m}$	5.1	4	6.5

Table 5.5: Summary of cutting patterns in the feed direction given vibrational amplitude for  $f = 2 \mu\text{m} / \text{rev}$

### 5.3.3 Cutting Parameter Filtering and the Surface Finish Lobes over a Broadband of Disturbance Frequencies

The filter curves of section 5.3 have been depicted over the range of possible relative tool / workpiece movement as defined by the surface finish lobes. Using a feed rate of  $2 \mu\text{m} / \text{rev}$  as an example, this means that the range of possible spatial frequencies in the feed direction is between 0 and 250 1/mm. However, it is known from the surface finish lobes that the range of spatial frequencies repeats itself indefinitely over a possible range of disturbance frequencies. Similarly, the filter curves also repeat themselves in this manner. The '(b)' portion of the filter curves in this section have plotted the maximum dominant spatial frequency *versus* resulting error amplitude on the cut workpiece, in the feed direction. However, they could just as easily have reported the input relative tool / workpiece spatial frequency *versus* the resulting error amplitude.

In figure 5.25, the resulting maximum FFT amplitude of the cut surface is plotted against the input disturbance frequency,  $f_d$ , for a feed rate of  $2 \mu\text{m} / \text{rev}$  and a vibrational amplitude of 15 nm. The surface finish lobes for this spindle speed and feed rate are also included. Figure 5.25 illustrates how the filter curves described in

this section can be related directly to an input frequency,  $f_d$ .

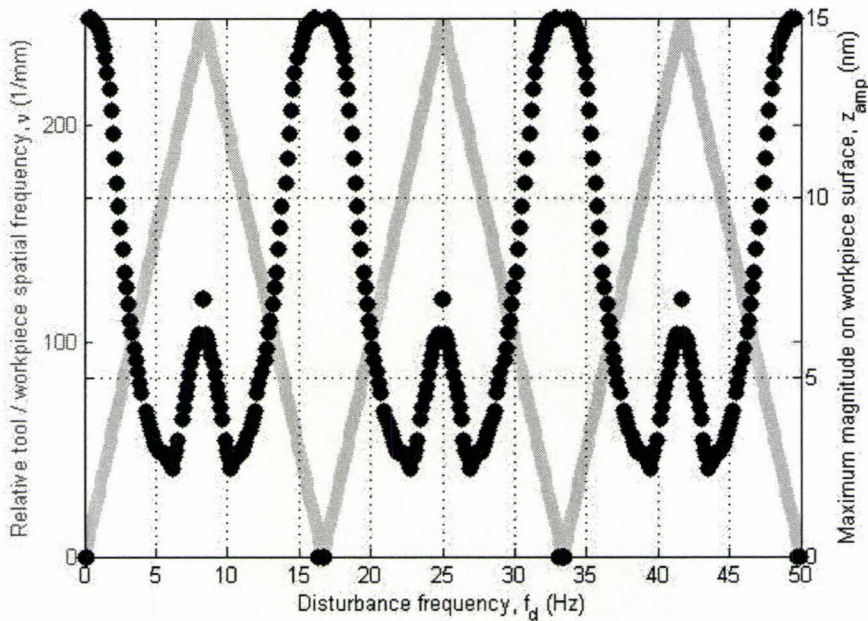


Figure 5.25: Surface finish lobes and maximum vibrational amplitude,  $N = 1000$  RPM and  $f = 2 \mu\text{m} / \text{rev}$ ,  $d = 5 \mu\text{m}$ ,  $R_n = 0.630 \text{ mm}$ ,  $z_{amp} = 15 \text{ nm}$

In figure 5.26, several points on the surface finish lobes are used to illustrate the workpiece surface pattern for a feed rate of  $2 \mu\text{m} / \text{rev}$ . At the bottom left, a surface resulting from an input relative tool / workpiece spatial frequency of  $10 \text{ 1/mm}$  is shown. The dominant wavelength is  $100 \mu\text{m}$  and the amplitude is close to  $15 \text{ nm}$ , as is expected from the surface curves in figures 5.22(a) and 5.22(b), and also in figure 5.25. For an input spatial frequency of  $50 \text{ 1/mm}$ , some attenuation occurs, and for an input spatial frequency of  $100 \text{ 1/mm}$  even more attenuation is apparent. Finally, for an input spatial frequency of  $240 \text{ 1/mm}$ , the attenuation is pronounced. Also, the dominant spatial frequency is smaller than the input spatial frequency, at approximately  $20 \text{ 1/mm}$ . Again, this pattern and attenuation matches the prediction of the filter curves. Note in this last example that the input spatial frequency of  $240$

1/mm is visible in the smaller ‘ripple’ of the curve, and this ripple should not be mistaken for feed marks.

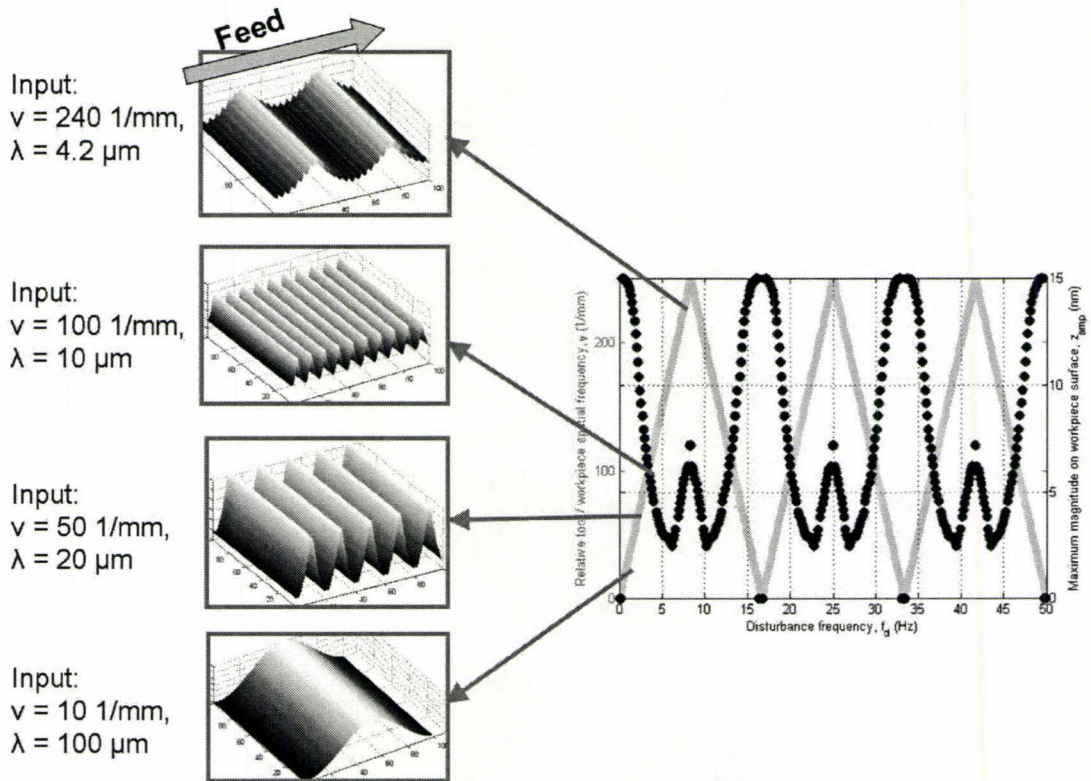


Figure 5.26: Simulated surfaces illustrating workpiece waviness,  $N = 1000$  RPM and  $f = 2$   $\mu\text{m} / \text{rev}$ ,  $d = 5$   $\mu\text{m}$ ,  $R_n = 0.630$  mm,  $z_{amp} = 15$  nm

In figure 5.25, zero waviness amplitude points are where the surface finish lobe is zero. In figure 5.27, the surface finish lobe is shown between 15 Hz and 18 Hz. It is apparent from figure 5.25 that the climb to a wavelength approaching infinity is very abrupt. Wavelengths and spatial frequencies in the vicinity of such a point are summarized in table 5.6.

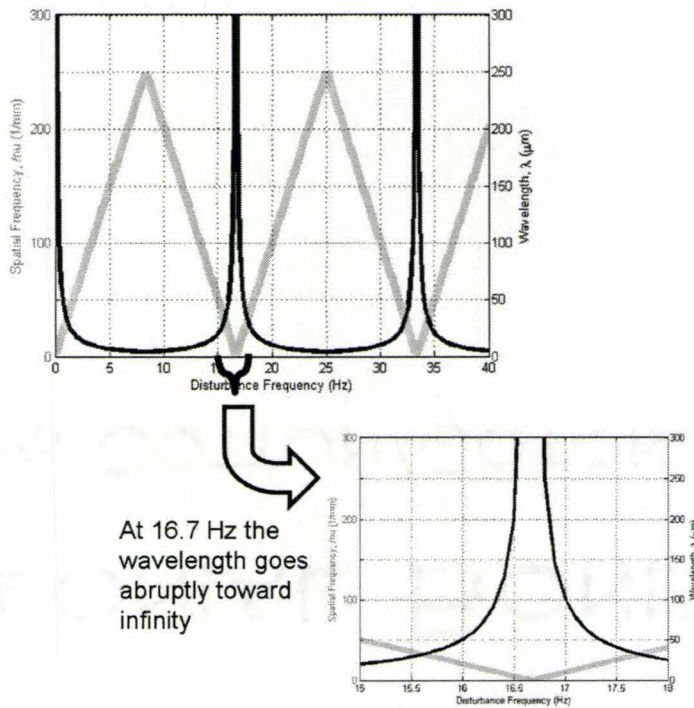


Figure 5.27: The surface finish lobe where the spatial frequency is zero,  $f = 2 \mu\text{m} / \text{rev}$

$f_d$ (Hz)	Wavelength ( $\mu\text{m}$ )	Spatial Frequency (1/mm)
14	12.5	80
15	20	50
16	50	20
16.5	200	10
16.67	$\rightarrow \infty$	$\rightarrow 0$
16.8	250	4
17	200	5
18	25	40

Table 5.6: Rapid change in wavelength near where the surface finish lobe approaches zero ( $\nu$ , 1/mm)

## 5.4 Experimental Validation and Discussion of the Filtering Effect

In this section, it is shown that the filter shapes conveyed in section 5.3 exist in practice on ultra precision face turned workpiece surfaces machined in the presence of vibrations.

An aluminum 6061-T6 workpiece was ultra precision face turned with a single point diamond tool on an ASG 2500 with cutting conditions described in table 5.1. An accelerometer was placed on the spindle housing and another at the tool location to measure relative tool / workpiece vibration, as discussed in chapter 3, and data was acquired synchronously during cutting from both sensors.

The relative tool / workpiece FFT from the ultra precision machining of both workpieces are shown in figures 5.28 and 5.29, respectively. From figures 5.28 and 5.29, it is clear that during the face turning of both workpieces, relative tool workpiece vibrations occurred, of various magnitude and frequency. Additional curves pertaining to this accelerometer data acquisition are provided in Appendix A, figures A.7, A.8, A.9, A.1, A.2 and A.3.

Once diamond turned, the workpiece surfaces were measured with white light interferometry. The surface data was then bandpass filtered with the Zygo software prior to export for analysis in Matlab. The bandpass filter and resolution used for each workpiece are described in table 5.7. Comparing values found in table 5.7 with those found in table 5.3, one can see that all but the very low anticipated spatial frequencies caused by the relative tool / workpiece vibrations are observable in the white light interferometry measurements. The bandpass filtering values used accommodate

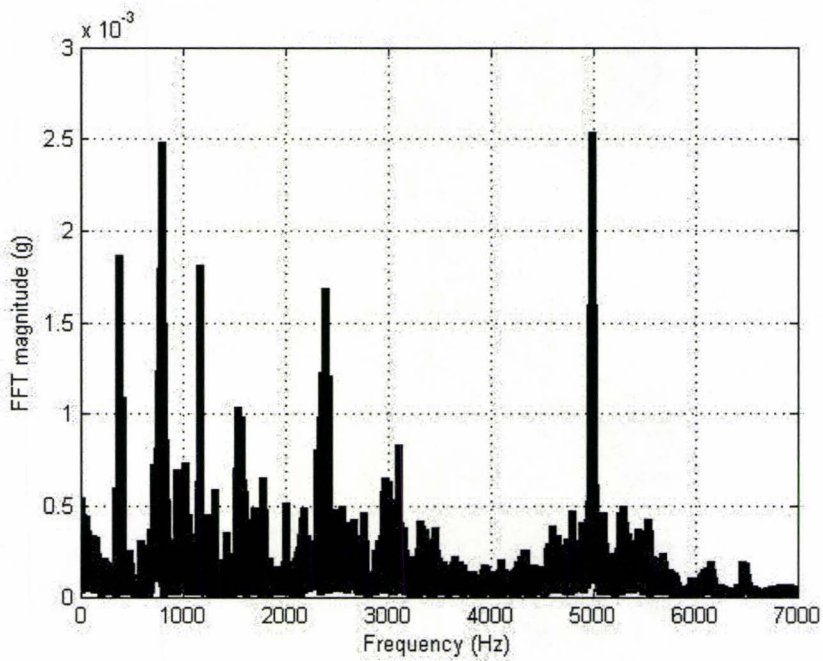


Figure 5.28: Relative tool / workpiece acceleration FFT of  $f = 4 \mu\text{m} / \text{rev}$  and  $N = 1201.3 \text{ RPM}$  measured during ultra precision face turning on the ASG 2500, number of averages = 103,  $\Delta f = 0.8548 \text{ Hz}$

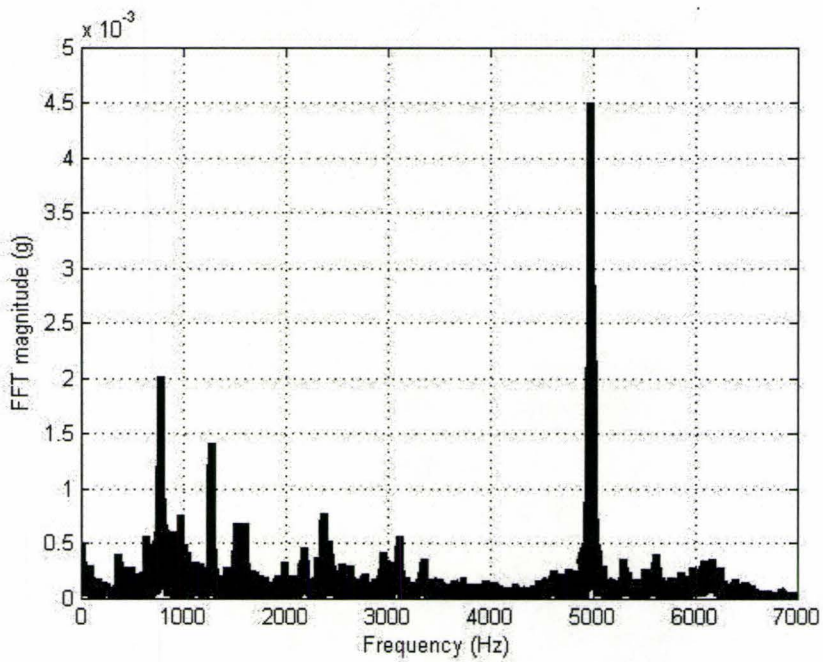


Figure 5.29: Relative tool / workpiece acceleration FFT of  $f = 2 \mu\text{m} / \text{rev}$  and  $N = 1000$  RPM measured during ultra precision face turning on the ASG 2500, number of averages = 103,  $\Delta f = 0.8548$  Hz

the measurement distance in the workpiece feed direction and also the measurement resolution in the workpiece feed direction.

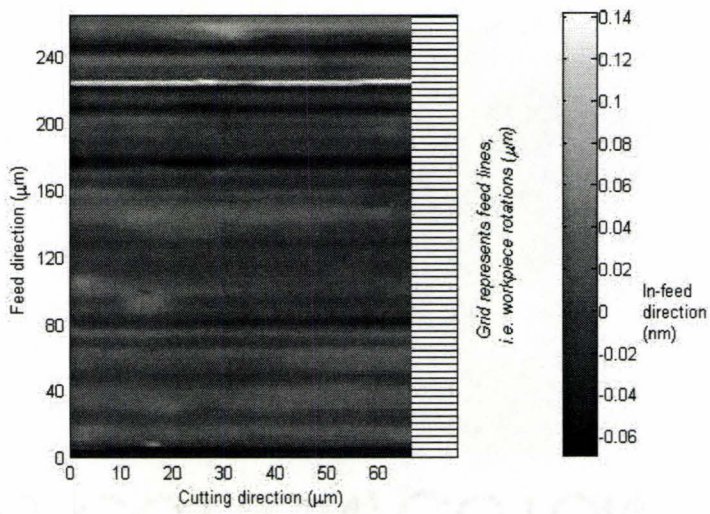
Parameter	units	Workpiece $f = 4 \mu\text{m}$ / rev and $N = 1201.3$ RPM	Workpiece $f = 2 \mu\text{m}$ / rev and $N = 1000$ RPM
Maximum filter spatial frequency	1/mm	300.3	270.3
Minimum filter spatial frequency	1/mm	5.2	5.3
Minimum filter wavelength	$\mu\text{m}$	3.3	3.7
Maximum filter wavelength	$\mu\text{m}$	190.9	188.9
Measurement resolution (feed direction)	$\mu\text{m}$	0.56	0.55

Table 5.7: Measurement and filtering parameters of white light interferometry

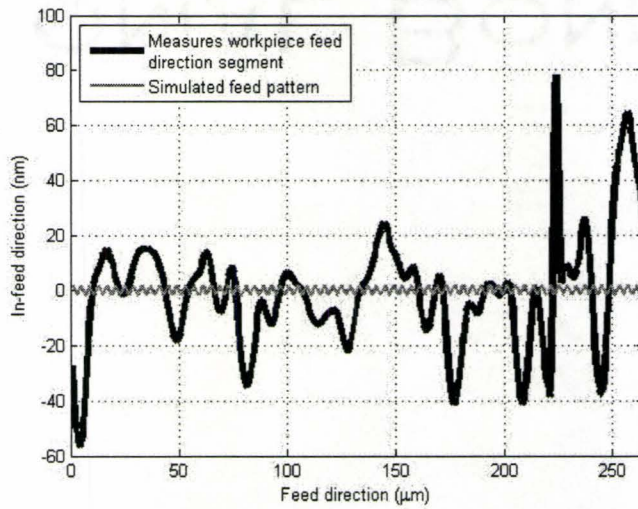
Images of the measured surfaces are presented in figures 5.30(a) and 5.31(a). In each case, the horizontal axis is the cutting direction and the vertical axis is the feed direction. The in-feed direction is described by the gray scale bar. On the right hand side of each image a grid showing the feed spacing is included. Since the observable patterns in the feed direction are of much greater wavelength than the feed lines, they represent waviness and not surface roughness errors.

In figures 5.30(b) and 5.31(b), individual feed direction segments are shown for each workpiece. Also, a simulated feed pattern is provided for contrast. Again, it is clear from figures 5.30(b) and 5.31(b) that the dominant observable pattern is waviness and not surface roughness, based on the observable wavelength.

Finally, FFTs of the white light interferometry measured surfaces of figures 5.30(a) and 5.31(a) were performed in the feed directions. Results are provided in figures 5.32

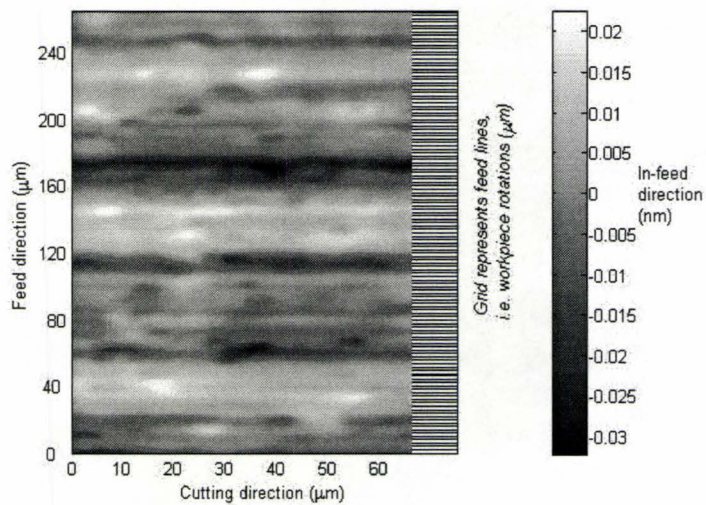


(a) White light interferometry measured cut surface, zoom 400x

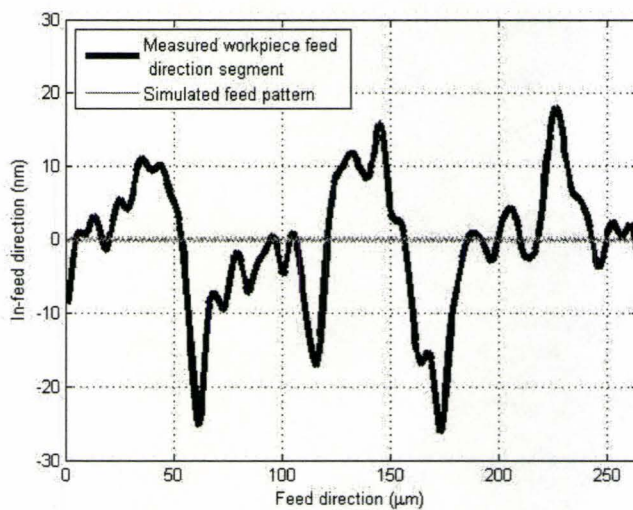


(b) White light interferometry measured segment compared with simulated feed pattern

Figure 5.30: Workpiece white light interferometry measured surface,  $f = 4 \mu\text{m} / \text{rev}$ ,  $N = 1201.3 \text{ RPM}$ ,  $d = 5 \mu\text{m}$ ,  $R_n = 0.630 \text{ mm}$



(a) White light interferometry measured cut workpiece surface, zoom 400x



(b) White light interferometry measured segment compared with simulated feed pattern

Figure 5.31: Workpiece white light interferometry measured surface,  $f = 2 \mu\text{m} / \text{rev}$ ,  $N = 1000 \text{ RPM}$ ,  $d = 5 \mu\text{m}$ ,  $R_n = 0.630 \text{ mm}$

and 5.34, and are compared with the filter shapes of section 5.3.

In figure 5.32, the range of possible observable spatial frequencies is from 5.2 1/mm to 300.3 1/mm, as described in table 5.7. From table 5.3, the possible range of spatial frequencies caused by relative tool / workpiece vibration is 0 to 125 1/mm.

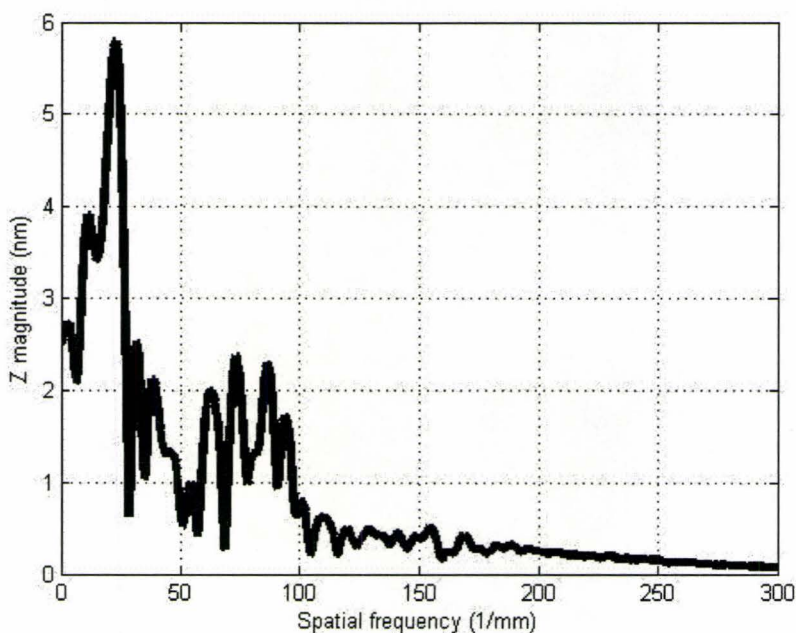


Figure 5.32: White light interferometry measured cut workpiece surface for  $f = 4 \mu\text{m}$  / rev,  $N = 1201.3$  RPM,  $d = 5 \mu\text{m}$ ,  $R_n = 0.630$  mm

The largest peak observed in figure 5.32 is 5.8 nm at 22.9 1/mm. After approximately 30 1/mm, peaks do not exceed about 2.5 nm. At 100 1/mm there is a distinct tapering off, with vibrations well attenuated by 125 1/mm. There is no spike at 250 1/mm, the feed rate, despite being observable for the resolution and bandpass filtering used. Results in figure 5.32 are consistent with the workpiece filter shapes presented in section 5.3 for  $f = 4 \mu\text{m}$ . To further illustrate, these filter shapes are presented in conjunction with the measured surface in figure 5.33.

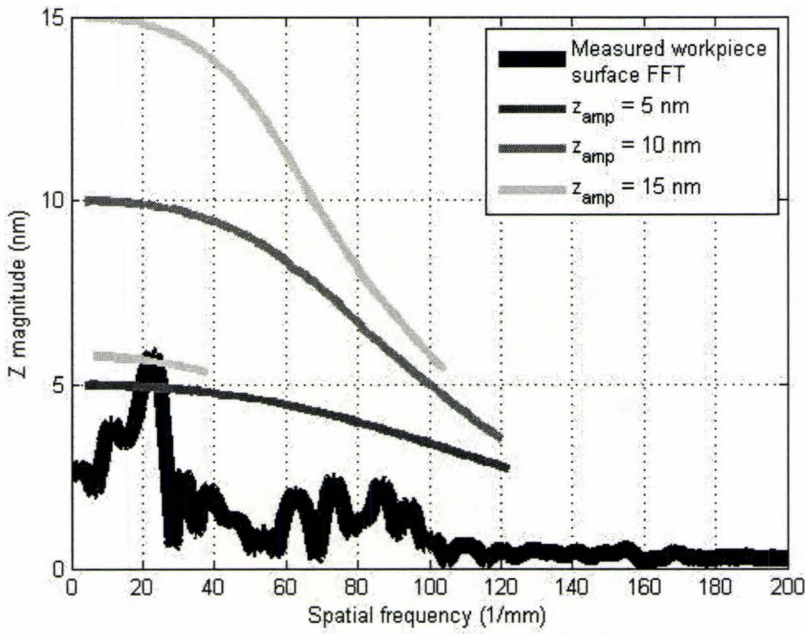


Figure 5.33: White light interferometry measured cut workpiece surface and simulated filter lines for  $f = 4 \mu\text{m} / \text{rev}$ ,  $N = 1201.3 \text{ RPM}$ ,  $d = 5 \mu\text{m}$ ,  $R_n = 0.630 \text{ mm}$

Now consider figure 5.34 for the  $f = 2 \mu\text{m} / \text{rev}$  and  $N = 1000 \text{ RPM}$ . From table 5.7, observable frequencies range between  $5.3 \text{ 1/mm}$  to  $270.3 \text{ 1/mm}$ . Also from table 5.3, the feed direction spatial frequencies caused by relative tool / workpiece vibration for these cutting conditions range from  $0$  to  $250 \text{ 1/mm}$ .

In figure 5.34, a large spike of  $3.6 \text{ nm}$  occurs at  $10.7 \text{ 1/mm}$  and another of  $3.3 \text{ nm}$  occurs at  $18.9 \text{ 1/mm}$ . Between about  $37 \text{ 1/mm}$  and  $100 \text{ 1/mm}$ , the magnitude slopes downward considerably. After about  $155 \text{ 1/mm}$  there is practically no activity at all. The shape observed in figure 5.34 is very like that described for the filter curves for  $f = 2 \mu\text{m} / \text{rev}$  in section 5.3. Despite the possibility to observe spatial frequencies up to  $270 \text{ 1/mm}$  as described in table 5.7, in figure 5.34 spatial frequencies on the workpiece surface not visible after approximately  $160 \text{ 1/mm}$ . Overall, the attenuation

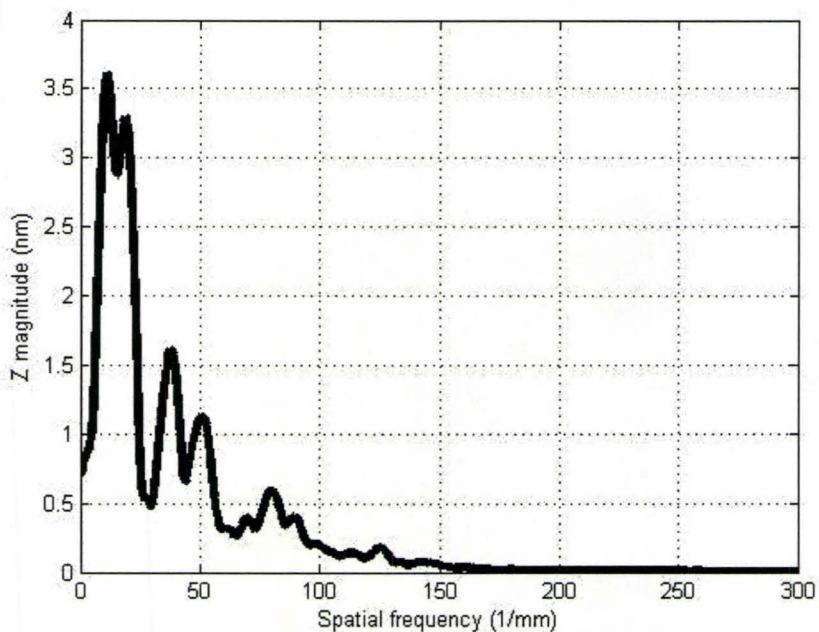


Figure 5.34: White light interferometry measured cut workpiece surface for  $f = 2 \mu\text{m} / \text{rev}$ ,  $N = 1000 \text{ RPM}$ ,  $d = 5 \mu\text{m}$ ,  $R_n = 0.630 \text{ mm}$

is more severe than for the case presented in figure 5.32 for a feed rate of  $4 \mu\text{m} / \text{rev}$ . The same sharpness of attenuation is apparent in the feed rate of  $2 \mu\text{m} / \text{rev}$  filter curves.

In figure 5.35, the FFT of the measured surface is compared with the filter curves. Again the predicted shape is displayed from the FFT results of the white light interferometry measured surface. Since the same dominant output spatial frequency is possible for multiple input spatial frequencies, the filter curves included in figure 5.35 appear to be more numerous than in figure 5.33 for a feed rate of  $4 \mu\text{m} / \text{rev}$ .

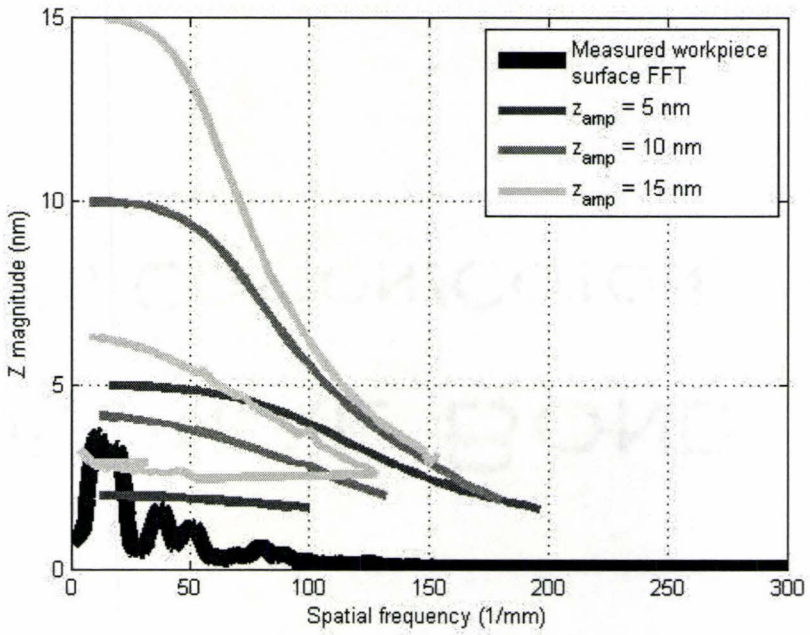


Figure 5.35: White light interferometry measured cut workpiece surface and simulated filter lines for  $f = 2 \mu\text{m} / \text{rev}$ ,  $N = 1000 \text{ RPM}$ ,  $d = 5 \mu\text{m}$ ,  $R_n = 0.630 \text{ mm}$

## 5.5 Mitigating the Effects of Vibration in Ultra Precision Machining

In section 4.7, applications of the surface finish lobes were discussed. Included was a discussion of changing the feed direction wavelength caused by a disturbance frequency to one approaching infinity via a particular combination of spindle speed and feed rate, as illustrated in figure 4.24. In figure 4.24, the intention was to find the point on the surface finish lobe where the spatial frequency was equal to zero.

In figure 5.25, the surface finish lobes and filtering effect are shown for a feed rate,  $f$ , of  $2 \mu\text{m} / \text{rev}$  and a vibrational amplitude,  $z_{amp}$ , of  $15 \text{ nm}$  over  $100 \text{ Hz}$ . The same lobe and filter is shown in figure 5.36 for  $16.7 \text{ Hz}$  in order to simplify the discussion of the mitigation of the vibrational effect. The discussion, however, can be applied to a broad band of disturbance frequencies. In figure 5.36 two regions are labeled: Option 1 and Option 2.

### 5.5.1 Option 1 for Vibrational Mitigation on the Surface Finish Lobe

In figure 5.36, the first opportunity to mitigate the vibrational effect on the cut workpiece surface in the feed direction is labeled 'Option 1.' This is the scenario of approaching an infinitely long feed direction wavelength described in section 4.7. While there is a significant potential pay-off to this approach, there are several complications.

If there is a small shift in the disturbance frequency for a given set of cutting conditions, a very large magnitude surface finish error will occur. This can be seen in

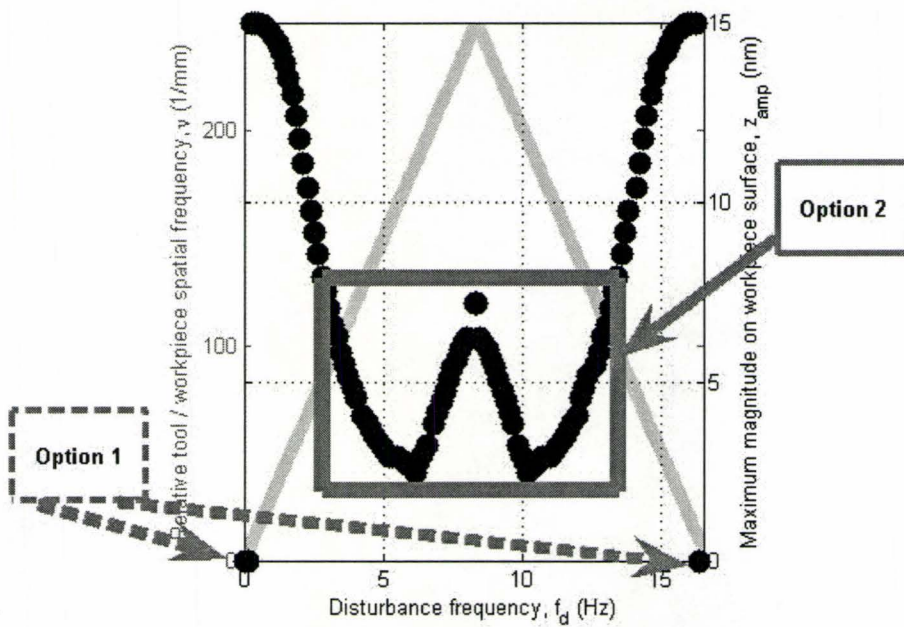


Figure 5.36: Regions of opportunity to mitigate the vibrational effect on the cut workpiece surface,  $N = 1000$  RPM and  $f = 2 \mu\text{m} / \text{rev}$ ,  $d = 5 \mu\text{m}$ ,  $R_n = 0.630$  mm,  $z_{amp} = 15$  nm

figure 5.36, and also in figure 5.25 where the rapid wavelength change in the vicinity of 'Option 1' is depicted. In figure 5.36, consider the black dot at 0 Hz. Just after 0 Hz the next point has a magnitude of 15 nm. This means that misjudging or having a variable disturbance frequency could mean producing the maximum error amplitude on the cut surface.

Further, this approach assumes very accurate and very precise control of the spindle speed and the feed rate. In figure 5.37, the effect of an error in the spindle speed on the relative tool / workpiece motion is shown. The nominal spindle speeds are based on the results of figure 4.24 which shows the machining conditions needed to create a spatial frequency of 0 1/mm when the disturbance frequency is 37 Hz. The spatial frequency of relative tool / workpiece motion in the feed direction changes more slowly with error for the faster spindle speed of 1110 RPM, compared to the alternative 555 RPM. In chapter 4, section 4.7, a spindle speed error of 0.7 RPM was identified via the surface finish lobes. Overall the effect of an imprecise spindle speed on the surface finish error is not as severe as it is for a changing disturbance frequency.

Another key issue also occurs when pursuing 'Option 1.' This is that adjusting the cutting parameters to push a particular feed direction wavelength toward infinity only works when there is just one significant disturbance frequency.

### **5.5.2 Option 2 for Vibrational Mitigation on the Surface Finish Lobe**

In figure 5.36, the second opportunity to mitigate the vibrational effect on the cut workpiece surface in the feed direction is labeled 'Option 2.' In this scenario, the

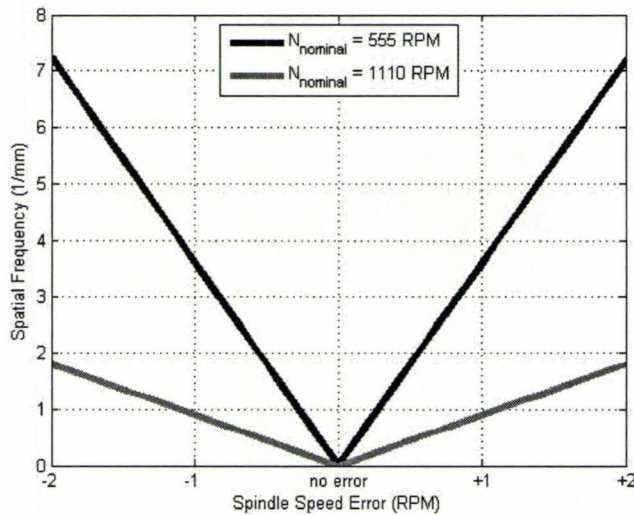


Figure 5.37: Effect of deviation of spindle speed from nominal on the resulting surface finish lobe

resulting cut surface amplitudes equal to or less than half of the tool / workpiece vibrational amplitude are noted by the gray box. What this means is that with these cutting conditions, between about 3 Hz and 13 Hz a 50 per cent or greater attenuation of vibration is expected. As illustrated in figure 5.25, this pattern repeats itself. Thus, for 60 per cent of possible disturbance frequencies, the surface finish error amplitude on the cut workpiece surface will be equal to or less than half the amplitude of relative tool / workpiece vibration. As already noted, these results correspond to a relative tool / workpiece amplitude of 15 nm, and a feed rate is  $2 \mu\text{m} / \text{rev}$ . Overall, targeting a region of the surface finish lobe provides good and also realistic attenuation of vibration.

### 5.5.3 Mean Arithmetic Roughness, $R_a$

So far, in term of surface finish error, several measures have been discussed. First, for a harmonic error a classification has occurred, describing an error as either form, waviness or surface roughness. Also the peak-to-valley error has been described for an ideal geometric surface roughness, specifically  $R_t$  of equation 3.1. The filtering effect curves of this chapter also represent a peak-to-valley error. The curves describe a harmonic amplitude. Since twice the amplitude is the peak-to-valley height, the filter effect curves also represents a type of  $R_t$  measure.

Another surface finish error descriptor is the mean arithmetic roughness,  $R_a$ . As indicated in chapter 2, this is also a surface finish measure used in ultra precision machining. In Stephenson and Agapiou this is described as the “average absolute deviation of the workpiece from the centreline” [[48], p. 632]. The equation from [48], using the nomenclature of this thesis, is

$$R_a = \frac{1}{L} \int_0^L |z| dx \quad (5.41)$$

where  $z$  is the in-feed height,  $x$  is in the feed direction, and  $L$  is the feed direction sample length. In [48],  $R_a$  is described as the parameter most commonly used to describe surface finish. In Shaw, the finish-machining range for  $R_a$  in turning for conventional machining is  $0.75 \mu\text{m}$  to  $1.5 \mu\text{m}$  [45]. Meanwhile, in ultra precision machining an  $R_a$  value of less than  $10 \text{ nm}$  is sought. Further, if a periodic pattern exists on the workpiece surface (i.e. waviness) then post-processing may be required even if the amplitude is less than  $10 \text{ nm}$ .

Equation 5.41 describes the calculation of  $R_a$  for a continuous surface. A sampled surface like that acquired with white light interferometry is discrete. In this case  $R_a$

is calculated as follows, based on [4]

$$R_a = \frac{1}{q} \sum_0^q |z| \quad (5.42)$$

In equation 5.42,  $q$  is the number of data points in the sample. The data series  $z$  is mean zeroed before its use in equation 5.42.

#### **5.5.4 Cutting Conditions Used to Illustrate the Mitigation of Vibrations on the Workpiece Surface**

For the remainder of this chapter, ‘Option 2’ of section 5.5 is pursued. Further, for this option, the ability of different feed rates to mitigate the vibrational effect on the cut workpiece surface is studied. It is shown that a filtering effect similar to that described earlier in this chapter also applies to the mean arithmetic roughness parameter  $R_a$ . Also, the effect of feed rate on vibrational mitigation can be used to improve workpiece surface finish. To do this, the surface finish resulting from two different feed rates of  $2 \mu\text{m} / \text{rev}$  and of  $10 \mu\text{m} / \text{rev}$  are compared. The cutting conditions considered in this section are listed in table 5.8. It will be shown that the significant difference in surface finish error for these two machining conditions is not due to the difference in the ideal geometric surface roughness,  $R_t$ , of equation 3.1. Instead, it is because of the difference in the mitigation of the relative tool / workpiece vibrations on the cut surface, in the form of waviness errors.

The surface finish lobe bounds for each feed rate of table 5.8 are summarized in table 5.9.

Cutting Parameter	Symbol	Units	Workpiece	Workpiece
Feed rate	$f$	$\mu\text{m} / \text{rev}$	10	2
Nominal spindle speed	$N$	RPM	1196.3	1000
Depth of cut	$d$	$\mu\text{m}$	5	5
Tool nose radius	$R_n$	mm	0.630	0.630

Table 5.8: Cutting conditions for finish turning of 100 mm diameter aluminum 6061-T6 workpiece

Parameter	units	Workpiece $f = 10 \mu\text{m} / \text{rev}$	Workpiece $f = 2 \mu\text{m} / \text{rev}$
Maximum nominal spatial frequency	1/mm	50	250
Minimum nominal spatial frequency	1/mm	0	0
Minimum nominal wavelength	$\mu\text{m}$	20	4
Maximum nominal wavelength	$\mu\text{m}$	$\rightarrow \infty$	$\rightarrow \infty$

Table 5.9: Summary of surface finish lobes for  $f = 10 \mu\text{m} / \text{rev}$  and  $f = 2 \mu\text{m} / \text{rev}$

### 5.5.5 Filter Curves for a Feed Rate of $10 \mu\text{m} / \text{rev}$ and for a Feed Rate of $2 \mu\text{m} / \text{rev}$

So far the filtering effect for feed rates of  $4 \mu\text{m} / \text{rev}$  and  $2 \mu\text{m} / \text{rev}$  have been discussed for vibrational amplitudes of 5 nm, 10 nm and 15 nm. In this section the behavior of a feed rate of  $2 \mu\text{m} / \text{rev}$  and of  $10 \mu\text{m} / \text{rev}$  are compared.

In figures 5.38, 5.39, 5.40 and 5.41 the feed direction relative tool / workpiece movement and cut workpiece surface peak magnitudes are given for a feed rate of  $10 \mu\text{m} / \text{rev}$  and vibrational amplitudes of 5 nm, 10 nm, 15 nm and 20 nm. The peak vibrational frequency of the cut workpiece surface matches that of the relative tool workpiece movement in all cases, similar to the case illustrated in figure 5.12(a) for a feed rate of  $4 \mu\text{m} / \text{rev}$ .

In figures 5.38, 5.39, 5.40 and 5.41 it is clear that the level of vibrational attenuation for a feed rate of  $10 \mu\text{m} / \text{rev}$  is considerably less than that achieved with a feed rate of  $2 \mu\text{m} / \text{rev}$ , as shown in figures 5.19(b), 5.20(b) and 5.21(b).

For completeness, the filter plots for a feed rate of  $2 \mu\text{m} / \text{rev}$  and a vibrational amplitude of 20 nm are provided in figures 5.42(a) and 5.42(b). These are like the plots in subsection 5.3.2. In figure 5.42(a), the peak input spatial frequencies are compared with the peak output spatial frequencies. In figure 5.42(b), the vibrational mitigation of the vibration on the cut surface is indicated. The attenuation is considerable compared with the equivalent plot for a feed of  $10 \mu\text{m} / \text{rev}$  in figure 5.41.

Similar to figures 5.36 and 5.25, the cut workpiece surface peak magnitude with a vibrational amplitude of 15 nm is plotted with the surface finish lobes for a feed rate of  $10 \mu\text{m} / \text{rev}$  in figure 5.43. The spindle speed of 1196.3 RPM from table 5.8 dictates the disturbance frequency range of each lobe on the horizontal axis. The

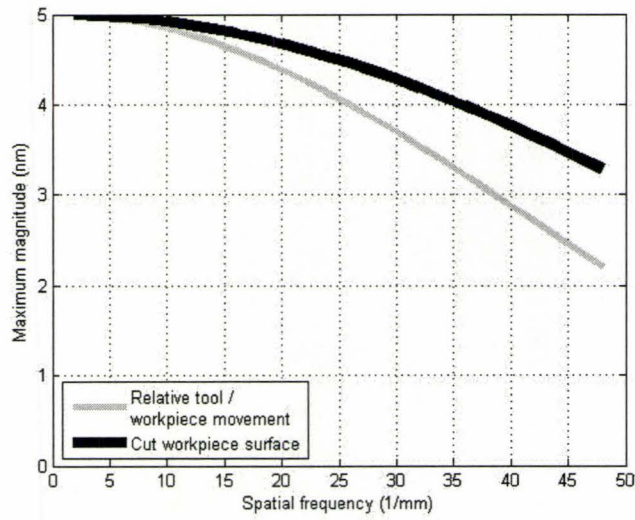


Figure 5.38: Filtering effect based on FFT results for  $d = 5 \mu\text{m}$ ,  $R_n = 0.630 \text{ mm}$ ,  $f = 10 \mu\text{m / rev}$ , and  $z_{amp} = 5 \text{ nm}$

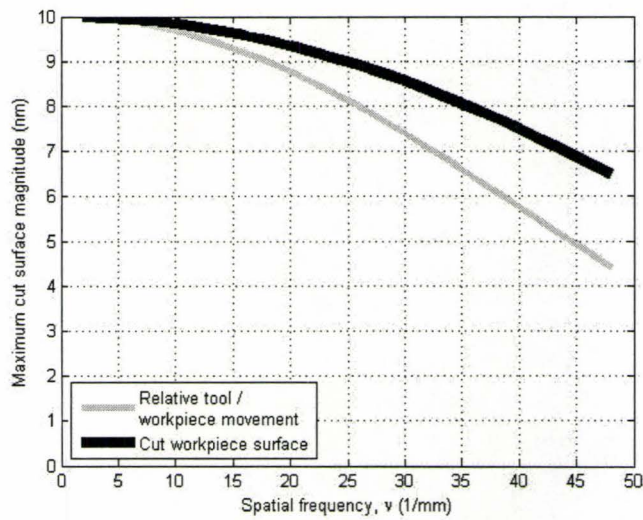


Figure 5.39: Filtering effect based on FFT results for  $d = 5 \mu\text{m}$ ,  $R_n = 0.630 \text{ mm}$ ,  $f = 10 \mu\text{m / rev}$ , and  $z_{amp} = 10 \text{ nm}$

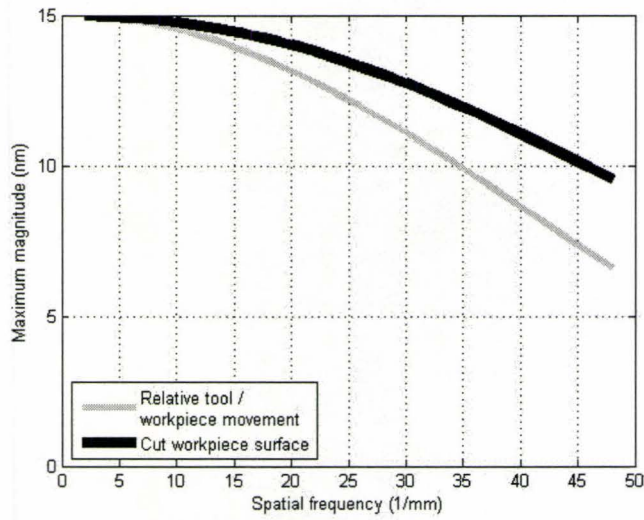


Figure 5.40: Filtering effect based on FFT results for  $d = 5 \mu\text{m}$ ,  $R_n = 0.630 \text{ mm}$ ,  $f = 10 \mu\text{m} / \text{rev}$ , and  $z_{amp} = 15 \text{ nm}$

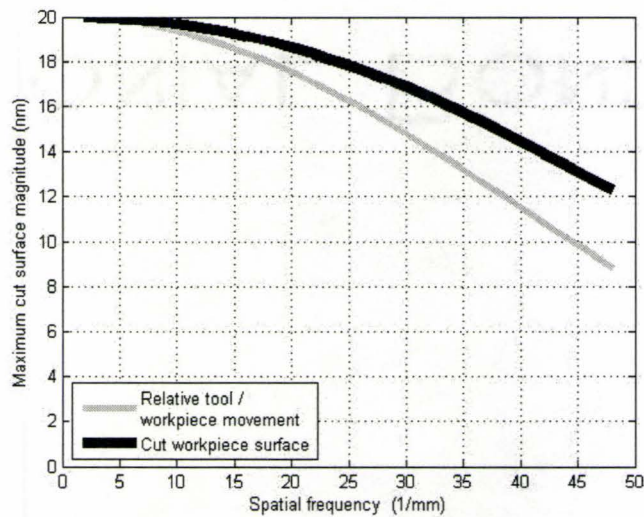
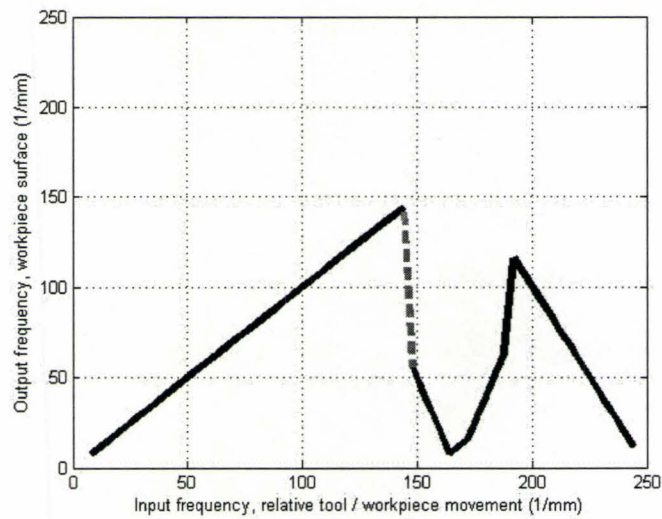
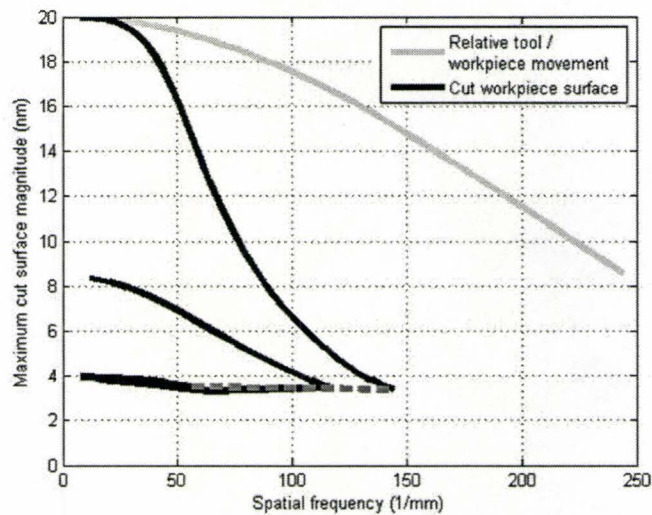


Figure 5.41: Filtering effect based on FFT results for  $d = 5 \mu\text{m}$ ,  $R_n = 0.630 \text{ mm}$ ,  $f = 10 \mu\text{m} / \text{rev}$ , and  $z_{amp} = 20 \text{ nm}$



(a) Relative tool / workpiece spatial frequency and resulting spatial frequency on the cut workpiece surface, based on maximum FFT magnitude



(b) Maximum spatial FFT magnitude and frequency for relative tool / workpiece motion and cut workpiece surface

Figure 5.42: Filtering effect based on FFT results for  $d = 5 \mu\text{m}$ ,  $R_n = 0.630 \text{ mm}$ ,  $f = 2 \mu\text{m} / \text{rev}$ , and  $z_{amp} = 20 \text{ nm}$

surface finish lobe pattern repeats itself indefinitely over a broad band of disturbance frequencies, as does the filtering phenomenon. As expected from the filter curves for a feed rate of  $10 \mu\text{m} / \text{rev}$  already shown, the attenuation of vibrations is considerably less than for the feed rate of  $2 \mu\text{m} / \text{rev}$ , over a broad band of disturbance frequencies.

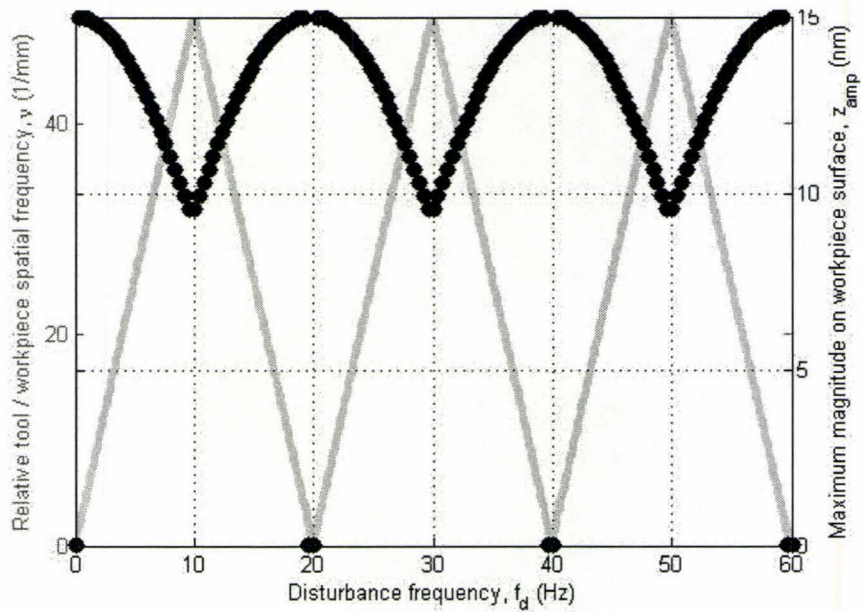


Figure 5.43: Surface finish lobes and maximum vibrational amplitude,  $N = 1000$  RPM and  $f = 10 \mu\text{m} / \text{rev}$ ,  $d = 5 \mu\text{m}$ ,  $R_n = 0.630 \text{ mm}$ ,  $z_{amp} = 15 \text{ nm}$

### 5.5.6 Maximum Vibrational Amplitude Discussion With Respect to the Surface Finish Lobes

In figure 5.40, for a feed rate of  $10 \mu\text{m} / \text{rev}$  and a vibrational amplitude of  $15 \text{ nm}$ , the best vibrational attenuation occurs at the end of the cut workpiece surface curve where the waviness amplitude on the cut surface is  $9.53 \text{ nm}$ . At this point the attenuation of relative tool / workpiece vibration on the cut surface is 37 per cent.

In figure 5.21(b) for a feed rate of  $2 \mu\text{m} / \text{rev}$  and a vibrational amplitude of 15 nm, the most extreme attenuation of vibration occurs with an output spatial frequency of 128 nm, and an amplitude of 2.56 nm. At this point attenuation is 83 per cent.

Ultimately, figures 5.40 and 5.21(b) indicate that there is more opportunity for attenuation of waviness error on the surface ultra precision machined with the smaller feed rate.

In figure 5.44, the surface finish lobes are shown for the feed rate of  $10 \mu\text{m} / \text{rev}$ , and the regions of best attenuation are noted. From figure 5.44, a vibrational attenuation of between 26 per cent and 37 per cent on the cut surface is achievable only within 8 Hz of a possible 20 Hz. In other words, an attenuation of between 26 per cent and 37 per cent is possible for 40 per cent of all disturbance frequencies.

In figure 5.45, for a feed rate of  $2 \mu\text{m} / \text{rev}$ , a vibrational attenuation of between 37 per cent and 87 per cent is possible over 11.7 Hz of 16.7 Hz, or equivalently over 79 per cent of all possible disturbance frequencies. Note that the starting attenuation of 37 per cent is the best attenuation possible for a feed rate of  $10 \mu\text{m} / \text{rev}$ . Further illustrated in figure 5.45 is that 58 per cent to 87 per cent attenuation is possible over 6.7 Hz of 16.7 Hz, or over 40 per cent of all possible disturbance frequencies. In figure 5.46 the attenuation results are summarized, showing the superior vibrational attenuation of the lower feed rate.

In figure 5.47, the filtering effects for both machining conditions are shown together. Like in figure 5.25, the input spatial frequency is plotted against peak magnitude, as opposed to the output spatial frequency. The better attenuation capabilities of the lower feed rate is again clear in figure 5.47.

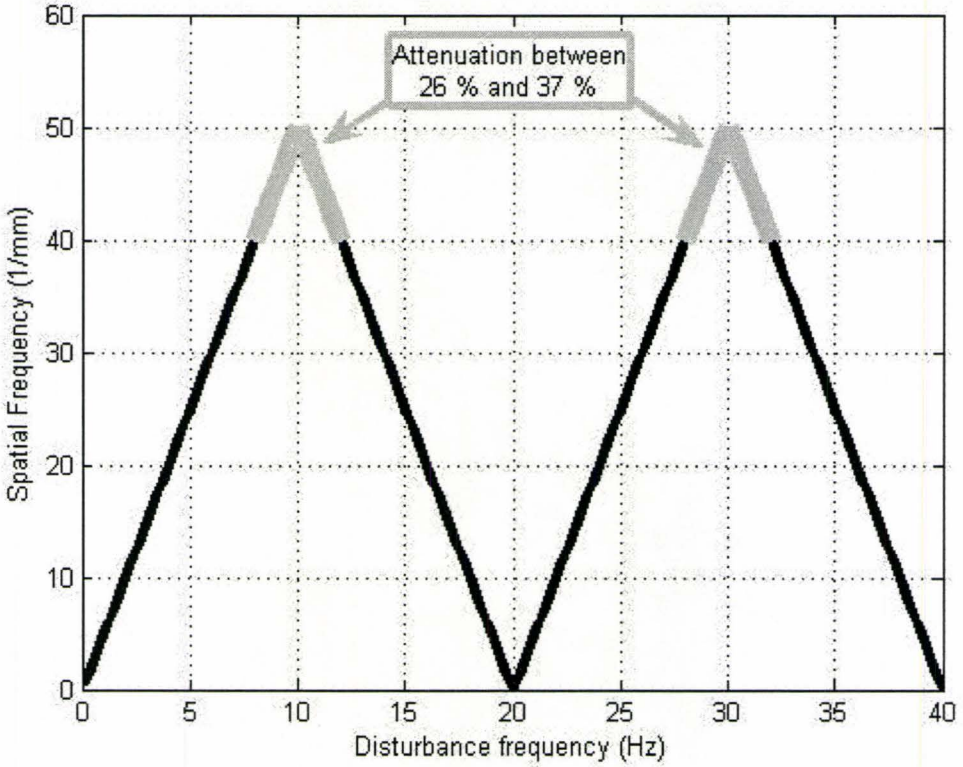


Figure 5.44: Surface finish lobes and regions of best vibrational attenuation for  $f = 10 \mu\text{m} / \text{rev}$ ,  $N = 1196.3 \text{ RPM}$ ,  $d = 5 \mu\text{m}$ ,  $R_n = 0.630 \text{ mm}$ ,  $z_{amp} = 15 \text{ nm}$

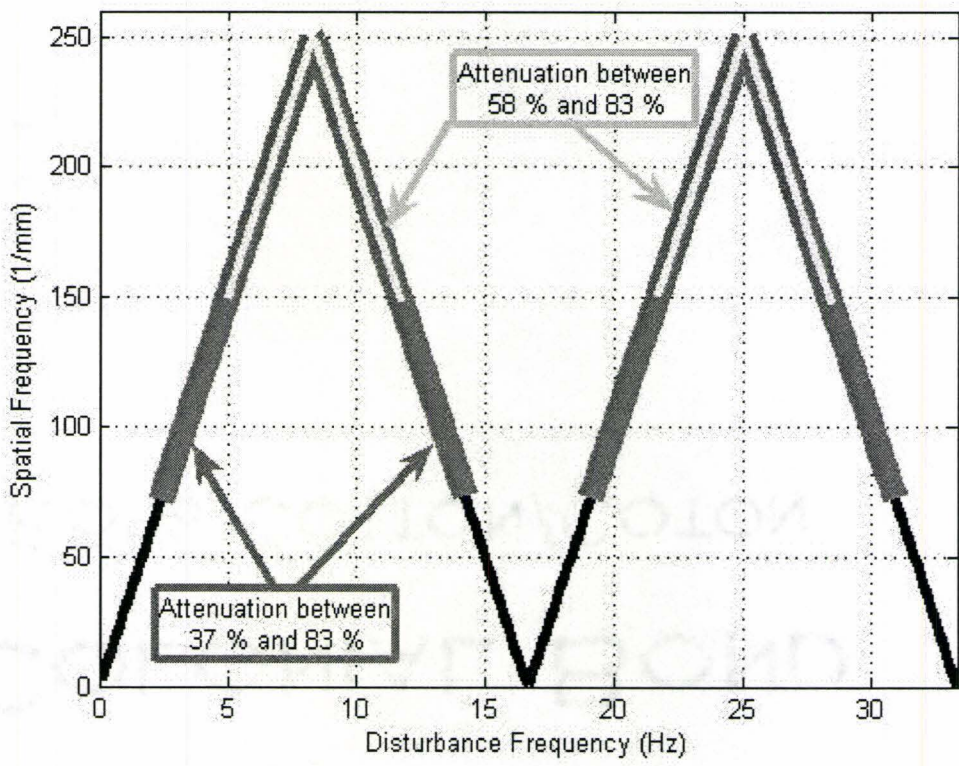


Figure 5.45: Surface finish lobes and regions of best vibrational attenuation for  $f = 2 \mu\text{m} / \text{rev}$ ,  $N = 1196.3 \text{ RPM}$ ,  $d = 5 \mu\text{m}$ ,  $R_n = 0.630 \text{ mm}$ ,  $z_{amp} = 15 \text{ nm}$

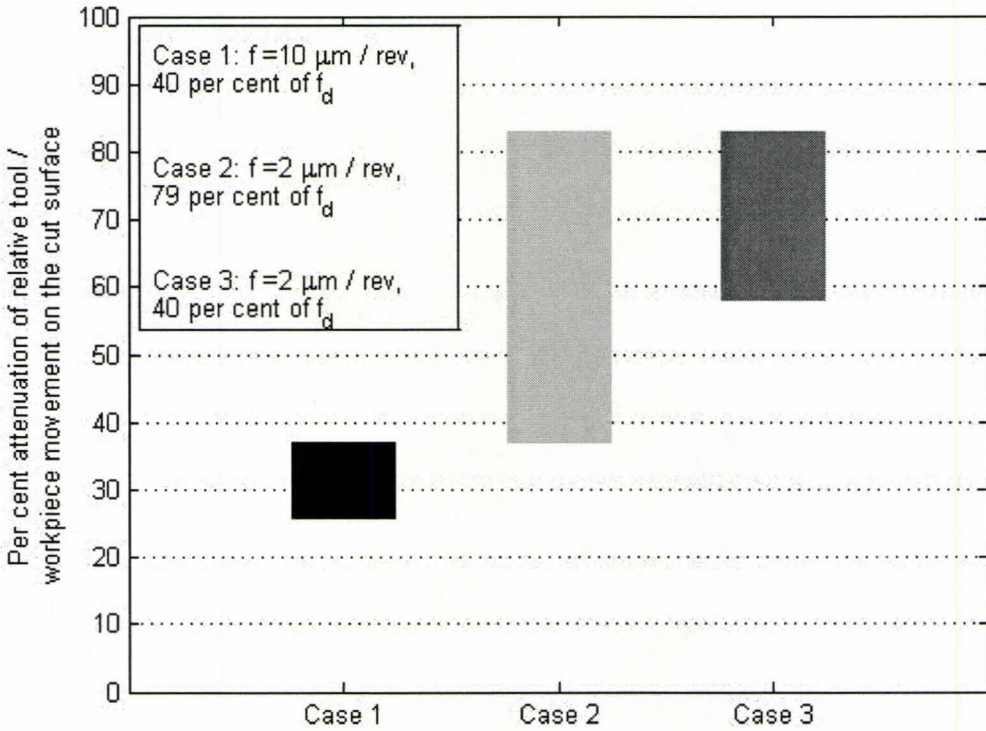


Figure 5.46: Summary of vibrational attenuation results for  $f = 10 \mu\text{m} / \text{rev}$  and  $f = 2 \mu\text{m} / \text{rev}$ ,  $d = 5 \mu\text{m}$ ,  $R_n = 0.630 \text{ mm}$ ,  $z_{amp} = 15 \text{ nm}$

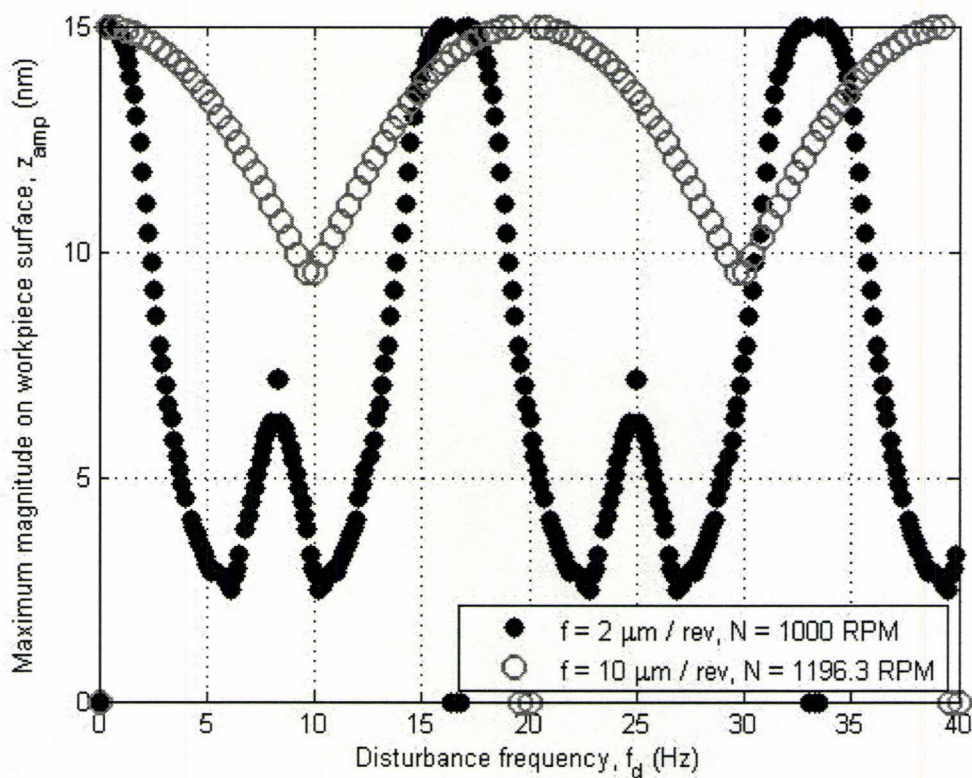


Figure 5.47: Maximum vibrational amplitude for  $f = 2 \mu\text{m} / \text{rev}$  and  $N = 1000 \text{ RPM}$ , and  $f = 10 \mu\text{m} / \text{rev}$  and  $N = 1196.3 \text{ RPM}$ ,  $d = 5 \mu\text{m}$ ,  $R_n = 0.630 \text{ mm}$ ,  $z_{amp} = 15 \text{ nm}$

## 5.6 The Filtering and Frequency Shifting Effect of Cutting Parameters on Surface Roughness Error in the Presence of Relative Tool / Workpiece Vibration

Significant observations have been made regarding the effects of relative tool / workpiece vibrations on the ideal geometric surface roughness,  $R_t$ , of equation 3.1. This phenomenon has already been mentioned in subsection 5.2.5. It is found that with vibrational amplitude, the ideal geometric surface roughness can be either decreased or its frequency on the workpiece changed or obscured. As already noted, the spatial frequency where one would expect to see the ideal geometric surface roughness is equivalent to the feed rate. For clarity, for a feed rate,  $f$  in  $\mu\text{m} / \text{rev}$ , the associated spatial frequency  $\nu_{feed}$  in  $1/\text{mm}$  is

$$\nu_{feed} = \frac{1000}{f} \quad (5.43)$$

For the feed rates of  $10 \mu\text{m} / \text{rev}$  and  $2 \mu\text{m} / \text{rev}$ , the associated spatial frequencies are noted in table 5.10. The marks left on a surface by the feed are commonly described as the “feed lines.” Also, in table 5.10 are the predicted roughness values,  $R_t$ , from equation 3.1, and half the  $R_t$  value representing the approximate expected magnitude from an FFT of the feed lines.

As one would predict, the slower feed rate of  $2 \mu\text{m} / \text{rev}$  is anticipated to give a much smoother finish with an  $R_t$  of  $0.80 \text{ nm}$  compared with the predicted  $R_t$  associated with a feed rate of  $10 \mu\text{m} / \text{rev}$  at  $19.84 \text{ nm}$ .

Roughness Value	Units	Workpiece $f = 10 \mu\text{m} / \text{rev}$	Workpiece $f = 2 \mu\text{m} / \text{rev}$
$\nu_{feed}$	1/mm	100	500
$R_t$	nm	19.84	0.80
$R_t/2$	nm	9.82	0.40

Table 5.10: Predicted surface roughness  $R_t$  for  $f = 10 \mu\text{m} / \text{rev}$  and for  $f = 2 \mu\text{m} / \text{rev}$ , both with  $R_n = 0.630 \text{ mm}$

### 5.6.1 The Vibrational Effect on Feed Lines for a Feed Rate of $10 \mu\text{m} / \text{rev}$

For vibrational magnitudes of 5 nm, 10 nm, 15 nm and 20 nm, the resulting feed mark magnitudes were considered over the range of possible spatial frequencies, i.e. 0 to 50 1/mm for a feed rate of  $10 \mu\text{m} / \text{rev}$ , according to the surface finish lobes. Firstly, it was found that for all spatial frequencies with these vibrational magnitudes, the feed line magnitude always occurred at the expected  $\nu_{feed}$  of 100 1/mm.

In figure 5.48, the feed mark magnitudes for the four listed vibrational magnitudes are shown over the range of spatial frequencies. When there is no vibration, the FFT magnitude at 100 1/mm is identical, and similar to the predicted  $R_t/2$  of table 5.10. All vibrational magnitudes also show a decrease with increasing spatial vibration frequency. This decrease in magnitude is more pronounced with a larger vibrational amplitude,  $z_{amp}$ . This is a significant observation since otherwise imprecise conclusions might be drawn from studying the magnitude of feed lines on a surface machined in the presence of relative tool / workpiece vibration.

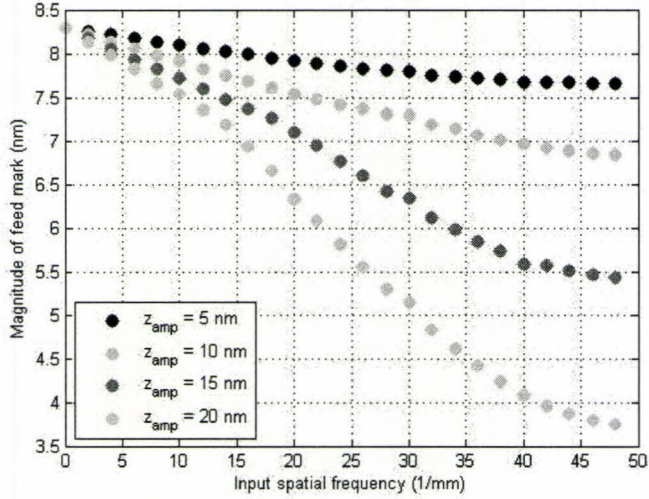


Figure 5.48: Magnitude of surface roughness (caused by feed), based on FFT results, for  $d = 5 \mu\text{m}$ ,  $R_n = 0.630 \text{ mm}$ ,  $f = 10 \mu\text{m} / \text{rev}$ , and  $z_{amp} = 5 \text{ nm}$ ,  $10 \text{ nm}$ ,  $15 \text{ nm}$  and  $20 \text{ nm}$

### 5.6.2 The Vibrational Effect on Feed Lines for a Feed Rate of $2 \mu\text{m} / \text{rev}$

With the smaller feed of  $2 \mu\text{m} / \text{rev}$ , the feed lines become lost on the surface with relative tool / workpiece motion. In other words, with these machining conditions, the feed lines no longer occur at the expected  $\nu_{feed}$  of  $500 \text{ 1/mm}$ . Thus, for this analysis it was necessary to extend the search range for the feed line. From the surface finish lobes it was known *a priori* that the relative tool / workpiece movement ranged between  $0$  and  $250 \text{ 1/mm}$  in the feed direction. In an attempt to find the feed lines, the maximum FFT magnitude search for each simulated surface was between the range of  $350 \text{ 1/mm}$  and  $600 \text{ 1/mm}$ .

In figures 5.49(a) and 5.49(b), the results for a small vibrational amplitude,  $z_{amp}$ , of  $5 \text{ nm}$  are shown. In figure 5.49(a), the spatial frequency in the range of  $350 \text{ 1/mm}$

and 600 1/mm with the maximum magnitude is indicated on the vertical axis, while the input spatial frequency of vibration is shown on the horizontal axis. Figure 5.49(a) indicates that for very small and for very large spatial frequencies of relative tool / workpiece vibration in the feed direction, the feed lines are visible on the workpiece surface with a spacing of  $2\mu\text{m}$ , or equivalently a spatial frequency of 500 1/mm. Interestingly, these regions correspond to the regions with the least attenuation of vibrational effect according to figure 5.19(b). In figure 5.49(a), with the exception of a few points in the middle, the feed line spatial frequency changes with vibrational amplitude, and is no longer found at the expected 500 1/mm. In figure 5.49(b), the magnitudes at the actual spatial frequencies are shown.

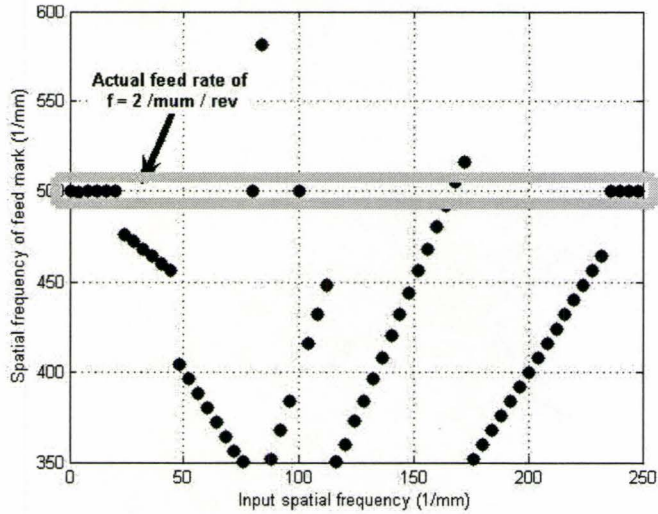
In figures 5.50(a) and 5.50(b), the trend is again demonstrated, this time for a larger vibrational amplitude,  $z_{amp}$ , of 15 nm, and the same trends were observed.

These results indicate that the amplitude and also spacing of feed lines in ultra precision machining can be significantly altered by relative tool / workpiece vibration.

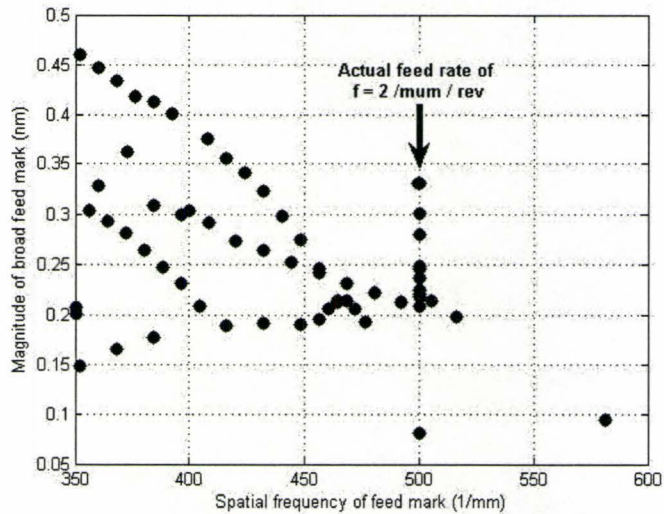
## **5.7 The Filtering Effect of Cutting Parameters on Vibration According to Mean Arithmetic Roughness, $R_a$**

### **5.7.1 Filtering the Cut Workpiece Surface to Properly Attribute the Error Source**

In section 5.6, the effect of vibrations on the feed marks were illustrated. However, considering only the effect of the geometric surface roughness on the surface finish

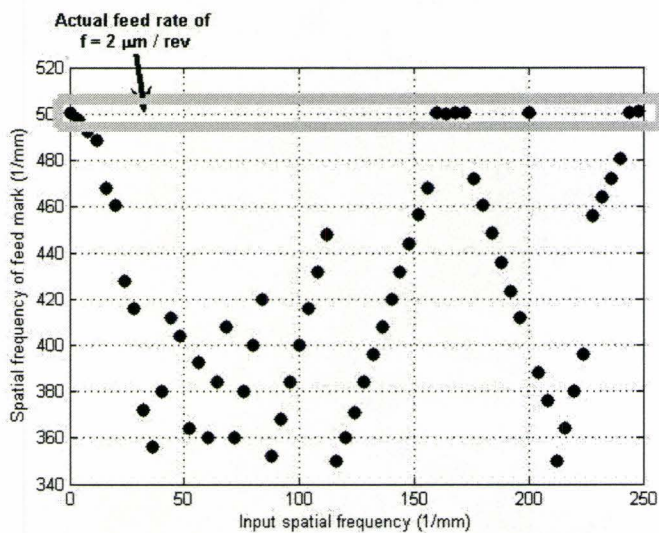


(a) Feed mark spatial frequency for each input spatial frequency (Searching between 350 1/mm and 600 1/mm)

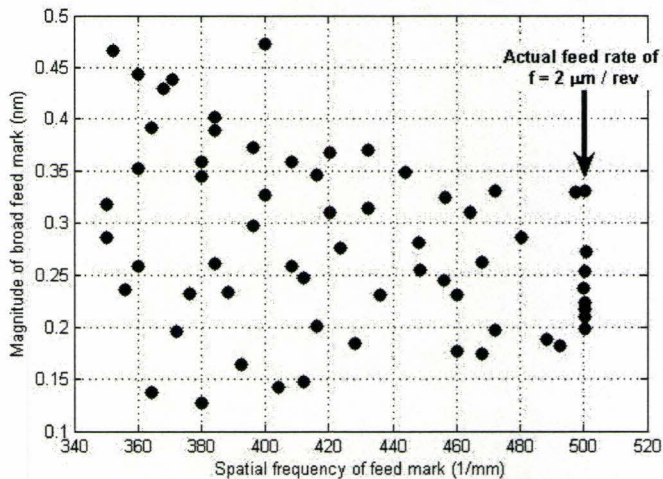


(b) Magnitude of surface roughness (caused by feed) for each input spatial frequency

Figure 5.49: Filtering effect on the surface roughness, based on FFT results, for  $d = 5 \mu\text{m}$ ,  $R_n = 0.630 \text{ mm}$ ,  $f = 2 \mu\text{m} / \text{rev}$ , and  $z_{amp} = 5 \text{ nm}$



(a) Feed mark spatial frequency for each input spatial frequency (Searching between 350 1/mm and 600 1/mm)



(b) Magnitude of surface roughness (caused by feed) for each input spatial frequency

Figure 5.50: Filtering effect on the surface roughness, based on FFT results, for  $d = 5 \mu\text{m}$ ,  $R_n = 0.630 \text{ mm}$ ,  $f = 2 \mu\text{m} / \text{rev}$ , and  $z_{amp} = 15 \text{ nm}$

is misleading and does not take into account the majority of surface error caused by vibration. Further, it has been illustrated that even on surfaces machined with the faster ultra precision feed rate of  $10 \mu\text{m} / \text{rev}$ , the vibrational magnitudes exceed that of the feed lines. For examples, see figures 3.7, 3.6, and 4.18. In these cases the magnitudes of waviness error exceed the error associated with the feed lines. Thus, if a workpiece is machined in the presence of some unwanted relative tool / workpiece vibration, then the study and mitigation of waviness errors is a major concern.

Simulated cut workpiece surfaces are filtered so that the appropriate error source is credited with the surface  $R_a$ . The range of tool / workpiece spatial frequencies known from the surface finish lobes, as well as the feed rate spatial frequencies, are used to determine the frequency cut-offs.

To identify form and waviness errors, a low-pass filter was used on the simulated cut surface data. Conversely, to identify surface roughness error attributable to the feed rate, a high-pass filter was used on the simulated cut surface data. In both instances ninth order Butterworth filters are employed. Overall, to use a quality measure in the study of surface waviness error due to vibration,  $R_a$  is a more logical choice than  $R_t$ . In simulation, the peaks and valleys are controlled. However, when measuring an actual cut workpiece, non-harmonic peaks and valleys can exist on the surface that are not caused by the relative tool / workpiece vibration. Meanwhile, it is the periodic waviness pattern caused by harmonic relative tool / workpiece motion that is of interest in this work.

### Butterworth Filters for a Feed Rate of 10 $\mu\text{m}$ / rev

In figures 5.51 and 5.52, the low pass and high pass filters are used with the simulated cut surface data, with a feed rate of 10  $\mu\text{m}$  / rev. Ninth order Butterworth filters are built in Matlab, and both high pass and low pass filters have a cut-off spatial frequency of 70 1/mm. The Butterworth filter was chosen because its response is flat in magnitude [32], as evidenced by the horizontal line in figures 5.51 and 5.52. The cost of this flat response is a roll-off that is less than other options [32]. However, increasing the filter order increases roll-off steepness, providing better attenuation [40]. For a ninth order Butterworth filter, the roll-off is -180 dB / decade. Also, at the cut-off frequency, the gain is  $\frac{1}{\sqrt{2}}$  or -3 dB [40]. The sampling rate is 1000 1/mm, meaning that the lowest observable spatial frequency is just less than 500 1/mm. The highest expected frequency event is the feed rate at 100 1/mm.

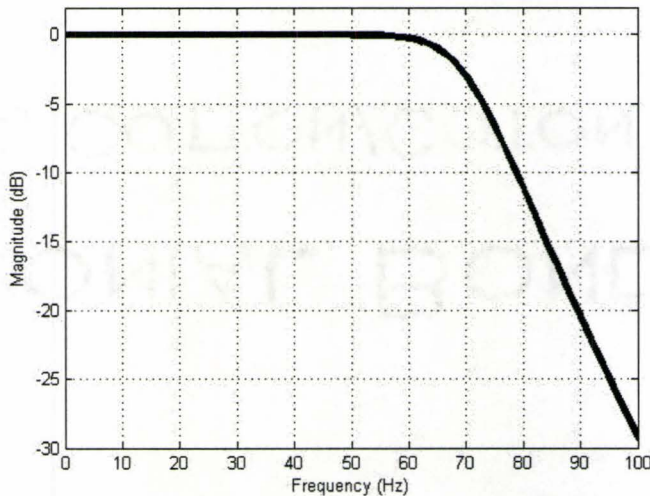


Figure 5.51: Ninth order low pass Butterworth filter for cut surface simulation data,  $f = 10 \mu\text{m}$  / rev, cut-off  $\nu = 70$  1/mm

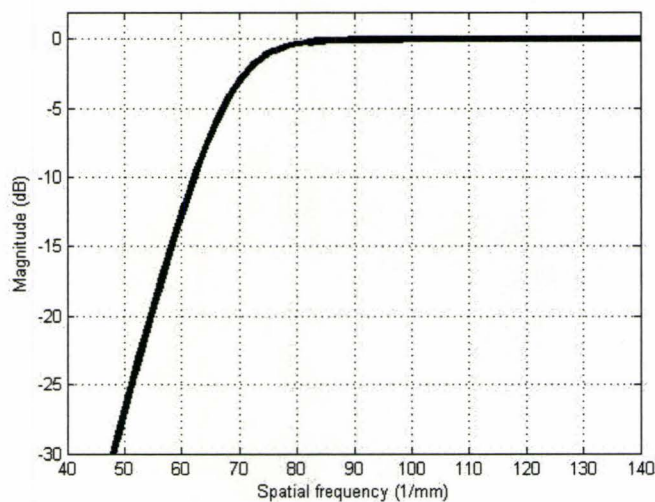


Figure 5.52: Ninth order high pass Butterworth filter for cut surface simulation data,  $f = 10 \mu\text{m} / \text{rev}$ , cut-off  $\nu = 70 \text{ 1/mm}$

### Butterworth Filters for a Feed Rate of $2 \mu\text{m} / \text{rev}$

Figures 5.53 and 5.54 show the Butterworth filters for the feed rate,  $f$ , of  $2 \mu\text{m} / \text{rev}$ . The cut-off spatial frequency is  $260 \text{ 1/mm}$  for both filters. The sampling rate is  $5000 \text{ 1/mm}$ , meaning the lowest observable feed rate is just less than  $2500 \text{ 1/mm}$ . Meanwhile, the highest expected frequency event is the feed rate at  $500 \text{ 1/mm}$ .

In Appendix B, the  $R_a$  curves generated for the feed rates of  $10 \mu\text{m} / \text{rev}$  and  $2 \mu\text{m} / \text{rev}$  are provided for the unfiltered simulated cut workpiece surface and also for the high pass and low pass filtered simulated cut workpiece surfaces. When the feed rate is  $10 \mu\text{m} / \text{rev}$ , for relative tool / workpiece vibrational amplitudes of greater than  $10 \text{ nm}$ , the  $R_a$  of low pass filtered data is greater than for the high pass filtered data. Further, for the feed rate of  $2 \mu\text{m} / \text{rev}$ , the low pass filtered surface has the largest error values. Overall, the waviness error is the most significant component of

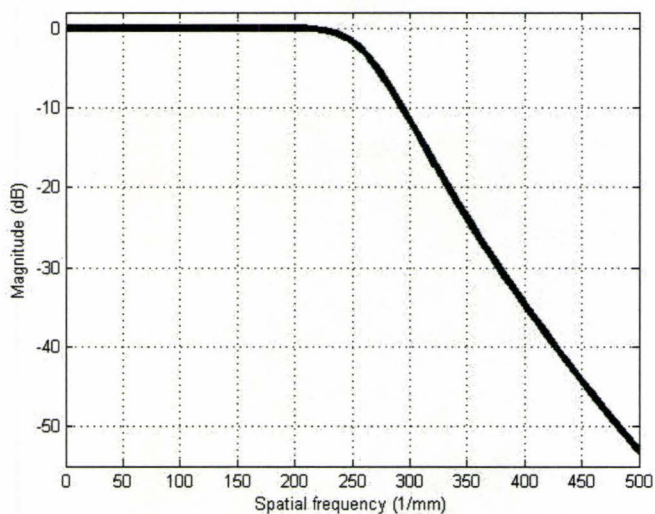


Figure 5.53: Ninth order low pass Butterworth filter for cut surface simulation data,  $f = 2 \mu\text{m} / \text{rev}$ , cut-off  $\nu = 260 \text{ 1/mm}$

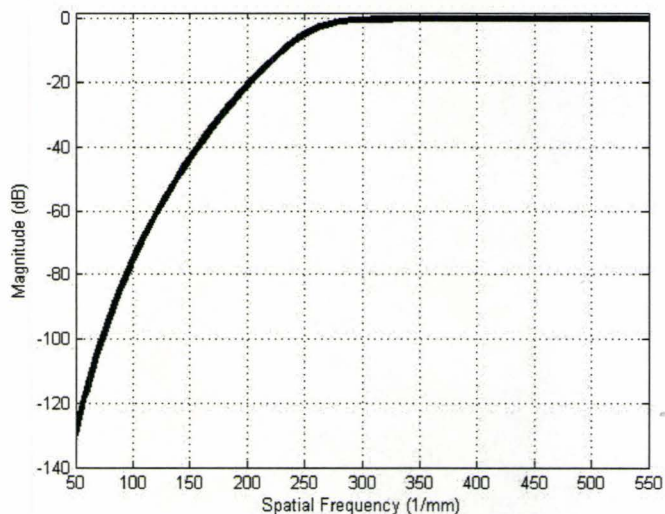


Figure 5.54: Ninth order high pass Butterworth filter for cut surface simulation data,  $f = 2 \mu\text{m} / \text{rev}$ , cut-off  $\nu = 260 \text{ 1/mm}$

the mean arithmetic roughness,  $R_a$ .

### 5.7.2 Comparing Low Pass Filtered Mean Arithmetic Roughness Curves

The relative tool / workpiece vibration is considered to be the primary contributor to cut workpiece surface error. Further, this vibration mainly creates dominant waviness errors. Low pass filtering the simulated cut workpiece surface means that focus can be placed on the contribution of waviness to the mean arithmetic roughness,  $R_a$ . In this section, the low pass filtered  $R_a$  curves are compared for the feed rates of  $10 \mu\text{m} / \text{rev}$  and  $2 \mu\text{m} / \text{rev}$ .

In figures 5.55, 5.56, 5.57 and 5.58, the predicted mean arithmetic roughness resulting from relative tool workpiece vibration is shown for the two machining conditions of table 5.8, over a disturbance frequency range of 40 Hz, and for vibrational amplitudes of 5 nm, 10 nm, 15 nm and 20 nm respectively. Predictably, due to the surface finish lobes, this  $R_a$  pattern continues indefinitely over a broad band of disturbance frequencies. The shape of these curves is similar to the magnitude filter curves presented earlier in this chapter for feed rates of  $10 \mu\text{m} / \text{rev}$  and  $2 \mu\text{m} / \text{rev}$ , and shown together in figure 5.47 for a vibrational amplitude of 15 nm. As in figure 5.47, the 'Option 2' region for mitigation of vibrations covers a much larger range of possible values than 'Option 1.' Overall, the contribution of relative tool / workpiece vibrations on the surface finish error described by  $R_a$  is significantly greater for the larger feed rate. Also, it is far more likely for this larger feed rate that a larger surface finish error will occur over a broadband of possible disturbance frequencies.

Consider figure 5.58 describing the predicted  $R_a$  for both machining conditions

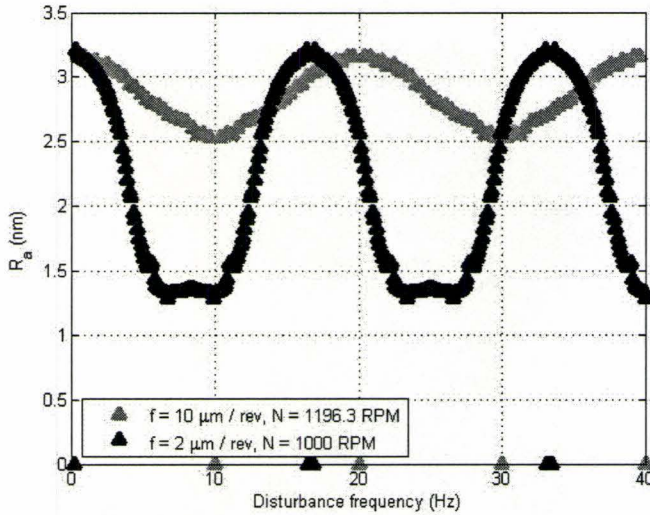


Figure 5.55: Comparing low pass filtered data  $R_a$  curves for different machining conditions,  $d = 5 \mu\text{m}$ ,  $R_n = 0.630 \text{ mm}$ , , and  $z_{amp} = 5 \text{ nm}$

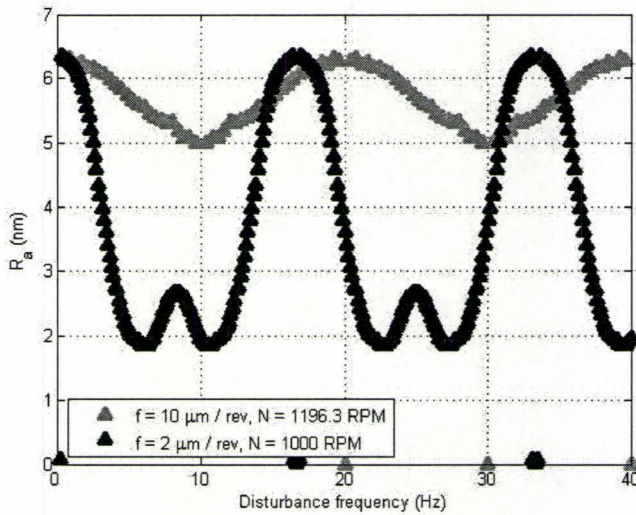


Figure 5.56: Comparing low pass filtered data  $R_a$  curves for different machining conditions,  $d = 5 \mu\text{m}$ ,  $R_n = 0.630 \text{ mm}$ , , and  $z_{amp} = 10 \text{ nm}$

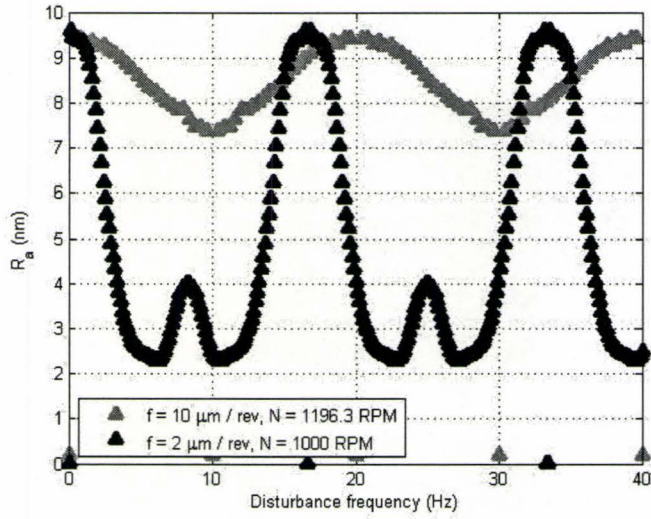


Figure 5.57: Comparing low pass filtered data  $R_a$  curves for different machining conditions,  $d = 5 \mu\text{m}$ ,  $R_n = 0.630 \text{ mm}$ , , and  $z_{amp} = 15 \text{ nm}$

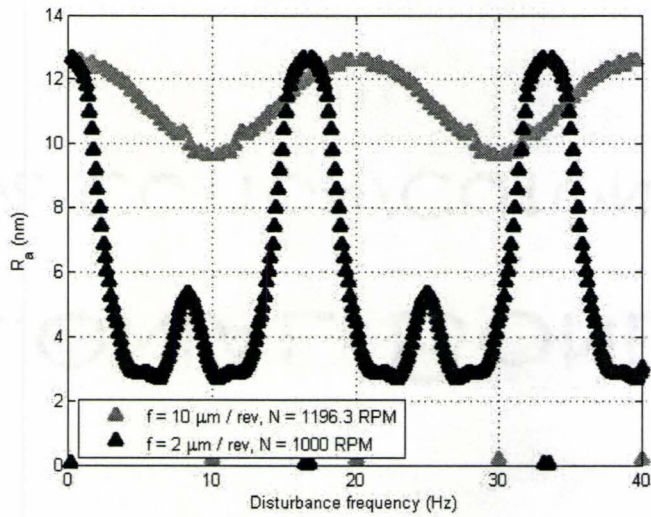


Figure 5.58: Comparing low pass filtered data  $R_a$  curves for different machining conditions,  $d = 5 \mu\text{m}$ ,  $R_n = 0.630 \text{ mm}$ , , and  $z_{amp} = 20 \text{ nm}$

when the vibrational amplitude is 20 nm. The mean  $R_a$  for the feed rate of  $10 \mu\text{m} / \text{rev}$  over 40 Hz is 10.7 nm. Meanwhile, for the feed rate of  $2 \mu\text{m} / \text{rev}$ , the mean  $R_a$  is approximately half this value at 5.5 nm. Similarly, for a vibrational amplitude of 15 nm the corresponding average  $R_a$  values for each feed rate are 8.1 nm and 4.7 nm. The results for each vibrational amplitude are summarized in figure 5.59. Thus, for the faster feed rate the average  $R_a$  error caused by relative tool / vibrations is larger than for the slower feed rate. Further, the average error difference increases with an increase in vibrational amplitude. This analysis can, of course, be extended over a broad band of disturbance frequencies.

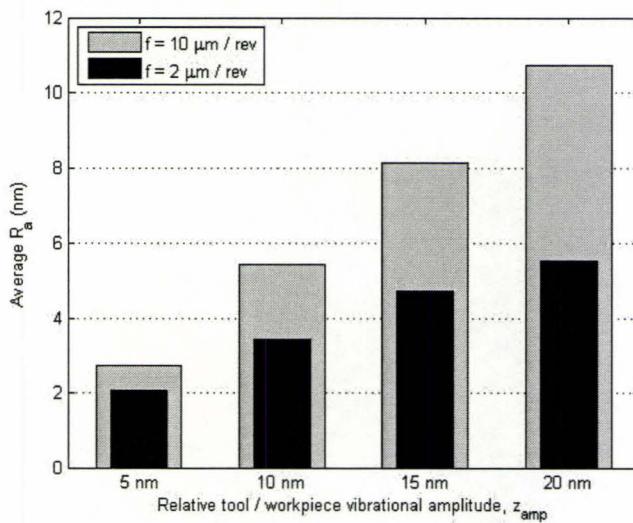


Figure 5.59: Average  $R_a$  values for each machining condition for all vibration amplitudes,  $d = 5 \mu\text{m}$ ,  $R_n = 0.630 \text{ mm}$

Figure 5.60 shows the low pass filtered  $R_a$  curve from figure B.8(b) versus the disturbance frequency in Hz. As already discussed in chapter 4, the spindle speed essentially stretches or squeezes the disturbance frequency range of the surface finish lobe. Thus, a larger spindle speed means that one surface finish lobe straddles more

disturbance frequencies. From figure 5.60, it is evident that with a larger spindle speed, a better likelihood of vibration attenuation is possible.

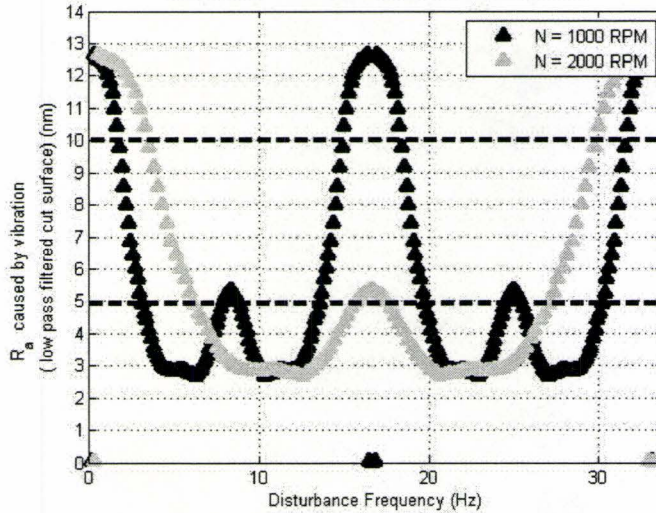


Figure 5.60: Comparing low pass filtered data  $R_a$  curves with different spindle speeds,  $d = 5 \mu\text{m}$ ,  $R_n = 0.630 \text{ mm}$ ,  $f = 2 \mu\text{m} / \text{rev}$ , and  $z_{amp} = 20 \text{ nm}$

## 5.8 Experimental Validation of Vibrational Mitigation and Discussion

With experimental work it is shown that the workpiece ultra precision machined with a slower feed rate has a better surface finish than the workpiece ultra precision machined with the faster feed rate. However, the difference in surface finish is not caused by the in-feed direction height of feed lines, as predicted by the ideal geometric surface roughness,  $R_t$ , of equation 3.1. Instead, the improvement is the result of the vibrational attenuation caused by cutting parameters, as described in this chapter.

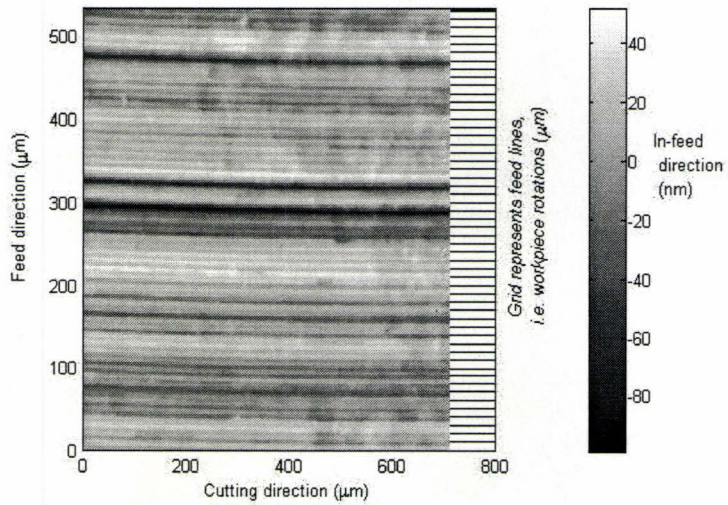
In table 5.11 the workpiece surface metrology is described for both cutting conditions. The filtering is based on sampling and field of view.

Parameter	units	Workpiece 1, $f$ = 10 $\mu\text{m} / \text{rev}$ , $N$ = 1196.3 RPM	Workpiece 2, $f$ = 2 $\mu\text{m} / \text{rev}$ , $N$ = 1000 RPM
Maximum filter spatial frequency	1/mm	149.3	270.3
Minimum filter spatial frequency	1/mm	2.6	5.3
Minimum filter wavelength	$\mu\text{m}$	6.7	3.7
Maximum filter wavelength	$\mu\text{m}$	384.6	188.9
Measurement resolution (feed direction)	$\mu\text{m}$	1.12	0.55

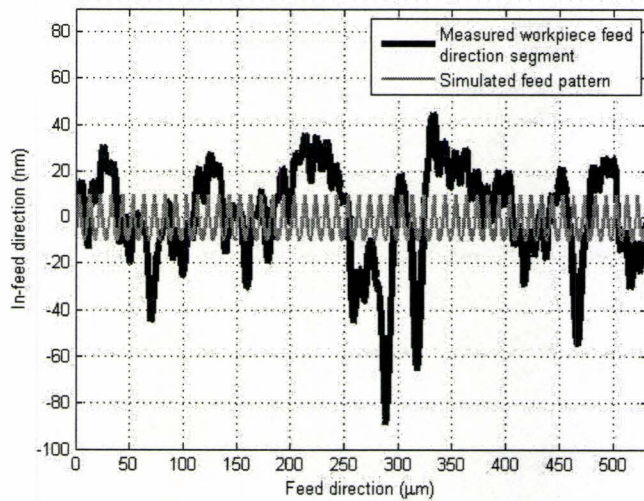
Table 5.11: Measurement and filtering parameters of white light interferometry

In figures 5.61(a), the white light interferometry image for the workpiece surface ultra precision machined with a feed rate of 10  $\mu\text{m} / \text{rev}$  is given. As has already been described, the spacing of the dominant pattern is waviness and not feed. This is further illustrated in figure 5.61(b). The feed direction FFT of this surface is given in figure 5.62. The feed line magnitude in figure 5.62 is 7.97 nm. It is estimated that the largest waviness amplitude in figure 5.62 of 17.86 nm at approximately 17 1/mm is caused by a relative tool / workpiece vibration with an amplitude of 19 nm, according to the filter plot of figure 5.63. The feed mark magnitude of figure 5.62 is less than the ideal geometric surface roughness expected without vibration present.

In figure 5.64(a), the white light interferometry image for the workpiece ultra precision machined with a feed rate of 2  $\mu\text{m} / \text{rev}$  is given. The filtering used with this view (based on sampling) cuts off information beyond 270.3 1/mm. This means that



(a) White light interferometry measured cut workpiece 1 surface, zoom 200x



(b) White light interferometry measured segment of workpiece 1 compared with simulated feed pattern

Figure 5.61: Workpiece 1 white light interferometry measured surface,  $f = 10 \mu\text{m} / \text{rev}$ ,  $N_{\text{nominal}} = 1196.3 \text{ RPM}$ ,  $d = 5 \mu\text{m}$ ,  $R_n = 0.630 \text{ mm}$

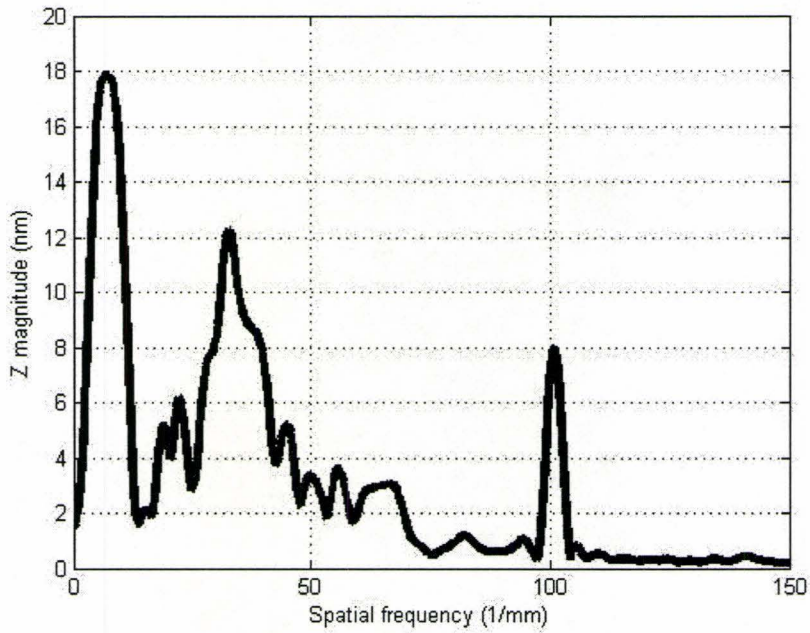


Figure 5.62: FFT of the white light interferometry measured cut workpiece 1 surface for  $f = 10 \mu\text{m} / \text{rev}$ ,  $N = 1196.3 \text{ RPM}$ ,  $d = 5 \mu\text{m}$ ,  $R_n = 0.630 \text{ mm}$

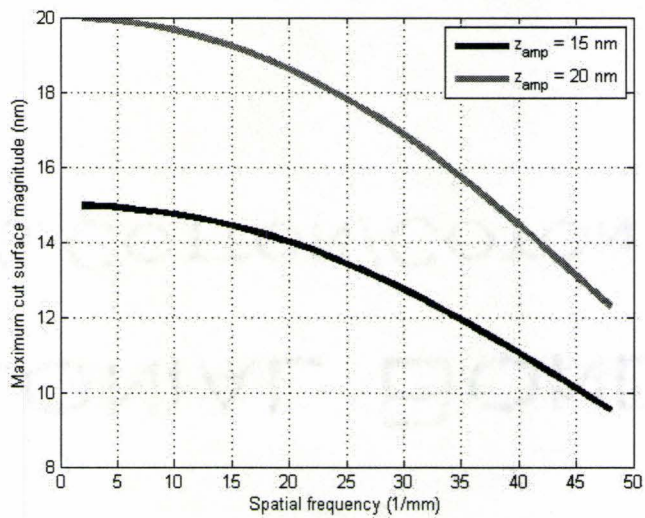
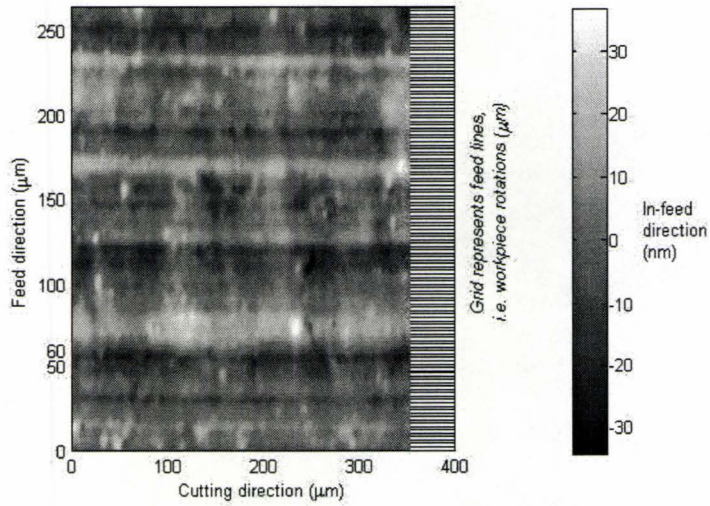


Figure 5.63: The resulting cut workpiece surface error amplitude (filtering effect) based on FFT results for  $f = 10 \mu\text{m} / \text{rev}$ ,  $N = 1196.3 \text{ RPM}$ ,  $d = 5 \mu\text{m}$ ,  $R_n = 0.630 \text{ mm}$

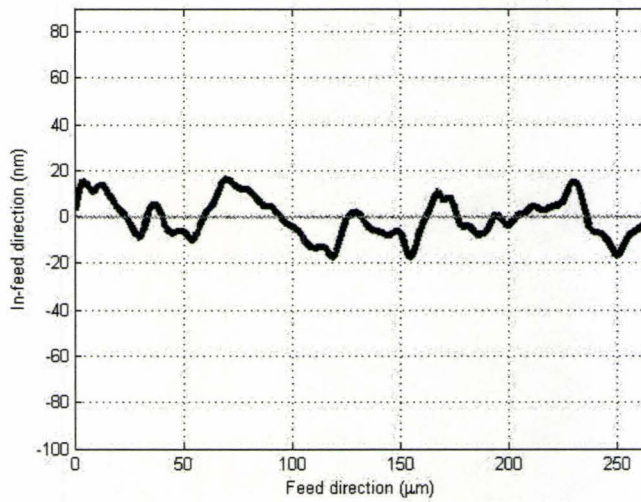
feed lines at 500 1/mm would not be visible in this image, and all periodic phenomenon observed is waviness error. Again, this is further illustrated in figure 5.64(b). The theoretical magnitude for a feed line without vibrations for these cutting conditions is 0.33 nm, from section 5.6. Since the Zygo resolution in the in-feed direction is larger at 0.5 nm, the feed line without vibrations was not detectable. Meanwhile, the waviness amplitudes observed in figure 5.64(b) are much greater than the predicted geometric surface roughness. This is further evidenced in the feed direction FFT of the surface in figure 5.65, where the largest waviness pattern has an amplitude of over 6 nm.

Examining figures 5.62 and 5.65, one can see that the filtering phenomenon of section 5.4 and subsection 5.5.5 is again illustrated. In figure 5.62 for a feed rate of 10  $\mu\text{m} / \text{rev}$ , the dominant spatial frequencies on the workpiece surface taper off before 50 1/mm, and overall show a gradual attenuation as the spatial frequency increases. Meanwhile, in figure 5.65 for a feed rate of 2  $\mu\text{m} / \text{rev}$ , spatial frequencies are no longer apparent after approximately 130 1/mm, and an attenuation is observable as the spatial frequency increases. Overall, the waviness magnitude for the feed rate of 10  $\mu\text{m} / \text{rev}$  is considerably greater than for the feed rate of 2  $\mu\text{m} / \text{rev}$ . The same vertical axis scaling was used in figures 5.61(b) and 5.64(b), and also in figures 5.62 and 5.65, in order to contrast the pronounced vibrational error magnitude on the workpiece surface for the larger feed rate.

Figure 5.66 and 5.67 show the in-situ relative tool / workpiece vibrations during cutting for each surface. As described in chapter 3, accelerometers at both the spindle housing and tool locations are used to synchronously acquire data during cutting. Similar vibrations occurred in the machining of both surfaces. The feed rate of 10



(a) White light interferometry measured cut workpiece 2 surface, zoom 400x



(b) White light interferometry measured segment of workpiece 2 compared with simulated feed pattern

Figure 5.64: Workpiece 2 white light interferometry measured surface,  $f = 2 \mu\text{m} / \text{rev}$ ,  $N_{\text{nominal}} = 1000 \text{ RPM}$ ,  $d = 5 \mu\text{m}$ ,  $R_n = 0.630 \text{ mm}$

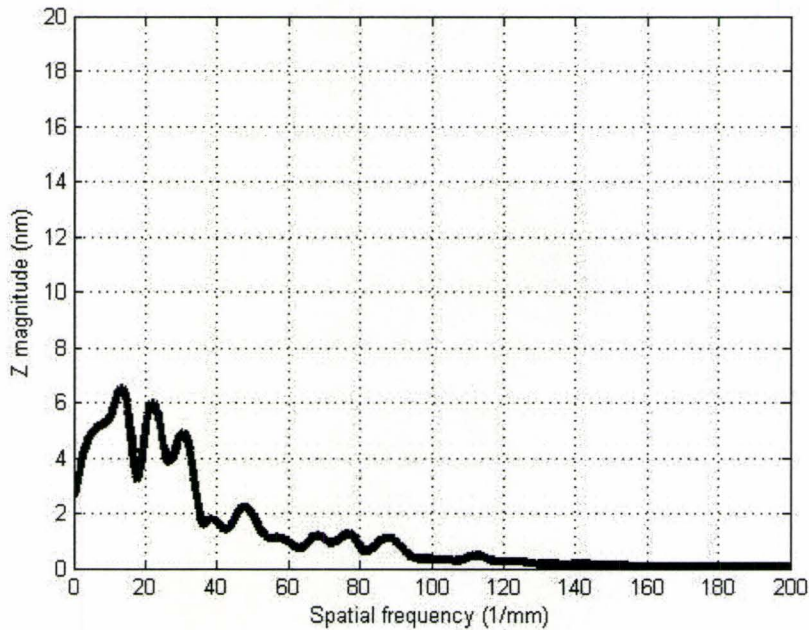


Figure 5.65: FFT of the white light interferometry measured cut workpiece 2 surface for  $f = 2 \mu\text{m} / \text{rev}$ ,  $N = 1196.3 \text{ RPM}$ ,  $d = 5 \mu\text{m}$ ,  $R_n = 0.630 \text{ mm}$

$\mu\text{m} / \text{rev}$  cutting process experienced a large spike at 787 Hz and another at 4990 Hz. Meanwhile, the feed rate of  $2 \mu\text{m} / \text{rev}$  cutting process experienced a larger spike at 4983 Hz. Additional curves pertaining to the accelerometer data acquisition are provided in Appendix A, figures A.10, A.11, A.12, A.4, A.5 and A.6.

As already noted, the poorer surface finish for the feed rate of  $10 \mu\text{m} / \text{rev}$  is due to the effect of vibrations rather than the effect of geometric surface roughness in the form of feed marks. Low pass filtering each feed direction segment of figure 5.61(a) further illustrates this concept. A resulting feed direction segment is shown in figure 5.68. This is the same segment depicted in figure 5.61(b), but run through the low pass Butterworth filter with a cut-off frequency of 70 1/mm.

The mean arithmetic roughness,  $R_a$ , is calculated for each feed direction segment

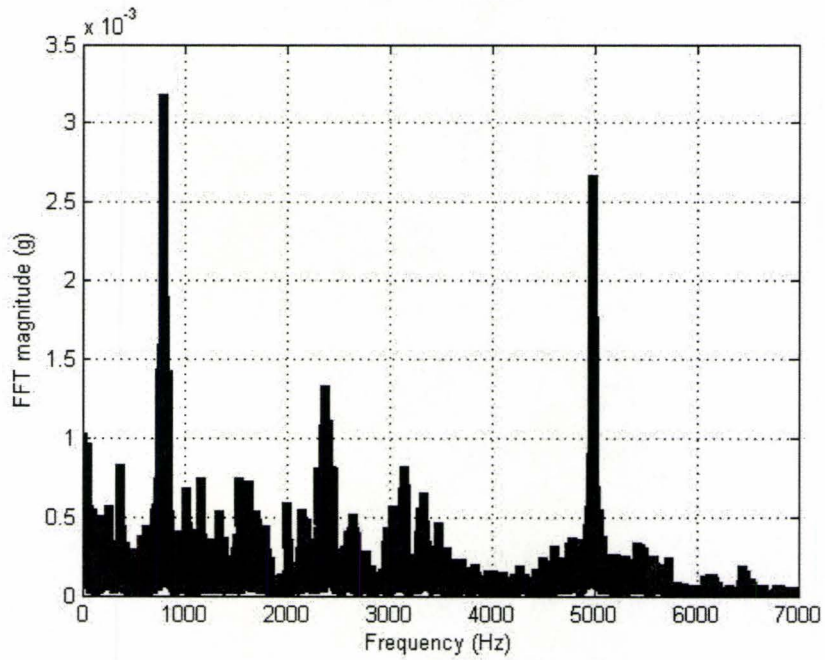


Figure 5.66: Relative tool / workpiece acceleration FFT for workpiece 1,  $N = 1196.3$  RPM,  $f = 10 \mu\text{m} / \text{rev}$ , number of averages = 103,  $\Delta f = 0.8548$  Hz

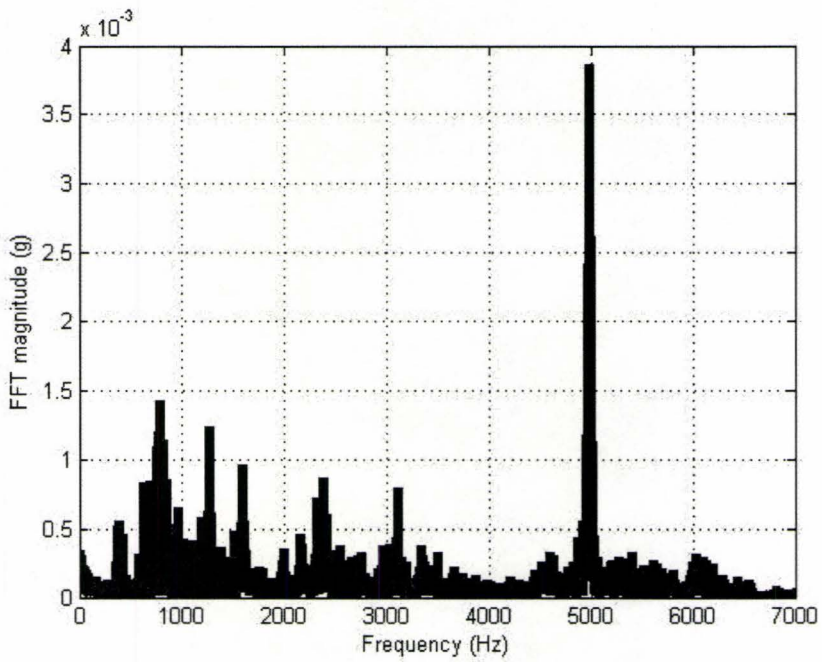


Figure 5.67: Relative tool / workpiece acceleration FFT for workpiece 2,  $N = 1000$  RPM,  $f = 2 \mu\text{m} / \text{rev}$ , number of averages = 103,  $\Delta f = 0.8548$  Hz

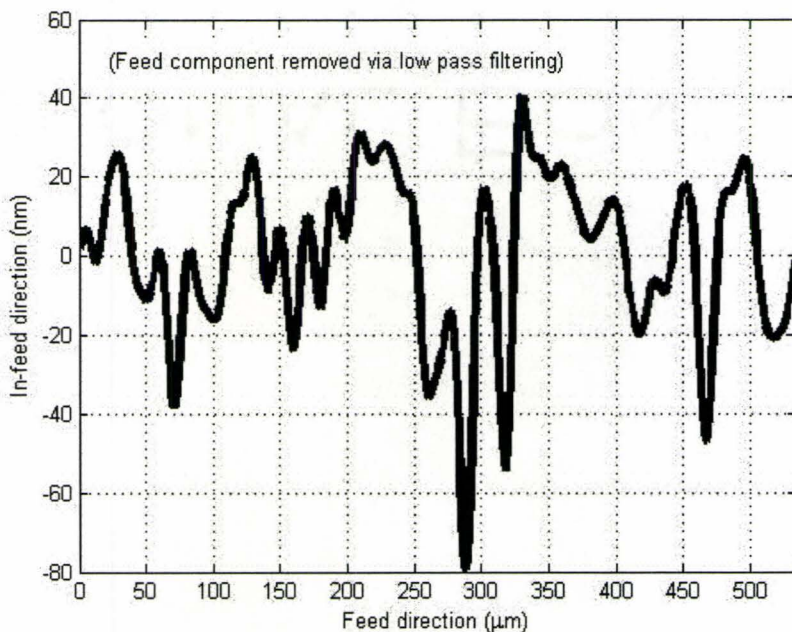


Figure 5.68: Low pass filtered white light interferometry measured workpiece 1 segment  $f = 10 \mu\text{m} / \text{rev}$ ,  $N = 1196.3 \text{ RPM}$ ,  $d = 5 \mu\text{m}$ ,  $R_n = 0.630 \text{ mm}$

with and without low pass filtering. The results are presented in figure 5.69. The gray dots show the  $R_a$  values for each radial segment with the effect of feed included. Meanwhile, the black dots show the  $R_a$  values for each radial segment without the effect of feed included, i.e. after being first low pass filtered. While the  $R_a$  values without the effect of feed marks is less, the majority of error clearly comes from lower spatial frequency components. Thus, while the feed marks do contribute, their effect is less than that of the relative tool / workpiece vibration.

In table 5.12 the  $R_a$  results of figure 5.69 are summarized. The ‘imported surface’ refers to the white light interferometry image as it appears in figure 5.61(a), i.e. the surface without additional Butterworth filtering. One might expect more distinction between the imported  $R_a$  and low pass filtered  $R_a$  values. The similarity likely exists

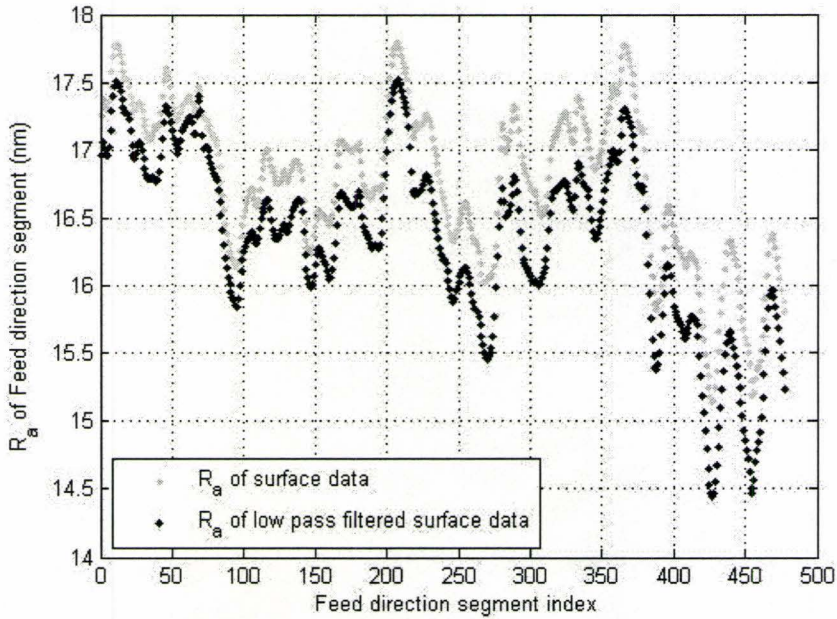


Figure 5.69:  $R_a$  for each feed direction segment of the white light interferometry workpiece 1 image,  $f = 10 \mu\text{m} / \text{rev}$ ,  $N = 1196.3 \text{ RPM}$ ,  $d = 5 \mu\text{m}$ ,  $R_n = 0.630 \text{ mm}$

because of the inclusion of non periodic events, like the large dip of figures 5.61(b) and 5.68 at around  $290 \mu\text{m}$  in the feed direction. In the calculation of  $R_a$ , this dip would obscure the lower value expected with the removal of the tool feed marks.

$R_a$ measure (nm)	imported surface	low pass filtered
mean	16.77	16.36
standard deviation	0.58	0.66
maximum	17.79	17.52
minimum	15.13	14.44

Table 5.12:  $R_a$  summary for the imported and low pass filtered white light interferometry data of figure 5.61(a) for workpiece 1

To further explore the effect of vibration, the two peaks of figure 5.62 were used in a simulation. The greatest peak has an amplitude of approximately 18 nm at 17 1/mm, and the second peak has an amplitude of approximately 12 nm at 33 1/mm.

As already noted, from the filter curve of figure 5.41, the amplitude of relative tool / workpiece motion to cause the first peak is approximately 19 nm. Meanwhile, from the filter curve of figure 5.40 and 5.63, the amplitude of relative tool / workpiece motion to cause the second peak is approximately 15 nm.

In figure 5.70, the simulated cut surface is provided. This is a similar image to figure 5.61(b), but without any additional spikes or smaller amplitude periodic behavior. The cut workpiece surface is created from the superposition of two harmonic relative tool / workpiece motions in the feed direction, the first with an amplitude of 19 nm and a spatial frequency of 17 1/mm, and the second with an amplitude of 15 nm and a spatial frequency of 33 1/mm. The phase angle for each individual harmonic motion was zero. The calculated  $R_a$  for this plot is 14.97 nm. By considering only the top two relative tool / workpiece harmonic vibrations, the predictive accuracy of the model is 89 per cent of the actual workpiece error.

In figure 5.71, the simulated surface is put through the low pass Butterworth filter to remove the feed component, like the segment shown in figure 5.68. The calculated  $R_a$  for the surface in figure 5.71 is 13.98 nm. This is 2.38 nm from the mean  $R_a$  of the filtered experimental surface in table 5.12, and 0.46 nm from the minimum  $R_a$  value. The absence of spikes and other frequency components has likely contributed to this discrepancy. Overall the predicted low pass filtered  $R_a$  has an accuracy of 85 per cent compared with the experimental value. This means that by only considering the waviness error caused by the two main relative tool / workpiece vibrations, 85 per cent of the total surface finish error is described.

In figure 5.72, the  $R_a$  values for the surface with a feed rate of 2  $\mu\text{m}$  / rev of figure 5.64(a) is shown for each feed direction segment. Only the low pass filtered

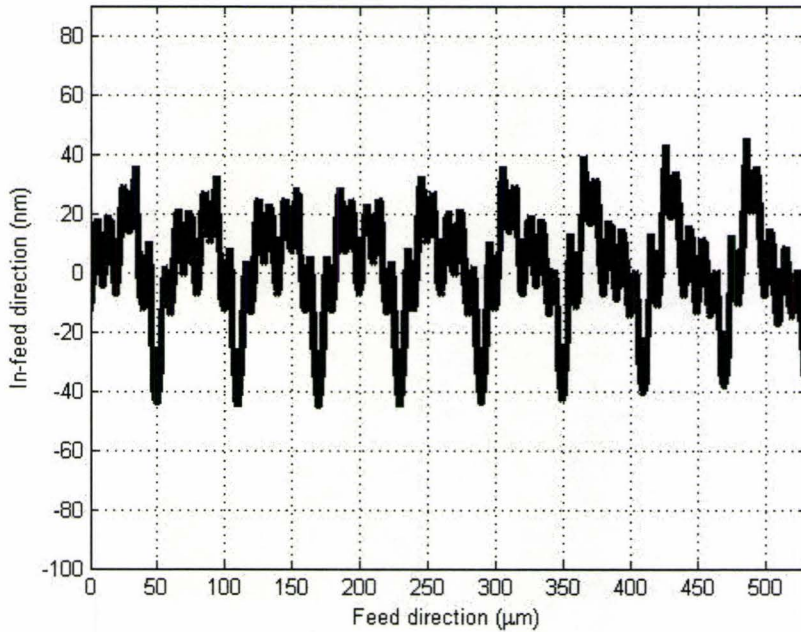


Figure 5.70: Simulated workpiece 1 cut surface based on the top two peaks of figure 5.62 and the filter curves of figures 5.41 and 5.40,  $f = 10 \mu\text{m} / \text{rev}$

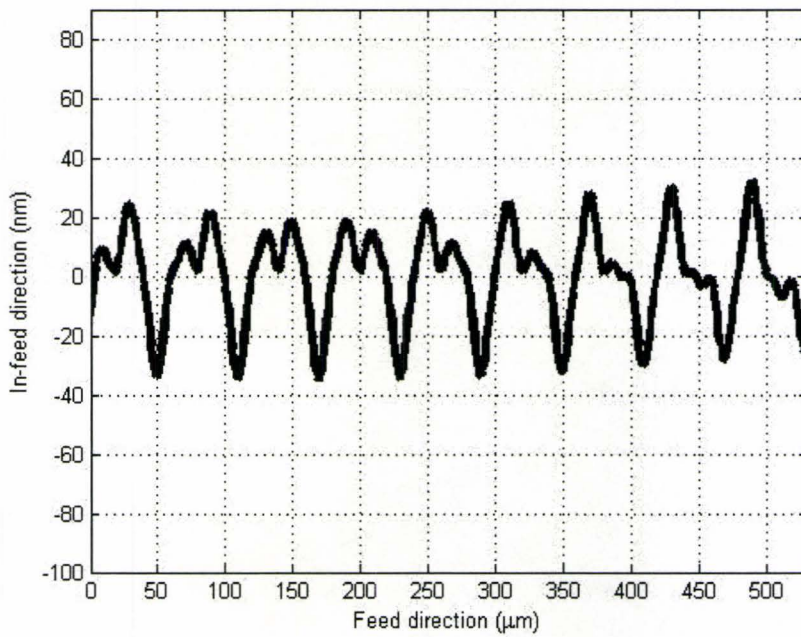


Figure 5.71: Simulated workpiece 1 cut surface based on the top two peaks of figure 5.62 and the filter curves of figures 5.41 and 5.40, with low pass filtering,  $f = 10 \mu\text{m} / \text{rev}$

$R_a$  is shown because the image resolution restricts the visible wavelength range as has already been discussed. The feed lines are not visible with this view, and yet a definite periodicity occurs in figures 5.64(a), 5.64(b) and 5.65, indicating relative tool / workpiece vibration.

The  $R_a$  results for this feed rate are summarized in table 5.13. The mean  $R_a$  error is considerably less for this surface than for the one machined with a feed rate of  $10 \mu\text{m} / \text{rev}$ , as predicted.

Overall, the mean arithmetic surface roughness,  $R_a$ , caused by the relative tool / workpiece vibration for the feed rate of  $2 \mu\text{m}$  is approximately 43 per cent of the  $R_a$  for the surface created with a feed rate of  $10 \mu\text{m} / \text{rev}$ . These findings are consistent with the predictive  $R_a$  curves of section 5.7.

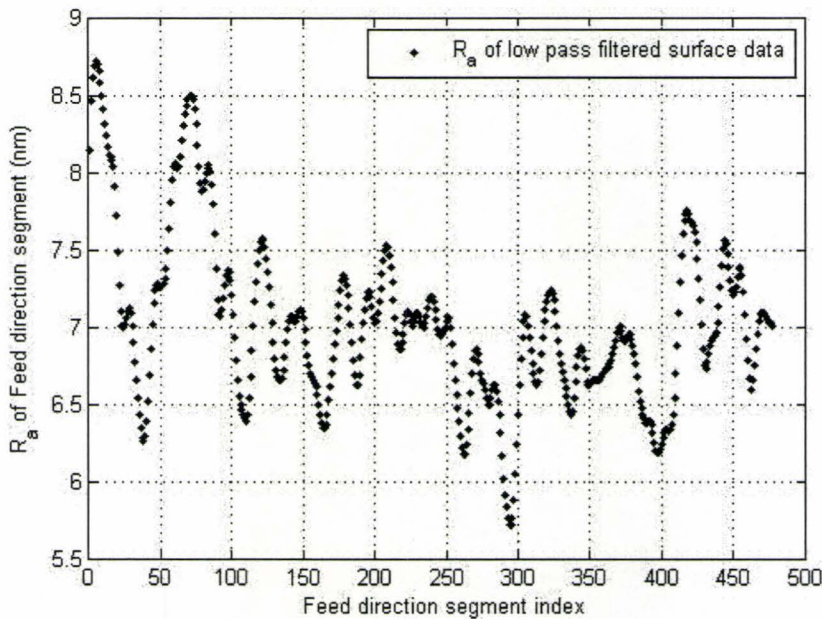


Figure 5.72:  $R_a$  for each feed direction segment of the white light interferometry workpiece 2 image,  $f = 2 \mu\text{m} / \text{rev}$ ,  $N = 1196.3 \text{ RPM}$ ,  $d = 5 \mu\text{m}$ ,  $R_n = 0.630 \text{ mm}$

$R_a$ measure (nm)	low pass filtered
mean	7.02
standard deviation	0.55
maximum	8.72
minimum	5.72

Table 5.13:  $R_a$  summary for the imported and low pass filtered white light interferometry data of figure 5.64(a) for workpiece 2

## 5.9 Chapter Summary

In this chapter, the transfer of vibrational amplitude to the ultra precision face turned workpiece surface has been described. This mapping has occurred using the surface finish lobes for guidance, and can be applied over a broadband of disturbance frequencies. It has been found that over a range of possible spatial frequencies, the workpiece surface error decreases with an increase in spatial frequency. Also, the effect of relative tool / workpiece motion on the ideal geometric surface roughness has been noted. Overall, better attenuation of relative tool / workpiece vibrations occurs with a decrease in the feed rate. Also, vibrations are again found to be the greatest source of ultra precision workpiece inaccuracy. The filtering effect of cutting parameters in ultra precision machining, specifically sections 5.2, 5.3 and 5.4, is the subject of publication [37]. The filtering and frequency shifting effect of cutting parameters on surface roughness error in the presence of relative tool / workpiece vibration, and the filtering effect of cutting parameters on vibration according to mean Arithmetic roughness,  $R_a$ , are the subject of publication [38].

## Chapter 6

# Contributions and Conclusions

Contributions of this thesis are listed in section 6.1 along with resulting publications, and conclusions are provided in section 6.2.

### 6.1 Contributions

Contributions of this Ph.D. thesis include:

- Ability to interpret localized surface finish data and to identify error sources
  - Development of theory
  - Procedure based on employing limited resolution and image size of the Zygo Newview 5000, white light surface topography measurement
  - Quantification of relative tool / workpiece vibrations as a significant source of surface finish error in ultra precision machining
- Surface finish lobes and application

- Broadband consideration of the effect of disturbance frequency on surface finish
- Study of machining parameters and their effect on surface finish with the presence of disturbance frequency
- Clear distinction between vibration induced waviness pattern and geometric surface roughness caused by the tool feed
- Identification of the interaction between cutting parameters and broadband disturbance frequency on the surface finish
  - The filtering effect on waviness error
  - The filtering effect on surface roughness error
  - The filtering effect on mean arithmetic roughness error
- Formulated method for improving surface finish in ultra precision machining
  - Based on developed theory

### 6.1.1 Publications

The following publications have resulted from this thesis:

#### Conference Proceedings

- P. A. Meyer, S. C. Veldhuis, and M. A. Elbestawi. Ultra Precision Machine Tool Structural Vibration and Performance Analysis. In *21st Canadian Congress of Applied Mechanics CANCAM 2007 Proceedings*, 2007. [35]

- P. A. Meyer, S. C. Veldhuis, and M. A. Elbestawi. Ultra Precision Machining Disturbance Frequency Extraction from Finished Surface Metrology. In *23rd ASPE (American Society of Precision Engineering) and 12th ICPE (International Conference on Precision Engineering)*, 2008. Portland, Oregon, U.S.A. [36]

### Submitted Journal Articles

- P. A. Meyer, S. C. Veldhuis, and M. A. Elbestawi. Predicting the Effect of Vibration on Ultra Precision Machining Surface Finish as Described by the Surface Finish Lobes. *International Journal of Machine Tools & Manufacture*, vol. 49, pp. 1165-1174, 2009. [39]
- P. A. Meyer, S. C. Veldhuis, and M. A. Elbestawi. The Filtering Effect of Cutting Parameters on Workpiece Accuracy in the Presence of Vibration for Ultra Precision Machining. *International Journal of Machine Tools & Manufacture*, 2009. Submitted. [37]
- P. A. Meyer, S. C. Veldhuis, and M. A. Elbestawi. Improving Surface Finish in Ultra Precision Machining by Mitigating the Vibrational Effect via Cutting Parameter Selection. *Precision Engineering*, 2009. Submitted. [38]

Additional technical presentations given during the Ph.D. thesis include [34] and [35].

## 6.2 Conclusions

In this thesis, the effect of unwanted relative tool / workpiece vibrations on the ultra precision diamond face turned workpiece surface has been studied. Waviness patterns caused by unwanted relative tool / workpiece vibrations on the workpiece surface were identified as a major source of inaccuracy. Then, the repeating nature of the waviness pattern on the workpiece surface in the feed direction was quantified with the surface finish lobes. Using the surface finish lobes for guidance, the filtering effect of the machining parameters on the manifestation of vibrations on the cut workpiece surface was identified. Finally, the improved surface achievable with a lower feed rate was explained via the developed theory. It was shown that while a slower feed rate does have a smaller ideal geometric surface roughness, in ultra precision machining the attenuation of unwanted vibrations by cutting parameters is the key reason for the improvement in surface finish. Overall, with the development of this framework, the accuracy enhancement of ultra precision machining is facilitated.

# Appendix A

## Additional Experimental Information

### A.1 Sensor Details

Details of sensors used in testing are provided in table A.1 from [23].

Accelerometer	Kistler 8702B25	Kistler 8702B50
Threshold nom. ( <i>grms</i> )	0.002	0.004
Sensitivity $\pm 5\%$ (mV / g)	200	100
Resonant Frequency mounted, nom. (kHz)	54	54
Frequency Response $\pm 5\%$ (Hz)	1 ... 8000	0.5 ... 10000
Mass (sic.) (grams)	8.7	8.7

Table A.1: In-situ vibration measurement accelerometer, selected specifications [23]

## A.2 *In Situ* Cutting Accelerometer Data

### A.2.1 Spindle Speed of 1000 RPM and Feed Rate of 2 micrometres per revolution, Radius 1

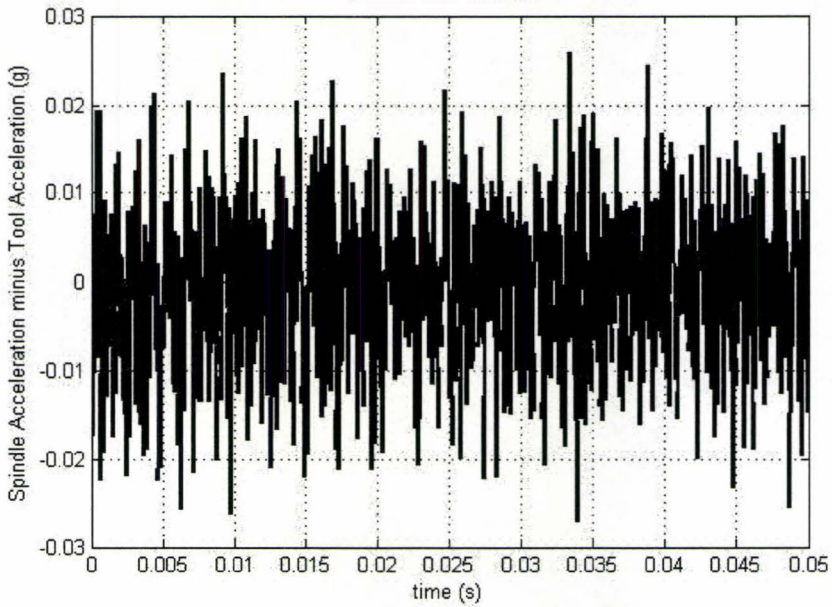


Figure A.1: Measured relative tool / spindle acceleration,  $N = 1000$  RPM,  $f = 2 \mu\text{m} / \text{rev}$

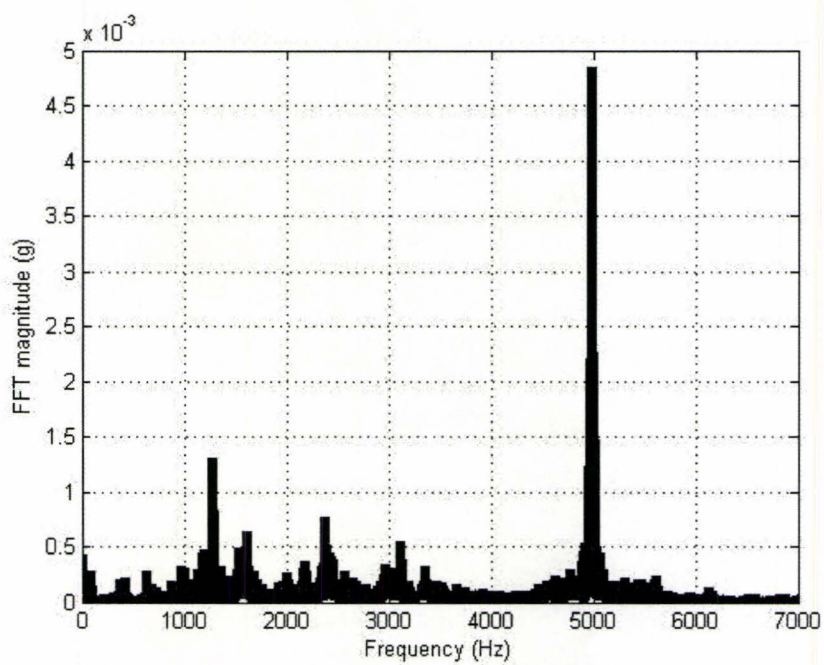


Figure A.2: Spindle acceleration FFT,  $N = 1000$  RPM,  $f = 2 \mu\text{m} / \text{rev}$ , number of averages = 103,  $\Delta f = 0.8548$  Hz

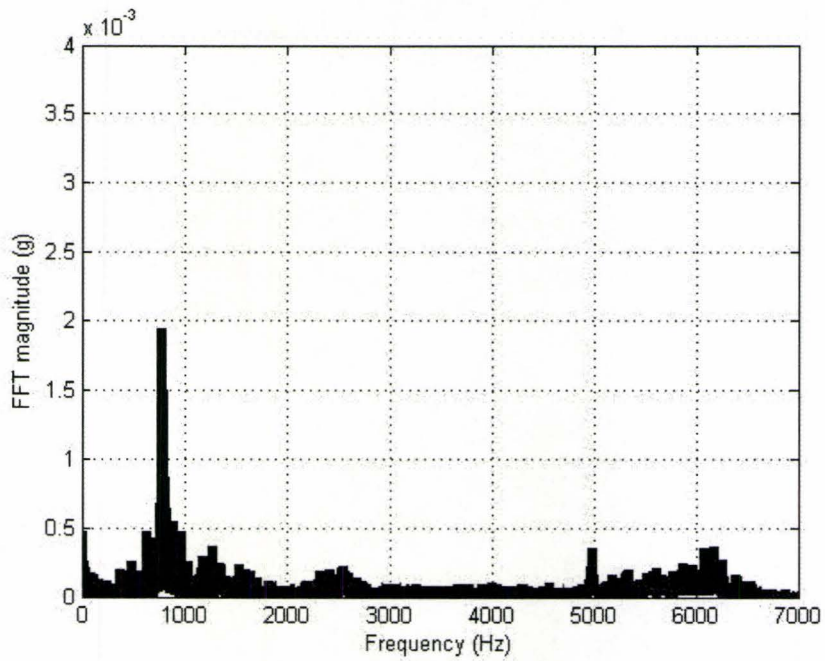


Figure A.3: Tool acceleration FFT,  $N = 1000$  RPM,  $f = 2 \mu\text{m} / \text{rev}$ , number of averages = 103,  $\Delta f = 0.8548$  Hz

### A.2.2 Spindle Speed of 1000 RPM and Feed Rate of 2 micrometres per revolution, Radius 2

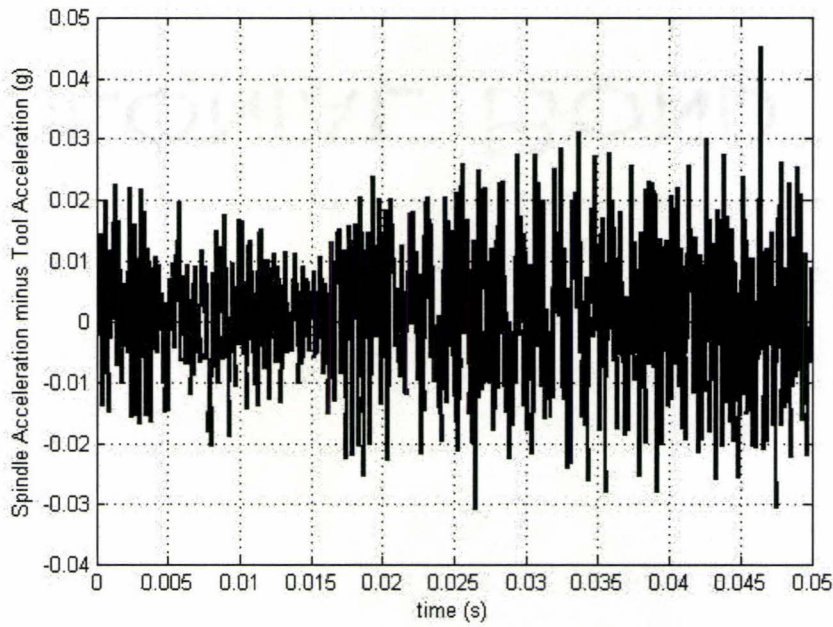


Figure A.4: Measured relative tool / spindle acceleration,  $N = 1000$  RPM,  $f = 2 \mu\text{m} / \text{rev}$

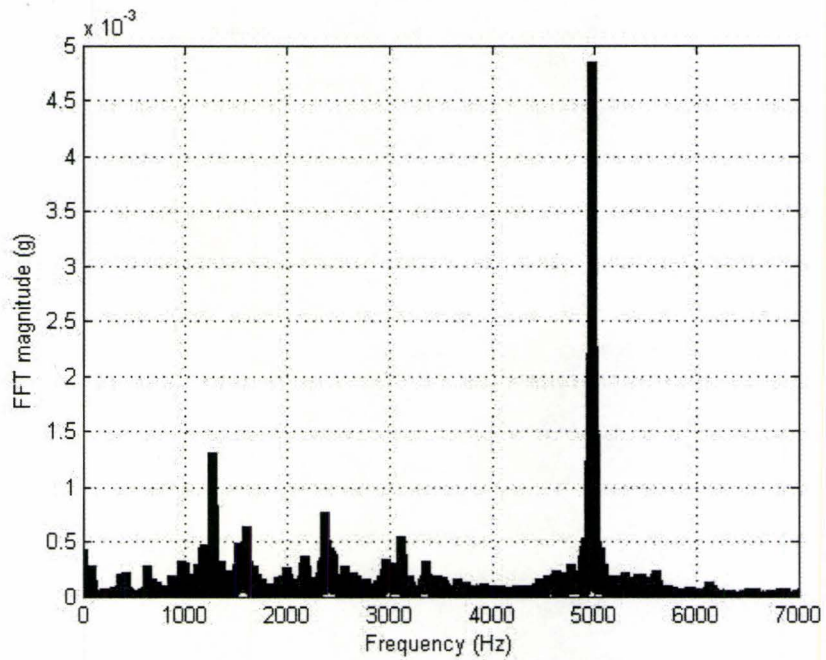


Figure A.5: Spindle acceleration FFT,  $N = 1000$  RPM,  $f = 2 \mu\text{m} / \text{rev}$ , number of averages = 103,  $\Delta f = 0.8548$  Hz

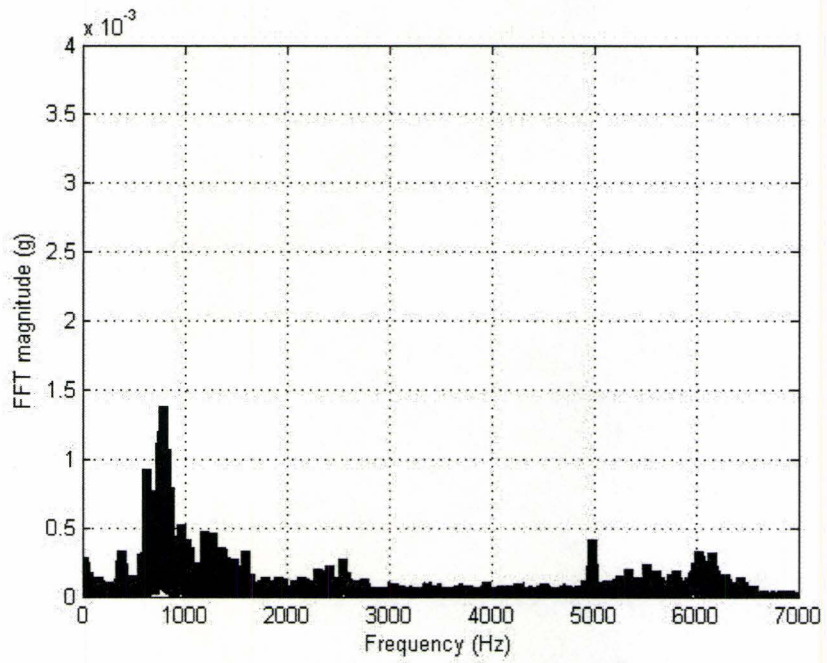


Figure A.6: Tool acceleration FFT,  $N = 1000$  RPM,  $f = 2 \mu\text{m} / \text{rev}$ , number of averages = 103,  $\Delta f = 0.8548$  Hz

### A.2.3 Spindle Speed of 1201.3 RPM and Feed Rate of 4 micrometres per revolution

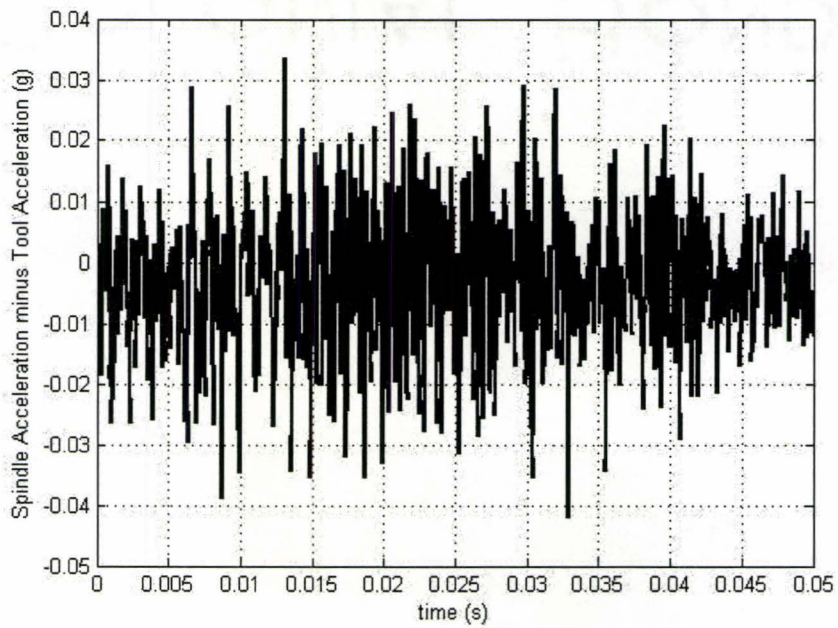


Figure A.7: Measured relative tool / spindle acceleration,  $N = 1201.3$  RPM,  $f = 4 \mu\text{m} / \text{rev}$

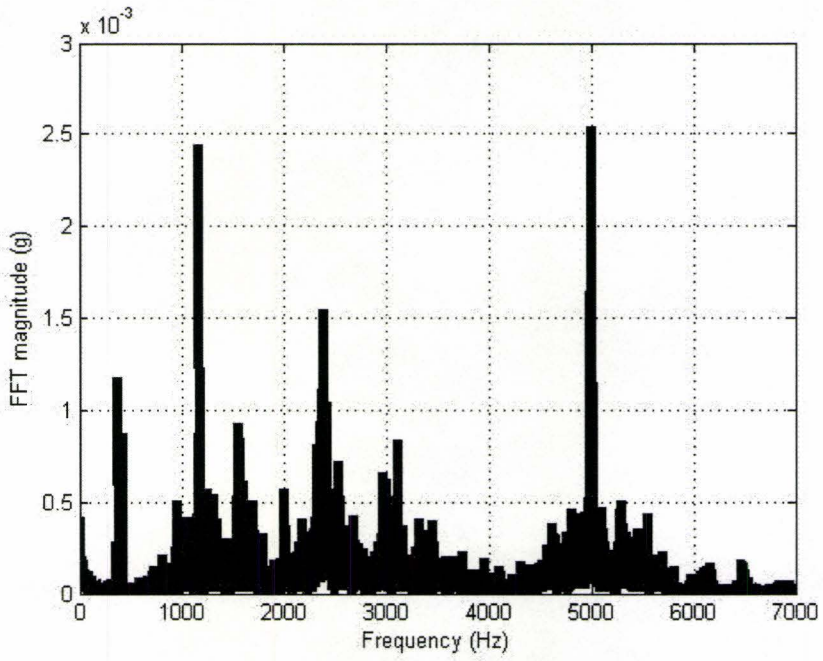


Figure A.8: Spindle acceleration FFT,  $N = 1201.3$  RPM,  $f = 4 \mu\text{m} / \text{rev}$ , number of averages = 103,  $\Delta f = 0.8548$  Hz

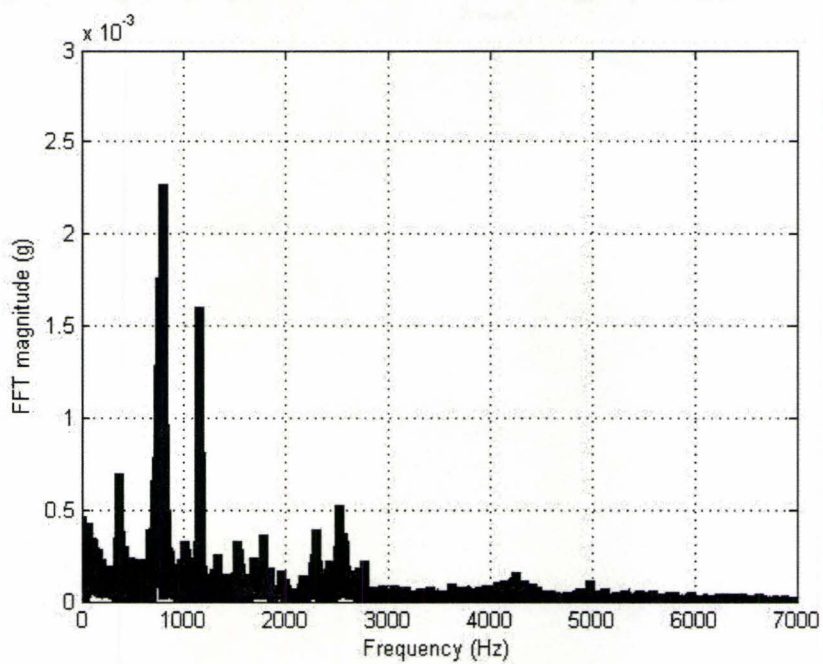


Figure A.9: Tool acceleration FFT,  $N = 1201.3$  RPM,  $f = 4 \mu\text{m} / \text{rev}$ , number of averages = 103,  $\Delta f = 0.8548$  Hz

### A.2.4 Spindle Speed of 1196.3 RPM and Feed Rate of 10 micrometres per revolution

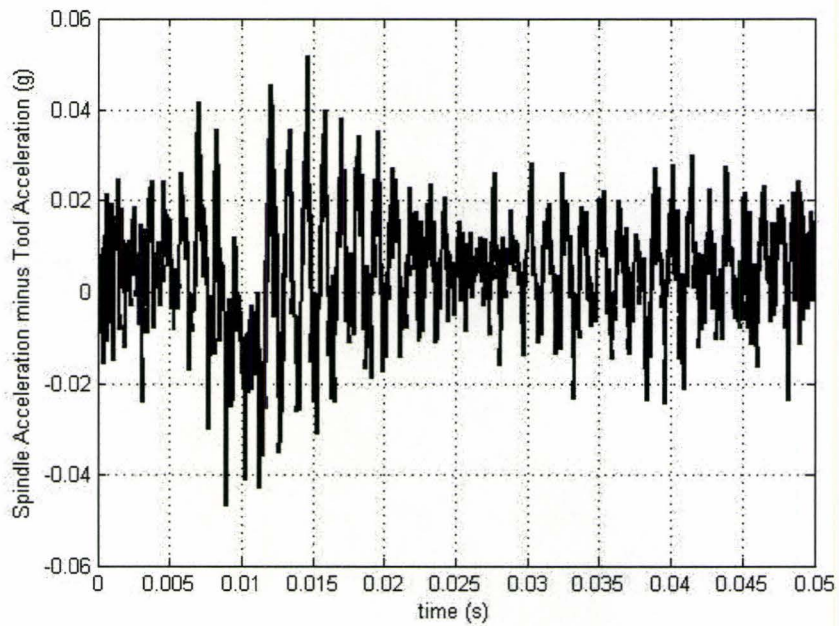


Figure A.10: Measured relative tool / spindle acceleration,  $N = 1196.3$  RPM,  $f = 10 \mu\text{m} / \text{rev}$

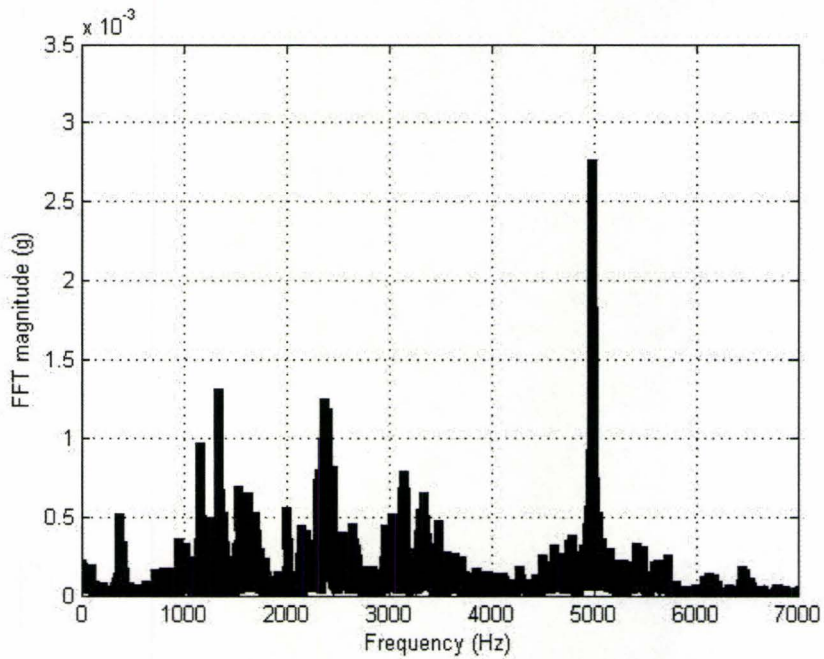


Figure A.11: Spindle acceleration FFT,  $N = 1196.3$  RPM,  $f = 10 \mu\text{m} / \text{rev}$ , number of averages = 103,  $\Delta f = 0.8548$  Hz

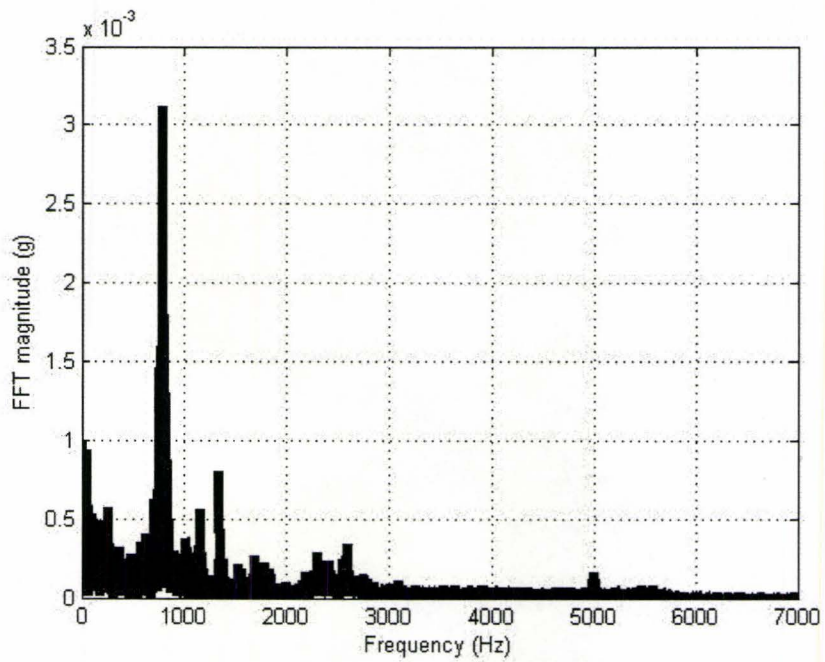


Figure A.12: Tool acceleration FFT,  $N = 1196.3$  RPM,  $f = 10 \mu\text{m} / \text{rev}$ , number of averages = 103,  $\Delta f = 0.8548$  Hz

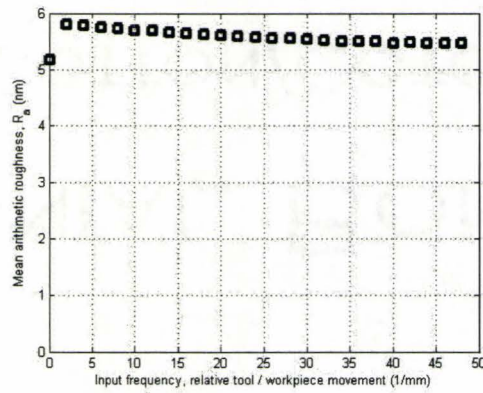
## Appendix B

# Mean Arithmetic Roughness, $R_a$ , Curves

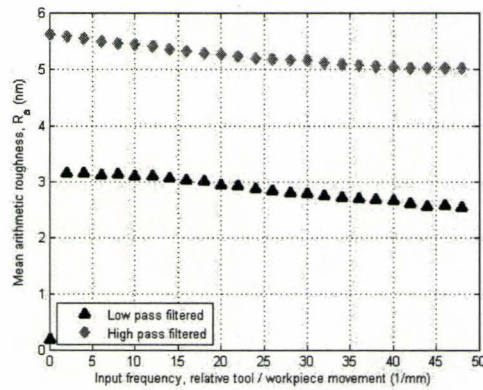
### B.1 Predicted Mean Arithmetic Roughness Curves for a Feed Rate of $10 \mu\text{m} / \text{rev}$

In figure B.1(a), the calculated  $R_a$  on a simulated surface without any filtering is shown. Then in figure B.1(b) the calculated  $R_a$  of the low pass and high pass filtered surfaces is shown. In this case, for a vibrational amplitude of 5 nm, the surface finish error caused by the feed marks exceeds the vibrational amplitude.

In figures B.2(a) through B.4(b), the same  $R_a$  curves are shown for vibrational amplitudes of 10 nm, 15 nm and 20 nm. As the vibrational amplitude is increased, the roughness observed is less and less caused by the feed and more and more a consequence of the relative tool / workpiece vibration. While the calculated  $R_t$  for this feed rate from equation 3.1 appears significance, in fact the waviness error is a



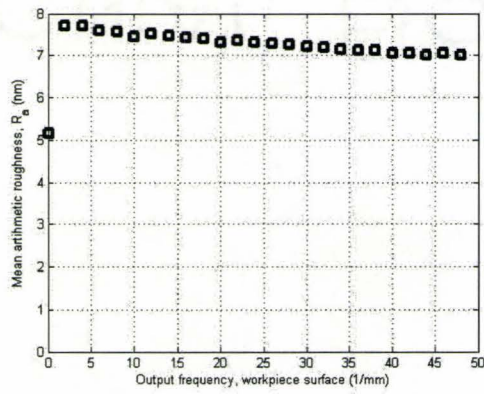
(a)  $R_a$  based on simulated cut workpiece surface for all spatial frequencies



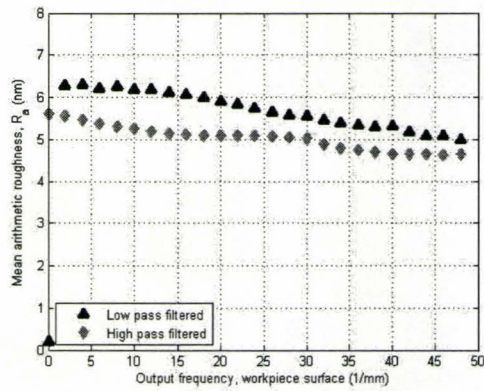
(b)  $R_a$  based on simulated and filtered cut workpiece surfaces

Figure B.1:  $R_a$  from simulated cut surface,  $d = 5 \mu\text{m}$ ,  $R_n = 0.630 \text{ mm}$ ,  $f = 10 \mu\text{m} / \text{rev}$ , and  $z_{amp} = 5 \text{ nm}$

greater contributor to surface finish error when the relative tool / workpiece movement is 10 nm or greater.

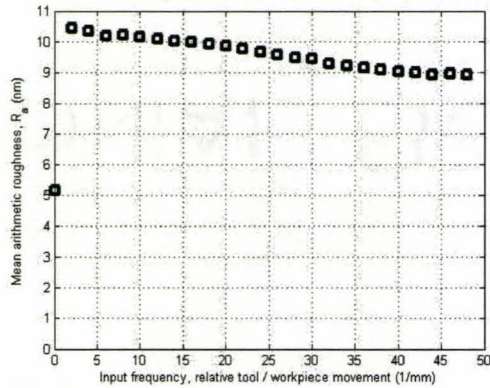


(a)  $R_a$  based on simulated cut workpiece surface for all spatial frequencies

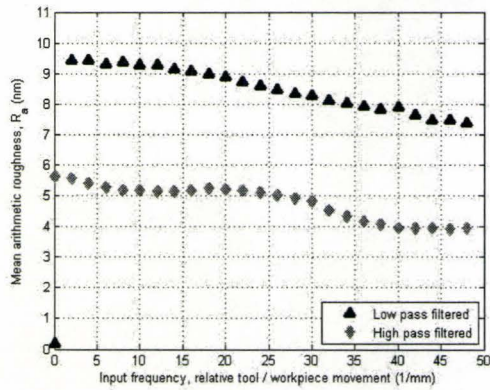


(b)  $R_a$  based on simulated and filtered cut workpiece surfaces

Figure B.2:  $R_a$  from simulated cut surface,  $d = 5 \mu\text{m}$ ,  $R_n = 0.630 \text{ mm}$ ,  $f = 10 \mu\text{m} / \text{rev}$ , and  $z_{amp} = 10 \text{ nm}$

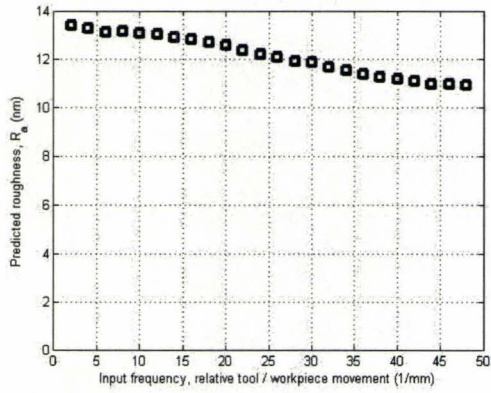


(a)  $R_a$  based on simulated cut workpiece surface for all spatial frequencies

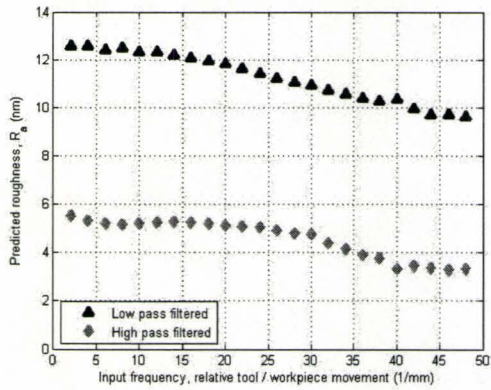


(b)  $R_a$  based on simulated and filtered cut workpiece surfaces

Figure B.3:  $R_a$  from simulated cut surface,  $d = 5 \mu\text{m}$ ,  $R_n = 0.630 \text{ mm}$ ,  $f = 10 \mu\text{m} / \text{rev}$ , and  $z_{amp} = 15 \text{ nm}$



(a)  $R_a$  based on simulated cut workpiece surface for all spatial frequencies

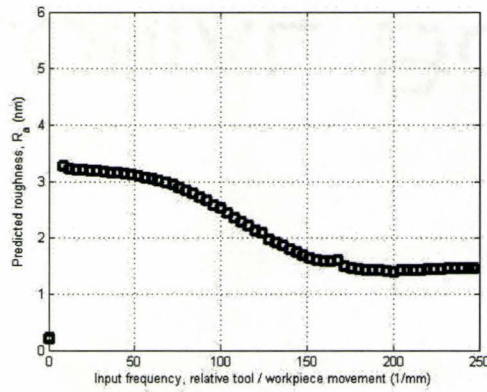


(b)  $R_a$  based on simulated and filtered cut workpiece surfaces

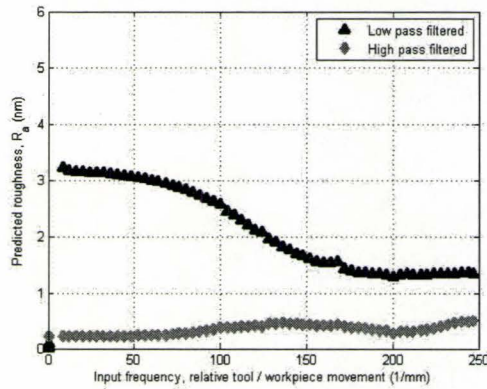
Figure B.4:  $R_a$  from simulated cut surface,  $d = 5 \mu\text{m}$ ,  $R_n = 0.630 \text{ mm}$ ,  $f = 10 \mu\text{m} / \text{rev}$ , and  $z_{amp} = 20 \text{ nm}$

## **B.2    Predicted Mean Arithmetic Roughness Curves for a Feed Rate of $2 \mu\text{m} / \text{rev}$**

The same plots are created in figures B.5(a) through B.8(b) for the feed rate of  $2 \mu\text{m} / \text{rev}$ . It is clear from the  $R_a$  values observed in the (b) portion of graphs that the surface error is caused primarily by the vibration and is therefore a function of waviness type errors. Overall, for both feed rates the  $R_a$  curves are very similar in shape to the filter curves produced earlier in chapter 5.

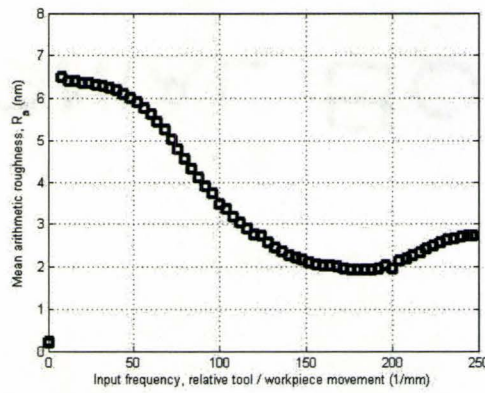


(a)  $R_a$  based on simulated cut workpiece surface for all spatial frequencies

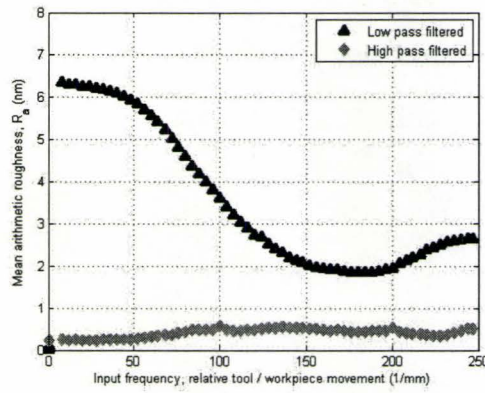


(b)  $R_a$  based on simulated and filtered cut workpiece surfaces

Figure B.5:  $R_a$  from simulated cut surface,  $d = 5 \mu\text{m}$ ,  $R_n = 0.630 \text{ mm}$ ,  $f = 2 \mu\text{m} / \text{rev}$ , and  $z_{amp} = 5 \text{ nm}$

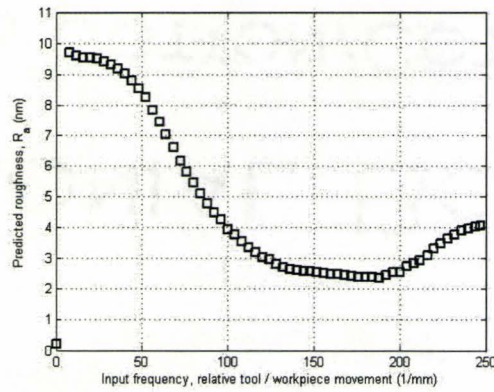


(a)  $R_a$  based on simulated cut workpiece surface for all spatial frequencies

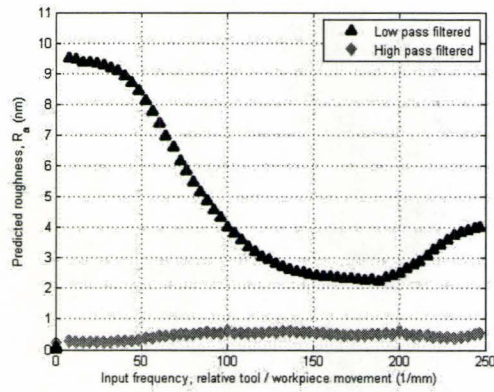


(b)  $R_a$  based on simulated and filtered cut workpiece surfaces

Figure B.6:  $R_a$  from simulated cut surface,  $d = 5 \mu\text{m}$ ,  $R_n = 0.630 \text{ mm}$ ,  $f = 2 \mu\text{m} / \text{rev}$ , and  $z_{amp} = 10 \text{ nm}$

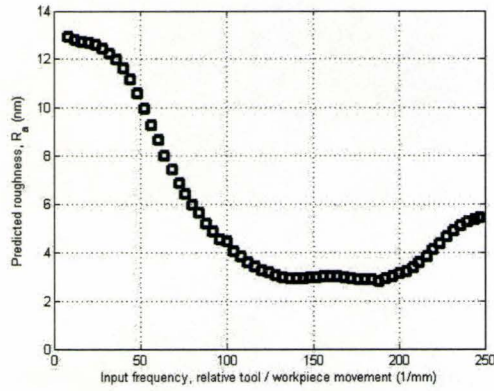


(a)  $R_a$  based on simulated cut workpiece surface for all spatial frequencies

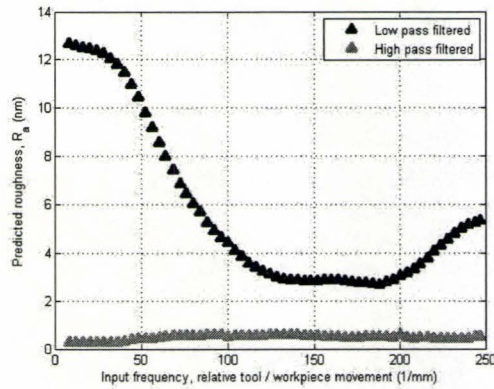


(b)  $R_a$  based on simulated and filtered cut workpiece surfaces

Figure B.7:  $R_a$  from simulated cut surface,  $d = 5 \mu\text{m}$ ,  $R_n = 0.630 \text{ mm}$ ,  $f = 2 \mu\text{m} / \text{rev}$ , and  $z_{amp} = 15 \text{ nm}$



(a)  $R_a$  based on simulated cut workpiece surface for all spatial frequencies



(b)  $R_a$  based on simulated and filtered cut workpiece surfaces

Figure B.8:  $R_a$  from simulated cut surface,  $d = 5 \mu\text{m}$ ,  $R_n = 0.630 \text{ mm}$ ,  $f = 2 \mu\text{m} / \text{rev}$ , and  $z_{amp} = 20 \text{ nm}$

## References

- [1] <http://www.itrc.org.tw/Research/Nano/instrument/zygo/zygo.htm>, 2009. Zygo Newview 5000 image source.
- [2] E. Abele and U. Fiedler. Creating stability lobe diagrams during milling. *Annals of the CIRP*, 53(1):309–312, 2004.
- [3] Yusuf Altintas. *Manufacturing Automation*. Cambridge University Press, Cambridge, 2000.
- [4] The American Society of Mechanical Engineers. *ASME B46.1-2002 Surface Texture (Surface Roughness, Waviness, and Lay) An American National Standard*. New York, N.Y., 2002. (Revision of ASME B46.1-1995).
- [5] G. Byrne, D. Dornfeld, and B. Denkena. Advancing cutting technology. *Annals of the CIRP*, 52(2):483–507, 2003.
- [6] C. F. Cheung, X. Q. Jiang, S. To, W. B. Lee, T. C. Kwok, and H. F. Li. A Study of Pattern and Feature Analysis of Surface Generation in Fast Tool Servo Machining of Optical Microstructures. In *Proceedings ASPE (American Society for Precision Engineering) 21st Annual Meeting, Monterey, California, 15-20 October, 2006*.
- [7] C. F. Cheung and W. B. Lee. Modelling and simulation of surface topography in ultra-precision diamond turning. *Proc Instn Mech Engrs Part B*, 214:463–480, 2000.
- [8] C. F. Cheung and W. B. Lee. Study of Factors Affecting the Surface Quality in Ultra-Precision Diamond Turning. *Materials and Manufacturing Processes*, 15(4):481–502, 2000.

- [9] C. F. Cheung and W. B. Lee. A theoretical and experimental investigation of surface roughness formation in ultra-precision diamond turning. *International Journal of Machine Tools & Manufacture*, 40:979–1002, 2000.
- [10] C. F. Cheung and W. B. Lee. Characterisation of nanosurface generation in single-point diamond turning. *International Journal of Machine Tools & Manufacture*, 41:851–875, 2001.
- [11] Chi Fai Cheung and Wing Bun Lee. A multi-spectrum analysis of surface roughness formation in ultra-precision machining. *Precision Engineering*, 24:77–87, 2000.
- [12] G. H. Choi and G. S. Choi. Application of minimum cross entropy to model-based monitoring in diamond turning. *Mechanical Systems and Signal Processing*, 10:615–631, 1996.
- [13] Marc Crudele and Thomas R. Kurfess. Implementation of a fast tool servo with repetitive control for diamond turning. *Mechatronics*, 13:243–257, 2003.
- [14] L. De Chiffre, H. Kunzmann, G. N. Peggs, and D. A. Lucca. Surfaces in precision engineering, microengineering and nanotechnology. *Annals of the CIRP*, 52/2/2003:1–18, 2003.
- [15] D. B. DeBra. Vibration isolation of precision machine tools and instruments. *Annals of the CIRP*, 41(2):711–718, 1992.
- [16] D. Dornfeld, S. Min, and Y. Takeuchi. Recent Advances in Mechanical Micro-machining. *Annals of the CIRP*, 55(2):745–768, 2006.
- [17] G. F. Franklin, J. D. Powell, and A. Emami-Naeini. *Feedback Control of Dynamic Systems*. Addison-Wesley Publishing Company, Inc., Don Mills, Ontario, 1986.
- [18] G. F. Franklin, J. D. Powell, and M. Workman. *Digital Control of Dynamic Systems*. Addison Wesley Longman, Inc., Don Mills, Ontario, 3rd edition, 1998.
- [19] Cyril M. Harris and Allan G. Piersol, editors. *Harris' Shock and Vibration Handbook*. McGraw-Hill Companies, Inc., New York, NY, 5th edition, 2002.
- [20] N. Ikawa, R. R. Donaldson, R. Komanduri, W. König, P. A. McKeown, T. Mori-waki, and I. F. Stowers. Ultraprecision metal cutting - the past, the present and the future. *Annals of the CIRP*, 40(2):587–594, 1991.

- [21] Renato Goulart Jasinevicius, Jaime Gilberto Duduch, Arthur Jose Vieira Porto, and Benedito Morais Purquerio. Critical aspects on the behavior of material from the mechanical tool-workpiece interaction in single point diamond turning. *Journal of the Brazilian Society of Mechanical Sciences*, 21:509–518, 1999.
- [22] Kistler. Impulse Force Hammer. 9726A\_000-274a-05.05 Specifications, Kistler Instrument Corporation, 2005.
- [23] Kistler. K-Shear  $\otimes$  Accelerometers. 8702B\_000-239a-04.06 Specifications, Kistler Instrument Corporation., 2006.
- [24] Tae Jo Ko and Dong Woo Cho. Fuzzy pattern recognition for tool wear monitoring in diamond turning. *Annals of the CIRP*, 41/1/1992:125–128, 1992.
- [25] F. Koenigsberger and J. Tlustý. *Machine Tool Structures*, volume 1. Pergamon Press, Toronto, 1970.
- [26] R. Komanduri and L. M. Raff. A review on the molecular dynamics simulation of machining at the atomic scale. *Proc Instn Mech Engrs*, 215 Part B:1639–1672, 2001.
- [27] W. B. Lee and C. F. Cheung. A dynamic surface topography model for the prediction of nano-surface generation in ultra-precision machining. *International Journal of Mechanical Sciences*, 43:961–991, 2003.
- [28] X. Liu and K. Cheng. Modelling the Machining Dynamics of Peripheral Milling. *International Journal of Machine Tools & Manufacture*, 45, 2005.
- [29] Nuno M. M. Maia and Júlio M. M. Silva, editors. *Theoretical and Experimental Modal Analysis*. Research Studies Press Ltd., Taunton, Somerset, England, 1997.
- [30] Eric R. Marsh and Adam J. Schaut. Measurement and simulation of regenerative chatter in diamond turning. *Precision Engineering*, 22(4):252–257, October 1998.
- [31] T. Masuzawa. State of the art of micromachining. *Annals of the CIRP*, 49(2):1–16, 2000.
- [32] MathWorks. *The Student Edition of MATLAB: Version 4: User's Guide / the Mathworks Inc.* Prentice-Hall, Inc., Englewood Cliffs, New Jersey 07632, 1995.

- [33] Joseph McGeough, editor. *Micromachining of Engineering Materials*. Marcel Dekker, Inc., 2002. Chapter 5, by John Corbett, Cranfield University, Bedford, England.
- [34] P. A. Meyer. Enhancing the Accuracy of Ultra Precision Machining with Active Vibration Isolation. Poster submitted to the MMRI Board of Advisors Poster Competition, MMRI Open House, November 22, 2004.
- [35] P. A. Meyer, S. C. Veldhuis, and M. A. Elbestawi. Enhancing the Accuracy of Ultra Precision Machining with Active Vibration Isolation. In *McMaster University Women in Science and Engineering (WISE) Initiative First International Women's Day Research Conference, Hamilton, Ontario, Canada, 2007*.
- [36] P. A. Meyer, S. C. Veldhuis, and M. A. Elbestawi. Ultra Precision Machining Disturbance Frequency Extraction from Finished Surface Metrology. In *23rd ASPE (American Society of Precision Engineering) and 12th ICPE (International Conference on Precision Engineering)*, 2008. Portland, Oregon, U.S.A.
- [37] P. A. Meyer, S. C. Veldhuis, and M. A. Elbestawi. The Filtering Effect of Cutting Parameters on Workpiece Accuracy in the Presence of Vibration for Ultra Precision Machining. *International Journal of Machine Tools & Manufacture*, 2009. Submitted.
- [38] P. A. Meyer, S. C. Veldhuis, and M. A. Elbestawi. Improving Surface Finish in Ultra Precision Machining by Mitigating the Vibrational Effect via Cutting Parameter Selection. *Precision Engineering*, 2009. Submitted.
- [39] P. A. Meyer, S. C. Veldhuis, and M. A. Elbestawi. Predicting the Effect of Vibration on Ultra Precision Machining Surface Finish as Described by the Surface Finish Lobes. *International Journal of Machine Tools & Manufacture*, 49:1165–1174, 2009.
- [40] A. V. Oppenheim, A. S. Willsky, and I. T. Young. *Signals and Systems*. Prentice-Hall, Inc., Englewood Cliffs, New Jersey 07632, 1983.
- [41] Eugene I. Rivin. Vibration isolation of precision equipment. *Precision Engineering*, 17:41–56, 1995.
- [42] J. Roblee. Telephone meeting with Dr. Jeffrey W. Roblee, Vice President Engineering, Precitech Inc., August 17 2005.

- [43] T. Sata, M. Li, S. Takata, H. Hiraoka, C. Q. Li, . Z. Xing, and X. G. Xiao. Analysis of Surface Roughness Generation in Turning Operation and its Applications. *Annals of the CIRP*, 34(1):473–476, 1985.
- [44] SDRL. Structural Dynamics Research Lab (SDRL) at University of Cincinnati, Vibrations III (20-263-663) Course Notes. <http://www.sdrl.uc.edu/academic-course-info/vibrations-iii-20-263-663/>, 2008.
- [45] Milton C. Shaw. *Metal Cutting Principles*. Oxford University Press, New York, 1984.
- [46] A. H. Slocum. *Precision Machine Design*. Prentice-Hall, Inc., New Jersey, 1992.
- [47] Alex Sohn, Lucas Lamonds, and Ken Garrard. Modeling of Vibration in Single-Point Diamond Turning. In *Proceedings ASPE (American Society for Precision Engineering) 21st Annual Meeting, Monterey, California, 15-20 October, 2006*.
- [48] David A. Stephenson and John S. Agapiou. *Metal Cutting Theory and Practice*. Marcel Dekker, Inc., 1997.
- [49] G. Sweeney. *Vibration of Machine Tools*. The Machinery Publishing Co. Ltd., Brighton, Sussex, 1971.
- [50] Gan Sze-Wei, L. Han-Seok, M. Rahman, and F. Watt. A Fine Tool Servo System for Global Position Error Compensation for a Miniature Ultra-Precision Lathe. *International Journal of Machine Tools & Manufacture*, 47:3102–3110, 2007.
- [51] Shuhei Takasu, Masami Masuda, and Takahsi Nighiguchi. Influence of Study Vibration with Small Amplitude Upon Surface Roughness in Diamond Machining. *Annals of the CIRP*, 34(1):463–467, 1985.
- [52] N. Taniguchi. *Nanotechnology: Integrated Processing Systems for ultra-Precision and Ultra-Fine Products*. Oxford University Press, 1996. (cited in [33]).
- [53] George Thusty. *Manufacturing Processes and Equipment*. Prentice Hall, Upper Saddle, New Jersey, 2000.
- [54] J. Thusty, S. Smith, and C. Zamudio. Evaluation of cutting performance of machining centers. *Annals of the CIRP*, 40(1):405–410, 1991.
- [55] J. Thusty, W. Zaton, and F. Ismail. Stability Lobes in Milling. *Annals of the CIRP*, 32(1):309–313, 1983.

- [56] Stephen Albert Tobias. *Machine-Tool Vibration*. Blackie, London, 1965.
- [57] J & M Diamond Tool. J & m diamond tool: Pcd and cbn information. 2001. <http://www.diamondtool.com/pcdcbm2a.html#anchor40084>.
- [58] Edward M. Trent and Paul K. Wright. *Metal Cutting*. Butterworth-Heinemann, Boston, 4th edition, 2000.
- [59] Jiachun Wang, Dan Li, and Dong Shen. Integrated Passive and Active Vibration Control of Ultra-Precision Lathe. *High Technology Letters*, 6(4):25–28, Dec 2000.
- [60] Gai Yuxian, Li Dan, and Dong Shen. Active vibration isolation system for sub-microultra-precision turning machine. *High Technology Letters*, 6(3):40–43, August 2000.
- [61] C.L. Zhang, D.Q. Mei, and Z.C. Chen.  $H_\infty / \mu$  robust control of vibration for an ultra-precision grinding machine. *Key Engineering Materials*, 259-260:682–686, 2004.
- [62] Zygo Corporation. *Newview 5000 System Manual OMP-0471G*, 2002.